SAPIENZA
UNIVERSITÀ DI ROMA

A search for Long-Lived Particles with the ATLAS Experiment

Scuola di dottorato Vito Volterra

Dottorato di Ricerca in Fisica – XXXIV Ciclo

Candidate

Iacopo Longarini

Thesis Advisor

Prof. Stefano Giagu

A thesis submitted in partial fulfillment of the requirements
for the degree of Doctor of Philosophy in Physics

January 2022

Thesis defended on 31 May 2022
in front of a Board of Examiners composed by:

Prof. Riccardo Bellan
Prof. Irene Di Palma
Prof. Maura Pavan

A search for Long-Lived Particles with the ATLAS Experiment
Ph.D. thesis. Sapienza – University of Rome

This thesis has been typeset by LaTeX and the Sapthesis class.

Version: May 27, 2022

Author's email: iacopo.longarini@gmail.com

To my grandmother, Iolanda,
and her example of a life lived
with happiness and love

Abstract

It is well assessed that the Standard Model (SM) correctly predicts the behaviour of the Universe at the infinitely small scale, but is not the definitive theory that we are looking for.

In this thesis a search for new phenomena is performed using $139\,\mathrm{fb}^{-1}$ of pp collision data provided by the Large Hadron Collider (LHC) and collected by the ATLAS Experiment, aiming to identify light neutral particles that decay outside the innermost region of the detector. Such exotic decays yield collimated bundles of SM leptons or quarks, identified exploiting dedicated triggers, custom reconstructed objects and discriminated against the SM and non-collision background with sophisticated deep-learning-based classifiers. The results of the search show no disagreement with the expected backgrounds and are used to constrain simplified models that predict the existence of long-lived particles.

To further extend the constraint put by the searches for visible decays of long-lived particles, the result of an ATLAS search for events with large energetic jets and missing transverse momentum is reinterpreted in terms of two different models. Thanks to this approach, the case where such exotic particles are recoiling against an initial-state-radiation jet and leave ATLAS without being detected can be constrained.

Finally, this thesis will cover a study dedicated to the upgrade of the trigger system of the ATLAS experiment, that is necessary for the correct operation under the conditions of the High-Luminosity LHC. Studies related to the firmware logic and to the radiation-tolerance tests of the on-detector electronic boards are presented.

Contents

Introduction

The ultimate goal of particle physics is to build a theory capable of describing the mechanisms that govern the Universe at the infinitely small scale.

So far, the Standard Model has provided a description of the interactions of all known fundamental particles. Its predictions are continuously being tested by the particle physics community, which decade after decade has found perfect agreement with experimental data. Nearly ten years ago, the observation of a particle consistent with the Higgs Boson reconfirmed the validity of the SM and, since then, the experiments at the Large Hadron Collider have made great efforts to study and measure its properties, which have always been found in perfect agreement with the theoretical predictions.

However, it is well known that the Standard Model cannot be the complete theory that we are looking for. *New Physics* is needed to describe experimental phenomena not predicted by the SM, or to solve theoretical problems inherent in the theory. The search for this New Physics has been pursued by the particle physics community for decades, but no solution has yet been found.

The masses of new particles predicted by many beyond-Standard Model theories have been constrained up to the TeV scale. In this thesis, the search for New Physics will be addressed with a different approach, probing a different region of the *lifetime axis*. Particles with macroscopic proper lifetimes are everywhere in the SM; therefore, the search for new phenomena predicting exotics *Long-Lived Particles* (LLPs) is well motivated from both the theoretical and experimental point of view.

Although LLPs are predicted by many beyond-Standard Model theories, this thesis will put the attention on simplified models: minimal extensions of the Standard Model which can be derived as limits of more complete theoretical frameworks. In many simplified models an entire *Dark Sector* of particles is predicted, along with a electromagnetic-like force with its massive mediator: the *dark photon*. These models can be probed by making a minimal assumption: the ordinary photon is supposed to mix with the dark photon with a small coupling constant, which together with its mass originates its long proper lifetime. In this way a rich phenomenology is obtained, but a more interesting scenario for experiments at the LHC is when exotics decays of the Higgs boson produce such long-lived particles in the final state.

These assumptions are exploited in this thesis, where the search for long-lived dark photons is performed in the outermost region of the ATLAS detector, attempting to probe the region of the phase space where the dark photon is light enough to yield displaced decays in leptons or light quarks that are extremely collimated (displaced *Dark-Photon Jets* or *Lepton Jets*). This experimental signature is incredibly challenging, since custom object reconstruction is necessary, sophisticated triggers for long-lived particles must be used and advanced techniques for an efficient background rejection need to be adopted.

The results that are presented here are based on the entire dataset collected between 2015 and 2018, corresponding to $139\,\mathrm{fb}^{-1}$ of data and have been published in [1]. The outcome of the search show that the ATLAS Experiment is competitive to other dedicated searches based on different production modes of the dark photon. Previous results on this signature were published by the ATLAS Collaboration in [2], which are superseded by the ones presented in this thesis. The improvements brought by this work include a revised event selection and the use of dedicated deep-learning-based taggers that play a crucial role in the background rejection.

Theoretical models that predict long-lived particles usually adopt mechanisms like small couplings or compressed scenarios, where the proper decay lifetimes of a given particle can be arbitrarily large. In such cases, dedicated signatures like the displaced Dark-Photon Jet become less and less efficient as more LLPs escape the detector before decaying. In this thesis, this scenario is probed by exploiting events where missing transverse momentum recoils against a highly energetic jet (*monojet* events). Latest results from the ATLAS monojet analysis [3] are reinterpreted to put constraints on the scenario of extremely long-lived particles.

The analyses presented in this thesis leverage the most recent ATLAS data. The next series of runs of data-taking will start in 2022, but to achieve an even higher statistic sensitivity, the LHC will undergo a series of upgrades that will increase its luminosity by a factor five. In its High-Luminosity phase, the number of simultaneous interactions per bunch crossing happening at the LHC will increase up to 200, providing an even more challenging environment in which precision tests of the Standard Model and New Physics searches will be performed by the experiments. One of the main limiting aspect for this kind of searches at that time will be the trigger, upgrades of the ATLAS Muon Trigger are necessary given the harsh radiation environment at the High-Luminosity LHC and are carried out by many people involved in the collaboration. My personal contributions to the upgrade of the ATLAS Muon Barrel Trigger are also documented in this thesis.

This thesis is organised as follows. Chapter 1 gives a brief summary of the Standard Model and the theoretical frameworks related to the searches presented in this thesis. Chapter 2 describes LHC and the ATLAS Experiment and how the identification of physics objects is performed. Chapter 3 summarises the truth-level properties of the long-lived particle models studied in this thesis, as well as introducing the dedicated triggers and reconstructed objects that are defined for their search. After an overview of the challenging backgrounds in chapter 4, the displaced Dark-Photon-Jet analysis is presented with detail in chapter 5. Finally, chapter 6 gives detail on the reinterpretation study of the monojet analysis, while chapter 7 gives, after a brief introduction on the ATLAS Phase-II upgrade, an overview of the related studies to which I participated.

Personal contributions

I have been the main analyst of the displaced Dark-Photon-Jet analysis, of which details are given along chapters 3, 4 and 5. I was responsible of the production of simulated signal events, as well as of the development of the deep-learning-based classifiers that are used for the background suppression. In addition, I contributed to the analysis framework that processes data and simulated events, implementing the selection for the signal regions that exploit the gluon-gluon-fusion production mode of the Higgs boson. I defined the strategy for the background estimation and for the evaluation of the systematic uncertainties related to the aforementioned signal regions. Finally, I was responsible of the interpretation of the results of the analysis.

I contributed to the monojet reinterpretation study that is detailed in chapter 6, especially on the interpretation of models that involve long-lived dark photons. I have been editor of the ATLAS Public Note that document the result [4].

Concerning the studies on the upgrade of the ATLAS Muon Barrel Trigger presented in chapter 7, I developed the firmware for the on-detector boards and contributed to the irradiation tests of the voltage regulators of the boards.

All the figures including the *ATLAS* label have been adapted from papers published by the collaboration, while figures including the *ATLAS Preliminary* label are included in public notes or conference notes. In both cases a reference to the public paper or note, which has been internally reviewed by the collaboration, is reported. Other figures and material that has been adapted from published documents are accompanied with a reference to the original publication, while figures and tables without reference have been produced by me.

Chapter 1

Beyond the bounds of the Standard Model

The understanding of the world we live in has been a mission of mankind since its origin. As centuries passed, the evolution of science and technology allowed subsequent improvements of the techniques and the tools that we use to inspect nature.

Nowadays, our best tool describing nature from the microscopic point of view is the Standard Model of Elementary Particles, which provides a unified description of three of the four fundamental forces: the electromagnetic, strong and weak interactions, using the language of Quantum Field Theory (QFT). Until now, no experimental evidence that the gravitational interaction can be explained with QFT has been found.

This chapter gives a brief overview of the Standard Model and its current limitations, introducing the motivations for the search of long-lived particles at an experiment like ATLAS.

1.1 Quantum fields and their dynamics

The Standard Model gives a description of nature in terms of fundamental particles, i.e. particles with no substructure, as local fields (ψ) expressed as function of their space-time coordinate (x). The lagrangian formalism introduced in classical mechanics is extended to quantum field theory to provide its dynamics.

The SM dynamics is described in terms of a lagrangian density[1] $\mathcal{L}$, function of the field ψ and its derivatives $\partial_\mu\psi$, satisfying the principle of least action:

$$\delta\mathcal{S} = \delta \int d^4x\, \mathcal{L}(\psi, \partial_\mu\psi) = 0\,,$$

which corresponds the requirement of the action $\mathcal{S}$ to be stationary.

---

[1] As common practice in quantum field theories, the terms lagrangian and lagrangian density will be treated as equivalent.

The expression of the SM lagrangian ($\mathcal{L}_{\text{SM}}$) must be driven by the symmetries observed in nature. Noether theorem ensures that any continuous symmetry of the lagrangian yields a conserved current and charge. Hence, a formulation of $\mathcal{L}_{\text{SM}}$ must take into account translational, rotational and boost invariance, ensuring also gauge invariance under the local symmetry group

$$SU(3)_C \otimes SU(2)_L \otimes U(1)_Y \,.$$

The transformation group $SU(3)_C$ is related to the theory of Quantum Chromo-Dynamics (QCD), describing the strong nuclear force, and the $SU(2)_L \otimes U(1)_Y$ is the symmetry group of the unified electromagnetic and weak interactions. These will be briefly summarised in the next sections.

1.1.1 Electroweak interactions

Charged fermions are represented in quantum field theory as Dirac spinors (ψ), satisfying the Dirac lagrangian:

$$\mathcal{L} = \bar{\psi}(i\gamma^\mu \partial_\mu - m)\psi \,; \tag{1.1}$$

where γ^μ are the Dirac matrices and m is the mass term of the charged particle.

Electromagnetic interactions originate under the requirement of invariance under local transformations of the $U(1)$ symmetry group:

$$\psi(x) \rightarrow \psi'(x) = e^{i\alpha(x)}\psi(x)$$

in which $\alpha(x)$ defines the transformation in each point of the space-time. Equation 1.1 is invariant under such transformation if the electromagnetic field, A_μ, is introduced by replacing the ∂_μ operator with the covariant derivative:

$$D_\mu = \partial_\mu + ieA_\mu \,,$$

where e is the electric charge of the fermion. Including the kinetic term of the electromagnetic field, $-1/4F_{\mu\nu}F^{\mu\nu}$, of which the tensor field is defined as $F_{\mu\nu} = \partial_\nu A_\mu - \partial_\mu A_\nu$, the lagrangian of Quantum Electrodynamics (QED) can be obtained:

$$\mathcal{L} = \bar{\psi}(i\gamma^\mu D_\mu - m)\psi - \frac{1}{4}F_{\mu\nu}F^{\mu\nu} \,. \tag{1.2}$$

It is important to notice that the invariance under the $U(1)$ transformation holds only in the case of a massless A_μ field, which in this case corresponds to the massless photon (γ) observed in nature. Moreover, the electric charge conservation is directly implied by Noether theorem for this lagrangian and symmetry group.

The theory of electroweak interactions, proposed by Weinberg [5] and Salam [6], introduced the idea that the electrodynamics and the weak interactions, the latter described by the effective field theory introduced by Fermi, originate as manifestation of invariance under transformations of the same symmetry group:

$$SU(2)_L \otimes U(1)_Y \,.$$

The symmetry group $SU(2)_L$, in which the L stands for left-handed, allows for a parity-violating theory in which only the left-handed component of fermions and right-handed component of anti-fermions are interacting. Invariance under $SU(2)_L$ transformations originates the conservation of the isospin I; left-handed fermions are paired in isospin $I = 1/2$ doublets, while right-handed ones are $I = 0$ isospin singlets.

Fermions described by the Standard Model are grouped in leptons and quarks, where all of them are coupled to the electroweak interactions. Leptons can be arranged as the following left-handed doublets and right-handed singlets:

$$\begin{pmatrix} \nu_e \\ e \end{pmatrix}_L, e_R, \begin{pmatrix} \nu_\mu \\ \mu \end{pmatrix}_L \mu_R, \begin{pmatrix} \nu_\tau \\ \tau \end{pmatrix}_L, \tau_R$$

in which, for each family of leptons, only the left-handed neutrino is introduced, as no observation of an interacting right-handed neutrino has been made. A similar representation is introduced for the three quark families, of which both right and left-handed component is given for *up*-types (u, c, t) and *down*-types (d, s, b).

$$\begin{pmatrix} u \\ d \end{pmatrix}_L, u_R, d_R, \begin{pmatrix} c \\ s \end{pmatrix}_L, c_R, s_R, \begin{pmatrix} t \\ b \end{pmatrix}_L, t_R, b_R,$$

The $SU(2)_L$ invariance is preserved only if three massless vector fields are introduced: W^i_μ $(i = 1, 2, 3)$, with g being the coupling constant to SM fermions. On the other hand, the lagrangian must be also invariant under transformations of the group $U(1)_Y$, where the hypercharge Y is a function of the third component of the isospin (I_3) and the electrical charge (Q):

$$Y = 2(Q - I_3)\,;$$

to satisfy this invariance a fourth vector field B_μ must be introduced, with coupling g' to both left and right-handed fermions.

Given these requirements, a possible expression of the electroweak lagrangian for a generic fermionic field (ψ) is the following:

$$\mathcal{L}_{\text{EWK}} = \bar{\psi}_L i\gamma^\mu D_\mu \psi_L - \frac{1}{4}\sum_{i=(1,2,3)} W_{\mu\nu}W^{\mu\nu} - \frac{1}{4}B_{\mu\nu}B^{\mu\nu}\ ,$$

where the covariant derivative assumes the form:

$$D_\mu = i\partial_\mu + \sum_{i=(1,2,3)} \frac{i}{2} g\sigma_i W^i_\mu + g'YB_\mu\ , \tag{1.3}$$

in which σ are the Pauli matrices and the tensors $W^i_{\mu\nu}$ and $B_{\mu\nu}$ are defined as:

$$\begin{aligned} W^{\mu\nu}_i &= \partial_\nu W^i_\mu - \partial_\mu W^i_\nu + i\varepsilon^{ijk} W^j_\mu W^k_\nu \\ B^{\mu\nu} &= \partial_\nu B_\mu - \partial_\mu B_\nu\,. \end{aligned}$$

The four massless vector bosons introduced above are not the ones observed in nature, which instead originate as a combination of the four. The W^+ and W^- bosons of the weak interaction arise from the combination of W^1 and W^2:

$$W^{\pm}_{\mu} = \frac{1}{\sqrt{2}}(W^1_{\mu} \mp iW^2_{\mu}),$$

while the photon and the Z boson are given by a mixing of the B and W^3 fields:

$$\begin{aligned} A_{\mu} &= \sin\theta_W W^3_{\mu} + \cos\theta_W B_{\mu}, \\ Z_{\mu} &= \cos\theta_W W^3_{\mu} - \sin\theta_W B_{\mu}, \end{aligned}$$

in which the mixing angle θ_W is known as the Weinberg angle and can be expressed in terms of the couplings g and g'

$$\begin{aligned} \sin\theta_W &= \frac{g'}{\sqrt{g^2 + g'^2}}, \\ \cos\theta_W &= \frac{g}{\sqrt{g^2 + g'^2}}, \end{aligned}$$

the coupling constant of the A_{μ} field, e, is written in terms of g (g') and θ_W:

$$e = g\sin\theta_W = g'\cos\theta_W .$$

This kind of mixing ensures that the $W^{\pm}$ bosons only interact with the left-handed component of the fermionic field, while instead the Z boson couples to both left and right-handed particles, although with different couplings.

Again, as mentioned for the QED lagrangian, the $SU(2)_L \otimes U(1)_Y$ symmetry holds only if the vector bosons are massless. Since experimental results show that the interaction of W and Z bosons is limited to a short-range, a corresponding mass term for these three vector bosons must be introduced in such a way that the mass of the W and Z is dynamically generated.

1.1.2 The Brout-Englert-Higgs Mechanism

The problem of a mass term violating the gauge invariance is solved by the Brout-Englert-Higgs mechanism. In the context of a lagrangian which is symmetric under $SU(2)_L \otimes U(1)_Y$, the Brout-Englert-Higgs mechanism introduces a isospin doublet of complex scalar fields:

$$\Phi = \begin{pmatrix} \phi^+ \\ \phi^0 \end{pmatrix} = \frac{1}{\sqrt{2}} \begin{pmatrix} \phi_1 + i\phi_2 \\ \phi_3 + i\phi_4 \end{pmatrix} .$$

In the lagrangian, a corresponding kinetic term and a potential (V) are introduced:

$$\mathcal{L} = (D^{\mu}\Phi)^{\dagger}(D_{\mu}\Phi) - V(\Phi), \tag{1.4}$$

where the potential can be expressed as

$$\begin{aligned} V(\Phi) &= \mu^2 \left(\Phi^\dagger \Phi\right) + \lambda \left(\Phi^\dagger \Phi\right)^2 \\ &= \mu^2 \Phi^2 + \lambda \Phi^4 \,. \end{aligned}$$

The parameter λ must be positive for the potential to have a finite minimum, which must be the case for a stable theory, while the sign of μ^2 determines if the minimum is degenerate or not. If $\mu^2 > 0$ the potential has a minimum at

$$\phi_1 = \phi_2 = \phi_3 = \phi_4 = 0 \,,$$

while for $\mu^2 < 0$ the minimum is degenerate on the hyper-surface defined by the condition

$$\Phi^\dagger \Phi = \sqrt{\frac{-\mu}{\lambda}} \,.$$

If we choose a particular minimum with $\phi_1 = \phi_2 = \phi_4 = 0$, the vacuum expectation value of Φ, i.e. the expectation value of the field in the minimum, becomes:

$$\langle 0|\Phi|0\rangle = \frac{1}{\sqrt{2}} \begin{pmatrix} 0 \\ v \end{pmatrix} \,,$$

where $v = \sqrt{-\mu^2/\lambda}$.

It can be shown, by applying perturbation theory around these minima, that the terms for three new massless scalar bosons appear in the lagrangian. These three bosons do not correspond to any particle observed in nature and can be removed with an opportune $SU(2)$ gauge-fixing. Once this gauge-fixing is performed, the expression of the field Φ around its minimum includes a single massive scalar field, the Higgs boson $h(x)$:

$$\Phi = \begin{pmatrix} 0 \\ v + h(x) \end{pmatrix} \,, \tag{1.5}$$

Using the definition for D_μ of equation 1.3, the expression of the kinetic term $(D^\mu \Phi)^\dagger (D_\mu \Phi)$ evaluated in the vacuum expectation value produces the following terms:

$$\frac{1}{2}\left(\frac{g^2 v^2}{4}\right)\left[\left(W_\mu^1\right)^2 + \left(W_\mu^2\right)^2\right] + \frac{1}{2}\left(\frac{v^2}{4}\right)\left(g W_\mu^3 - g' B_\mu\right)^2 \,,$$

which can be written in term of the $W_\mu^\pm$ and $Z_m u$ fields as:

$$\frac{1}{2}\left(\frac{g^2 v^2}{4}\right)\left[\left(W_\mu^+\right)^2 + \left(W_\mu^-\right)^2\right] + \frac{1}{2}\left(\frac{g^2 v^2}{4\cos^2\theta_W}\right) Z_\mu^2 \,.$$

or, after defining $m_W = gv/2$ and $m_Z = m_W/\cos\theta_W$,

$$\frac{1}{2} m_W^2 \left[\left(W_\mu^+\right)^2 + \left(W_\mu^-\right)^2\right] + \frac{1}{2} m_Z^2 Z_\mu^2 \,.$$

which are the mass terms of the $W^\pm$ and Z boson. It is important to notice that these three mass terms are originated dynamically by the symmetry breaking, and were not included in the original $SU(2) \otimes U(1)$ lagrangian. In such way the $SU(2)$ symmetry is broken, while the resulting lagrangian is still invariant under $U(1)$ and the electromagnetic field, A_μ, is massless.

This mechanism is hereby used to generate the W and Z boson masses without violating the $SU(2)$ symmetry in the original lagrangian, but the same problem applies to the mass term of fermionic fields. In fact, the mass term of Dirac lagrangian, can be written as

$$-m^2\bar{\psi}\psi = -m^2\left(\bar{\psi}_R\psi_L + \bar{\psi}_L\psi_R\right) \ ,$$

which is not conserved under $SU(2) \otimes U(1)$. On the other hand, an interaction term between the Higgs doublet Φ and a fermionic field (a muon will be considered as example), of the form

$$-y_\mu \left[\begin{pmatrix} \bar{\nu}_\mu & \bar{\mu} \end{pmatrix}_L \begin{pmatrix} \phi^+ \\ \phi^0 \end{pmatrix} \mu_R + \bar{\mu}_R \begin{pmatrix} \phi^{+^*} & \phi^{0^*} \end{pmatrix} \begin{pmatrix} \nu_\mu \\ \mu \end{pmatrix}_L \right] \ ,$$

can be added to the lagrangian, as it does not induce any explicit violation of the symmetry. After symmetry breaking and after the ϕ fields are replaced with the ones in equation 1.5, the following terms are generated:

$$-\frac{y_\mu}{\sqrt{2}} v\left(\bar{\mu}_L\bar{\mu}_R + \bar{\mu}_R\bar{\mu}_L\right) - \frac{y_\mu}{\sqrt{2}} h\left(\bar{\mu}_L\bar{\mu}_R + \bar{\mu}_R\bar{\mu}_L\right) \ ,$$

where the first one can be interpreted as a mass term for the muon, given in terms of its coupling with the Higgs y_μ and the vacuum expectation value v:

$$m_\mu = \frac{y_\mu v}{\sqrt{2}} \ ,$$

whilst the second term gives rise to an interaction between the Higgs boson and the muon. The same procedure applies to other leptons and can be applied also to down-type quarks. Masses for the up-type quarks are generated in a similar way when considering the hermitian conjugate of the Higgs doublet. In any case, the mass of all Dirac fermions is dynamically generated after the symmetry breaking, and is defined by the coupling of the fermion to the Higgs field.

$$m_f = \frac{y_f v}{\sqrt{2}} \ .$$

1.1.3 Strong interactions

The current description of strong interactions, which have been initially hypothesised to explain the stability of atomic nuclei, is given by the theory of Quantum Chromo-Dynamics. This theory corresponds to a $SU(3)$ local gauge symmetry and describes the interactions between quarks.

A local $SU(3)$ gauge transformation of a fermionic field can be written as:

$$\psi(x) \rightarrow \psi'(x) = \exp\left[i\frac{g_s}{2}\alpha_a(x)\lambda_a\right]\psi(x) \ ,$$

here the sum over repeated Latin indices is implied, running from 1 to 8 as the number of the Gell-Mann matrices λ_a. Given the fact that the λ_a are 3×3 matrices, another degree of freedom must be added to the waveform of the fermionic field, which is interpreted as the *colour charge* of quarks.

To satisfy this gauge invariance, the covariant derivative must be rewritten including eight colour-charged fields, the gluons, which are responsible of the interaction between quarks:

$$D_\mu = \partial_\mu + i\frac{g_s}{2}G^a_\mu \lambda_a \ ,$$

while the G^a_μ fields transform under $SU(3)$ as:

$$G^{a\prime}_\mu = G^a_\mu - \frac{1}{g_s}\partial_\mu \alpha^a(x) - f_{abc}\alpha^b G^c_\mu \ ,$$

where f_{abc} are the structure constants of $SU(3)$ defined by $[\lambda_a; \lambda_b] = 2if_{abc}\lambda_c$.

Differently from photons, gluons are color-charged and the interaction between two of them is not forbidden. It can be shown, although with a qualitative explanation, that separating two quarks at relatively long distance is less convenient, in terms of energy, than creating quark-antiquark pairs to rearrange the two quarks in a colorless state. This concept is known as *color confinement* and provides an explanation of the short-range of the strong interaction. In high-energy physics experiments, when a highly energetic quark or gluon is emitted, it rearranges in a boosted state of many collimated color-neutral hadrons known as hadronic jet.

Another consequence of the gluon self-interaction is the concept of *asymptotic freedom*, for which the coupling constant of QCD interactions decreases at relatively large energies, making a perturbative calculation of QCD diagrams possible only in the high-energy limit.

1.2 The success of the Standard Model and the discovery of the Higgs boson

The Standard Model is the summary of the current knowledge on elementary particle physics, putting together the quantum theory of fields, the local gauge principle and the Brout-Englert-Higgs mechanism. This set of theoretical concepts has been in place since the late 1960s, finding strong experimental support by the first observation of the W and Z bosons at CERN during 1980s.

Nowadays, the experiments at the Large Hadron Collider are continuously testing the predictions made by Standard Model. Many recent cross section measurements made by the ATLAS collaboration are shown in Fig 1.1, together with their ratio to the predicted theoretical values; as no significant disagreement is found between measured and predicted cross sections, these results give additional support to the SM theory.

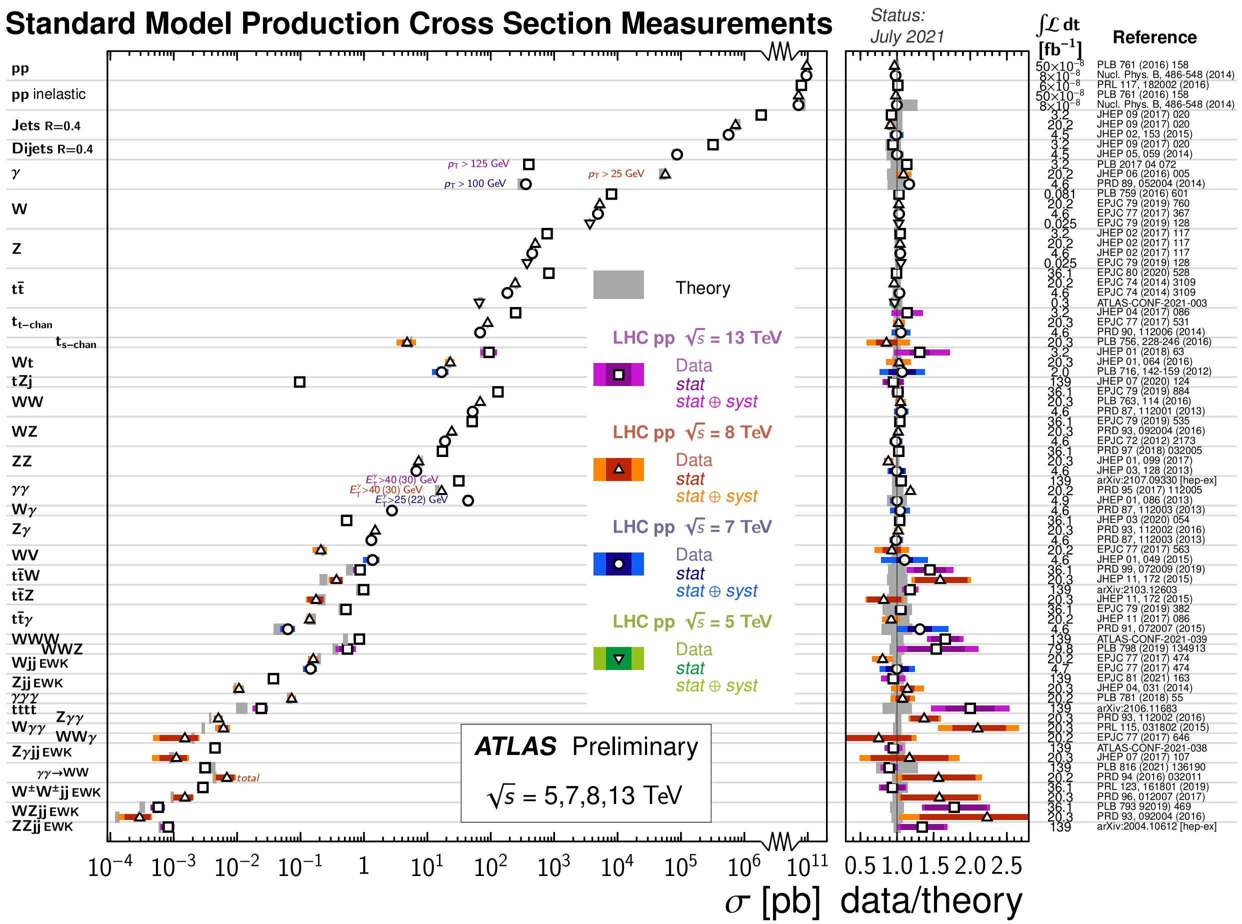

Figure 1.1. Summary of total and fiducial production cross sections for several different SM processes, measured by the ATLAS collaboration [7]. The ratio between theoretical predictions and data is also given, showing no disagreement between data and SM. References for each measurement are reported in the figure.

The Higgs boson has been eluding the experimental evidence until its discovery in 2012, year in which the ATLAS [8] and CMS [9] collaborations have announced its first observation. The resonance found in the invariant mass spectrum of two photons (Fig. 1.2 (a)) and ZZ^* pairs (Fig. 1.2 (b)) was found to be a scalar particle with mass of $125\,\mathrm{GeV}$, consistent with the Higgs boson of the SM.

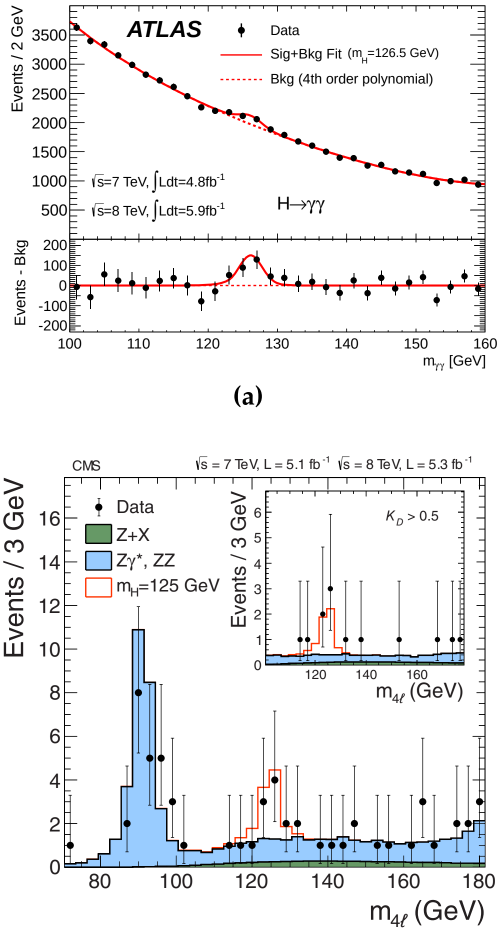

(a)

(b)

Figure 1.2. The invariant mass distribution of photon pairs observed by ATLAS [8] (a) and four leptons observed by CMS [9] (b). The resonance at $m_{\gamma\gamma} = 125\,\mathrm{GeV}$ was found to be consistent with the Higgs boson.

Following its observation, both ATLAS and CMS collaborations started an intense program of measurements of the Higgs boson properties which is still ongoing. The main production modes at the energies of the LHC are: gluon-gluon fusion (ggF), vector-boson fusion (VBF), associated vector-boson production (VH) and associated production with a top-antitop quark pair ($t\bar{t}H$). Main leading order Feynman diagrams contributing to these processes are shown in Fig. 1.3, while the corresponding predicted production cross sections at different center-of-mass energy, $\sqrt{s}$, are given in Table 1.1.

The dominant decay modes of the SM Higgs boson are in $b\bar{b}$ and WW^*, followed

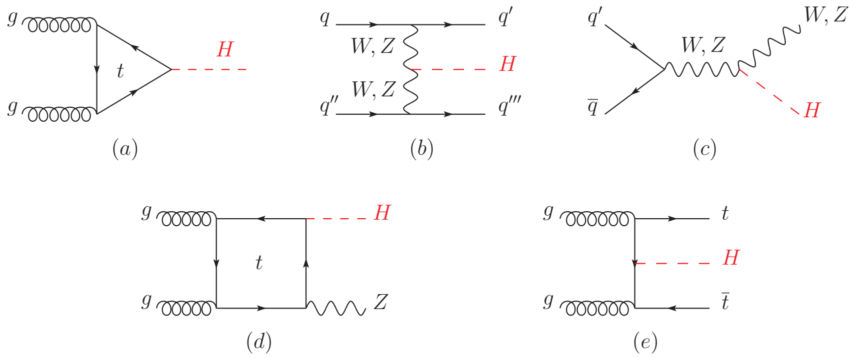

Figure 1.3. Leading order diagrams for different Higgs boson production modes: ggF (a), VBF (b), VH (c,d), $t\bar{t}H$ (e) [10].

$\sqrt{s}$ (TeV)	Production cross section (in pb) for $m_H = 125$ GeV					
	ggF	VBF	WH	ZH	$t\bar{t}H$	total
7	$16.9^{+4.4\%}_{-7.0\%}$	$1.24^{+2.1\%}_{-2.1\%}$	$0.58^{+2.2\%}_{-2.3\%}$	$0.34^{+3.1\%}_{-3.0\%}$	$0.09^{+5.6\%}_{-10.2\%}$	19.1
8	$21.4^{+4.4\%}_{-6.9\%}$	$1.60^{+2.3\%}_{-2.1\%}$	$0.70^{+2.1\%}_{-2.2\%}$	$0.42^{+3.4\%}_{-2.9\%}$	$0.13^{+5.9\%}_{-10.1\%}$	24.2
13	$48.6^{+4.6\%}_{-6.7\%}$	$3.78^{+2.2\%}_{-2.2\%}$	$1.37^{+2.6\%}_{-2.6\%}$	$0.88^{+4.1\%}_{-3.5\%}$	$0.50^{+6.8\%}_{-9.9\%}$	55.1
14	$54.7^{+4.6\%}_{-6.7\%}$	$4.28^{+2.2\%}_{-2.2\%}$	$1.51^{+1.9\%}_{-2.0\%}$	$0.99^{+4.1\%}_{-3.7\%}$	$0.60^{+6.9\%}_{-9.8\%}$	62.1

Table 1.1. Predictions for the production cross sections of the Standard Model Higgs boson, for the leading production modes and different values of center-of-mass energy [10].

by the decay in gg, $\tau^+\tau^-$ and ZZ^*. A lot of effort has been put, by the ATLAS and CMS collaboration, in providing the measurement of the production cross sections and decay branching ratios of the Higgs boson in different channels and to measure the coupling of the Higgs boson to vector bosons and fermions. The measured cross section times branching ratio of the Higgs, scaled to the SM value is shown in Fig. 1.4. To date, all recent ATLAS [11] and CMS [12] results concerning the Higgs boson are not showing discrepancies between the experimental measures and the corresponding predictions from the SM.

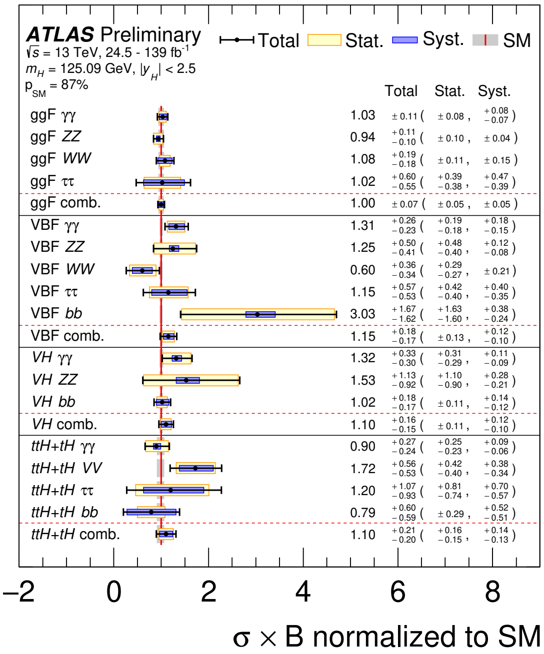

Figure 1.4. Cross section times branching ratio of the Higgs boson, normalised to the expected values from the SM. The main production mechanisms are shown, as long as the main decay modes. Combined measurements are also shown, in which the SM expected value is assumed for the branching fraction in each decay mode [11].

1.3 Beyond-SM physics and where to look for it

Many recent tests of the Standard Model and the discovery of the Higgs Boson have established the validity of this theory up to the electroweak scale. However, there are still many open questions and experimental observations which are not explained by the SM, a very brief and non-exhaustive list of them is given below:

- The SM picture does not include gravity, although its effect is not relevant at the energy scale of modern particle physics experiments, it will become effective for particles of mass equal to the Planck mass ($\mathcal{O}(10^{19})$ GeV). A *theory of everything* should also include an explanation of the gravitational interaction.

- If the SM is valid up to the scale of the Planck mass, then some unnatural *fine-tuning* is required to cancel the diverging corrections to the Higgs boson mass, in order to keep its value at the electroweak scale. This problem, which arises from the large differences in the strength of the four fundamental forces, is known as the *hierarchy problem*.

- Neutrinos are supposed to be massless in the SM, while numerous experimental observations of neutrino oscillations are explainable only if their mass term is non-zero. However, the estimated values of neutrino masses are much smaller than the ones of other SM particles, suggesting that their mass terms may originate with a different mechanism than the Brout-Englert-Higgs one.

- A large number of experimental cosmological and astrophysical observations suggest that the visible matter (or *ordinary matter*) represent roughly 20% of the mass of the Universe, the remaining 80% appears *dark* to any kind of radiation. A complete theory of everything should include an explanation for the nature of the *Dark Matter*.

- The observable Universe appears to be rich in ordinary matter with respect to anti-matter. If this asymmetry have arisen during the early life of the Universe, the only mechanism in the SM which could have given origin to such asymmetry is the violation of the CP symmetry. Despite CP-violating effects are found in the weak interactions of quarks, this effect is not sufficient to explain the asymmetry inferred from experimental measurements.

The term beyond-SM physics (bSM) refers to the theories which are extending the SM in order to provide an explanation for the currently open questions.

Many theoretical models provide a solution to one (or more) of the aforementioned problems; from the point of view of an experimental physicist, experiments at the LHC have been searching for signatures of bSM physics since the first data-taking runs and, as the amount of collected data increases, probing new physics at the TeV scale is becoming more and more accessible.

Unfortunately, no evidence of new physics has been found yet. This perplexing outcome leaves us with the following three possibilities: given that this new physics must exists, or we need a larger dataset to observe it, or it is at an energy scale above the one reachable at the LHC, or *we are just looking in the wrong place!*

The last possibility is the one that will be explored in this thesis. The following sections will focus on the possibility of searching new physics with nowadays experiments, at current LHC energies, but in a different region of the *lifetime* axis.

1.3.1 The lifetime frontier

Particles of the Standard Model span a wide range of lifetimes[2], ranging from the Z boson ($\sim 2.6 \times 10^{-25}\,\mathrm{s}$) to the electron, which is considered stable (see Fig. 1.5 for other examples). The long lifetime of a particle can originate by its interactions, which may have a small coupling constant or have a small phase space accessible, up to the case in which a particle is stable because is the lightest state accessible by an interaction. As Long-Lived Particles are everywhere in the Standard Model, nothing forbids the bSM physics that we are looking for to be rich in LLPs.

Experiments at particle colliders are commonly designed with an inner spectrometer, surrounded by a calorimeter system and an outer muon spectrometer; while most of the bSM searches target particles produced in the vicinity of the point

---

[2] Here *lifetime* and *mean proper lifetime* will be treated as equivalent terms, indicating the proper decay time in the frame of reference of the particle.

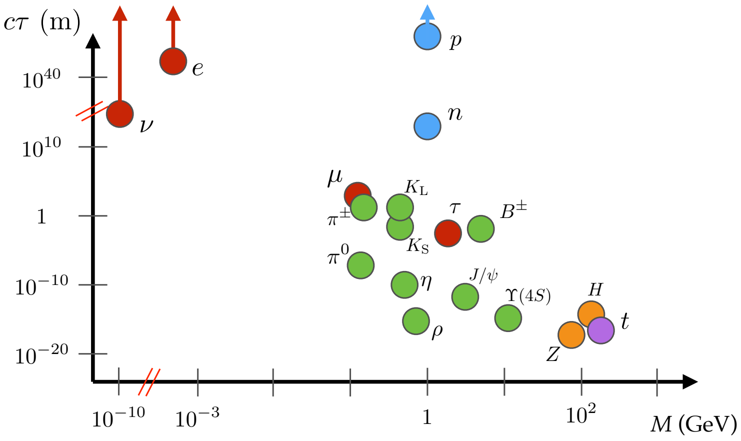

Figure 1.5. Mean proper lifetime ($c\tau$) as a function of the mass (M) for a selection of SM particles. Image taken from [13].

in which collisions take place, LLPs can in principle travel macroscopic distances and even decay outside the inner spectrometer. This can originate a variety of signatures like displaced vertices in the muon spectrometer; localised energy distributions in the calorimeter without associated tracks; displaced leptons or lepton pairs and other signatures visible in Fig. 1.6. These correspond to many bSM physics search possibilities which can be covered at nowadays experiments.

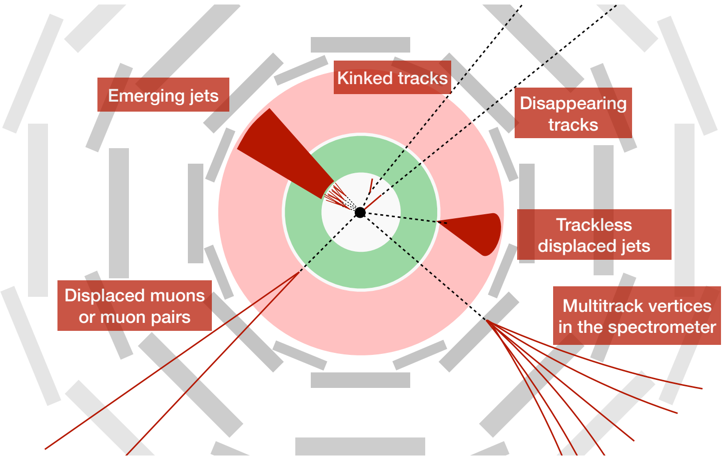

Figure 1.6. Few examples of possible long-lived particle signatures in a modern detector at a particle collider.

However, searching for these unconventional signatures implies the development of dedicated triggers or object reconstruction algorithms. These signatures can also be mimicked by mis-reconstructed objects or detector noise, which limits the use of simulated Monte Carlo events for the background estimation, keeping the search for LLPs a challenging topic at modern high-energy physics experiments.

1.3.2 Dark Sector models

Long-lived particles are predicted in theoretical models which attempt to solve the limitations of the SM, following a *top-down* approach in which the theoretical problem motivates the solution. An alternative *bottom-up* approach follows the inverse path, starting from simplified models which are not the starting point of a theory, but are simple SM extensions focused on the experimental signature, which eventually would arise as a limit of a complete theory. A possible *bottom-up* approach in predicting LLPs consists in predicting an entire SM-like sector of particles, referred to as *Dark Sector* (DS), which in the simplest scenario is charged under a new $U(1)_{\mathrm{D}}$ symmetry.

To access such scenario at a hadron collider, one must admit an interaction (or *portal*) between SM and Dark Sector particles.

The Vector Portal

One possible solution is the *vector portal*, in which the vector mediator of the DS, often called *dark photon* (γ_d) is coupled to the SM photon via a kinetic mixing term of the form:

$$\mathcal{L} \supset \frac{1}{2}\varepsilon F'_{\mu\nu}F^{\mu\nu} \, ,$$

where $F'_{\mu\nu}$ is the field strength tensor of the dark photon and ε is the coupling constant, which can be arbitrarily small [14]. This term enables the decay of the γ_d in pairs of charged SM fermions.

A non-zero mass of the γ_d (m_{γ_d}), is then assumed to avoid an interaction at infinite range and to originate a mean proper lifetime of the dark photon (τ_{γ_d}). In such case the decay width of the γ_d into a pair of charged leptons is given by [14]:

$$\Gamma_{\gamma_d \to l\bar{l}} = \frac{1}{3}\alpha\epsilon^2 m_{\gamma_d}\sqrt{1-\frac{4m_l^2}{m_{\gamma_d}^2}}\left(1+\frac{2m_l^2}{m_{\gamma_d}^2}\right) \, ,$$

while the decay width to quarks, for $m_{\gamma_d} > 2m_\pi$, can be expressed in terms of the ratio

$$R = \frac{\sigma_{e^+e^- \to \text{hadrons}}}{\sigma_{e^+e^- \to \mu^+\mu^-}} \, ,$$

evaluated at $\sqrt{s} = m_{\gamma_d}$ and is given by:

$$\Gamma_{\gamma_d \to \text{hadrons}} = \frac{1}{3}\alpha\epsilon^2 m_{\gamma_d}\sqrt{1-\frac{4m_\mu^2}{m_{\gamma_d}^2}}\left(1+\frac{2m_\mu^2}{m_{\gamma_d}^2}\right) R(\sqrt{s} = m_{\gamma_d}) \, .$$

This expression of the decay width gives the values of the γ_d branching ratio shown in Fig. 1.7 and yields the following approximated expression for the dark photon mean proper lifetime τ_{γ_d}:

$$\tau_{\gamma_d} \propto \left(\frac{10^{-4}}{\varepsilon}\right)^2 \left(\frac{100\,\mathrm{MeV}}{m_{\gamma_d}}\right) \, .$$

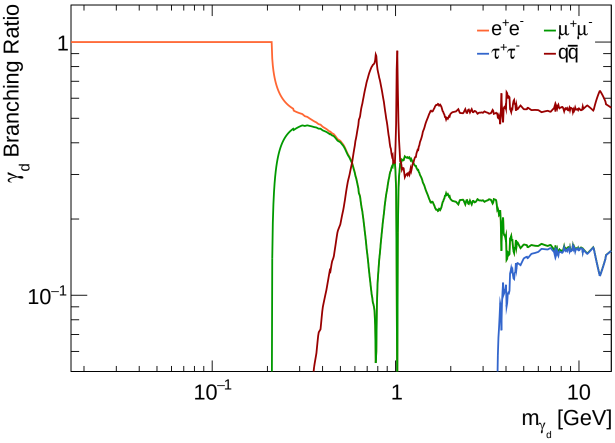

Figure 1.7. Dark photon branching ratio to a pair of charged leptons or quarks. Values for R are taken from [10].

This simplified Dark Sector model can be introduced also assuming that the vector portal between DS and SM is given by a kinetic mixing between the hypercharge electroweak boson B and the dark photon [15], originating a similar phenomenology.

A summary of the most recent constraints on the dark photon models, assuming the vector portal in both production and decay, is shown in figure 1.8 as a function of its mass and kinetic mixing term. These results leave a large gap for $\varepsilon < 10^{-4}$ and γ_d masses greater than $100\,\mathrm{MeV}$.

The Higgs Portal

Admitting a mass term for the dark photon implies that the terms for a Higgs-like boson (H'), with a non-zero vacuum expectation value, should be added to the lagrangian in addition to the kinetic and interaction term corresponding to the γ_d. If the field of the bSM Higgs-like boson is denoted as Φ', a potential of the following form can be included in the lagrangian:

$$\begin{aligned} V(\Phi,\Phi') =& \mu^2(\Phi^\dagger\Phi) + \lambda(\Phi^\dagger\Phi) \\ &+\mu'^2(\Phi'^\dagger\Phi') + \lambda'(\Phi'^\dagger\Phi') \\ &+k(\Phi^\dagger\Phi)(\Phi'^\dagger\Phi') \end{aligned}$$

where k is the coupling between the two fields. The electroweak symmetry breaking gives a non-zero vacuum expectation value to the field Φ', which generates the mass terms of the dark sector particles. This kind of interaction allows the decay of the SM Higgs boson into a pair of γ_d, or other particles of the Dark Sector charged under $U(1)_\mathrm{D}$, via the so-called *Higgs portal.*

A search for long-lived dark photons performed at the LHC can only benefit from the introduction of a Higgs portal, from which the dark photon can either be

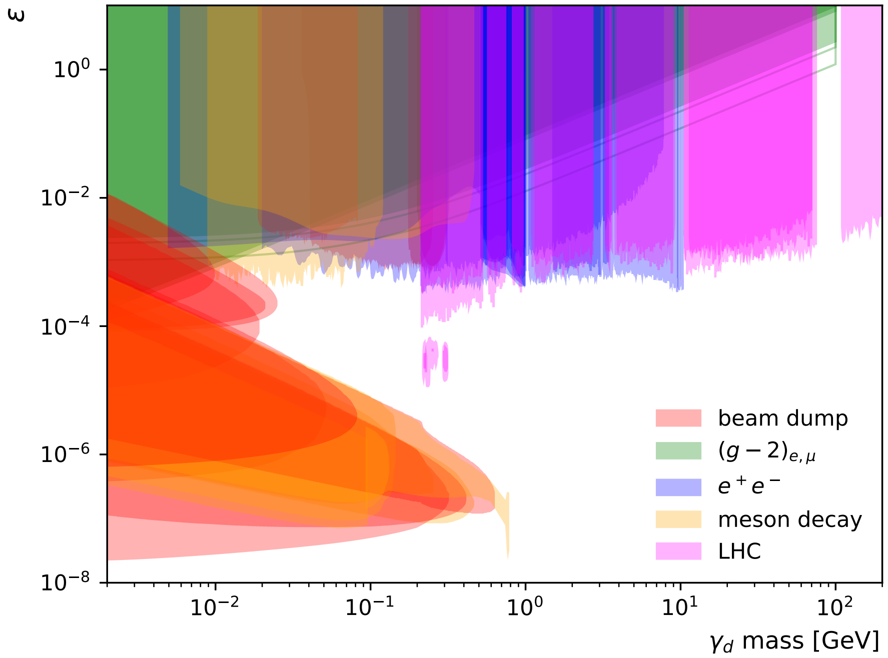

Figure 1.8. Recent constraints set on dark photon decays from various experiments assuming both production and decay via the vector portal. Results are shown for beam dump experiments (red), muon and electron magnetic moment (green), experiments at e^+e^- colliders (blue), meson decay (yellow) and LHC experiments (magenta). Plot made using the Darkcast framework presented in [16]. References for each constraint are available in [17].

produced by the decay of the Higgs boson, or radiated by fermions of the Dark Sector, without the need of a vector portal in both production and decay of the γ_d.

Given the limited size of LHC experiments, a fixed m_{γ_d} corresponds to a certain range of τ_{γ_d} accessible by physics searches. Hence, the production of dark sector particles via the Higgs portal allows to search for long-lived dark photons without considering a factor ϵ^2 in production.

Instead of considering the parameter k of the mixing between SM and bSM Higgs bosons, the branching ratio of the SM Higgs boson decaying to invisible particles ($B_{H\to\text{inv.}}$) is used as a parameter of the model. The most recent constraints on this parameter are given in [18] and correspond to $B_{H\to\text{inv.}} < 11\%$ @ 95% CL.

FRVZ model

In the remaining parts of this chapter, the processes that will be considered as benchmark models for the studies described in this thesis are reported.

The first model that will be considered is the Falkowsky-Ruderman-Volansky-Zupan (FRVZ) model [19, 20]. This Dark Sector model has similar features to the one introduced in the previous section, but provides a richer phenomenology in which multiple bSM particles are considered. The Higgs portal mechanism allow, via an exotic decay mode of the SM Higgs boson, the production of two DS particles (f_d), which are charged under the $U(1)_{\mathrm{D}}$ symmetry and decay to a γ_d and a *Hidden Lightest Stable Particle* of the dark sector (HLSP). The γ_d is then allowed to decay to SM particles via the vector portal, while the HLSP remains undetected.

The richer kinematics of this model, which is due to the presence of intermediate particles, is of particular interests in searches for LLPs at hadron colliders, as it can give a wide variety of signatures like multiple LLPs produced with different angular distribution, as well as invisible particles in the final state. Depending on the value of the $U(1)_{\mathrm{D}}$ coupling, more than one γ_d can be radiated, leading to showers of γ_d that yield a large number of displaced leptons. In this work, the coupling of the dark-$U(1)$ is assumed to be less than 0.01, hence the radiation of γ_d is suppressed. Nevertheless, the case of a higher γ_d multiplicity is studied by involving an additional dark sector scalar, s_d, that allows the production of four dark photons in the final state.

Diagrams of the processes generating two or four γ_d in the final state are shown in figure 1.9.

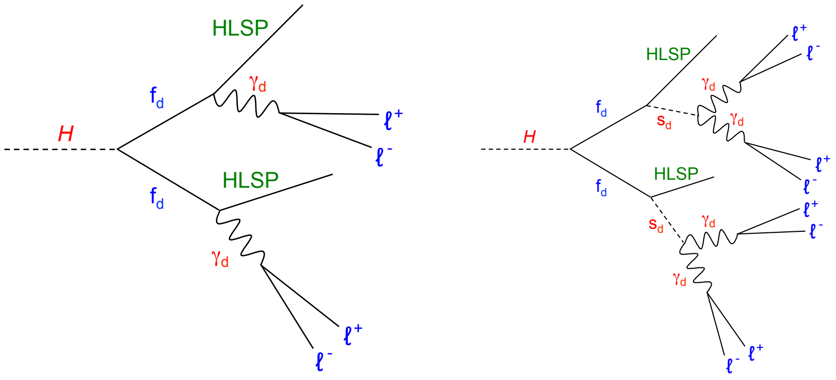

(a) **(b)**

Figure 1.9. Two diagrams yielding the production of two (a) or four (b) γ_d starting from the decay of a SM Higgs boson to DS particles.

Hidden Abelian Higgs Model

Another simplified model that predicts decays of the Higgs boson in a pair of dark photons is the Hidden Abelian Higgs Model (HAHM), which is described in [15]. In this case, the production via the Higgs portal of two γ_d is predicted, while their decay to SM charged fermions, is made possible via the vector portal. A diagram showing this process is given in figure 1.10.

The smaller number of particles that are considered in this case allow the production of two highly boosted dark photons, which is often helpful in the identification of their decay products, as it will be shown with more detail in chapter 3.

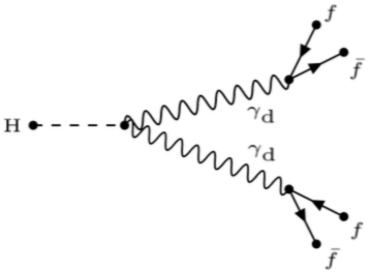

Figure 1.10. Diagram showing the decay mode of the H boson to two γ_d, which then decay via the vector portal to SM charged fermions, as predicted by the HAHM model.

Long-lived Higgs-like scalars

A third, even more simplified model, is based on a simple extension of the SM with a single scalar particle.

The model, discussed in [21], only assumes a mechanism similar to the aforementioned Higgs portal, where the SM Higgs mixes with the field of a bSM scalar particle, s. The $H \rightarrow ss$ process is allowed if the mass of the new scalar is $m_s < \frac{1}{2}m_H$ and the decay $s \rightarrow f\bar{f}$, where f are SM fermions, is allowed with a Yukawa-like coupling, as represented in figure 1.11.

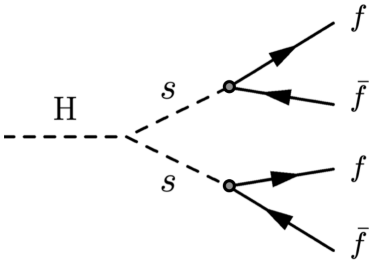

Figure 1.11. Production of two bSM scalar particles, s, via the decay of a H boson, which subsequently decay to pairs of SM fermions. Figure taken from [4].

For small coupling of the $s \rightarrow f\bar{f}$ decay, the bSM scalar is long-lived and its decay lead to displaced vertices. The branching ratio of its decay is shown in 1.12, where it is clearly shown that the main decay mode is $c\bar{c}$ for masses of the order of $5\,\mathrm{GeV}$, while above $10\,\mathrm{GeV}$ the main decay mode is in a $b\bar{b}$ pair.

This model was studied, in the context of this thesis, in chapter 6 probing the scenario where the s have a very large mean proper lifetime and many of them escape the detector before decaying.

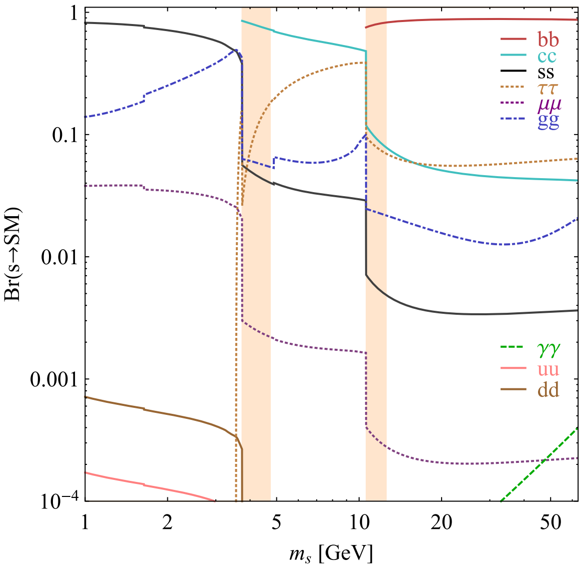

Figure 1.12. Decay branching ratio of the bSM scalar s to SM particles. Figure adapted from [21], the shaded regions corresponds to masses of the s where the calculation of the BR has to not be considered valid, as stated in [21].

Chapter 2

The ATLAS experiment at the Large Hadron Collider

If we want to study the infinitely small constituents of the Universe, we have to take into account the fact that quantum mechanics tells us that our microscope has a *resolving power* which is inversely proportional to the square of its *energy*. In other words, small-scale interactions can only be probed only with high-energy processes.

Relativistic kinematics shows that it is more efficient to *collide* two particles instead of realising a particle-target collision, consequently, high-energy particle colliders represent our best technology to shed light on the infinitely small. As the energy of the interactions increase, the energy and penetrating power of the products of such interactions also increase, implying that our *detectors* must be large enough to be able to identify these products.

This chapter will describe the most powerful particle collider available to date, the CERN's Large Hadron Collider (Section 2.1), and one of the four large experiments dedicated to the identification of collision products the ATLAS detector (Section 2.2). Details on the identification of particles in the ATLAS detector are given in Section 2.3.

2.1 The Large Hadron Collider

The Large Hadron Collider (LHC, [22]) is a proton-proton and heavy ion collider located at the *European Organisation for Nuclear Research* (CERN[1]), which is the leading center for experimental high-energy physics in which more than 12000 people from all over the world are involved.

The LHC project was approved in 1994 and its installation was performed during the 2000s in the 27 km circular tunnel located across the Swiss and French border at CERN. The first proton-proton collisions were realised in 2008 and the first period of data taking (Run-I) was completed between 2010 and 2012, with a

---

[1] CERN is an acronym for *Conseil européen pour la recherche nucléaire*, former name of the Organisation

center-of-mass energy ($\sqrt{s}$) of pp collisions gradually increased from 7 to $8\,\mathrm{TeV}$.

A second period of data-taking, known as Run-II, followed a two-year *Long Shutdown* of upgrades and lasted from 2015 to 2018, in which the collider has been operated at $\sqrt{s} = 13\,\mathrm{TeV}$ providing data for a massive physics program which is still ongoing, rich in bSM physics searches and precision tests of the Standard Model. The design center-of-mass energy for pp collisions was $14\,\mathrm{TeV}$ and during the Run-III, planned to start in 2022, an energy of $13.6\,\mathrm{TeV}$ will be reached.

2.1.1 The CERN accelerator complex

Particle beams used for collisions at LHC are accelerated up to the nominal energy in multiple stages which are summarised in Figure 2.1.

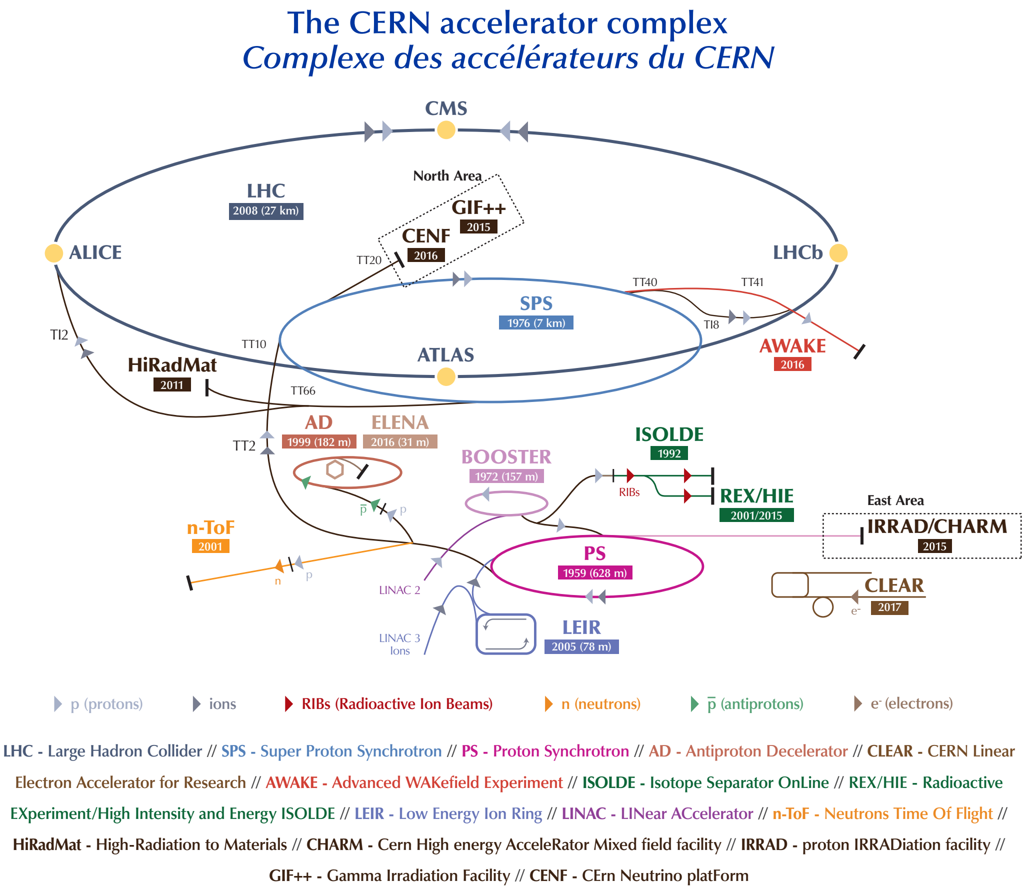

Figure 2.1. Schematics of the CERN accelerator complex (as 2018), showing the path of different particle beams in different facilities available at CERN. Image taken from [23]

During the Run-II, protons obtained by the ionisation of hydrogen atoms started their path inside the LINAC2, a $30\,\mathrm{m}$ long linear accelerator, designed to squeeze them in bunches and raise their energy up to $50\,\mathrm{MeV}$. Then, the proton bunches were sent through three consequent circular accelerators: the Proton Synchrotron Booster (PSB), the Proton Synchrotron (PS) and the Super Proton Synchrotron (SPS), in which their energy was increased to 1.4, 25 and $450\,\mathrm{GeV}$, respectively.

These three accelerators were already present at CERN and were used in the past for different purposes: the PS started its operation in 1959 as the CERN's first synchrotron, while the SPS has been used since 1976 and also worked as a proton-antiproton collider between 1981 and 1990, then as an intermediate electron-positron accelerator for the Large Electron Positron Collider (LEP). Nowadays their main purpose is to accelerate proton and ion beams for the LHC and to provide beams for other CERN facilities.

2.1.2 The machine

Once the protons are accelerated by the SPS to the nominal energy, bunches of 1.15×10^{11} protons, separated by a *bunch spacing* of $25\,\mathrm{ns}$ are injected in the LHC. Being a pp collider, two separate rings are required to maintain the trajectory and accelerate the two counter-rotating beams, which are focused and brought to collision in four different interaction points (IPs), around which the four large LHC experiments are placed: ATLAS [24] and CMS [25] were designed for the discovery of the Higgs boson, and the study of the SM properties at the TeV scale, as well for the search of beyond-SM physics; LHCb [26] is dedicated to heavy flavour precision measurements while ALICE [27] is designed for the study of heavy ion collisions.

The LHC is made of 1232 dipoles which need to generate a magnetic field sufficient enough to maintain the circular trajectory of the two proton beams. Given the design energy of $7\,\mathrm{TeV}$ per beam, an intense magnetic field of $8\,\mathrm{T}$ is required to keep the protons on the desired path. Such magnetic field is reached with the use of superconducting NbTi cables, cooled down below $2\,\mathrm{K}$ using superfluid helium. Additional higher order magnets are used to focus the LHC bunches and guide the beams to the interaction point.

Radio-frequency cavity systems, also based on superconducting technology, are used to capture and accelerate the bunches, using a $400\,\mathrm{MHz}$ frequency to keep the proton bunch structure.

2.1.3 Luminosity, pileup and bunch crossing modes

The LHC is designed for a maximum center-of-mass energy of $14\,\mathrm{TeV}$, but beside the high energy, in order to collect enough statistics for the physics programs, a large event rate must be obtained. In particle accelerator technology, the parameter which relates the number of interactions (N) per second to the cross section (σ) of a certain process is the luminosity (L), defined by:

$$\frac{dN}{dt} = L \cdot \sigma \ ,$$

from which follows that its measurement unit is $[\text{length}]^{-2}\,[\text{time}]^{-1}$. A simple estimate for the luminosity is the following:

$$L = \frac{N_1 N_2 k f}{4\pi \sigma_x \sigma_y} \, ,$$

where N_1 and N_2 are the number of protons in the two colliding bunches, k is the number of bunches circulating at a certain moment in each of the LHC beams, f is the revolution frequency of a bunch, while the denominator is an estimate of the transverse size of the bunches, in which σ_x and σ_y are the RMS of the spatial distribution of the protons along the plane orthogonal to the proton direction. This expression of the luminosity is corrected by additional multiplicative factors, which take into account the small (but non-negligible) collision angle and other effects.

Once the two LHC beams are brought into collision, the so-called *stable beam* condition, the detectors can start their *data-taking runs*, recording events for physics purposes. During this period the luminosity starts to decrease exponentially, due to the loss of protons from the bunches, caused either by the collisions or by other secondary effects. This condition usually lasts from 10 to 15 hours, after which the beam is deviated, protons are safely dumped and the preparation of another run starts. The conditions of the LHC evolved during the Run-II, yielding an increase of the luminosity, which at it maximum reached $2.1 \times 10^{34}\,\text{cm}^{-2}\text{s}^{-1}$ in the ATLAS interaction point.

The integral of the luminosity delivered in a certain time interval defines the *integrated luminosity* ($\mathcal{L}_{\text{int}}$):

$$\mathcal{L}_{\text{int}} = \int L \, dt \, ,$$

which is a parameter relating the number of events, of a given process with known cross section, produced in the corresponding time interval:

$$N = \mathcal{L}_{\text{int}} \cdot \sigma \, ,$$

given that, it is common to express the integrated luminosity in b^{-1}. During Run-II, the total integrated luminosity collected by ATLAS and available for physics is equal to $139\,\text{fb}^{-1}$, as shown in Fig. 2.2. This luminosity corresponds to the one of all data-taking runs in which all ATLAS subsystems were operating at normal conditions, a list of these runs (*Good Runs List*, GRL) is provided by the Collaboration.

The large luminosity reached at LHC imply that a large dataset is available for SM precision measurements and bSM physics searches. On the other hand, this also implies a large number of proton-proton collisions per bunch crossing (BC), hence multiple superimposed events which must be taken into account when processing the signals from the detector during object reconstruction. The term *pileup* is often used in high-energy physics experiments to refer to the mean number of multiple collisions happening during a single bunch crossing, an estimate of the pileup μ is given by:

$$\mu = \frac{\mathcal{L}_{\text{int}} \sigma}{k f} \, ,$$

in ATLAS, during Run-II, the mean pileup level was $\langle \mu \rangle = 33.7$. Fig. 2.3 show the pileup distribution for each year of the Run-II data taking.

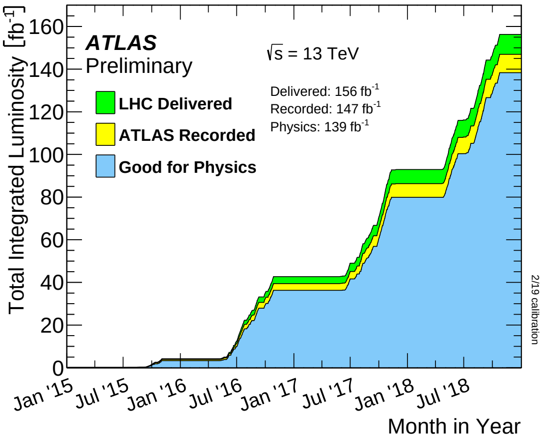

Figure 2.2. Integrated luminosity delivered by LHC in collisions, recorded by ATLAS and available for physics analyses during Run-II [28].

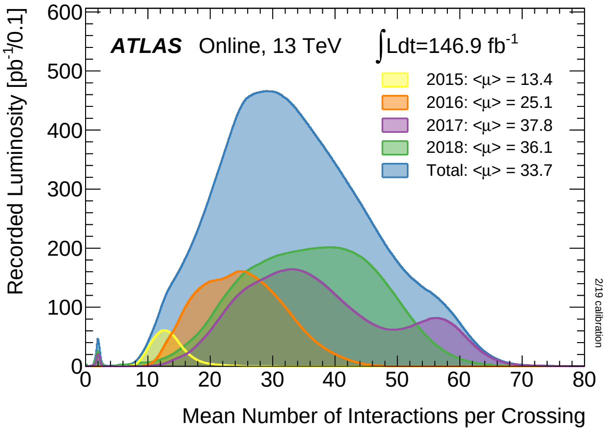

Figure 2.3. Distribution of the mean number of interactions per bunch crossing during Run-II and during each data-taking year [28].

The nominal LHC configuration for *pp* collisions contains 3564 bunch crossings per revolution. The filling scheme of the LHC bunches is such that not all of them are actually filled with protons. In each beam, *bunch trains* of subsequent filled bunches are interleaved by at least eight subsequent *empty* ones, as described in [29]. By shifting the bunch trains of the two beams, four possible bunch crossing modes are obtained:

- *Paired* bunch crossings, where both bunches are filled with protons;
- *Unpaired* bunch crossings, where one of the two bunches is empty;
- *Unpaired Isolated* bunch crossings, which are identical to the Unpaired ones, but the empty bunch is proceeded and followed by three other empty bunches;
- *Empty* bunch crossings, where none of the two bunches are filled, and both are proceeded and followed by at least five empty bunches.

The paired configuration is the nominal one used for physics programs, while the three other ones are mostly used for studying background events, as described in [30].

2.2 The ATLAS experiment

ATLAS is one of the two general-purpose detectors at LHC, designed to identify particles originating in *pp* collisions. In order to guarantee an almost full coverage of the solid angle, ATLAS has a cylindrical design centered in the interaction point, with radius of $22\,\mathrm{m}$ and a length of $44\,\mathrm{m}$. A layout of the detector is visible in Fig. 2.4, from which is clearly visible that it relies on many sub-detectors with different purposes, briefly described in the following:

- The Inner Detector (ID) is the closest one to the IP and is composed of multiple layers of different technologies of tracking detector. Its main purposes are the identification of the tracks left by the particles and the measurement of their momentum, thanks to the magnetic field in which is immersed. Another important purpose, following from the reconstruction of the tracks, is the identification of the primary and secondary vertices.
- A calorimeter system is situated outside the inner detector and has the purpose of measuring the energy of charged and neutral particles, by absorbing the energy of the electromagnetic and hadronic showers originated by them.
- An external Muon Spectrometer (MS) surrounds the whole detector with the purpose of measuring the momentum of muons, which are minimum ionising particles escaping the calorimeter system. It is based on gas detectors immersed in a toroidal magnetic field.

More details on each sub-detector are given in the following sections.

2.2.1 Coordinate system and geometry

ATLAS uses a right-handed coordinate system, defined as following:

- The origin of the coordinate system lies in the LHC interaction point;
- The X-axis is horizontal and points from the IP to the center of the LHC ring;
- The Y-axis points upwards and is perpendicular to X and to the local beam direction;
- The Z-axis is aligned with the beam direction, oriented in such a way that the XYZ system is right-handed.

The detector is divided along the Z-axis in two sides: the region at positive z is defined as *side A*, the region at negative z is named *side C*, while the name *side B* is

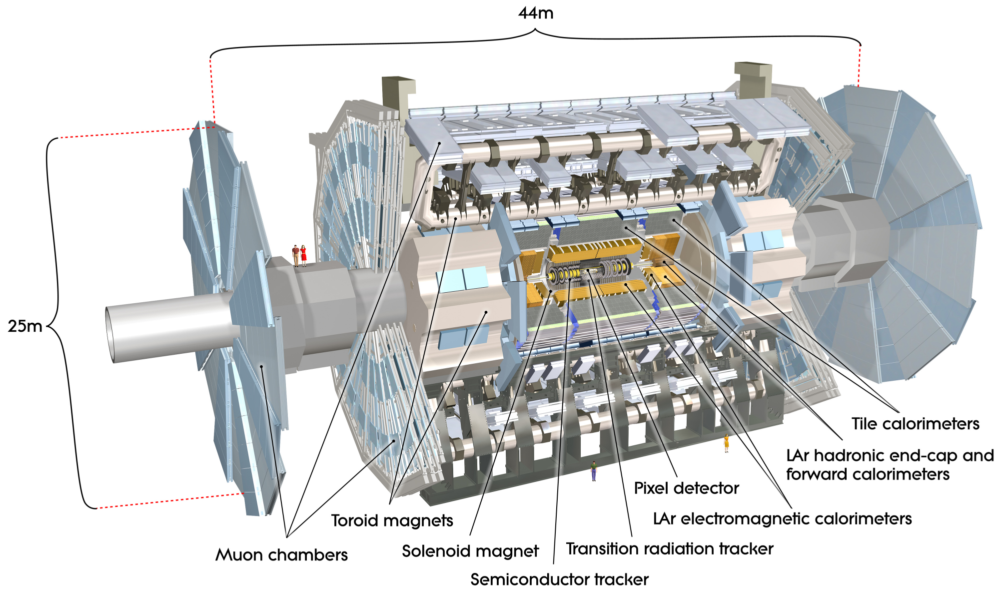

Figure 2.4. Rendering of the ATLAS detector highlighting the position of the various sub-detectors [31].

reserved for detector components installed in correspondence of the $z = 0$ plane. A picture of the ATLAS detector and its location at the CERN Intersection Point 1, showing a graphical representation of the detector coordinate system is given in Fig. 2.5.

The cylindrical geometry of the detector immediately suggests the definition of three regions: the region defined as *barrel* (corresponding to the curved surface of the cylinder) and the two delimiting *endcaps* (corresponding to the two circles closing the volume); these two terms are widely used in the identification of many ATLAS subsystems.

The Cartesian coordinate system is often less used in physics analyses and (z, ϕ, θ) coordinates are preferred, with ϕ, θ being the azimuthal and polar angle, respectively. The ϕ coordinate is chosen such that $\phi = 0$ corresponds to the direction of the X-axis and ranges in $(-\pi, \pi]$, while the θ coordinate is chosen such that $\theta = 0$ corresponds to the direction of the Z-axis.

In a hadron collider the exact momentum of the colliding partons originating the primary interaction is unknown, hence a coordinate which allows to write differential quantities, which are invariant under Lorentz transformations along the Z-axis, is preferred. The *rapidity* y is defined in terms of the energy E and the longitudinal component of the momentum of a particle (p_z), as:

$$y = \frac{1}{2} \log \left(\frac{E + p_z}{E - p_z} \right) ,$$

with the advantage that dy is Lorentz-invariant under transformations along the beam axis. In the limit of ultra-relativistic particles, the rapidity converges to the

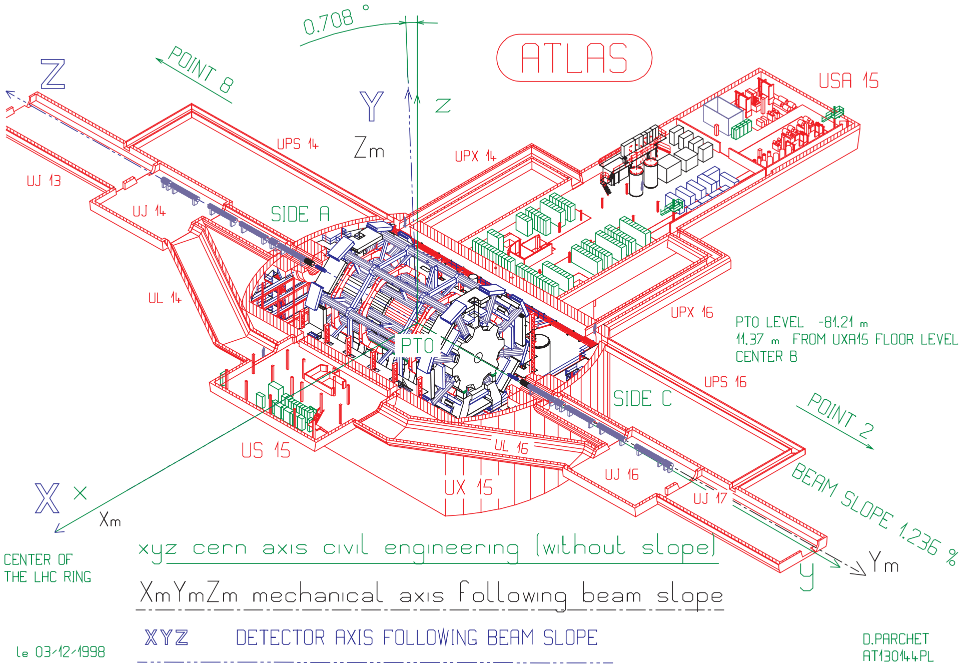

Figure 2.5. Technical overview of the ATLAS detector coordinate system. The naming convention of the ATLAS and other service caverns are also shown [32].

pseudorapidity η, which relates to the θ coordinate by:

$$\eta = -\log\tan\left(\frac{\theta}{2}\right) ;$$

the pseudorapidity is 0 for objects in the XY-plane and its value becomes infinite as η approaches 0 (and so $-\infty$ for $\theta \to \pi$).

The momentum of the partons in the transverse (XY) plane is considered negligible, so the ϕ coordinate is also Lorentz-invariant, and distances between objects defined as

$$\Delta R = \sqrt{\Delta\eta^2 + \Delta\phi^2}$$

are also Lorentz-invariant. Another consequence is that the sum of the projection of the momentum in the transverse plane (transverse momentum, p_{T}) of all the final-state particles must be zero; hence the *missing transverse momentum* (often called missing transverse energy, missing E_{T} or $E_{\mathrm{T}}^{\mathrm{miss}}$) is defined as the magnitude of the negative vector sum of the transverse momentum associated to the visible particles.

2.2.2 Magnet system

Both the Inner Detector and the Muon Spectrometer need a magnetic field to infer the momentum of a particle, by measuring the parameters of the track reconstructed from hit patterns. In ATLAS three superconducting magnet systems are used [33]:

the Central Solenoid provides the magnetic field for the Inner Detector, while the air-core Barrel Toroid and two Endcap Toroids provide a toroidal field for the Muon Spectrometer. A graphical scheme of the magnet system is shown in figure 2.6.

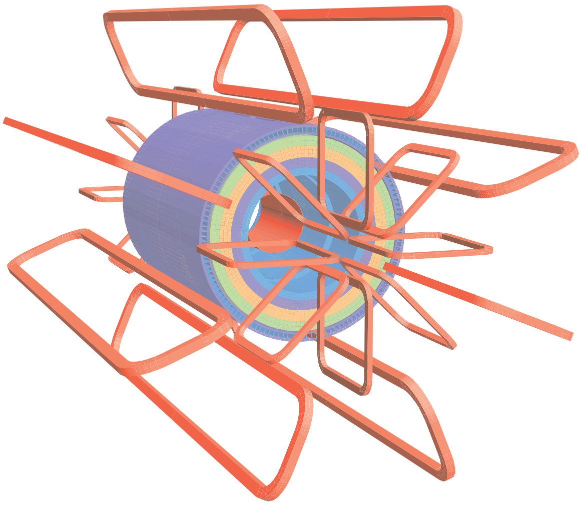

Figure 2.6. Graphical representation of the ATLAS magnet system [24]. The coils of the Barrel and Endcap Toroids are depicted in red, while the Central Solenoid is shown in blue. The different colored layers represent a modelling of the barrel calorimeter system.

The Central Solenoid surrounds the barrel region of the ID and it is made of a single superconducting coil. Its design has been studied to minimise the material in front of the calorimeter, in order to avoid unwanted energy losses; this is achieved by using a shared vacuum vessel for both the superconducting coil and the liquid-Argon electromagnetic calorimeter.

The Barrel Toroid is made of eight superconducting coils which extends up to a length of $26\,\mathrm{m}$, producing a $0.5\,\mathrm{T}$ toroidal magnetic field for the barrel region of the Muon Spectrometer, while the two Endcap Toroids are each made of eight coils contained in a common vacuum vessel, generating a field of $1\,\mathrm{T}$.

2.2.3 Inner detector

The Inner Detector is made of three different sub-detectors: the Pixel Detector, the Semiconductor Tracker and the Transition Radiation Tracker, described in the next paragraphs. Each play a complementary role in the identification of particle tracks, as well as in the reconstruction of primary and secondary vertices. During LHC collisions, approximately 1000 particles per bunch crossing originate from the interaction point; given that tracks are reconstructed by the identification of the pattern of *hits* left by the particle in the sensitive material of the tracker, a fine granularity of this detector is required to reach the desired performances.

The ID is entirely contained in a cylindrical volume of radius $1150\,\mathrm{mm}$, extending up to $z = \pm 3512\,\mathrm{mm}$ and is able to identify tracks up to $|\eta| \leq 2.5$. A rendering of the ID and a schema showing the positions of different sub-detectors are shown in figure 2.7 and figure 2.8, respectively.

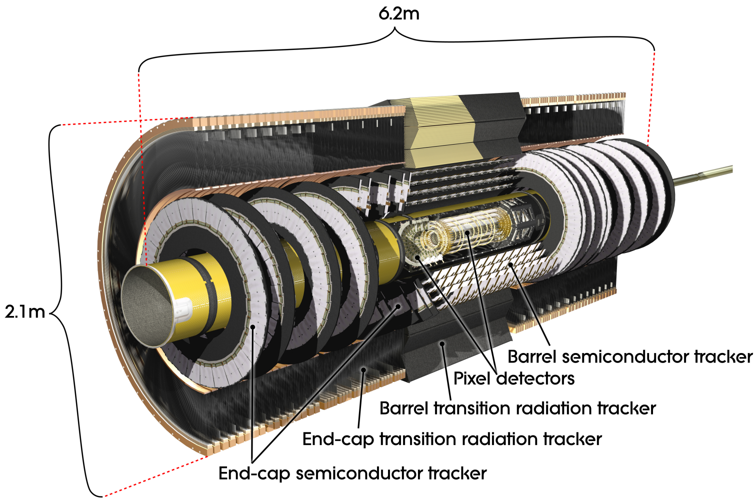

Figure 2.7. Rendering of the Inner Detector and its sub-components [24].

Pixel detector

The innermost part of ATLAS consists in four layers of silicon pixel detectors in the barrel and three disks in each of the endcaps. The three outer layers of the barrel were present since Run-I and are positioned at a radius of 50.5, 88.5 and $122.5\,\mathrm{mm}$ from the beam pipe, while the disks are placed at a longitudinal distance of 49.5, 58.0 and $65.0\,\mathrm{mm}$. The same design of the pixel sensors is used in both the endcap disks and the barrel layers, by using modules with a size of $50 \times 400, \mu\mathrm{m}^2$, providing a resolution of $10\,\mu\mathrm{m}$ in the transverse plane and $115\,\mu\mathrm{m}$ along z (or r in the disks).

The innermost barrel layer has been installed around a new beam pipe during the *Long Shutdown I* and takes the name of *Insertable B-Layer* (IBL) [35]. This additional layer is placed at a radial distance of $33.5\,\mathrm{mm}$ and is equipped with sensors with an area of $50 \times 250\,\mu\mathrm{m}^2$, with a hit resolution of $8\,\mu\mathrm{m}$ in the transverse plane and $40\,\mu\mathrm{m}$ along z.

Semiconductor Tracker

The Semiconductor Tracker (SCT) surrounds the Pixel detector with four cylindrical layers of silicon microstrip in the barrel, covering the radial range of $299\,\mathrm{mm} < r < 563\,\mathrm{mm}$ and extending along z up to $\pm 749\,\mathrm{mm}$. Nine disks with the same microstrip sensors are placed in each endcap, covering the $853\,\mathrm{mm} < z < 2720\,\mathrm{mm}$. SCT sensors are identical in the disks and in the barrel layers, with a native resolution of $17\,\mathrm{mm}$ in the $r - \phi$ plane and $580\,\mathrm{mm}$ along the z direction (or r direction in the disks).

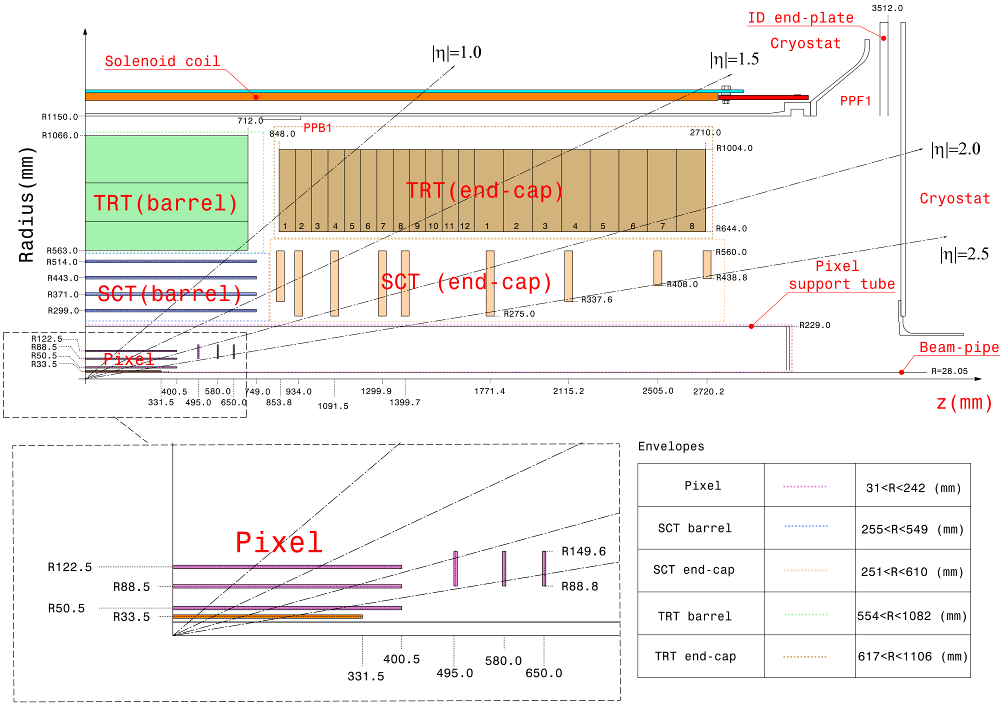

Envelopes		
Pixel	⋯	31<R<242 (mm)
SCT barrel	⋯	255<R<549 (mm)
SCT end-cap	⋯	251<R<610 (mm)
TRT barrel	⋯	554<R<1082 (mm)
TRT end-cap	⋯	617<R<1106 (mm)

Figure 2.8. Schematics ($r - z$ view) of a quadrant of the Inner Detector. The bottom-left panel shows a magnified view of the Pixel Detector [34].

Transition Radiation Tracker

Larger radii are covered by the Transition Radiation Tracker (TRT), which is made of many layers of gaseous straw tubes and plastic fibres which provide transition radiation. Each gaseous straw is filled with a mixture of 70% Xe, 27% CO_2 and 3% O_2 and is able to collect the ionisation left by a charged particle thanks to the 1.5 kV difference between the central wire and the straw wall. Plastic fibres induce transition radiation when are crossed by a charged particle and the corresponding photon is re-absorbed by the Xe atoms resulting in different readout signal. Given the dependence on β of the transition radiation emission probability, the identification of these photons allows for additional discrimination power between electrons and charged pions.

The barrel region of the TRT is made of three rings and 20 modules in each endcap, covering up to $|\eta| = 2$ and is able to provide the $r - \phi$ position in the barrel and the $z - \phi$ position in the endcap with a nominal resolution of 130 µm per tube.

2.2.4 Calorimeter System

The Calorimeter System of ATLAS is based entirely on sampling calorimeters which cover the pseudorapidity range of $|\eta| \leq 4.9$. Different technologies are used to cover different radiation environment and to contain hadronic and electromagnetic showers originated by high-energy particles. In the barrel, the electromagnetic (EM) calorimeter is more than 22 radiation lengths (X_0) thick, while the total thickness (EM and hadronic calorimeter) corresponds approximately to 11 interaction lengths (λ). The different sub-detectors composing the ATLAS Calorimeter System are described in the following and are visible in figure 2.9.

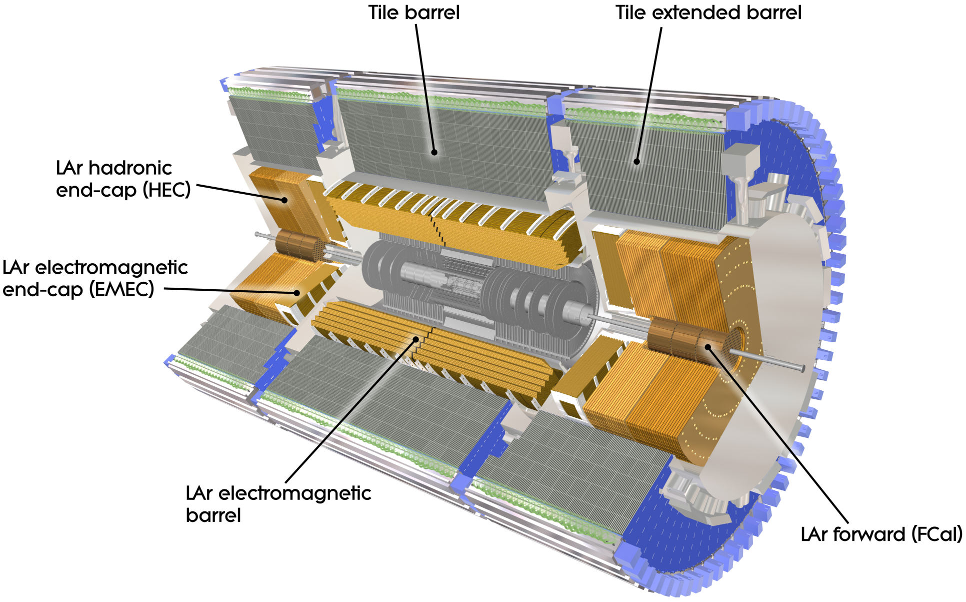

Figure 2.9. Rendering of the ATLAS Calorimeter System and its sub-components [24].

Electromagnetic Calorimeters

The EM calorimeter (ECAL) [36] is divided into a barrel part ($|\eta| \leq 1.475$) and two Endcap Electromagnetic Calorimeters (EMEC) ($1.375 < |\eta| < 3.2$). Both sections are made of accordion-shaped layers of lead absorber, kapton electrodes and a gas gap filled with liquid argon (which gives the name Liquid-Argon Calorimeter, LAr). The accordion shape allows a very uniform performance, in terms of linearity and resolution, along the ϕ coordinate.

The barrel section is divided in two parts for each ATLAS side, with a gap of $4\,\mathrm{mm}$ in the middle and it extends up to $|z| = 3100\,\mathrm{mm}$, while in the radial direction covers the range $1.4\,\mathrm{m} < r < 2\,\mathrm{m}$ [37]. Each endcap part extends in $|z|$ between $3.70\,\mathrm{m}$ and $4.75\,\mathrm{m}$ and in r between $330\,\mathrm{mm}$ and $2098\,\mathrm{mm}$. Within $|\eta| \leq 2.5$ the ECAL is segmented in three sections in depth, while the number of layers in the complementary endcap region is divided in two sections. For $|\eta| \leq 1.8$ a presampler detector, which is a separate thin liquid Ar layer, used to improve the energy resolution.

The barrel and the two endcap sections are installed in three different cryostats, to maintain the temperature of $89\,\mathrm{K}$ to keep the argon in its liquid phase, where the barrel one is shared with the Central Solenoid and the endcap ones are common for the electromagnetic and the LAr hadronic calorimeter. The gaps between the two cryostats, known as transition region, are filled with services and cables for the inner detector and the barrel LAr; this results in less precise measurements which are especially treated in physics analyses. The energy resolution of the EM calorimeter is:

$$\frac{\sigma(E)}{E} = \frac{10\%}{\sqrt{E\,[\mathrm{GeV}]}} \oplus 0.7\% \; .$$

Hadronic Calorimeters

The hadronic calorimeter (HCAL) uses different technologies depending on the region of the detector.

In the barrel the *Tile Calorimeter* surrounds the EM calorimeter cryostat covering the range $|\eta| < 1.0$, while two *Tile Extended Barrel* calorimeters cover $0.8 < |\eta| < 1.7$. This region is made of steel absorber interleaved with plastic scintillating tiles, extending from $2.28\,\mathrm{m}$ to $4.25\,\mathrm{m}$, segmented in three layers along its depth.

The Hadronic LAr Endcap Calorimeter (HEC) uses liquid argon as active medium, interleaved with a copper absorber, to cover the range $1.5 < |\eta| < 3.2$ and is divided in two wheels with an outer radius of $2.03\,\mathrm{m}$, each divided in two layers along the z direction. The pseudorapidity region between 3.1 and 4.9 is covered by the LAr Forward Calorimeter (FCal) which is designed to cope with very high radiation levels. To reduce the amount of neutron in the cavity of the inner detector, originating from the back-splash of hadrons in the FCal, its position is displaced by about $1.2\,\mathrm{m}$ with respect to the EMEC inner surface. This constraint in size requires the use of a denser material: the first of the three modules encountered along z uses copper absorber and is optimised for the identification of electromagnetic showers, while the outer two uses tungsten and act as hadronic calorimeters.

Within the range $\eta < 3.2$ the energy resolution is:

$$\frac{\sigma(E)}{E} = \frac{50\%}{\sqrt{E\,[\mathrm{GeV}]}} \oplus 3\% \; ,$$

while for the FCal the resolution becomes:

$$\frac{\sigma(E)}{E} = \frac{100\%}{\sqrt{E\,[\mathrm{GeV}]}} \oplus 10\% \; .$$

As in the case of the electromagnetic calorimeter, the gaps between the Barrel Tile Calorimeter and the two Extended Barrel are used for services and cabling, reducing the resolution in the corresponding η intervals. A set of plastic *Tile Gap* scintillators cover the gap region between the two parts of the Tile Calorimeter, corresponding to $1.0 < |\eta| < 1.2$. Similar scintillators are installed in the crack region between the two cryostats of the EM calorimeter (*Crack Scintillators*) and cover the range $1.2 < |\eta| < 1.6$.

2.2.5 Muon Spectrometer

The ATLAS Muon Spectrometer is based on four sub-detectors, two of which are used for the main purpose of precision tracking, while the other two provide fast signals, with lower resolution, allowing a fast *trigger* for interesting events. The whole system is supported by a light and open structure in air and is embedded in the magnetic field of the ATLAS toroids, which deviates the particle trajectories in the $z-r$ plane, allowing for a measurement of the muon momentum with a relative resolution of $2 \div 3\%$ for most of the kinematic range, reaching 10% for momenta of the order of $1\,\mathrm{TeV}$.

The system is divided, as the rest of the detector, in a barrel part (up to $|\eta| = 1.05$) and two endcap parts. In the barrel, the geometry of the muon system follows the layout of three coaxial cylinders centered in the IP, named *Barrel-Inner* (BI), *Middle* (BM) and *Outer* (BO), at radii of approximately $5\,\mathrm{m}$, $7.5\,\mathrm{m}$ and $10\,\mathrm{m}$. A gap at $\eta = 0$ divides the barrel MS in two sides to allow services for the Central Solenoid, the Calorimeter System and the Inner Detector, while additional gaps are present in correspondence of the supporting structure of the detector, as explained in [24].

In the endcaps, three wheel-shaped structures cover the region at large pseudorapidity, named *Endcap-Inner* (EI), *Middle* (EM) and *Outer* (EO)[2], placed at $|z|$ distances of $7.4\,\mathrm{m}$, $14\,\mathrm{m}$ and $21.5\,\mathrm{m}$ from the interaction point. Another *Endcap-Extra* (EE) set of precision chambers is placed at $|z| = 10.8\,\mathrm{m}$ to identify muons which cross the transition region between the barrel and the endcap.

As visible from figure 2.10, different *Muon Chambers* exploiting different detector technologies are used: *Monitored Drift Tubes* (MDTs) and *Cathode Strip Chambers* (CSCs) are used for precision measurements, while *Resistive Plate Chambers* (RPCs) and *Thin Gap Chambers* (TGCs) are used for trigger.

In the barrel, the position of the MDT and RPC chambers is arranged to achieve the maximum ϕ coverage, hence the three cylinders are divided in eight octants, each divided in small and large sectors, as visible in figure 2.11. Figure 2.12 shows a detailed representation of the position of the different MS sub-detectors in the bending $(r-z)$ plane.

A brief description of the chambers used in the ATLAS muon system is given in the following sections.

Precision chambers

Monitored Drift Tubes are used for the precision measurement of the muon tracks within $-2.7 < \eta < 2.7$, and up to $-2 < \eta < 2$ in the EI. The main component of the MDT chambers are the aluminum drift tubes with a diameter of $\sim 30\,\mathrm{mm}$, filled with a $93\% : 7\%$ mixture of Ar and CO_2, where the ionisation left by a particle is collected by a coaxial anode wire kept at a potential of $3\,\mathrm{kV}$. Multiple tubes are arranged in two *multilayers* of three or four layers of tubes placed along the $r-z$ plane, yielding a resolution up to $3\,\mu\mathrm{m}$.

---

[2] These are also named: Small Wheel, Big Wheel and Outer Wheel

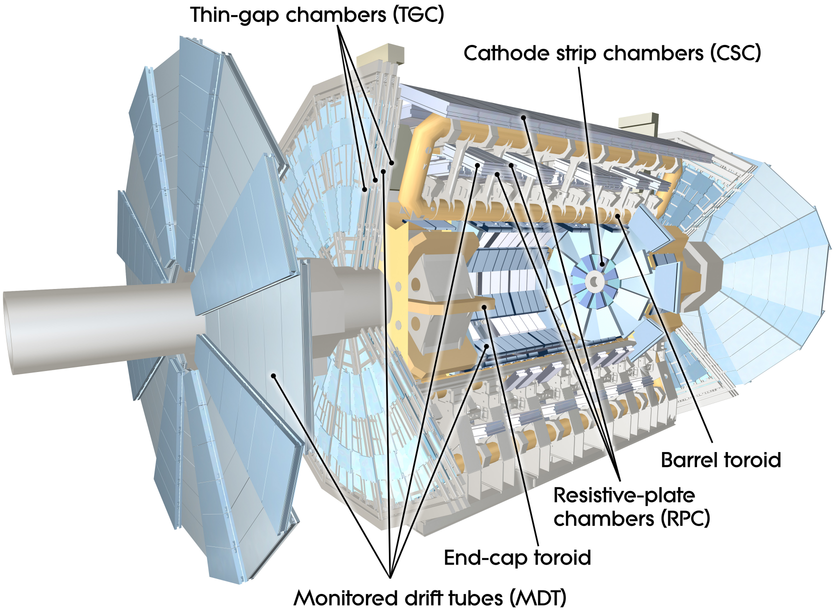

Figure 2.10. Overview of the ATLAS Muon Spectrometer [24].

In the $-2 < \eta < 2.7$ region of the Small Wheel, the particle rate exceeds the safe limit for MDTs of $150\,\mathrm{Hz/cm^2}$, hence only in this portion of the spectrometer Cathode Strip Chambers are used, as they can cope with a rate up to $1\,\mathrm{kHz/cm^2}$. The CSCs are multi-wire proportional chambers based on a $80\% : 20\%$ mixture of Ar and CO_2, organised in quadruplets providing four independent measurements of the η and ϕ coordinates with a resolution of $5\,\mathrm{mm}$ per chamber.

Trigger chambers

Resistive Plate Chambers are used in the barrel, up to $|\eta| < 1.05$ to provide a rapid signal which can be used for triggering events. The two resistive plates are separated by $2\,\mathrm{mm}$ gaps filled with $97\% : 3\%$ $C_2H_2F_4$ and C_4H_{10}, kept at a potential difference of $9.8\,\mathrm{kV}$. The high voltage is rapidly discharged when a charged particle ionises the gas inside the gap, leading to a signal yielding a trigger timing resolution of about $1\,\mathrm{ns}$. A segmentation of the plate in *strips* of width between $25\,\mathrm{mm}$ and $35\,\mathrm{mm}$ allows a preliminary position measurement of the hit left by a track. RPCs are instrumented only in the BM and BO layers, with two RPC doublets (oriented to measure both the η and ϕ coordinates) sandwiching the BM MDT chambers, and a single doublet for the BO layer chambers, as shown in figure 2.11.

Thin Gap Chambers are multi-wire proportional chambers providing the trigger information in the region $1.05 < |\eta| < 2.4$ and are instrumented in the EI and EE layers of the MS. They use a gas mixture of $55\% : 45\%$ CO_2 and n-pentane, with anodes parallel to the MDT wires and cathode strips along the radial direction, providing a two-dimensional measurements of a hit with a time resolution of the order of $5\,\mathrm{ns}$.

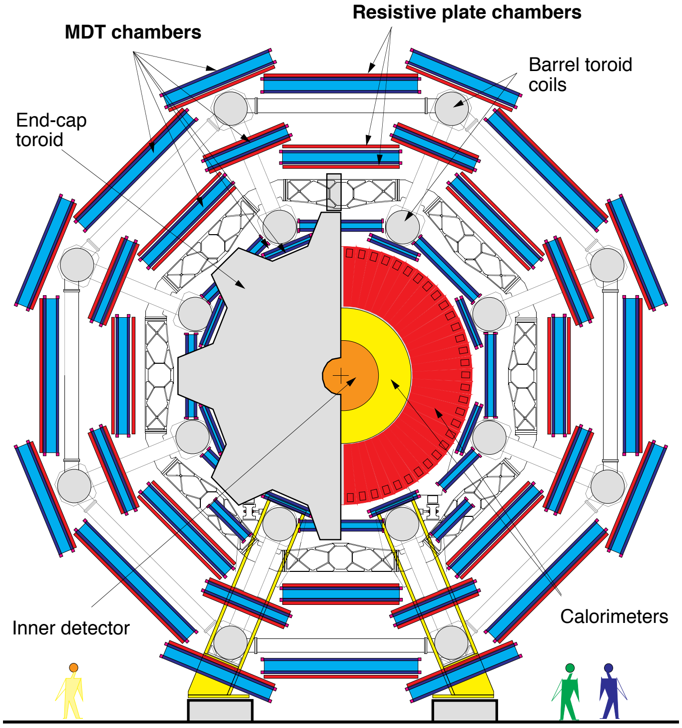

Figure 2.11. Schematics of the MS barrel in the transverse plane, showing both MDT and RPC chambers position divided in eight large and eight small sectors [38].

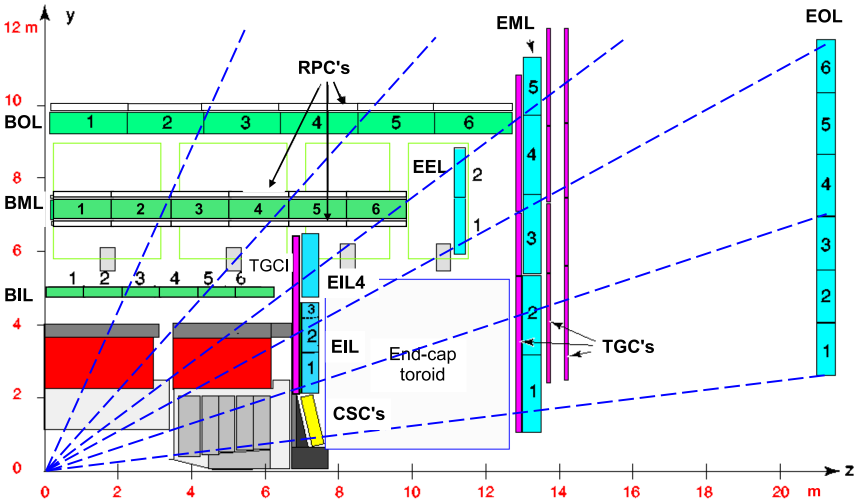

Figure 2.12. Schematics of a quadrant of the MS sub-detector in the bending plane ($r - z$). The path of muons with infinite momentum is shown as blue dashed lines [24].

2.2.6 Trigger system

The collision rate of LHC proton bunches during Run-II was of $40\,\mathrm{MHz}$, corresponding to one bunch crossing every $25\,\mathrm{ns}$. Considering that in order to save the full information of a single event approximately $1.5\,\mathrm{MB}$ of data are written, if ATLAS had to record every single event that is produced, it would need $60\,\mathrm{TB}$ per second! This immense data rate is not compatible with modern technology for data storage, but most of the events originating from pp collisions are also soft parton scattering which do not contain any interesting physics signature, hence given that there is no need to save such a large rate of events, a preliminary selection is done *before* the event is recorded. This selection is made by the ATLAS Trigger System and it is done partially with dedicated electronics, which exploits basic information from the detectors, and partially with software algorithms relying on a preliminary reconstruction of the event [39].

The *Level 1* (L1) trigger is entirely based on electronics which elaborates pipelined information from the Muon System (L1Muon), the Calorimeter system (L1Calo), plus the L1 Topological Processor (L1Topo). The L1Muon trigger is produced from the information sent by the readout electronics of the three RPC and TGC trigger stations. The information allows to form a hit pattern in the η and ϕ coordinates which is passed to dedicated on-detector boards, which match the hit pattern with pre-defined coincidence matrices, centered on the middle trigger station, corresponding to different trigger thresholds. Information from the first two RPC or TGC stations is combined to produce a trigger with a Low-p_{T} threshold, while a High-p_{T} trigger is obtained by the combined information of the three trigger stations. The information from the TGC stations is also combined with a coincidence in the Tile Calorimeter to reduce the rate of fake triggers in the region $1.05 < |\eta| < 1.3$ [40]. The L1Calo trigger combines the digitised information from the calorimeter front end electronics, and is divided in two parts. One part performs a search for photons, electrons, taus and jets using the full granularity available and providing triggers with different E_{T} thresholds, based on combined information of the EM and hadronic calorimeter. The other part performs a scalar and vector sum of the E_{T} to provide a $E_{\mathrm{T}}^{\mathrm{miss}}$ trigger with different thresholds. The L1Topo provides a decision based on combined L1Calo and L1Muon items, including their relative position and thresholds, energy threshold inside a ΔR cone, combined mass and correction to the $E_{\mathrm{T}}^{\mathrm{miss}}$ [41]. The final trigger accept/reject decision is made by the Central Trigger Processor (CTP), which takes the combined output of the L1Tau, L1Calo and L1Topo triggers.

The L1 Trigger output rate peaks at a maximum of $100\,\mathrm{kHz}$ and, for each event accepted, the front end electronics reads out the information from the full detector. Data is initially sent to the *Read Out Driver* (ROD), which performs an initial pre-processing, then is sent to the *Read Out System* (ROS) to buffer the data. At this point the η and ϕ coordinates of the L1 *Regions-of-Interest* (RoI) are sent through the second trigger level: the *High Level Trigger* (HLT). The HLT is entirely software-based and runs on processing unit farms, using data fragments within a RoI to reconstruct physics object which are inputs of various trigger algorithms, known as *trigger chains*, which make a selection based on the object kinematics, isolation criteria, or even the presence of unconventional signatures. If a trigger algorithm returns a positive decision, data corresponding to that event are saved to a permanent storage facility. The typical output rate of the HLT farm during Run-II was of $1.2\,\mathrm{kHz}$, with an average of $1.2\,\mathrm{GB/s}$ of data sent to permanent storage [42].

Different teams from the ATLAS collaboration have maintained the list of active trigger chains during the data-taking periods, to keep the threshold of the corresponding selections as low as possible. If during the runs the output rate of a certain L1 trigger or HLT chain becomes too high, and affects the rate of other triggers, a *prescale* factor can be applied, selecting only one over N triggered events. Normally, events selected by *prescaled* triggers are not used for physics searches, but are still saved for performance studies.

2.2.7 Event simulation

Many aspects of the physics studies done by the ATLAS Collaboration are based on simulated Monte Carlo (MC) events, spanning from the calibration of the subdetectors to the computation of the expected number of events in physics analyses. An brief summary of the simulation process is given below, while a more detailed overview is available in [43].

Simulated events are generated starting from the hard-scattering process up to the computation of the particles in the final state, including the hadronisation of quarks and gluons. Eventual decay processes in which the particles are involved are, by default, simulated if they happen with a proper decay length of $c\tau < 10\,\mathrm{mm}$. An exception is made for the case of long-lived particles, for which this limit on the maximum $c\tau$ is relaxed and their decay is simulated also at longer distances.

Once the final-state particles are determined, their interaction with the detector must be simulated. For this step, an accurate model of the ATLAS detector has been implemented with the software GEANT4 [44], which is kept updated with any modification that happens to the detector, including misalignment and distortions. The output of this step is a *hits* file containing all the information on the energy deposits in the sensitive material of the detector.

At this stage, simulated hits are used as input to a *digitization* step, overlaid with simulated hits from pileup and backgrounds originating from the LHC beams. As the simulation step is usually very intensive in terms of computing power, these additional hits file are simulated once and are added at this point to reduce the CPU-time of the simulation. The digitization step simulates the electric signals induced in the read-out components of the detector and possible electronic noise. Once these signals are generated, they are sent to an emulation of the RODs, and finally are processed by the same algorithms that evaluate the HLT chains and compute the event reconstruction of real data.

In MC events, the *truth*-level information of the hard-scattering particles and their decay products is kept and stored for analysis purposes.

2.3 Object reconstruction in ATLAS

Once an event is accepted by the ATLAS Trigger, the electronic signals produced by each detector sub-component described in section 2.2 are recorded and saved to disk.

At this stage, the raw information obtained by these signals needs to be processed in order to find the candidates for electrons, muons, photons, jets, etc., in a step that is called *physics object reconstruction*. These objects are the closest representation available of the underlying particles that produced the corresponding signature, but natural imperfections in the reconstruction process are always present and treated during a specific *calibration* step.

The last stage of the reconstruction consists in producing a file format, containing each recorded event and the relevant physics objects needed for the physics analysis. The software responsible for the reconstruction, calibration, and also for the HLT trigger implementation is Athena [45], which is based on the Gaudi [46] framework for data processing in HEP experiments.

In the following a description of how detector signatures are reconstructed as physics objects is given.

2.3.1 Inner Detector Tracks and Primary Vertices

The average number of pp interactions per bunch crossing leads to a large density of track in the ID. The identification of the tracks left by charged particles becomes an even more challenging task during high-luminosity runs, as many collision vertices can originate from a single bunch crossing. A clearly visible example of the large number of tracks originated in an event is given in figure 2.13.

The path of a charged particle produced in the ATLAS Interaction Point is deflected by the magnetic field resulting in a helical trajectory described by five parameters. The impact parameter in the transverse plane (d_0) and the one in the $z-r$ plane (z_0) are the distances of closest approach between a track and the Primary Vertex (PV) in the respective planes; the other three parameters are the θ and ϕ angles of the track momentum and the ratio q/p of the track charge and momentum.

The track reconstruction algorithm starts from the hits left in the Pixel and SCT detectors, which are initially clustered together in space-points. Three of these clusters become a seed for a particle track, to which other points are added via an algorithm based on the combinatorial Kalman filter [48]. At this point the track candidates are processed with an ambiguity solving algorithm, which relies on a set of parameters that includes the track momentum, the cluster multiplicity in each sub-detector, the χ^2 of the track fit and the presence of holes, defined as the number of intersection of a track with sensitive material in which no cluster hit is found.

Track candidates are rejected by the ambiguity solver if they fail to meet one of the following requirements, defining the *Loose* working point:

- $p_{\mathrm{T}} > 400\,\mathrm{MeV}$;

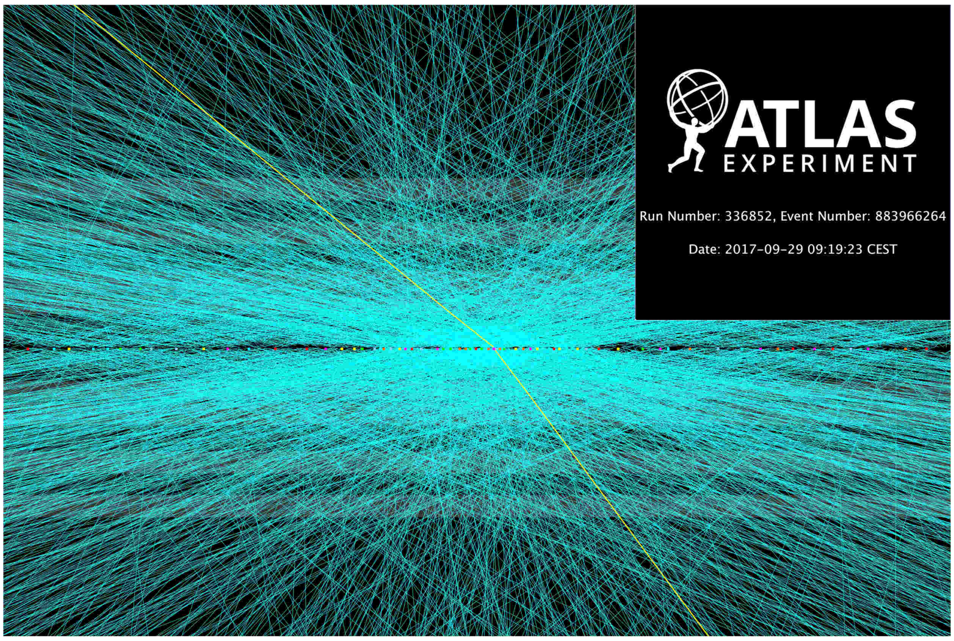

Figure 2.13. Display of the Inner Detector in a pp collision event, collected in September 2017, with a $Z \to \mu\mu$ candidate and 65 additional vertices. Image taken from [47].

- $|\eta| < 2.5$;
- At least 7 clusters in Pixel/SCT;
- At maximum one shared pixel cluster or two shared SCT clusters on the same layer;
- At maximum two holes in the Pixel/SCT and maximum one hole in the Pixel;
- $|d_0| < 2\,\text{mm}$;
- $|z_0 \sin\theta| < 3\text{mm}$.

On top of these, the *Tight-Primary* working point requires:

- At least 9 hits in Pixel/SCT (if $|\eta| \leq 1.65$);
- At least 11 hits in Pixel/SCT (if $|\eta| \geq 1.65$);
- Either one hit on the IBL or on the innermost pixel layer;
- No Pixel holes;

Track candidates are then extrapolated to the TRT and their parameters are updated after performing a high-resolution fit of the trajectory. A more complete overview of how tracking algorithms are implemented and their performance during Run-II is given in [49, 50].

Once the ID tracks have been reconstructed, a seed for a first vertex is searched between the intersections of the tracks and the beam line. An iterative algorithm involving the position of the vertex seed and the parameters of the tracks finds the optimal vertex position. The full procedure is described in [51]. Tracks found incompatible with the vertex are rejected and used as input for the identification of other vertices until no unassociated tracks are left. Once this step is completed, the Primary Vertex is identified as the one with largest $\sum p_{\mathrm{T}}^2$ of corresponding tracks. Other vertices are labeled as pileup vertices.

Inner detector tracks used in the analysis detailed in chapter 5 are *Tight-Primary* ID tracks, which also have $p_{\mathrm{T}} > 500\,\mathrm{MeV}$ and $|z_0 \sin\theta| < 1.5\,\mathrm{mm}$.

2.3.2 Jets

Hadronic jets are the final product of the hadronisation of a quark or a gluon and are composed of a multitude of collimated hadrons. Given that, their corresponding signature has to be found in both the ID and the Calorimeter System. The identification of a jet starts in the calorimeter, from the identification of clusters of localised energy deposits.

Calorimeter clusters

The high granularity of the ATLAS calorimeter allows to combine the signals, left by the particles interacting with the sensitive material of the detector, in clusters of topologically connected cells, known as *Topological Calorimeter Clusters* (or caloclusters, topoclusters). Their reconstruction algorithm is described below and is well documented in [52].

The formation of topoclusters starts with the identification of calorimeter cells with a signal ($E_{\text{cell}}^{\text{EM}}$) of which the absolute value is significantly larger than the average expected noise ($\sigma_{\text{noise,cell}}^{\text{EM}}$). Here both the signal and the noise are measured at the electromagnetic (EM) scale, which means that the energy is measured in a way that the prediction is correct for photons and electrons, while corrections for hadrons due to the non-compensating nature of the ATLAS calorimeter are not included. A cell becomes a seed for a calocluster if the signal sensitivity, defined as

$$\xi_{\text{cell}}^{\text{EM}} = \frac{\left|E_{\text{cell}}^{\text{EM}}\right|}{\sigma_{\text{noise,cell}}^{\text{EM}}}$$

is larger than 4. At this point all the *neighbouring* cells are added if their signal significance is larger than 2, where two cells are considered neighbouring if they are adjacent in the $\eta - \phi$ plane, or if they belong to different calorimeter segmentation layers but have at least partial overlap in (η, ϕ). Once a cell is added to the clusters the same requirement is tested on its neighbouring cells, repeating this step of the algorithm until the requirement of $\xi_{\text{cell}}^{\text{EM}} > 2$ is no more satisfied. Finally, all the cells adjacent to the ones belonging to the cluster, with $\xi_{\text{cell}}^{\text{EM}} > 0$, are added.

At this point clusters containing two or more signal maxima are split in multiple ones, then their four-momentum, position and other geometrical moments are identified, as discussed in [52]. As topoclusters can include cells belonging to different calorimeter samplings, the information of their energy and the position of their centroids are also computed for each sampling. Finally, an *origin* correction is applied to each cluster, based on their pseudorapidity and position in the calorimeter, to take into account the position of the primary vertex.

Jet identification

Once clusters have been reconstructed, their four-vectors are used as input to the anti-k_t jet clustering algorithm, presented in [53], which is an infrared and co-linear safe algorithm which is based on the evaluation of the distance metrics:

$$\begin{aligned} d_{ij} &= \min\left(\frac{1}{k_i^2}, \frac{1}{k_j^2}\right) \frac{\Delta R_{ij}^2}{R^2} \ , \\ d_{iB} &= \frac{1}{k_i^2} \ , \end{aligned}$$

where R is the radius parameter, set to 0.4, ΔR_{ij}^2 is the distance between two clusters in the rapidity-azimuth plane, k_i (k_j) is the transverse momentum of the i-th (j-th) topocluster. With such definition, d_{ij} measures the distance between two constituents, while d_{iB} represents the distance between a constituent and the beam.

The jet clustering algorithm is an iterative algorithm which at each step computes the two metrics for each cluster pair. Then if the minimum distance is a d_{ij}, the two i and j clusters are combined in a single constituent and are removed from the next iterations. On the other hand, if the minimum distance is a d_{iB} the i-th constituent is removed from the next iterations and is saved as a jet. The algorithm goes on until there are no more constituents in the input list. Quantities like the four-momentum, position, fraction of energy in each sampling, electromagnetic fraction $f_{\mathrm{EM}} = E_{\mathrm{ECAL}}/E$ and the timing with respect to the current bunch crossing are computed for each jet combining the information of the corresponding clusters.

Jets used in this thesis are identified from the sole calorimeter information and in literature are often referred to as *EMTopo jets*. During Run-II many ATLAS analyses started to use jet reconstructed with the *Particle Flow* algorithm, documented in [54], which exploits ID tracks in addition to clusters. This algorithm improves the accuracy of the measurement of the charged component of a jet, but is not reliable for searches which look for displaced LLP decays outside the acceptance of the Inner Detector.

Jet calibration

The energy of the jet is obtained from the one of its constituents, which as mentioned above are caloclusters measured at the EM scale and corrected for the position of the PV. A set of additional corrections, briefly described below, are applied to the

Jet Energy Scale (JES) and to the *Jet Energy Resolution* (JER), in order to match the expected energy corresponding to particles produced in a hadronic shower, to better match the energy of the incoming particles and to correct for several other effects. A more detailed overview of the JES and JER corrections is given in [55].

An initial correction is applied to the p_{T} of a jet, removing the contributions from surrounding activity in the calorimeter which is due to the presence of pileup vertices. This correction results in a reduction of the jet p_{T} and is implemented exploiting the average p_{T}-density in the $y - \phi$ plane and the actual area of a jet. A residual effect correction, dependent on the number of interactions per bunch crossing and the number of primary vertices, is applied to the jet transverse momentum.

At a second stage, an absolute correction of the JES and the jet η attempts to match the four-momentum of the reconstructed jet with the one of the particles originating the shower. This correction is derived by simulated events, using reconstructed jets after the origin and pileup corrections, matching the truth jet to the reconstructed one if the first is within a $\Delta R = 0.3$ cone centered in the second one. For such jets the energy response, defined as the ratio $E_{\text{reco}}/E_{\text{truth}}$, is computed and determined in bins of E_{truth}, then is inverted and applied to the EM scale jets. A similar correction is applied to the reconstructed value of η, parametrising the difference between η_{truth} and η_{reco} as a function of η and E_{truth}, this correction has a more significant effect for jets in the transition region between the barrel and the endcap, and between the endcap and forward calorimeter.

After the previous corrections have been applied, the difference of p_{T} between truth and reconstructed jets can vary, depending on many aspects like the jet energy distribution, the development of the shower along the calorimeter depth and the particle that initiates the shower. A set of sequential corrections, named *Global Sequential Calibration* are derived using five (or six for Particle Flow Jets) observables and applying the relative correction as a function of the truth p_{T} and η of the jet.

The last step of the jet calibration consists in applying correction factors derived in data events, measuring well known processes. These *in-situ* calibrations are divided in two classes, the first corrects the p_{T} response of jets in the forward region ($0.8 < |\eta| < 4.5$), to that of well-measured events in which two central jets ($|\eta| < 0.8$) are back-to-back in ϕ. A second step consists in balancing the p_{T} of central jets to a reference object which provides the correct p_{T} scale; for this purpose $Z \to ee$ or $Z \to \mu\mu$ are reference objects for the p_{T} up to $950\,\mathrm{GeV}$, while the balance to a set of low-p_{T} jets allows for a correction up to $2\,\mathrm{TeV}$.

Identification of jets from pileup

The *Jet Vertex Tagger* (JVT) is a k-nearest-neighbours classifier which has been developed for the identification of jets originating from hard-scattering vertices, rejecting the ones originating from pileup. This algorithm, which is documented in [56], is widely used in physics analyses and has also been used in the ones presented in this thesis.

The JVT operates on two variables: corrJVF and $R_{p_{\mathrm{T}}}$. The former stands for

Pileup-corrected Jet Vertex Fraction, and is defined as the scalar sum of the p_{T} of ID tracks associated with a jet, divided by the scalar sum of the p_{T} of all the tracks, corrected with a factor that takes into account the number of pileup tracks associated with a jet. The latter is the ratio between the scalar sum of the p_{T} of the tracks associated with a jet and its calibrated p_{T}.

The output score of the JVT is such that a score of 0 is predicted for pileup jets, while 1 is assigned to jets which originate from the hard scattering vertex. A default value of -0.1 is assigned to jets with no associated ID track. The distribution of the output score for simulated dijets events is shown in figure 2.14.

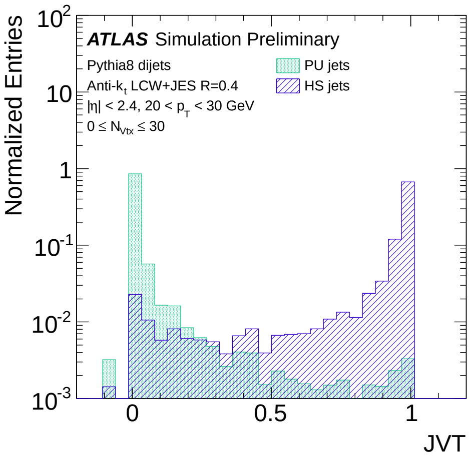

Figure 2.14. Distribution of the JVT output score for jets originating from the Hard Scattering vertex (HS) and pileup (PU) vertices. Figure taken from [56].

The usual approach adopted in physics analyses is to reject jets with low JVT score, in order to increase the purity of a sample of hard-scattering jets. In long-lived particle searches, rejecting jets with large JVT score will help in reducing the background of QCD multijet events, without affecting jets originating from LLP decays, as the latter are expected to leave no visible track in the ID.

Jet cleaning

Jets from pp collisions must be distinguished from the ones originating from non-collision background or large noise bursts in the calorimeter. Non-collision background is discussed with detail in chapter 4, and is due to either cosmic-rays crossing the calorimeter or muons originating in the interaction of LHC protons with the components of the accelerator, such as dipoles and collimators (*beam-induced background*).

A set of jet cleaning working points is defined to reject *fake jets* due to these sources. These working points are based on variables which are either energy ratios between different sub-sections of the calorimeter (e.g. the f_{EM}) and variables related to the signal shape left in calorimeter cells. A detailed description is given in [57].

The observables that take into account the quality of the signal are defined using the quadratic difference of the pulse shape in a LAr calorimeter cell with respect to the one expected by simulations of its electronic response, Q^{LAr}_{cell}, of which the definition is given in [57]. If $Q^{LAr}_{\text{cell}} > 4000$, the corresponding cell is considered to have a poor quality signal. Three jet-level quantities are defined from this variable: the average jet cell quality $\langle Q \rangle$, defined as the energy-squared weighted average of Q^{LAr}_{cell}, fraction of poor quality cells in LAr calorimeter $f^{\text{LAr}}_{\text{Q}}$ and the fraction of poor-quality cells in the HEC, $f^{\text{HEC}}_{\text{Q}}$, which for good jets originating from pp interactions are all expected to have values close to 0. An additional signal-quality variable is the negative energy, E_{neg} measured due to downward fluctuation of the signal in calorimeter cells, which absolute value is expected to be lower than $50\,\text{GeV}$.

The variables taking into account energy ratios of a jet are: the already defined f_{EM}, the jet charged fraction f_{ch}, defined as the ratio of the scalar sum of the p_{T} of the jet-associated tracks originating in the PV and the jet p_{T}, the f_{max}, defined as the maximum jet energy fraction among all calorimeter samplings and the jet f_{HEC}, which corresponds to the fraction of energy left in the endcap LAr hadronic calorimeter. Fake jets from non-collision background cross the calorimeter moving in a direction which is either the one of cosmic-rays, or parallel to the beam pipe in the case of beam-induced background. For this reason they exhibit low f_{ch} (as they are less likely to originate tracks associated to their energy deposits), low or high values of f_{EM} and high f_{max} due to the high probability of crossing one single calorimeter sampling.

In this thesis the cleaning working point chosen for jets originating in pp collisions is the *Loose* working point, which is designed for high good jet efficiency ($> 99.5\%$ for $p_{\text{T}} > 20\,\text{GeV}$), while maintaining fake jet rate as low as possible. A *Tight* working point is also defined in [57], which maximises the fake jet rejection while keeping the good jet efficiency above 95% for jets with $p_{\text{T}} > 20\,\text{GeV}$. For the peculiar case of jets originating from LLP decays, f_{EM} and $f_{\text{ch}} = 0$ can both assume very small values, hence a modified working point has been adopted when searching for LLPs, defining the *Loose-LLP* working point, which is identical to the Loose one, but with relaxed cuts on the EM energy fraction and a tighter cut on the negative energy. A list of cuts defining the Loose-LLP and the Loose working point is shown in table 2.1. A jet that satisfies at least one of the cuts, denoted with a check-mark in table 2.1, is recognised as a fake jet and not accepted by the corresponding working point.

B-tagging

Jets originating from heavy flavoured quarks, like bottom or charm, differ from the so-called *light jets* initiated by u, d, s or gluons. The main cause of this difference is that hadrons containing b-quarks have a relatively large mean proper lifetime and, at the energies of the LHC, they can travel few mm before decaying.

The identification of b- or c-jets, namely jets containing b or c hadrons, plays an important role in many physics analyses and it is used, in the search for dark photon decays presented in this thesis, to reject background events where a pair

	Loose-LLP	Loose
$f_{\mathrm{HEC}} > 0.5$ and $f_{\mathrm{Q}}^{\mathrm{HEC}} > 0.5$ and $\langle Q \rangle > 0.8$	✓	✓
$\lvert E_{\mathrm{neg}} \rvert > 60\,\mathrm{GeV}$	✓	✓
$f_{\mathrm{EM}} > 0.95$ and $f_{\mathrm{Q}}^{\mathrm{LAr}} > 0.8$ and $\langle Q \rangle > 0.8$ and $\lvert \eta \rvert < 2.8$	✓	✓
$f_{\max} > 0.99$ and $\lvert \eta \rvert < 2$	✓	✓
$f_{\mathrm{EM}} < 0.05$ and $f_{\mathrm{ch}} < 0.05$ and $\lvert \eta \rvert < 2$	×	✓
$f_{\mathrm{EM}} < 0.05$ and $\lvert \eta \rvert \geq 2$	×	✓
$\lvert E_{\mathrm{neg}} \rvert > 4\,\mathrm{GeV}$ and $f_{\max} > 0.85$	✓	×

Table 2.1. Cuts defining the Loose-LLP and Loose working points for fake jet rejection. If at least one of the cuts is satisfied by a jet, the jet is not accepted by the corresponding working points denoted with a check-mark. Additional details on these cuts are given in [57].

of top quarks are produced. The b-jet identification is performed using a set of low-level observables, obtained from tracks associated to the jets, which are then fed as input to a multivariate classifier, named *MV2*, which is briefly summarised in the following. Additional details on MV2 and on other b-tagging methods in ATLAS are given in [58] and [59].

The MV2 classifier is a boosted decision tree, trained to output a score between -1 and 1, where values close to 1 are assigned to jets which are more likely to contain one or more b-hadrons. Its inputs are the p_{T} and η of the jet, as well as the output variables of the following discriminants:

- *IP2D* and *IP3D* [58] are two log-likelihood discriminants, the former built on the transverse impact parameter of the tracks and the latter on both the transverse and longitudinal impact parameters.
- *SV1* [60] is an iterative algorithm that searches for a secondary vertex in the jet. It starts from two-track-vertex candidates and iterates on all the tracks evaluating the track-vertex association with a χ^2 test, until a vertex with invariant mass larger than $6\,\mathrm{GeV}$ is found. It outputs eight variables characterising the tracks, the vertex and their mutual association.
- The *JetFitter* [61] is a multi-vertex algorithm that attempts to reconstruct the decay chain of a b- or c-hadron. As the SV1, it outputs eight variables characterising the tracks and the vertex.

The working point of the MV2, used in the analysis described in chapter 5, is chosen selecting a cut on its output score that yield a b-tagging efficiency of 70%. Its output score is shown as example, for $t\bar{t}$ events, in figure 2.15.

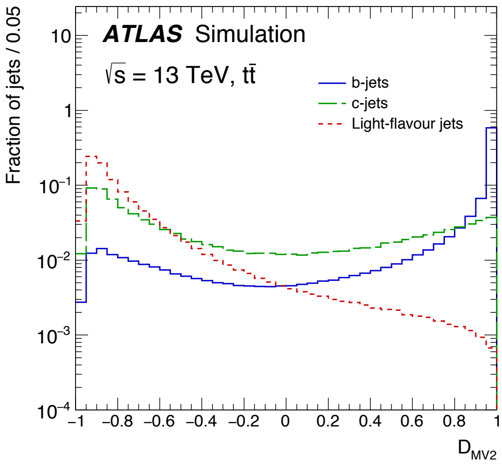

Figure 2.15. MV2 output score for b-, c- or light jets found in simulated $t\bar{t}$ events. Image taken from [59].

2.3.3 Electrons and photons

The reconstruction of electrons and photons exploits the ID and the EM calorimeter, as their signature is primarily the one originating from electromagnetic showers which in the case of electrons are matched to a track. An overview of the electron and photon reconstruction algorithm, which is discussed with great detail in [62], is given in the following.

The algorithm starts with a search for calorimeter clusters which have a large energy fraction in the ECAL ($f_{\text{EM}} > 0.5$), which are then associated to potential electron ID tracks using a matching in η and ϕ. At this stage, tracks and clusters are fitted with a Gaussian Sum Filter (GSF) method [63], which has better performance for particles which lose their energy via bremsstrahlung than the combinatorial Kalman filter, normally used for ID tracks.

After that, a seed cluster with $E > 1\,\text{GeV}$, matched to a track with at least four hits in the silicon trackers, is identified. Then, satellite clusters which may emerge from bremsstrahlung are also identified and their cells are added to the seed ones in a single *supercluster*. In order to be identified as satellite, one cluster must lie in a $\Delta\eta \times \Delta\phi = 0.075 \times 0.125$ window around the seed, or be within $\Delta\eta \times \Delta\phi = 0.125 \times 0.300$ and be matched to the same ID track.

A similar procedure searches for photon superclusters, which are seeded by $E > 1.5\,\text{GeV}$ clusters with no track-matching requirement. Satellite clusters are then added if they lie in a $\Delta\eta \times \Delta\phi = 0.075 \times 0.125$ window around the seed, or also if they match tracks from a photon conversion vertex which are also matched to the seed cluster.

The correspondence between tracks and clusters is re-computed using superclusters, defining electrons and photons objects to be used in the analysis stage. If an ambiguity is present and a supercluster can not be identified either as electron or a photon, both objects are created. At this point different selection criteria are applied to reconstructed electrons and photons, aiming to select the *prompt* ones originating from the hard-scattering vertex.

Electron identification and isolation criteria

After the supercluster reconstruction, electrons are selected with a likelihood discriminant which exploits variables related to the ID tracks, the supercluster and their mutual matching. In this way, fake electrons from converted photons, as well as non-prompt photons produced in the decay of other particles and mis-reconstructed deposits from hadronic jets can be rejected.

Four fixed values of the discriminant define four corresponding operating points: *VeryLoose*, *Loose*, *Medium* and *Tight*. The identification efficiency of the Loose, Medium and Tight operating points is shown in figure 2.16.

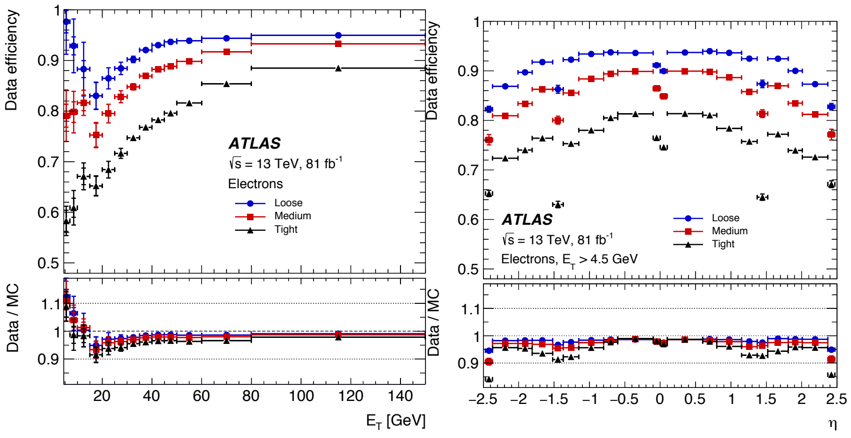

(a) **(b)**

Figure 2.16. Electron identification efficiency of the Loose, Medium and Tight working points in $Z \to ee$ data events, shown as a function of E_{T} (a) and η (b). Image taken from [62].

To further suppress non-prompt leptons from heavy flavour decays or the misidentification of light hadrons as electrons, isolation criteria are applied to tracks and energy clusters found in the vicinity of the electron candidate. Two important isolation variables used for this selection are: $E_{\mathrm{T}}^{\mathrm{cone20}}$, defined as the sum of the transverse energy of clusters found in a $\Delta R = 0.2$ cone around the candidate, excluding the clusters from the candidate itself and $p_{\mathrm{T}}^{\mathrm{varcone20}}$, defined as the sum of the p_{T} of the tracks in $\Delta R = \min\left(\frac{10\,\mathrm{GeV}}{p_{\mathrm{T}}^{\mathrm{track}}\,[\mathrm{GeV}]}, 0.2\right)$ around the candidate, excluding the ones associated to it.

Electrons used in the analysis described in chapter 5 are selected with the Tight cut of the likelihood discriminant and the Loose working point for the isolation, corresponding to the requirement of $E_{\mathrm{T}}^{\mathrm{cone20}}/p_{\mathrm{T}} < 0.2$ and $p_{\mathrm{T}}^{\mathrm{varcone20}}/p_{\mathrm{T}} < 0.15$.

Photons

Reconstructed photons are either superclusters without matching to an ID track, or superclusters which match two tracks, corresponding to the e^+e^- pair from a γ conversion. A set of identification criteria are applied to reconstructed photons, to select the prompt ones and reject fakes originating from hadronic jets.

The selection exploits variables related to the shower shape applying a cut-based selection, identifying three operating points, *Loose*, *Medium* and *Tight*. The corresponding efficiency is computed, respectively, by using an inclusive photon production dataset, $Z \to ll\gamma$ events and $Z \to ee$ events, the latter by applying a method which transforms the electron EM shower to resemble the one induced by a photon. Photons are not used by the LLP search described in this thesis and additional details on their reconstruction and selection can be found in [62].

2.3.4 Muons

Muons are reconstructed using mainly the information from the ATLAS Inner Detector and/or the Muon Spectrometer. As they are minimum-ionising particles the amount of energy lost in the Calorimeter System is negligible for most of the cases, but it can be used in correspondence with other matching signatures in the ID and the spectrometer.

The reconstruction of muon tracks in the ID proceeds as described in section 2.3.1, while the reconstruction in the MS starts from the identification of *muon segments*, straight lines identified in a single muon station with a Hough transform, on which details can be found in [64]. Muon segments from multiple stations are combined using a loose constraint based on the IP position and a parabolic trajectory, which is a first approximation of the muon path in the bending plane. The information in the non-bending plane is added and a χ^2 fit of the track is performed, taking into account the magnetic field and the energy lost in the detector material, as well of possible mis-alignment of the chambers. Once this preliminary muon track is obtained, the association of MS hits with the track is checked, removing outlier hits and including ones not used in the first place. Tracks are re-fitted, removing ambiguities between low-quality and high-quality tracks, keeping the ones which are identical in two stations, but share no hits in the third one, as they can originate from highly boosted muon pairs. *Stand-Alone MS tracks* built in this way are then back-extrapolated to the IP and their p_{T} is defined by expressing its value at the interaction point.

Five muon types are identified, depending on the information used during the reconstruction. If no ID track can be matched to a stand-alone MS track, a corresponding *MS Extrapolated* (ME) muon object is created, after taking into account the expected energy loss in the calorimeter. On the other hand, if ID tracks can be matched to MS ones, a combined fit can be performed, obtaining a *Combined* (CB) muon. *Inside-Out combined* (IO) muons are built starting from an ID track and searching for at least three loosely aligned hits in the MS, while *Segment-Tagged* (ST) muons are built from ID tracks which are matched to at least one MS muon segment.

Finally, *Calorimeter-Tagged* (CT) muons are identified from ID tracks matching an energy deposit in the calorimeter which is consistent with a minimum-ionising particle.

Multiple working points, defined by different sets of quality cuts applied to a muon object, allow to make a first selection on the reconstructed muons. These are the *Loose*, *Medium* and *Tight* working points, as well as the *High-*p_{T} and *Low-*p_{T} ones, which are discussed with great detail in [65]. The selection efficiency of the first three working points is shown in figure 2.17 for $J/\psi \to \mu\mu$ and $Z \to \mu\mu$ events.

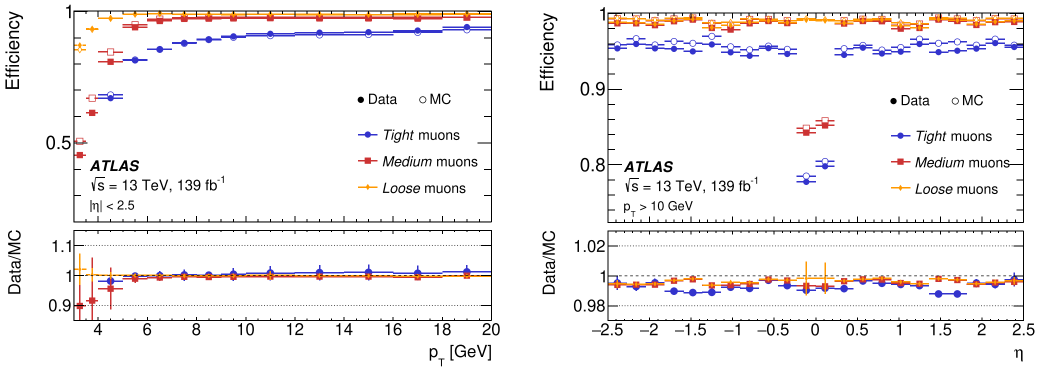

(a) **(b)**

Figure 2.17. Muon identification efficiency of the Loose, Medium and Tight working points. Figure (a) reports the efficiencies evaluated for $J/\psi \to \mu\mu$ data and MC events, as function of the muon p_{T}. Figure (b) reports the efficiency as function of the muon η for $Z \to \mu\mu$ data and MC events. Image taken from [65].

In the analysis described in chapter 5, the reconstruction of signatures of LLPs decaying into muons is performed with Stand-Alone MS tracks, as described in 3 while, in the identification of prompt muons, which is performed within $|\eta| < 2.5$, the requirements of the Medium working point are applied.

To satisfy the Medium working point the muon can only be either CB or IO, which have hits in at least two precision layers of the spectrometer (or at least one for $|\eta| < 0.1$). The compatibility between their charge-momentum ratio (q/p), expressing the agreement of q/p for the ID and MS, is defined as:

$$q/p \text{ compatibility} = \frac{|q/p_{\mathrm{ID}} - q/p_{\mathrm{MS}}|}{\sqrt{\sigma^2_{q/p,\mathrm{ID}} + \sigma^2_{q/p,\mathrm{MS}}}}$$

and is required to be smaller than 7 for Medium muons. The acceptance of this working point is extended up to $|\eta| < 2.7$ accepting also ME muons, requiring hits in three precision stations. In order to suppress fakes non-prompt muons, a set of isolation requirements is also applied, relying on similar variables as the ones used for electrons. Muons are selected by requiring the isolation in the calorimeter $E_{\mathrm{T}}^{\mathrm{cone20}}/p_{\mathrm{T}} < 0.3$ with the addition of the requirement on ID track isolation: $p_{\mathrm{T}}^{\mathrm{varcone30}}/p_{\mathrm{T}} < 0.15$ for muons with $p_{\mathrm{T}} < 50\,\mathrm{GeV}$ or $p_{\mathrm{T}}^{\mathrm{cone20}}/p_{\mathrm{T}} < 0.15$ for muons with $p_{\mathrm{T}} > 50\,\mathrm{GeV}$, where $p_{\mathrm{T}}^{\mathrm{cone20}}$ is defined as the sum of the momentum of the tracks found in a $\Delta R = 0.2$ cone around the muon ID track.

2.3.5 Missing transverse momentum

Missing transverse momentum is reconstructed as the negative vector sum of the transverse momentum of all reconstructed objects. The $E_{\mathrm{T}}^{\mathrm{miss}}$ is the key variable in all physics searches involving invisible particles in the final state and, in particular, events with large transverse momentum are signatures of bSM particles that can be produced at the LHC and escape the detector without interacting, as in the case of the analysis described in 6.

The reconstruction of the $E_{\mathrm{T}}^{\mathrm{miss}}$ is performed at the analysis stage, by manually including the reconstructed physics object (*hard term*), as well as additional signatures that are not associated to other objects (*soft term*). More precisely, the missing transverse momentum is defined as a 2D vector, with components in the (x, y) plane, to which a ϕ coordinate is associated, as defined by:

$$\vec{E_{\mathrm{T}}^{\mathrm{miss}}} = -\left(\sum_{\substack{\text{reco.} \\ \text{obj. k}}} + \sum_{\substack{\text{soft.} \\ \text{obj. n}}} \vec{p_{\mathrm{T}}}_n \right) .$$

A detailed description of the $E_{\mathrm{T}}^{\mathrm{miss}}$ definition and performance can be found in [66].

2.3.6 Overlap Removal

In order to avoid accidental double-counting of the reconstructed objects, a set of criteria of overlap removal is applied to electrons, muons and jets that are used in the search described in this thesis. The criteria are summarised in the following:

- If a electron-muon pair share the same ID track the muon is rejected, keeping the electron, if the muon is Calorimeter-Tagged. Otherwise the electron is discarded and the muon is kept.
- If a pair of electrons share the same ID track, the one with largest p_{T} is kept.
- Jets are discarded in favour of electrons if the latter are at $\Delta R < 0.2$, otherwise the electrons are discarded, keeping the jet, if the $\Delta R < 0.4$.
- Jets are kept, discarding muons, if their distance is $\Delta R < 0.4$. On the other hand, if the jet has less than three ghost associated tracks[3] and the muon is either ghost-associated to the jet or it is found at $\Delta R < 0.2$ from the jet axis, then the muon is kept and the jet discarded.

Only the objects that are not removed by the algorithm are considered.

---

[3] A track is considered ghost-associated if, after setting its pt to an infinitesimal value, it is still included in the jet by the clustering algorithm.

Chapter 3

Long-lived Dark Photon signatures at ATLAS

The ATLAS experiment was designed, built and calibrated targeting a specific set of signatures, which can be either prompt leptons, jets, photons or missing transverse momentum.

Aiming now at a search for displaced decays of light LLPs, the need of very specific triggers and dedicated object reconstruction appears. Leptons or jets originating from these decays usually show either unusual energy deposits, where a large fraction of the energy is left in the hadronic calorimeter, or highly-collimated MS tracks, in both cases without leaving any signature in the ID. These collimated jet-like structures are reconstructed as custom physics objects named displaced Dark-Photon Jets (DPJs).

This chapter will give an overview of the simulated Monte Carlo samples where Dark Photons are produced, as well as the details on how Dark-Photon Jets are triggered and reconstructed.

3.1 Signal Monte Carlo samples

The Monte Carlo samples used in the search for displaced dark photon decays, feature the production of either two or four γ_d in each event, either by the process described by the FRVZ model or the HAHM model, which were presented in section 1.3.2. In all cases the production of the dark photon is via the Higgs portal, while the decay of the γ_d in SM particles is assumed to happen only via the vector portal, with a branching ratio in charged leptons or quarks set as in figure 1.7.

The cross section for the Higgs boson production at $\sqrt{s} = 13\,\text{TeV}$ is used to estimate the expected number of events. The most recent values to date have been used, corresponding to the ones reported in table 1.1.

3.1.1 Simulated FRVZ events

For the FRVZ model, both the gluon-gluon fusion and associated production with a W boson are considered as production mechanisms of the Higgs boson. The associated production with a Z boson is not considered due to its smaller cross section. In this model, the dark photons originate from a process that involves additional dark sector particles (f_d, s_d or the HLSP), as already discussed in section 1.3.2.

The masses of the HLSP, of the hidden fermion f_d, or of the hidden scalar s_d are chosen well below the Higgs mass, and far from the kinematic threshold for the production of the γ_d, aiming at the production of two dark photons, or two pairs of dark photons, well separated in the transverse plane.

Multiple signal samples are produced, with dark photon masses (m_{γ_d}) ranging between $17\,\text{MeV}$ and $15\,\text{GeV}$ and with 2 or 4 γ_d in the final state. The mass range is chosen to extend the boundary of the previous ATLAS search [2], below the threshold for the production of two muons and above $2\,\text{GeV}$. For each mass point the corresponding proper decay lifetimes of the dark photon, $c\tau_d$, are optimised in order to maximise the number of decays happening between the end of the ECAL and the first muon station of the spectrometer.

An alternative set of signal samples is produced, considering only the ggF production mode, where the process is initiated by a bSM Higgs-like scalar, of which the mass is set to $800\,\text{GeV}$. These samples were produced in order to study the ideal scenario of highly boosted γ_d, for which a different choice of $c\tau_d$ was also made. In this case, the choice of the cross section times branching ratio for the production and decay of the $800\,\text{GeV}$ boson is arbitrary and, although the final results will be given in terms of this quantity, a reference value of $5\,\text{pb}$ will be adopted in some cases.

Table 3.1 reports the masses of the γ_d, f_d and HLSP, as well of the s_d (which is only considered in the $H \to 4\gamma_d + X$ process) and the values of $c\tau_d$ optimised for the case of the SM Higgs samples and the bSM scalar samples.

m_{γ_d} [GeV]	m_{f_d} [GeV]	m_{HLSP} [GeV]	m_{s_d} [GeV]	$c\tau_d$ [mm] (SM-Higgs samples)	$c\tau_d$ [mm] (bSM-scalar samples)
0.017	5	2	2	2	0.4
0.05	5	2	2	7	1
0.1	5	2	2	15	5
0.4	5	2	2	50	10
0.9	5	2	2	115	15
2	10	2	5	175	30
6	25	4	15	600	120
10	35	6	25	900	150
15	45	10	30	1000	235

Table 3.1. Parameters used for the Monte Carlo simulation of the production of two or four dark photons, with the process predicted by the FRVZ model.

All signal MC samples have been generated at the leading order, using MADGRAPH5_aMC@NLO 2.9.5 [67]. Parton showering and hadronisation have been simulated with PYTHIA 8.245 [68], with the NNPDF2.3LO[69] set of parton distribution functions, using the A14 [70] set of tuned parameters.

3.1.2 Simulated HAHM events

For the HAHM process, two γ_d are directly produced by the decay of the Higgs boson, as explained in section 1.3.2. In this case no intermediate particle is considered, obtaining two γ_d which have an average p_{T} which is approximately doubled with respect to the FRVZ model.

For this process, only the ggF production mechanism and the SM Higgs boson are considered. The proper lifetime $c\tau_d$ has been optimised, as done for the FRVZ samples, given the different average p_{T} of the dark photon. A list of the generated mass points and corresponding values of $c\tau_d$ is given in table 3.2.

m_{γ_d} [GeV]	$c\tau_d$ [mm]
0.017	1
0.1	8
0.4	25
2	80
10	450
15	500

Table 3.2. Mass and proper decay lifetime used for the Monte Carlo simulation of events with two dark photons, produced by the decay of a SM Higgs boson, as predicted by the HAHM model.

These signal MC samples have been generated at the leading order, using MADGRAPH5_aMC@NLO 2.9.5 [67], interfaced with PYTHIA 8.245 [68] for parton showering and hadronisation, using the NNPDF2.3LO[69] set of parton distribution functions and the A14 [70] set of tuned parameters.

3.1.3 Kinematics of truth-level Dark Photons

ggF production mode

In the previous two sections, two classes of samples have been introduced, in which dark photons are produced by the processes predicted in the FRVZ or HAHM model. To provide an overview on the main kinematic properties of the γ_d among these different production modes, a single mass point, with a $0.4\,\mathrm{GeV}$ dark photon, has been considered to produce the plots in figures 3.1 and 3.2, which are discussed in the following. Only the ggF production mode is considered for the moment.

In figure 3.1a, the p_{T} distribution of the γ_d is shown, where the primary difference between HAHM and FRVZ models appears: for the former, the p_{T} distribution has it maximum at $\sim 60\,\mathrm{GeV}$, i.e. half of the mass of the Higgs boson, while for the latter, the maximum of the p_{T} distribution is found at a smaller value. This is a direct consequence of the reduced number of particles in the HAHM model, but its main implication is that, at the analysis stage, any selection that will have a dependence on the p_{T} will be more efficient on this set of samples. A large fraction of the γ_d decays happen in the barrel region, as shown in figure 3.1b, while their decay length in the transverse plane (L_{xy}) show that a significant fraction of the decays happen outside the acceptance of the inner detector, i.e. at $L_{xy} > 1\,\mathrm{m}$, as visible in figure 3.2a.

The identification of Dark-Photon Jets is possible when the decay products of a γ_d are highly collimated, figure 3.2b show the ΔR between two γ_d decay products, which in most of the cases are contained in a $\Delta R = 0.4$ cone. Finally, figures 3.2c and 3.2d show the maximum and minimum azimuthal distance between the leading γ_d, i.e. the one with largest p_{T}, and the farthest, or closest, γ_d found in the event. From these last two figures it is clearly observed that in the samples for which 4 γ_d are produced, two pairs of collimated γ_d are produced with large separation in the transverse plane (*back-to-back*).

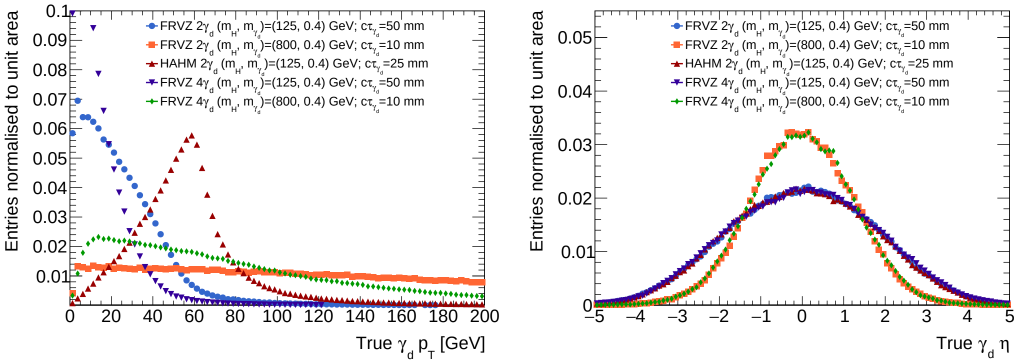

(a) **(b)**

Figure 3.1. Transverse momentum (left) and pseudorapidity (right) of the $0.4\,\mathrm{GeV}$ γ_d for the different set of samples generated with the ggF production mechanism.

In figures 3.3a and 3.3b the distributions of the dark photon p_{T} and the ΔR between two muons from a γ_d decay are shown, comparing different samples where dark photons with different masses are produced by the FRVZ process, with the SM Higgs and 2 γ_d in the final state. While the γ_d have a similar p_{T} distribution among different mass samples, figure 3.3b show that, if the identification of γ_d decays relies on a $\Delta R = 0.4$ cone, the efficiency of their reconstruction should drop for m_{γ_d} $2\,\mathrm{GeV}$.

WH production mode

For the samples in which the FRVZ process is initiated by a Higgs boson produced in association with a W boson, the kinematics of the dark photons slightly differs

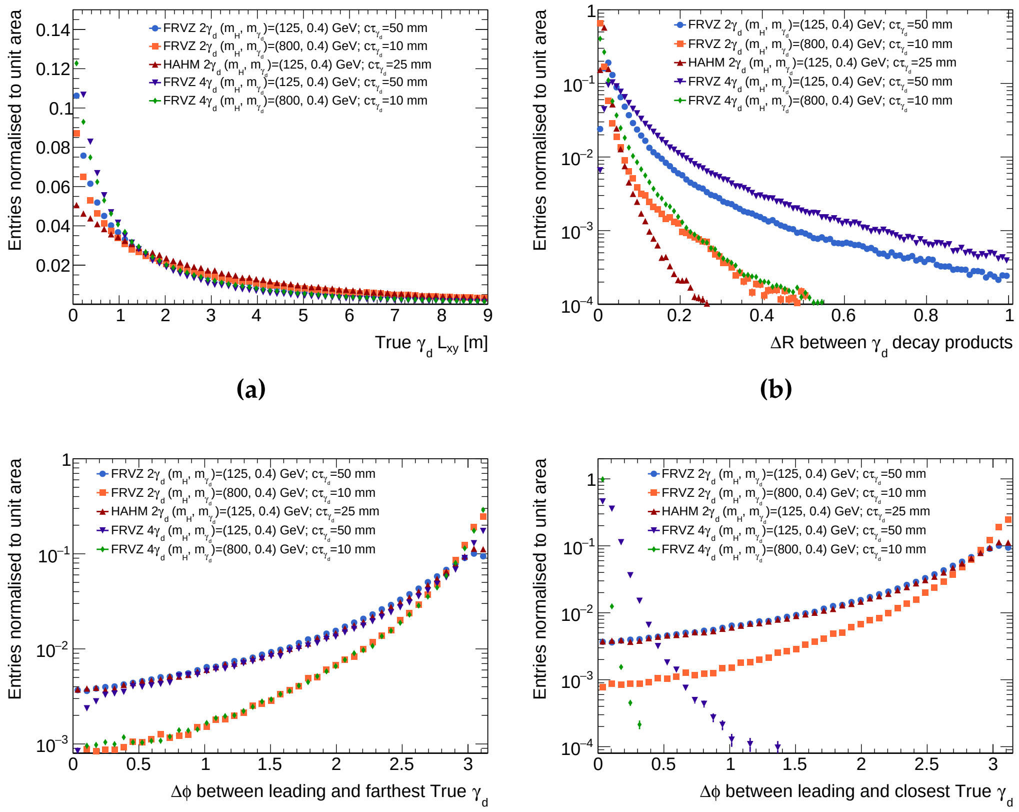

(a) **(b)**

(c) **(d)**

Figure 3.2. Kinematic properties of the 0.4 GeV dark photon mass point for the different set of samples generated: (a) decay length in the transverse plane (L_{xy}), (b) ΔR between two particles originating from a γ_d (top right), (c/d) maximum/minimum azimuthal distance between the γ_d of highest p_{T} and any other γ_d. Only the ggF production mode is considered in these plots.

from the ggF samples. The presence of a W boson recoiling to the Higgs boson implies larger p_{T} of the γ_d, as well as different angular distributions between the two dark photons.

The distributions of the transverse momentum of the γ_d, compared for $m_{\gamma_d} = 0.4$ GeV in ggF and WH samples is shown in figure 3.4a, while the same comparison is shown, in figure 3.4b for the ΔR opening between two particles originating from γ_d decays. Similar distributions of the two variables are found, hence no significant difference is expected in the efficiency of reconstructing dark photon decays.

A comparison between different masses of the dark photon, for the WH production mode of the Higgs boson, is shown in figure 3.5 for different kinematic variables. The dark photon p_{T} distribution, visible in 3.5a clearly show that most of the γ_d are generated with a transverse momentum of below 60 GeV, hence their different Lorentz boost imply that their decay products are less and less collimated the more the γ_d is heavy, as shown in figure 3.5b. Dark photons in samples with

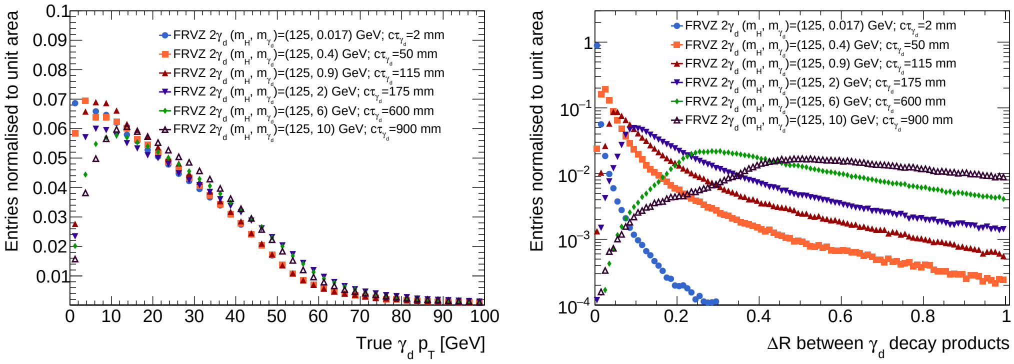

(a) **(b)**

Figure 3.3. Transverse momentum (left) and ΔR opening of two γ_d decay products (right) for different mass points of the FRVZ model, with the ggF production of the SM Higgs boson and 2 γ_d in the final state.

the WH production mode are not expected to be back-to-back between them, as shown in figure 3.5c, but a clear $\Delta\phi$ separation between a γ_d and the W boson can be observed, as visible in 3.5d.

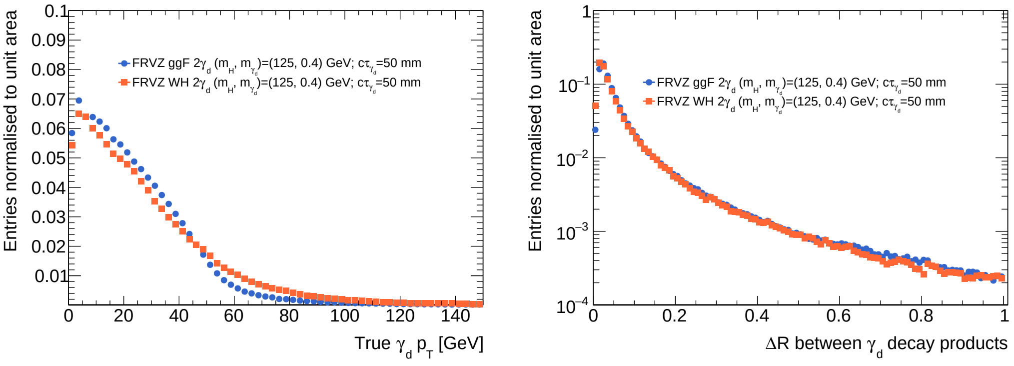

(a) **(b)**

Figure 3.4. Comparison between ggF and WH samples for $m_{\gamma_d} = 0.4\,\mathrm{GeV}$. The distribution of the dark photon p_T is shown in (a), while (b) shows the ΔR opening between two γ_d decay products.

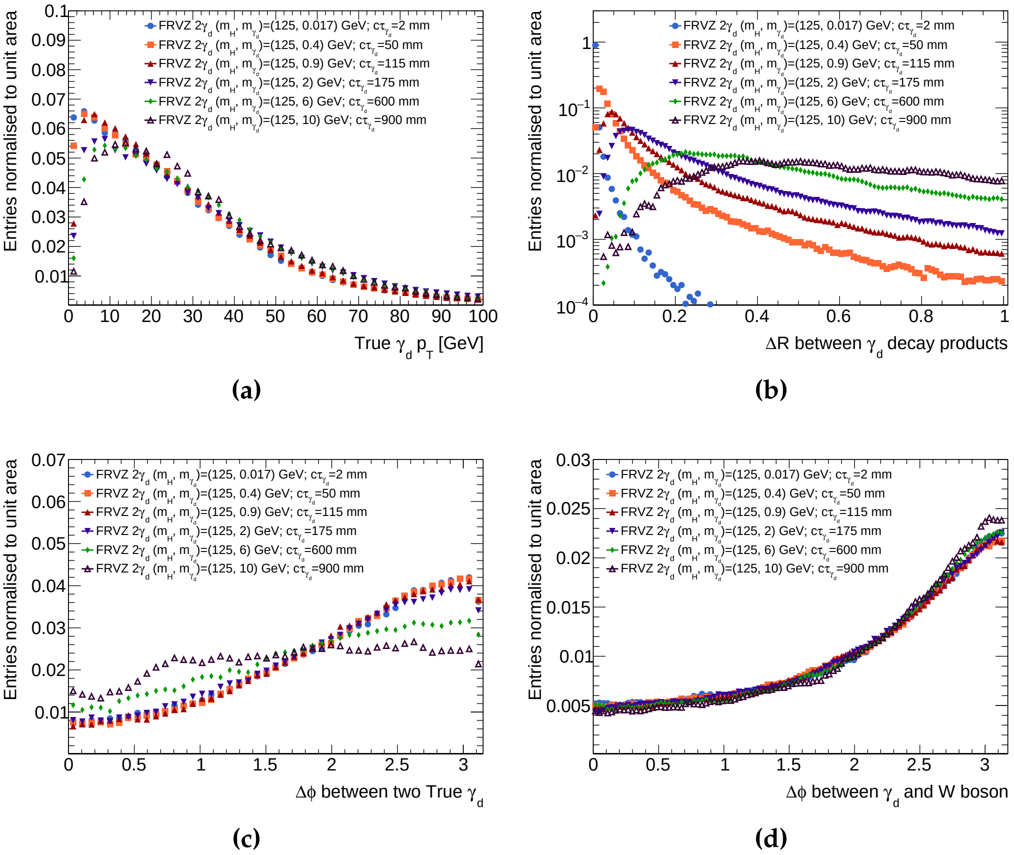

(a) **(b)**

(c) **(d)**

Figure 3.5. Kinematic comparison of samples with different m_{γ_d} with WH production mode. The γ_d transverse momentum is shown in (a), while the ΔR opening between γ_d decay products is shown in (b). The $\Delta\phi$ distributions between two dark photon, or a dark photon and the W boson, are visible in figures (c) and (d), respectively.

3.2 Triggers

A large fraction of the standard ATLAS triggers [71] are designed assuming prompt production and therefore are very inefficient in selecting the products of displaced decays. For this reason, when in the hard-scattering process there are no prompt leptons involved, as in the case of the gluon-gluon fusion production mode, it becomes necessary to trigger on the signature left by displaced γ_d decays. On the other hand, if a prompt muon or electron is present, like in the case of the WH production, it is possible to rely on a prompt lepton trigger to select the events.

The following sections will give an overview of the two triggers for displaced objects, that are used to select events in which the signature of a displaced dark photon is present. In both cases, the trigger algorithm is implemented at HLT and is seeded by the identification of a L1 trigger object. A brief description of all the other triggers, that have not been developed for the purpose of LLP identification, but that are still used in this study, is also presented. All the triggers that have been used were not prescaled during the relevant data-taking periods.

3.2.1 Narrow-Scan trigger

The Narrow-Scan trigger was introduced since the 2015 data-taking and adopts a specialised approach for a wide range of signal models featuring highly collimated muons. The Narrow-Scan algorithm begins with requiring a single L1 trigger muon object (*muon seed*). Other multi-muon triggers, which usually require more L1 muon objects, have large associated signal efficiency losses in the case where the muons are produced close together. These losses are mainly due to the limited granularity at L1, resulting in fewer reconstructed muon objects than the ones produced by one or more γ_d decays.

To compensate for the high rate from only one L1 muon object (which is matched at HLT), a *scan* is performed for another muon at HLT without requiring it to match a L1 muon object (*scan muon*). To limit the online resources consumption, while keeping a low-p_{T} threshold, the scan is limited to a narrow cone around the previously matched muon, where e.g. other constituents of a γ_d decay are expected to be found. In the trigger used in this thesis, none of the matched HLT muons is required explicitly to have a corresponding ID track.

The muon seed object is selected at L1 requiring a $p_{\mathrm{T}} > 20\,\mathrm{GeV}$, and the same threshold is applied to the HLT muon that is matched to it. The muon found in the scan procedure must lie in a cone of $\Delta R = 0.5$ around the seed and, in order to stay within the allocated trigger rate limits, it is selected with different requirements, applying increasing p_{T}-thresholds of 6, 10 and 15 GeV and vetoing the match with an ID track. Details on the evolution of these requirements, in 2015 and 2016, and the corresponding integrated luminosities are given in table 3.3.

The Narrow-Scan trigger is known to be costly and an alternative is needed for $L > 10^{34}\,\mathrm{cm}^{-2}\mathrm{s}^{-1}$. For the 2017-2018 data taking periods, three alternative narrow-scan triggers, which exploits the L1 Topological Processor, have been implemented.

Period	Integrated Luminosity	Scan muon requirements
2015 - all runs	3.2 fb^{-1}	6 GeV
2016 - first 99 runs	14.9 fb^{-1}	10 GeV and no matching ID track
2016 - last 88 runs	18.0 fb^{-1}	15 GeV and no matching ID track

Table 3.3. Narrow-Scan triggers in the 2015-2016 data taking periods, with corresponding selection on the scan muon and integrated luminosity.

For these years, at HLT, the seed muon is required to satisfy the *iloosems* isolation requirement, which imposes that the sum of the p_{T} of the tracks around the seed muon must be less than $3\,\mathrm{GeV}$. In addition, the HLT-requirement that the scan muon must not be matched by an ID track is relaxed.

The three different implementation of the Narrow-Scan trigger use three corresponding L1Topo seeds. The first two require, in addition to the $20\,\mathrm{GeV}$ seed muon, the presence of either a $40\,\mathrm{GeV}$ jet (Narrow-Scan + Jet) or a missing transverse momentum of $30\,\mathrm{GeV}$ (Narrow-Scan + $E_{\mathrm{T}}^{\mathrm{miss}}$), without applying any selection on these items at HLT, but only using this additional requirement to reduce the input rate of the Narrow-Scan algorithm. The third implementation requires a second muon at L1 with $p_{\mathrm{T}} > 6\,\mathrm{GeV}$, which must be found at a distance $\Delta R > 1$ from leading one and, as before, without applying any requirement on this additional object at HLT (Narrow-Scan + muon).

These triggers were not prescaled during the 2017-2018 LHC runs, the Narrow-Scan + Jet and Narrow-Scan + $E_{\mathrm{T}}^{\mathrm{miss}}$ were active during the full data taking period, while the Narrow-Scan + muon was not active for the first 73 runs of 2017. Details on the integrated luminosity, corresponding to the periods in which each trigger was active, as well as a summary of the L1Topo selection are given in table 3.4.

Trigger name	Integrated Luminosity [fb^{-1}]	additional L1Topo item
Narrow-Scan + Jet	102.9	jet with $E_{\mathrm{T}} > 40\,\mathrm{GeV}$
Narrow-Scan + $E_{\mathrm{T}}^{\mathrm{miss}}$	102.9	$E_{\mathrm{T}}^{\mathrm{miss}} > 30\,\mathrm{GeV}$
Narrow-Scan + Muon	97.2	$p_{\mathrm{T}} > 6\,\mathrm{GeV}$ muon at $\Delta R > 1$

Table 3.4. Details on the three implementations of the Narrow-Scan trigger in 2017-2018.

ATLAS triggers are usually developed for paired bunch crossings, but they are still kept active in empty or unpaired-isolated ones, which may result useful for background studies. Due to the limited detector activity in such events, some of the thresholds are lowered, as there is no strict requirement on the trigger rate. The Narrow-Scan trigger was active in empty bunch crossings for the full Run-II, and it was configured be seeded by a L1 muon with a $p_{\mathrm{T}} > 4\,\mathrm{GeV}$.

Narrow-Scan trigger efficiencies

The Narrow-Scan trigger efficiency has been computed as a function of the decay length in the transverse plane (L_{xy}) and the p_{T} of a dark photon, as shown in figures 3.6. This has been done for 2015 Narrow-Scan, which has the least stringent constraints on L1 objects, in order to better highlight the efficiency of the HLT algorithm.

To evaluate these efficiencies, a selection on the truth-level γ_d has been made requiring only γ_d decaying in two muons, for which one of the two satisfies $p_{\mathrm{T}} > 20\,\mathrm{GeV}$ and the other $p_{\mathrm{T}} > 6\,\mathrm{GeV}$. If more than one γ_d with these properties is present, only the leading one is considered, assuming that the Narrow-Scan trigger fires, the triggering γ_d is the leading one. As the Narrow-Scan trigger requires two collimated muons, it is expected that its trigger efficiency drops as the transverse decay length approaches the coordinate of the first layer of RPC detectors.

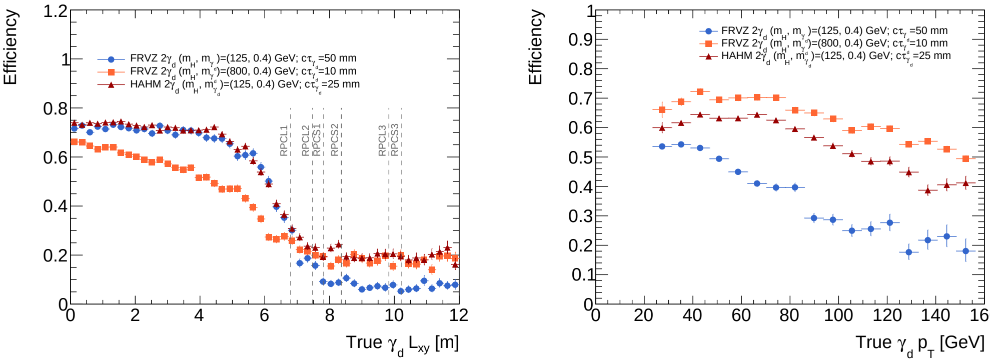

(a) **(b)**

Figure 3.6. The 2015 Narrow-Scan trigger efficiency for events with displaced decays of γ_d in a muon pair, for samples with $m_{\gamma_d} = 0.4\,\mathrm{GeV}$, generated with the ggF production mechanism. Figure a(b) shows the trigger efficiency for γ_d with $|\eta| < 1.1$ as a function of its L_{xy} (p_{T}). The vertical dashed lines show the position of the small and large RPC sectors, numbered from the inside to the outside.

Considering dark photons of similar p_{T} distributions, the minimum opening angle between its decay products increases with its mass, implying that the efficiency of this trigger will decrease. This is shown in figure 3.7, where multiple mass points of the FRVZ model, with 2 γ_d per event and the SM Higgs ggF production, are used to produce the efficiency of the Narrow-Scan as a function of the L_{xy}. On the other hand, this trigger efficiency can be lower for dark photons with very high p_{T}, where the two muons can not be resolved from the muon spectrometer. This effect can be observed in figure 3.6a for the case of γ_d originated from a $800\,\mathrm{GeV}$ scalar.

To give a more complete overview of the efficiency of the Narrow-Scan triggers along the different runs of data-taking, table 3.5 reports the efficiencies of the 2015 implementation of the trigger, compared to the logical or of the 2016 ones as well to the logical or of the Narrow-Scan implementations used in 2017 and 2018. The efficiency ranges are reported considering all the ggF signal MC samples of different

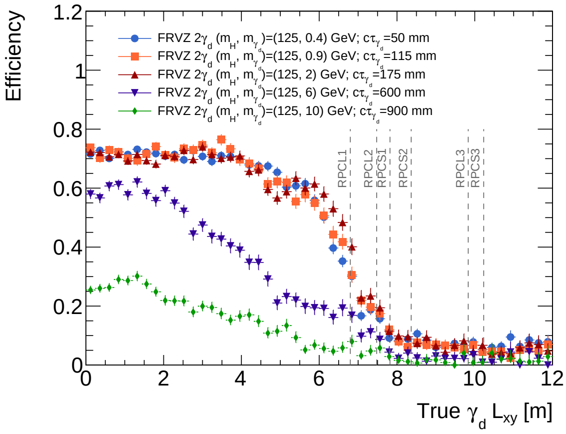

Figure 3.7. The 2015 Narrow-Scan trigger efficiency, as a function of the decay length in the transverse plane, for events with displaced decays of γ_d in a muon pair, for different m_{γ_d}, generated with the ggF production mechanism and the FRVZ model. The vertical dashed lines show the position of the small and large RPC sectors, numbered from the inside to the outside.

categories, where muonic decays of the dark photon are allowed. In all the cases the trigger efficiency is observed to decrease as the dark photon mass increases. No truth-level selection was applied in evaluating these efficiencies.

Process	Number of	m_H	Narrow-Scan trigger efficiency (%)		
	γ_d	[GeV]	2015	2016	2017-18
FRVZ	2	125	1.94 – 14.8	0.125 – 0.655	1.60 – 6.02
	4	125	2.34 – 14.5	0.185 – 1.72	1.94 – 6.13
	2	800	18.5 – 33.7	0.775 – 1.33	12.9 – 20.6
	4	800	32.7 – 59.8	2.56 – 6.84	23.4 – 37.5
HAHM	2	125	7.02 – 33.1	0.296 – 1.03	5.01 – 16.3

Table 3.5. Efficiency ranges of the different implementations of the Narrow-Scan trigger used during the Run-II. Presented ranges are referred to the 2015 implementation of the trigger and to the logical OR of the 2016 and 2017-18 versions, considering multiple MC mass samples for which dark photon decays into muons are allowed. Larger efficiencies are always observed in correspondence of smaller dark photon masses and, in general, an overall increase in efficiency is found for larger p_{T} of the γ_d and for higher γ_d multiplicity.

3.2.2 The CalRatio trigger

The CalRatio trigger [72] is designed to identify jets originating from LLP decays, which are expected to have a very low f_{EM} and leave no track in the ID. Two types of CalRatio triggers have been used in different data-taking periods, differing only on the selection applied at L1.

As LLPs with large p_{T} yield very collimated decay products, the most suitable L1 item for their identification is the L1 Tau trigger, which sums energy in a smaller ($\eta \times \phi = 0.4 \times 0.4$) region than the L1 Jet (0.8×0.8). In 2015-2016 runs, a L1 Tau trigger with an $E_{\mathrm{T}} > 60\,\mathrm{GeV}$ threshold was adopted, while a trigger from the L1 Topological processor, *LLP-NoMatch*, was used in 2017 and 2018. The L1 LLP-NoMatch trigger extends the identification of low-f_{EM} jets by requiring a L1 Tau trigger with $E_{\mathrm{T}} > 30\,\mathrm{GeV}$ and by vetoing the presence of any energy deposit with $E_{\mathrm{T}} > 3\,\mathrm{GeV}$ in the ECAL, within a cone $\Delta R = 0.2$ around the L1 Tau object.

The CalRatio algorithm at HLT requires the jet to have $|\eta| \leq 2.4$ (to ensure that ID tracks can be matched to it) and $E_{\mathrm{T}} > 30\,\mathrm{GeV}$. A selection requirement on the calorimeter energy ratio is then imposed, requiring $\log_{10}(E_{\mathrm{HCAL}}/E_{\mathrm{ECAL}}) \geq 1.2$ ($f_{\mathrm{EM}} \leq 0.06$) and, finally, an ID track veto is applied, rejecting jets which have at least a track with $p_{\mathrm{T}} > 2\,\mathrm{GeV}$ within $\Delta R = 0.2$ from the jet axis.

This version of the CalRatio HLT algorithm is easily satisfied by jets originated by Beam-Induced-Background (BIB) muons, which cross the detector in a parallel direction to the beam pipe. A BIB muon crossing the detector at a radius corresponding to the hadronic calorimeter, will likely induce energy deposits with the same ϕ coordinate and $f_{\mathrm{EM}} \sim 0$, leaving no track in the ID and a very specific cell timing pattern related to its radial and longitudinal coordinates. A more detailed explanation of these signatures will be given in section 4.2. To reduce the fake rate due to this background, a BIB-removal step has been included in the definition of the CalRatio HLT algorithm. This BIB removal algorithm rejects jets which have at least four calorimeter cells with $\Delta\phi < 0.2$ from the jet axis and a timing, t_{cell}, which is within $\pm 5\,\mathrm{ns}$ from the expected timing of a deposit left by a BIB.

An inclusive version of the CalRatio trigger, identical to the nominal one except that it does not include the BIB removal algorithm, can be used in combination with a veto on the nominal CalRatio trigger, to produce a BIB-enriched dataset in collision events (BIB dataset), which will be used for the studies presented in section 4.2.

Table 3.6 summarises the two versions of the CalRatio trigger, showing the integrated luminosity corresponding to the L1 item used.

Trigger name	Integrated Luminosity [fb^{-1}]	L1 item	BIB removal algorithm
CalRatio (*nominal*)	36.2	Tau ($E_{\mathrm{T}} > 60\,\mathrm{GeV}$)	✓
	102.9	LLP-NoMatch	✓
CalRatio (*inclusive*)	36.2	Tau ($E_{\mathrm{T}} > 60\,\mathrm{GeV}$)	×
	102.9	LLP-NoMatch	×

Table 3.6. Details on the different implementations of the CalRatio trigger in Run-II.

The CalRatio trigger was also active in empty and unpaired isolated bunch crossings, using only the L1 Tau seed with an E_{T} threshold of $30\,\mathrm{GeV}$.

CalRatio trigger efficiencies

To evaluate the CalRatio trigger efficiency, in a similar way to what has done for Narrow-Scan trigger, a pre-selection on γ_d has been applied at the truth level. Here, to focus on the sole efficiency of the HLT algorithm, the CalRatio trigger seeded from the L1 LLP-NoMatch trigger is shown, as it has a looser requirement at L1, with respect to the L1 Tau trigger with threshold at 60 GeV.

CalRatio trigger efficiencies are shown as functions of the L_{xy} and the p_{T} of the dark photon, in figures 3.8a and 3.8b, respectively. These efficiencies are obtained requiring, at the truth level, that the leading γ_d of an event decays with $|\eta| \leq 1.1$, in a pair of electrons or quarks and with $L_{xy} < 3.7\,\mathrm{m}$. As expected, the trigger is efficient only in the proximity of the HCAL, as it requires $f_{\mathrm{EM}} < 0.06$ to select the event and it is more efficient the more the p_{T} of the γ_d is large.

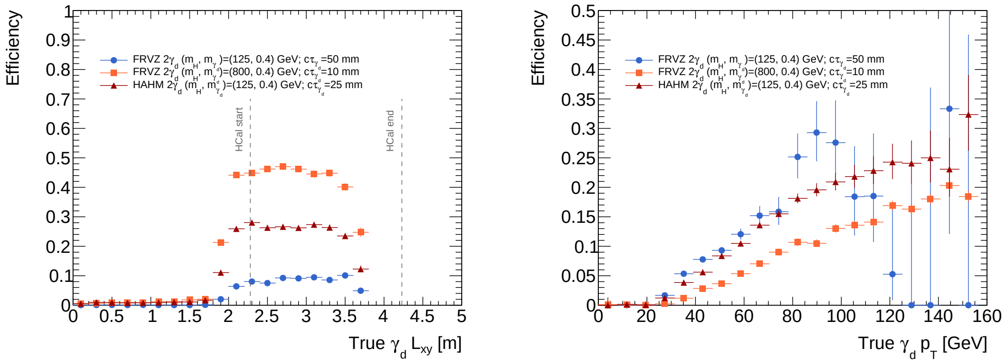

(a) **(b)**

Figure 3.8. The CalRatio trigger efficiency for events with displaced decays of γ_d in a quark or electron pair, considering only the trigger seeded by the L1 LLP-NoMatch. Different samples are shown, where 2 γ_d of $m_{\gamma_d} = 0.4\,\mathrm{GeV}$ are produced in the final state. Figure a (b) shows the trigger efficiency as a function of its L_{xy} (p_{T}). The vertical dashed lines mark the position of the beginning and the end of the barrel Tile Calorimeter.

The CalRatio trigger efficiency is shown for different values of the dark photon mass in figure 3.9, where only the FRVZ with SM Higgs samples and 2 γ_d in the final state are considered.

Table 3.7 reports the efficiency ranges for the two versions of the nominal CalRatio triggers used in 2015-16 and 2017-18, evaluated among different γ_d mass points. Larger values of the efficiency are found in correspondence of smaller branching ratios of the γ_d into muon pairs while, among different signal MC categories, higher efficiency values are found in correspondence of higher average p_{T} of the dark photons. In this case, no truth-level selection on the γ_d was applied.

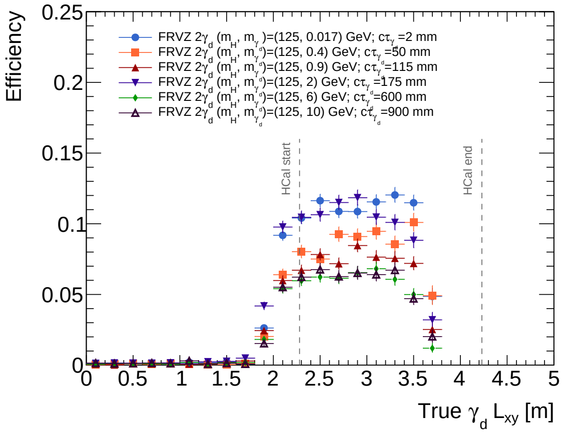

Figure 3.9. Efficiency, as a function of the dark photon L_{xy}, of the L1 LLP-NoMatch CalRatio trigger for events with displaced decays of γ_d in a quark or electron pair. Different samples are shown, where 2 γ_d of multiple mass points are produced in the final state, considering only the FRVZ model and the SM Higgs boson. The vertical dashed lines mark the position of the beginning and the end of the barrel Tile Calorimeter.

Process	Number of γ_d	m_H [GeV]	CalRatio trigger efficiency (%) 2015-16	2017-18
FRVZ	2	125	0.285 – 0.602	1.02 – 2.10
	4	125	0.106 – 0.291	0.258 – 0.950
	2	800	8.65 – 15.9	6.90 – 11.6
	4	800	5.84 – 9.05	3.48 – 6.85
HAHM	2	125	2.41 – 5.66	4.14 – 6.98

Table 3.7. Efficiency ranges of the 2015-16 (L1 Tau $E_{\mathrm{T}} > 60\,\mathrm{GeV}$) and 2017-18 (L1 LLP-Nomatch) implementations of the CalRatio trigger. Quoted ranges are evaluated among all the γ_d mass points available for a given process. Larger efficiencies are observed in correspondence of higher p_{T} of the dark photon or smaller branching ratio of the γ_d into muon pairs.

3.2.3 Other triggers

This section gives a description of the triggers which were developed for other purposes than the LLP identification, but are still efficient and available for this study. The evolution of the triggers for single or multiple muons are described in [40], while the single electron triggers are presented in [73].

Tri-muon MS-only

The Tri-muon MS-only trigger is a multi-muon trigger that selects events in which at least three L1 muon items are found, with a p_{T} threshold of 6 GeV. At the HLT, this trigger requires the confirmation of the three L1 muons, without explicitly asking for a matching with an ID track.

Although this trigger was not developed for LLP searches, it is expected to be effective in selecting events when multiple dark photons decay into a pair of muons. If all the γ_d decay into muon pairs before the end of the HCAL and if the angular separation between two muons is sufficient, or at least one dark photon decays close to the boundary between two different RoI, the L1 requirements can be satisfied and events with two or more dark photons can be selected.

This trigger was running without prescale for the full Run-II and it has been used in combination with the Narrow-Scan and the CalRatio triggers to identify events in which the Higgs boson is produced via the ggF mechanism. The same trigger with same thresholds was also active in empty bunch crossings.

Table 3.8 shows the Tri-muon trigger efficiency ranges, among different γ_d mass samples of different categories. The efficiencies are evaluated on all the MC samples where the decay $\gamma_d \to \mu\mu$ is kinematically allowed and without applying any truth-level selection. Larger efficiencies are found in correspondence of larger γ_d masses, i.e. in the cases of greater angular separation between the two decay products. Moreover, larger efficiencies are, in general, observed in the case of larger p_{T} and multiplicity of the dark photons.

Process	Number of γ_d	m_H [GeV]	Tri-muon MS-only trigger efficiency (%)
FRVZ	2	125	$1.60 - 2.55$
	4	125	$3.13 - 7.29$
	2	800	$3.59 - 6.56$
	4	800	$8.40 - 16.9$
HAHM	2	125	$3.61 - 4.70$

Table 3.8. Tri-muon MS-only trigger efficiency ranges among different γ_d mass scenarios. Among different signal categories, larger efficiencies are observed in the case of larger transverse momentum and multiplicity of the γ_d, as well of wider angular separation of the decay products.

Single lepton triggers

For the case in which the Higgs boson is produced in association with a W vector boson, a selection on the prompt lepton originating from the decay of the W can be used to trigger the event.

Single electron and single muon triggers are designed to select isolated prompt leptons and are available with different p_{T} thresholds and with different working points of the lepton isolation. The requirements for the lepton isolation at the HLT are based on the same criteria used during the object reconstruction, described in section 2.3.

In this thesis only the single lepton triggers, with lowest p_{T} thresholds and without prescale have been used. The detailed list of the trigger chains that have been used, with the corresponding period and integrated luminosity, is given in table 3.9. The threshold on the transverse momentum of the lepton was increased in 2016 due to the increased instantaneous luminosity: the electron (muon) p_{T} threshold was increased from 24 (20) to $26\,\mathrm{GeV}$.

Period	Lepton	HLT chain	Integrated Luminosity [fb^{-1}]
2015	e	HLT_e24_lhmedium_L1EM20VH	3.2
	μ	HLT_mu20_iloose_L1MU15	
2016-2018	e	HLT_e26_lhtight_nod0_ivarloose	135.7
	μ	HLT_mu26_ivarmedium	

Table 3.9. Lowest Single Lepton triggers without prescale factor available in the Run-II data taking periods. Details on each lepton trigger are given in [40] for muons and [73] for electrons.

3.3 Dark-Photon Jets

In this section the description of the custom physics object, which aim to select displaced dark photon decays is given. Dark-Photon Jets aim to identify displaced decays of long-lived particles in collimated muons, electrons or quarks. For such reason, two definitions of DPJs are given, based on two different detector signatures: two or more collimated stand-alone MS tracks, or a jet with low electromagnetic energy fraction.

With reference to the HAHM or the FRVZ model, a collection of muons and no jets in a narrow cone is a signature of one or more dark photons decaying to muons, while a low-f_{EM} jet is a signature for one or more γ_d decaying in electron or quarks outside the diameter of the ECAL. Starting from this first distinction, the classification of DPJs is defined according to the number of muons and jets found within a $\Delta R = 0.4$ opening cone, defining two exclusive categories, which are represented graphically in figure 3.10.

- If at least two muons and no jets are found in the cone, the DPJ is classified as a *muonic* DPJ (μDPJ);

- If a jet with $f_{\mathrm{EM}} < 0.4$ and no muons are found in the cone, the DPJ is classified as *calorimeter* DPJ (cDPJ).

In the FRVZ process with 2 dark photons in the final state, a pair of back-to-back DPJs is expected, while for the process with 4 γ_d, two back-to-back pairs of collimated γ_d may originate DPJs with more than 2 muons. A more detailed overview on the properties and the reconstruction of DPJs is given in the following sections.

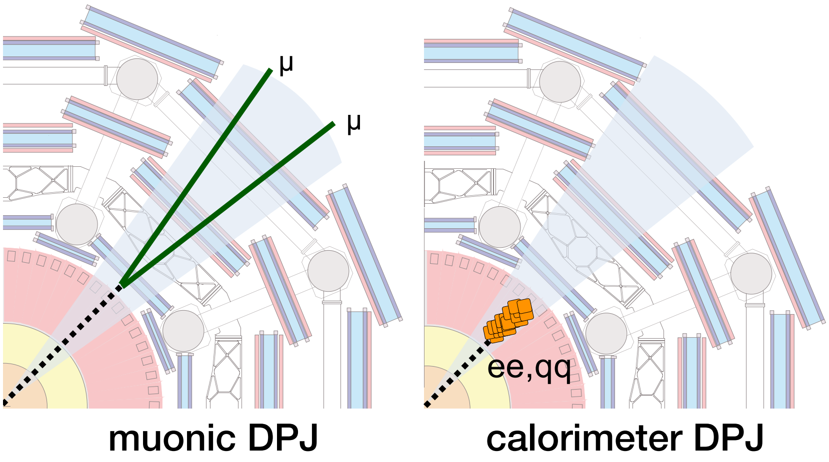

Figure 3.10. The two types of reconstructed DPJs: μDPJ (left) and cDPJ (right). Muonic DPJs are built from at least two collimated stand-alone MS tracks which do not match any jet. Calorimeter DPJs are built from jets with $f_{\mathrm{EM}} < 0.4$ which do not match any stand-alone MS tracks. Additional details on DPJ reconstruction are given in sections 3.3.1 and 3.3.2.

3.3.1 Muonic DPJs reconstruction

As muonic DPJs aim to identify dark photons decaying in a pair of muons outside the radial acceptance of the ID, a special selection on the information obtained from the Muon Spectrometer is needed. Stand-Alone MS tracks are built as described in section 2.3.4 and are used in combination with ID or Calorimeter information to build the different muon objects defined in ATLAS. To extend the radial acceptance of the analysis, stand-alone tracks are used only if they satisfy the following requirements:

- In order to discard muons originating in the IP, the track must not have been used to build a combined muon;
- The track must lie within the η-acceptance of the ID, in order to veto the presence of a combined muon, hence it must satisfy $|\eta| \leq 2.5$.
- The η coordinate of the track must not be in the $1.0 \leq |\eta| \leq 1.1$ range, to avoid the transition region between the barrel and the endcaps of the MS, which is a potential source of fake tracks;

Finally, a selection is made on the hits which have been used to build the track, with different requirements for tracks reconstructed in the barrel and in the endcaps:

- Barrel: the track must have hits in at least two MDT stations (≥ 3 hits in each MDT station, a total number of hits ≥ 10) and at least one RPC ϕ-hit;
- Endcap: the track must have ≥ 1 hit in the TGC stations and satisfy at least one of the following:
  - ≥ 10 hits in the MDT stations

- ≥ 3 hits in the CSC chambers and ≥ 3 hits in the EM/EO MDT stations.

Stand-Alone MS track satisfying this selection are combined using a Cambridge-Aachen clustering algorithm, described in [74], which combines the MS tracks lying within a cone of fixed size in the (η,ϕ) space. The algorithm starts from the track with highest p_{T}, searching for additional stand-alone MS tracks within the $\Delta R = 0.4$ cone around the initial track momentum vector. If a second stand-alone MS track is found in the cone, the axis of the cone is rotated to the vector sum of the momenta of the two tracks, and the search is repeated until no additional tracks are found. Muonic DPJs reconstructed in this way are discarded if a jet is found within $\Delta R = 0.4$ from it, to ensure the orthogonality between reconstructed DPJ types. Inner detector tracks are not explicitly vetoed, but it is important to notice that Stand-Alone MS-tracks are built using only the information of the Muon System. Nevertheless, a variable that takes into account the presence of ID tracks in the inner detector will be used in the definition of the analysis signal regions, as described in 5.1.1.

The μDPJ reconstruction efficiency is defined as the ratio of the number of γ_d decaying in $\mu^+\mu^-$, which are found in a $\Delta R = 0.4$ cone around a μDPJ, and the total number of γ_d decaying in two muons. This quantity is shown, for dark photons with $|\eta| < 1.1$ and for different L_{xy} and p_{T} bins, in figure 3.11, for the ggF samples with 2 γ_d in the final state and $m_{\gamma_d} = 0.4\,\mathrm{GeV}$, considering the HAHM model and the FRVZ model with both SM and bSM Higgs. The same efficiency, as a function of L_{xy}, is shown in figure 3.12 for the FRVZ model comparing different γ_d mass points. As expected, considering also the plot in figure 3.3b, the efficiency drops significantly above 2 GeV and outside the first layer of RPC detectors.

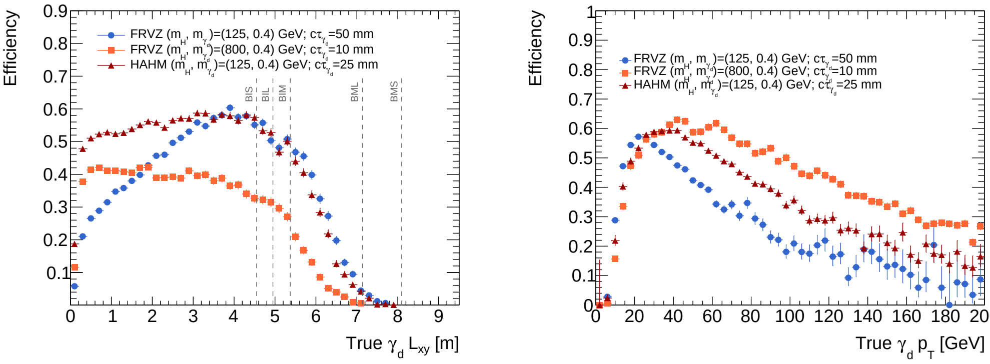

(a) **(b)**

Figure 3.11. The reconstruction efficiency for μDPJ produced by the decay of γ_d with $|\eta| < 1.1$ in muon pairs. (a) show the efficiency as a function of the transverse decay distance L_{xy}. (b) show the reconstruction efficiency as a function of the dark photon p_{T}. The vertical dashed lines show the position of the small and large RPC sectors, numbered from the inside to the outside.

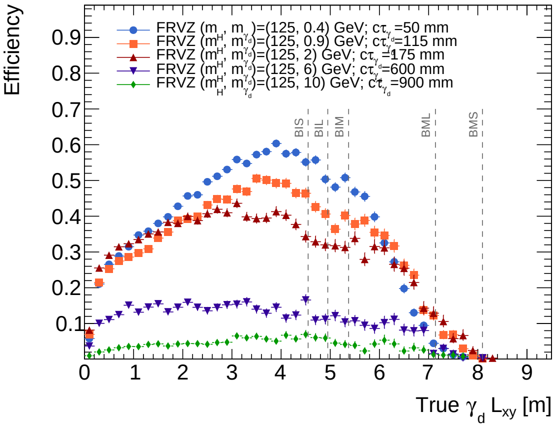

Figure 3.12. The reconstruction efficiency for μDPJs produced by the decay of γ_d with $|\eta| < 1.1$ in muon pairs, shown as a function of the γ_d L_{xy} for different mass points produced with the FRVZ model with $m_H = 125\,\text{GeV}$.

3.3.2 Calorimeter DPJ reconstruction

Calorimeter DPJ aim to identify the signature left by the decay of a LLP outside the radial acceptance of the ECAL. Highly collimated electrons or hadrons, produced by a dark photon decaying outside the ECAL volume, are usually reconstructed as a single jet with low EM fraction which have no associated ID track.

Calorimeter DPJ are EMTopo jets satisfying the following set of requirements:

- The jet must have a $p_{\text{T}} > 20\,\text{GeV}$, $f_{\text{EM}} < 0.4$ and it must lie in the pseudorapidity acceptance of the Inner Detector, i.e. it must satisfy $|\eta| < 2.5$;
- No Stand-Alone MS track must be present in a $\Delta R = 0.4$ cone centered in the jet axis;
- The Loose-LLP cleaning criteria, described in section 2.3.2, must be fulfilled by the jet.
- The energy left by the jet in the Tile Gap scintillators must be less than 10% of the total jet energy, as many fake jets with low f_{EM} are identified in this region due to the partial coverage of the calorimeter.

As for μDPJs, ID tracks are not explicitly vetoed. Although a variable that takes into account the cDPJ isolation in the ID will be used in the definition of the analysis signal regions, as it will be described in 5.1.1.

The cDPJ reconstruction efficiency is defined as the ratio of the number of γ_d decaying in e^+e^-, $q\bar{q}$ or $\tau^+\tau^-$, which are found in a $\Delta R = 0.4$ cone around a cDPJ, and the total number of γ_d decaying in two electron/quark/tau pairs. As done for the μDPJ, this quantity is shown in figure 3.13 for γ_d decaying in the barrel (i.e. with $|\eta| < 1.1$), as a function of the L_{xy} and p_{T} of the dark photon, for the ggF samples with 2 γ_d in the final state and $m_{\gamma_d} = 0.4\,\text{GeV}$, considering the HAHM model and the

FRVZ model with both SM and bSM Higgs. For the efficiency shown as a function of p_{T}, an additional requirement is applied on the dark photon, requiring its L_{xy} to be between $2\,\mathrm{m}$ and $4\,\mathrm{m}$. A comparison of the cDPJ reconstruction efficiencies, given as functions of the dark photon L_{xy}, is shown in figure 3.14 for different γ_d mass samples of the FRVZ model.

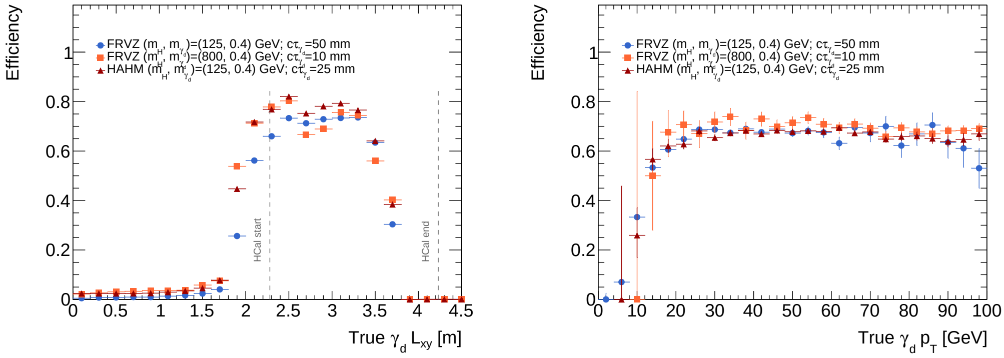

(a) **(b)**

Figure 3.13. The reconstruction efficiency for cDPJ produced by the decay of γ_d with $|\eta| < 1.1$ in electron/quark/tau pairs. (a) show the efficiency as a function of the L_{xy}. (b) show the reconstruction efficiency as a function of the dark photon p_{T} with the additional requirement that the γ_d decays happen with $2\,\mathrm{m} < L_{\mathrm{xy}} < 4\,\mathrm{m}$. The vertical dashed lines are delimiting the acceptance of the Tile Calorimeter.

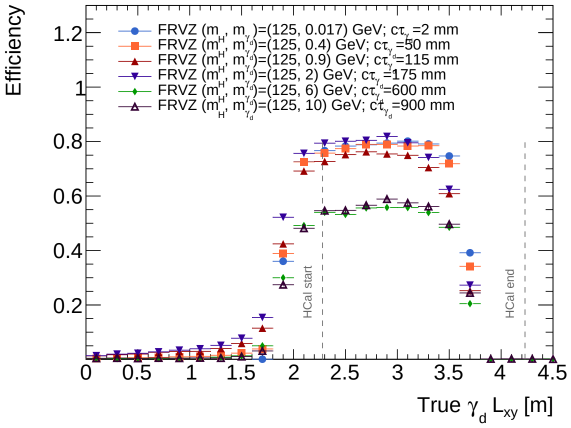

Figure 3.14. The reconstruction efficiency for cDPJs produced by the decay of γ_d with $|\eta| < 1.1$ in electron/quark/tau pairs pairs, shown as a function of the γ_d L_{xy} for different mass points produced with the FRVZ model, considering the ggF production and $m_H = 125\,\mathrm{GeV}$. On average, larger mass points correspond to a reduced p_{T} of the dark photon, hence to a reduced reconstruction efficiency.

Chapter 4

Challenging backgrounds for long-lived particles

Given the exotic nature of a search for LLP decays, the reconstruction of dedicated objects like the displaced Dark-Photon Jets can already remove a large fraction of the events collected during the LHC runs. On the other hand, there are physics signatures in ATLAS which can be easily identified as DPJs; their origin either comes from rare multijet events or non-collision background.

Such backgrounds are *uncommon*, because in many physics analyses they are easily suppressed with tight object quality criteria, as the signatures they produce strongly differ from more *common* signatures like prompt jets, leptons or missing transverse momentum. Unfortunately, the same set of criteria can reduce significantly the reconstruction efficiency of LLP signatures that, as in the case of DPJs, usually rely on looser constraints on reconstructed objects. This, in addition to the fact that the Monte Carlo simulation of such events is often unreliable or not available at all, motivates the use of sophisticated object taggers, which optimisation is based on data, to reduce as much as possible the contribution from these backgrounds.

This chapter will give an overview of how the aforementioned backgrounds contribute to the search for displaced Dark-Photon Jets, as well as introducing the dedicated object taggers that have been developed within the context of this thesis.

4.1 Rare jets

It is possible that either muonic or calorimeter DPJs gets reconstructed in events in which rare jets are present. In particular, jets with large momentum are such that their hadronic shower can not be entirely contained within the calorimeter (*punch-through jets*), can lead to many collimated tracks in the MS chambers, leaving a signature which can be reconstructed as muonic DPJs. On the other hand, jets with a large neutral component, which have many mis-reconstructed ID tracks, can be a significant source of calorimeter DPJs.

The definitions of μDPJ and cDPJ include a selection to reduce the fake rate from rare jets: the μDPJ reconstruction algorithm explicitly vetoes the presence of jets in a $\Delta R = 0.4$ cone around the DPJ, while for cDPJ, the cut applied on the jet f_{EM} help in mitigating the presence of fakes. Nevertheless, the total production cross section of multijet events is several orders of magnitude larger than the one assumed for the production of dark photons. Hence, very rare events in which jets are badly reconstructed and become a source of DPJs, will give in any case a significant contribution to a search which exploits this signature. On the other hand, the presence of rare jets, in associated production with the W and Z vector boson (*V+jet* events), becomes an important background when searching for γ_d produced by the decay of a Higgs boson, for which the associated production was considered.

Simulated background events are usually designed to reproduce the signature from correctly reconstructed prompt jet. For rare events, like punch-through or low-f_{EM} jets, this problem of inaccurate modelling of the events combines with the fact that the MC samples have a limited statistic. For these two reasons, the MC simulation of this background is unreliable for the estimation of this background in the signal regions, for which data-driven methods are preferred.

A dedicated jet tagger, discussed in the following, has been developed within the context of this thesis in order to discriminate jets originating from displaced γ_d decays from rare jets, originating from multijet events, providing a method to significantly reduce this background for cDPJ.

4.1.1 The QCD neural network tagger

In order to reduce the background from QCD multijet events, which lead to fake cDPJ, a per-jet tagger (QCD tagger) based on a Convolutional Neural Network (CNN) has been developed. A score ranging from 0 to 1 is assigned to each cDPJ, where a value close to 1 mean that the jet is likely originated from a γ_d decay and a value close to 0 is assigned to background-like jets.

QCD tagger inputs: 3D jet images

The QCD tagger is designed around the concept of *jet images*, which were initially inspired from the computer-vision techniques for face recognition and consist in grouping the energy released by a jet in a image-like structure, i.e. exploiting the most granular information available to build a 2D energy map of the jet.

Early studies on this concept applied to hadronic jets are detailed in [75], while the use of it, in combination with deep-learning techniques for image recognition, was initially studied using truth-level information in [76]. These ideas were initially published by the ATLAS Collaboration in [77], showing a CNN-based tagger which takes as input 2D jet images built from calorimeter clusters. The QCD tagger extends the concept of jet images using a 3D representation of jet energy deposits, of which details are given in the following, using the third dimension to better exploit features related to long-lived particles like the unconventional distribution of energy along the depth of the calorimeter.

In principle, calorimeter cells could be used to build jet images as they provide the most granular information on the energy deposits in ATLAS. Unfortunately, during the data-processing steps only caloclusters are saved, as saving all the calorimeter cells would imply an excessive disk occupancy per event. For each calocluster, the information on the (η, ϕ) coordinates of its centroid and the fraction of energy associated to it in each calorimeter sampling is available.

The jet images that are used for the QCD tagger are centered around the axis of the jet in the (η, ϕ) plane, defined as the direction of the its momentum vector. The (η, ϕ) space around the jet axis is divided in a 15×15 grid, corresponding to a $\eta \times \phi = 0.9 \times 0.9$ area, so that each cell of this 2D grid corresponds to a 0.06×0.06 portion of the (η, ϕ) space. At this point, the third axis is added to this grid, to take into account the energy released in different calorimeter samplings as an additional coordinate. Different regions of the calorimeter are segmented in a different number of samplings, hence to exploit all the calorimeter volume, three 3D grids are produced starting from the same 2D $\eta \times \phi$ grid, one accounting for the barrel samplings, one for the tile extended barrel and one for the endcap. Aiming to discriminate cDPJs that originate from LLPs, from the ones originating from prompt jets, only some of the the calorimeter samplings are considered while other are merged together, in particular:

- In the barrel region, all the calorimeter samplings from the ECAL are treated as a single one, while the three radial samplings of the Tile are considered separately. This lead to 4 segmentations along the third axis and a jet image which is a $15 \times 15 \times 4$ grid.
- In the transition region between the barrel and the endcap, only the three radial sampling of the Tile Extended Barrel are considered. The corresponding image is a $15 \times 15 \times 3$ grid.
- The EM endcap calorimeter is treated as a single sampling, while the four segmentations of the hadronic endcap calorimeter are considered separately, giving an image of $15 \times 15 \times 5$ cells.

Each cell of the three jet images is filled with the energy of the calorimeter clusters that leave a deposit in the corresponding η, ϕ and calorimeter sampling.

Neural network design and training

The 3D images representing the jet energy deposits are then converted to tensors and sent as input to a convolutional neural network. The network has been built using Keras 2.2.4 [78] with the TensorFlow backend [79]. Keras is a deep learning API which enables to build neural networks in a simplified language, using pre-built arrangement of neurons called *layers*. Among different configurations that have been tested, the best-performing one has been chosen and is briefly described in the following; as a detailed description of how these Keras layers work is not given in this thesis, the reader is referred to the Keras documentation [80] for further details.

CNNs are usually based on an initial set of convolution layers, which are helpful in extracting features from the images, followed by a dense neural network which performs the classification. In this case, as the input is made of three 3D tensors, three blocks of convolutional layers are used. Each block consist in two repetitions of a sequence of layers made of a 3D convolution layer, batch normalisation, leaky ReLu, 3D MaxPooling and Dropout. The outputs of these three blocks of the network are passed to three respective Dense layers with ReLu activation function, then are merged together and processed by a dense neural network. The output layer of the neural network has a sigmoidal activation function which provides an output score between 0 and 1. A schematic of the arrangement of the layers used for the definition of this tagger, is given in Figure 4.1.

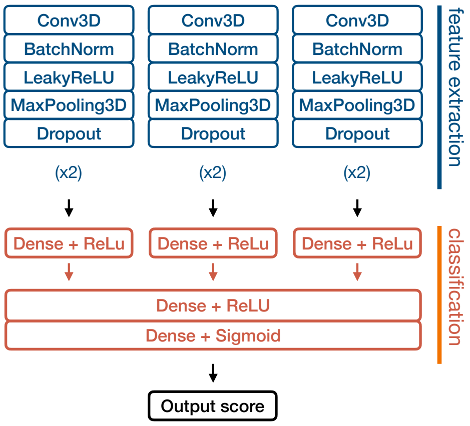

Figure 4.1. Layers used for the definition of the hDPJ CNN tagger. The three Conv3D layers at the top receive as inputs the three 3D tensors built from caloclusters.

In order to train the neural network to distinguish between cDPJ from QCD processes and Dark Photon decays, two datasets are produced collecting all cDPJ reconstructed in signal and QCD MC events.

The signal dataset is produced selecting reconstructed cDPJ from γ_d decays. Using only the ggF FRVZ samples with $m_{\gamma_d} = 0.4$, an equal number of cDPJ has been selected, from both the samples where the production is initiated by the SM Higgs and the $800\,\mathrm{GeV}$ scalar. In signal MC events there is still a non-negligible fraction of cDPJ identified from the hadronisation of spectator quarks or ISR products, hence it is required that the ΔR between the cDPJ and a truth-level dark photon is less than 0.4. No trigger has been applied in producing this dataset and all the simulated events have been considered.

The background sample is obtained from simulated multijet events, which are generated with PYTHIA 8.230 [68], with leading-order matrix elements for dijet production matched to the parton shower. The NNPDF2.3LO set [81] of parton distribution functions was used in the generation of the matrix element, while the simulation of the parton shower and of the multi-parton interactions have been performed using the A14 [70] set of parameters. During the event generation of these multijet MC samples, the production is sliced for different p_T of the leading parton. A dataset of reconstructed cDPJ was extracted from this MC samples, using slices where the p_{T} of the leading parton is between $60\,\mathrm{GeV}$ and $400\,\mathrm{GeV}$ and, as done for the signal, without applying any trigger requirement.

To make an unbiased validation and avoid overtraining the neural network, the initial sample of $\mathcal{O}(250K)$ cDPJ, from both signal and background events, is split $75\% - 25\%$ in a training and a validation dataset, where the latter is not used at the training step but only for an estimation of the performances of the tagger.

The distribution of the output score of the QCD tagger, for cDPJ in the aforementioned validation sample, is shown in figure 4.2. To give an idea of the network performances on the two classes, in the figure, the two different samples of signal cDPJ are combined in a single histogram, as the network is trained without distinguishing them. An unoptimised cut, applied as example at 0.5 on the output score, is found to have an efficiency of 0.92 for signal events and to allow a background rejection of 0.87.

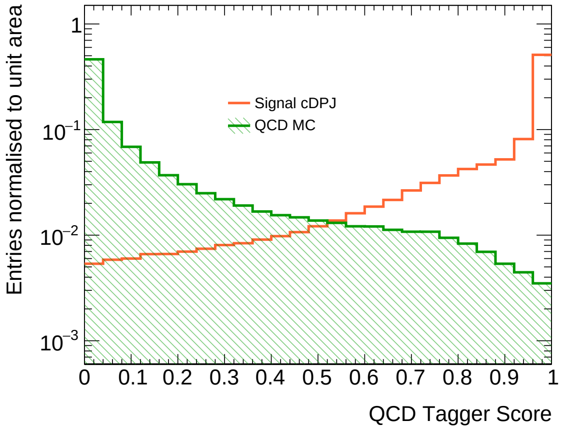

Figure 4.2. Output score of the QCD tagger for the validation datasets: signal events are cDPJ from γ_d decays, taken from FRVZ MC with $m_{\gamma_d} = 0.4\,\mathrm{GeV}$ and $m_H = 125\,\mathrm{GeV}$ and $m_H = 800\,\mathrm{GeV}$; background cDPJ are taken from simulated events from QCD processes, where the leading parton p_{T} is between $60\,\mathrm{GeV}$ and $400\,\mathrm{GeV}$.

To compare the performance of this tagger among the various signal mass points that are used in the Dark-Photon-Jet analysis, the distribution of its output score is shown, in figure 4.3a, for the $0.4\,\mathrm{GeV}$ mass point of the HAHM model and the FRVZ model with both the SM and bSM ggF production mode. Figure 4.3b instead, shows the same distributions, but for different m_{γ_d} samples of the FRVZ model with 2 γ_d and $m_H = 125\,\mathrm{GeV}$. In these two cases, no selection on the leading parton p_{T} of the QCD MC samples is applied. In all cases a good separation between QCD and signal samples is visible.

This tagger will be used, as explained in chapter 5, for the identification of the signal regions of the DPJ analysis that include calorimeter DPJs.

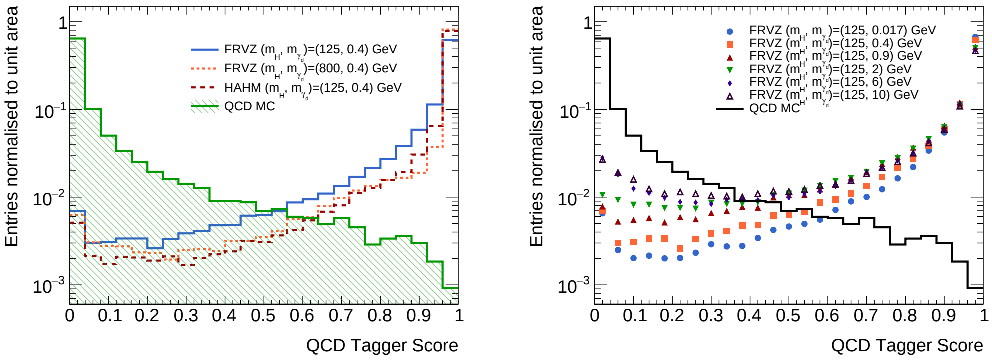

(a) **(b)**

Figure 4.3. The output score distribution of the QCD tagger for cDPJ from QCD events and different set of signals: (a) show different samples with a γ_d with mass of $0.4\,\mathrm{GeV}$, while different mass points of the FRVZ model are shown in (b).

4.2 Beam-Induced Background

As briefly mentioned in section 3.2.2, beam-induced background muons can leave signatures in the calorimeter that can be reconstructed as cDPJ. The origin of BIB muons has to be found in the unavoidable losses of the LHC proton beams and is summarised in the following section. A more detailed description can be found in [30].

4.2.1 Origin of BIB in ATLAS

Proton losses from the LHC beams populate the so-called *primary beam halo*. This halo has to be properly mitigated, with an efficient system of collimators, in order to avoid damage to the LHC superconducting magnets and to avoid as much as possible its interaction with the sensitive material of the detectors.

Two pairs of collimators are placed in two different positions of the LHC, far from the interaction points, to provide a two-stage cleaning of the beam. Particles that leave the beam core are intercepted by the *primary collimators*, but some of them scatter and produce secondary products which remain in the LHC acceptance, yielding the *secondary beam halo*. A set of *secondary collimators* is designed to reduce as much as possible this secondary halo, but some particle (*tertiary halo*) is still lost in the machine. Another pair of *tertiary collimators* is present at $|z| \sim 150\,\mathrm{m}$ from the ATLAS IP, to protect the quadrupole magnets which focus the beams right before entering the interaction region.

The so-called beam-induced background is made of particles produced in the interactions between the beam halo and the material of the collimators, or between the protons and residual gas in the beam pipe and are produced, in both cases, with large Lorentz boost along the z axis. In ATLAS this background is mitigated with a heavy shielding which is placed around the beam pipe in correspondence of the

LHC tunnel. Nevertheless, there are two cases in which these particles can still interact with the detector:

- Particles produced by the scattering of proton beam on the residual gas, in the immediate vicinity of the interaction region, can leave clusters of hits in the inner detector, especially in the pixel.
- High energy muons are mostly unaffected by the shielding and can leave radiative losses in the calorimeter, which are reconstructed as jets (often named *BIB-jets*).

An ATLAS event display showing a fake jet from BIB is shown in figure 4.4. In this event a BIB muon enters the detector at a radius which is in the acceptance of the ECAL, leaving energy deposits reconstructed as a jet with no associated tracks and a corresponding hit, with the same ϕ coordinate, in the CSC chambers of the endcap MS.

4.2.2 Collecting BIB in data

In order to study the beam-induced background contamination in reconstructed cDPJs, a dedicated sample has been collected, using the inclusive version of the CalRatio trigger. As anticipated in section 3.2.2, vetoing the nominal version of the CalRatio trigger and requiring the inclusive one allows to select events which, otherwise, would be discarded by the BIB removal algorithm of the nominal trigger.

This sample (*BIB dataset*) is obtained from collision data collected by ATLAS during Run-II, as no BIB MC simulation is available. In events selected with the aforementioned trigger logical condition, only the cDPJ which are found to be in $\Delta R < 0.4$ from the triggering object are used.

In the following, the main characteristics of the BIB jets are discussed and shown for events collected in this dataset. To compare this background to the one due to multijet events, a sample of fake cDPJ has been collected in simulated QCD events, using the same MC samples described in section 4.1.1, in events selected by explicitly vetoing the CalRatio trigger and requiring a single jet trigger with a $E_{\mathrm{T}} > 60\,\mathrm{GeV}$ threshold.

BIB muons are subject to the magnetic field of the system of dipoles and quadrupoles that are placed in the proximity of the interaction region. Muons at radii smaller than $\sim 1\,\mathrm{m}$ are deflected in the $x = 0$ and $y = 0$ planes by the focusing quadrupoles, while muons at larger radii are deflected in the $y = 0$ plane by the separation and recombination dipoles, originating a ϕ distribution with two prominent peaks at 0 and $\pm\pi$, as visible in figure 4.5a.

Another peculiar feature of BIB, which is especially relevant for the case of BIB jets, is the timing pattern. In ATLAS, the timing information of a hit in a certain sub-detector is always corrected by the expected time of flight from the interaction point, implying that any reconstructed object will always have a timing equal to 0. A BIB which leaves a hit in a given (r, z) position will have a timing, corrected from

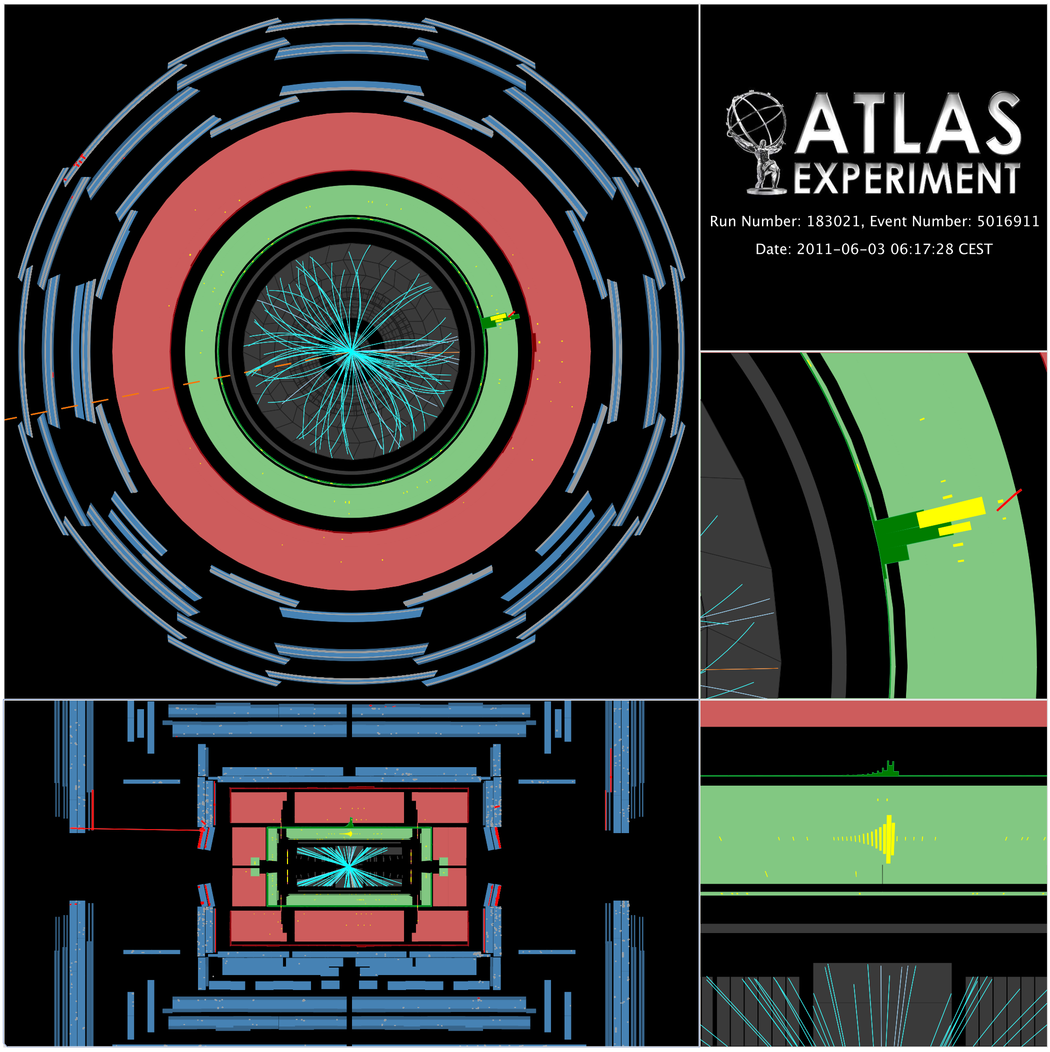

Figure 4.4. Event display collected by ATLAS in 2011, showing the signature left by a BIB muon. As visible from the bottom left picture the muon crosses the detector along the z axis, leaving hits in the LAr barrel calorimeter (yellow cells on green background) and a muon track (red horizontal line) in the CSC chambers. As visible from the top left figure, the ID tracks do not point to the reconstructed jet and the missing transverse momentum is denoted with a dashed line. Event display taken from [30].

the IP, which is given by:

$$t_{\text{BIB}} = \frac{\pm z - \sqrt{r^2 + z^2}}{c} \tag{4.1}$$

where the plus (minus) sign is taken for the BIB travelling from side C to side A (side A to side C). The distribution of the timing of a cDPJ from BIB is shown in figure 4.5b, where QCD jets are clearly distributed with timing close to 0 and BIB jets follow a different pattern.

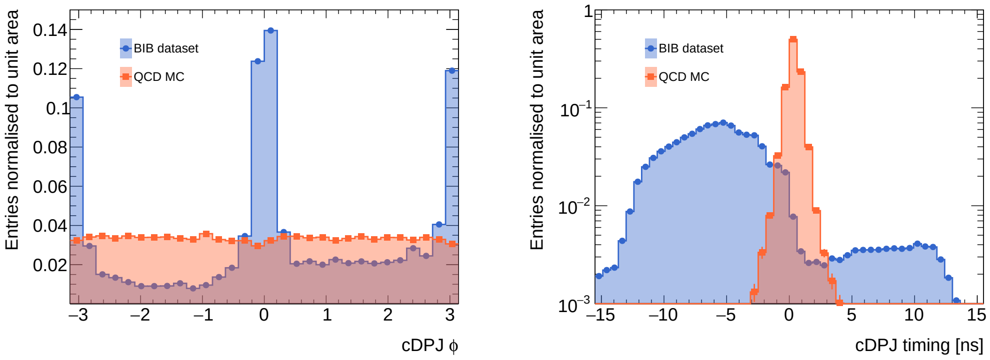

(a) **(b)**

Figure 4.5. Comparison of the ϕ coordinate (a) and the timing (b) of cDPJ reconstructed from jets originating from BIB or multijet MC events. The two peaks at $\phi = 0, \pm\pi$ originate as a consequence that the BIB muons are deflected in the $y = 0$ plane by the LHC dipoles.

The dependence of BIB jet timing on the longitudinal coordinate is more explicit in figure 4.6, where the cDPJ timing is shown as a function of its pseudorapidity. Different populations are visible in the figure:

- The region with timing ~ 0 and $|\eta| < 1$ is populated only by jets from collision products which, even if this selection is specific for BIB jets, are still present in this dataset due to non-negligible inefficiencies;
- The two populations in the semi-plane with negative timing are BIB jets originating from the two LHC beams, of which the timing is related to the η coordinate via equation 4.1. Energy deposits left at $z < 0$, by BIB moving from negative to positive z (i.e. in parallel with the bunches of the CA beam), are left with a timing which is equal to $-|z|/c$, to which the expected time-of-flight from the IP is subtracted. On the other hand, energy deposits left by BIB of the same beam at $z >> 0$ are saved with timing approaching 0.
- The two regions at $|\eta| \sim 2$ and t between -6 and $-10\,\text{ns}$, as well as the regions of the semi-plane at positive cDPJ timing and the regions at $|\eta| = 1.4$, are all populated by fake jets left by BIB moving in parallel with the next two bunch crossings.

Other helpful jet-related variables for the BIB identification were partially mentioned in section 2.3.2 and are summarised in the following:

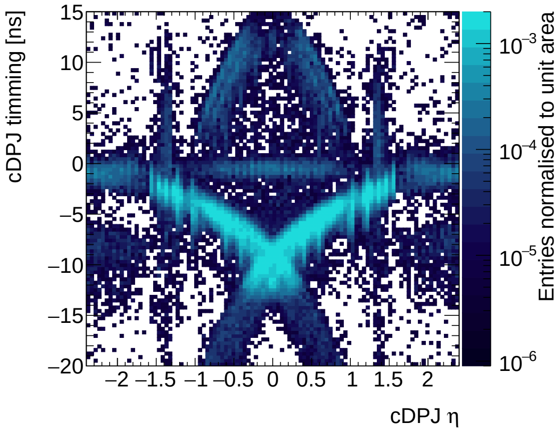

Figure 4.6. Timing shown as a function of the pseudorapidity for cDPJ of the BIB dataset.

- f_{max}, as BIB move along the z direction and can easily originate jets which energy is localised in a single sampling, yielding $f_{\text{max}} \sim 1$;

- f_{EM}, which is 0 for BIB crossing the detector at radii compatible with the hadronic calorimeter;

- f_{ch} is expected to be 0 for BIB, as no associated tracks are produced;

- f_{HEC} is expected to be larger than 0.5 for BIB, as they can enter the LAr endcap hadronic calorimeter from the outside and leave a large energy deposit in this fraction;

Nevertheless, these variables are more useful to discriminate BIB jets from prompt jets and can not be used in discriminating BIB from signal cDPJ from γ_d decays. For instance, f_{ch} is expected to be 0 for both signal and BIB, as well as the f_{EM}, which is also used in the definition of cDPJ. For the purpose of this analysis, the only variables which can be exploited are the ones related to the jet timing and ϕ coordinates, an additional discrimination will be provided by a dedicated tagger, which is presented in the next section.

4.2.3 The BIB neural network tagger

In order to provide an additional discriminant between signal jets and BIB jets, when searching displaced decays of γ_d, a jet tagger (*BIB tagger*) based on the same approach of the QCD tagger has been developed. The idea of using jet images for this tagger is motivated by the fact that BIB leave a very specific hit pattern in the calorimeter, which can be exploited to distinguish them from jets originating from the IP.

The BIB tagger shares the network architecture of the QCD tagger. Jet images are produced with the same criteria of the ones used in the QCD tagger and are also pre-processed, to remove the information associated to cluster energy, by setting to

1 (0) the cells for which a calocluster is (is not) found with matching coordinates. In other words, if no cluster is found in a given η, ϕ, sampling, the value of the corresponding cell is set to 0, or 1 otherwise. The architecture of the network is identical to the QCD tagger, but in addition, the jet (η, ϕ) coordinates are passed as inputs to the neurons of the dense neural network, in parallel to the convolution layers output.

The jet images that have been used in the training step of this tagger are the one from cDPJ in the BIB dataset, which has been described in section 4.2.2, and a corresponding dataset of cDPJ reconstructed by γ_d decays. Signal cDPJs used in the training steps are obtained from all the signal MC samples with γ_d produced by the decay of a heavy Higgs, selecting cDPJ in a $\Delta R = 0.4$ cone from a γ_d, in events triggered by the nominal CalRatio trigger.

This choice, of training this tagger in triggered signal events, is motivated by the fact that the trigger is also applied in the BIB dataset, and as the CalRatio selects jets with very low f_{EM}, a possible bias in the training could be introduced if signal and background cDPJs have a significantly different f_{EM} distribution. cDPJs from Dark Photons originating from the SM Higgs decay have not been used during the training step, given the low efficiency of the CalRatio triggers on these samples. To validate the training, the input sample consisting of $\mathcal{O}(130K)$ jets from both classes are divided $75 : 25$ in training and validation samples. The output score distributions of the BIB tagger for cDPJ from the BIB dataset and signal events are shown in figure 4.7, a clear distinction is visible from the plot. An unoptimised cut on the output score of the BIB tagger, applied at 0.5, yields a signal efficiency of 0.71 and a background rejection of 0.88.

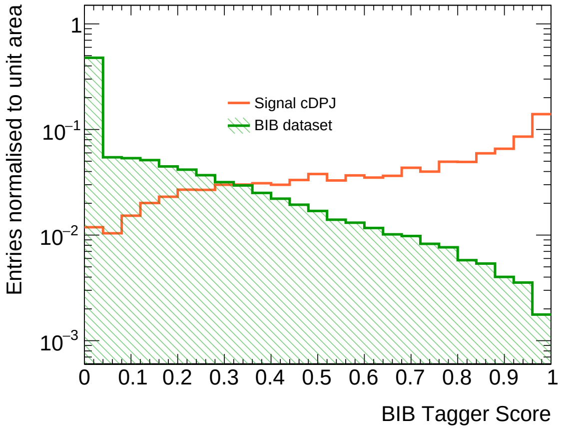

Figure 4.7. Output score of the BIB tagger for the validation datasets: BIB cDPJ are taken from the BIB dataset, while signal cDPJ are collected among signal FRVZ events with $m_H = 800\,\mathrm{GeV}$, triggered with the nominal CalRatio trigger, where the cDPJ is a seed of the triggering algorithm.

In order to check the behaviour of this tagger on signal cDPJ, which are not seeding the CalRatio trigger, its output score is shown in figures 4.8a and 4.8b, for signal cDPJ which are found in a $\Delta R = 0.4$ cone from a truth-level dark photon.

In particular, figure 4.8a show the output score for the $0.4\,\text{GeV}$ mass point of the HAHM model and the FRVZ model with both the SM and bSM ggF productions. On the other hand, figure 4.8b show the same distribution for signals with different m_{γ_d}, generated with the FRVZ model with 2 γ_d and $m_H = 125\,\text{GeV}$.

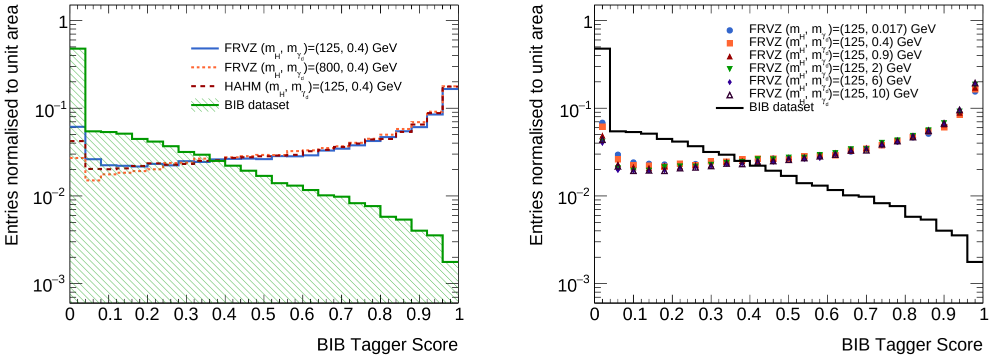

(a) **(b)**

Figure 4.8. Comparison of the output score of the BIB tagger for the background validation sample and different signal samples. The background sample is made of cDPJ from BIB seeding the CalRatio HLT algorithm. Two different sets of signals are shown: (a) show different samples with a γ_d with mass of $0.4\,\text{GeV}$, while different mass points of the FRVZ model are shown in (b).

As shown from the aforementioned figures, the BIB tagger is able to discriminate cDPJs originating from γ_d from ones due to BIB. Although, the lower discriminating power with respect to the QCD tagger, suggests that an optimisation of a cut on the BIB tagger score should be done with regard to the signal efficiency. This optimisation will be discussed in section 5.2.3.

4.3 Cosmic-ray muons

Cosmic-ray muons are produced by the shower of highly energetic particles, originating from extraterrestrial sources, which interact with the Earth's atmosphere. As the ATLAS cavern is placed deeply underground, only muons from cosmic-ray showers are sufficiently penetrating to be able to reach the detector.

Hits left by cosmic-ray muons in the MS, in coincidence with a pp collision, can originate fake μDPJ and be triggered by the Narrow-Scan or the Tri-muon triggers, on the other hand, radiative energy deposits can be triggered by the CalRatio and reconstructed as cDPJ, as they may cross the ATLAS hadronic calorimeter without leaving hits in the ECAL and the ID.

As in the case of BIB, cosmic-ray muons will leave very specific timing and geometrical patterns due to the fact that their origin is outside the detector, with timing uncorrelated from LHC collisions and with unusual direction of their momentum. These properties are exploited in order to mitigate this background in the displaced

DPJ analysis. In particular, for the case of μDPJ, a neural-network-based tagger has been implemented in order to reduce this background as much as possible.

4.3.1 Cosmic-ray dataset

As already mentioned in section 3.2, the triggers used for the search of displaced γ_d were also active, during the full Run-II, in Empty bunch crossings. The events selected by the trigger with this configuration are used to produce a dataset of both μDPJ and cDPJ originating from cosmic-rays, of which details are given below. A comparison of these datasets with DPJ from γ_d decays will be given in section 4.3.2.

A dataset of μDPJ has been collected selecting events triggered by the Narrow-Scan or the Tri-muon MS-only triggers, running when the bunch crossings are in the empty configuration. In addition, it is required that no interaction vertex must be found in the event and exactly one μDPJ must be reconstructed, to ensure the orthogonality with the analysis selection described in chapter 5. All Stand-Alone MS tracks used in the reconstruction of these μDPJ are then added to the dataset.

On the other hand, a dataset of cDPJ has been built by selecting events in empty bunch crossings, which are triggered by the CalRatio, collecting all the reconstructed cDPJ.

4.3.2 Properties of cosmic-ray muons in ATLAS

Hits left by cosmic-ray muons in the MS can be reconstructed as Stand-Alone MS tracks that have very specific topological and timing pattern.

As the momentum direction of cosmic-ray muons is downwards, an asymmetry in the ϕ distribution of the hits left in the MS is expected, with local maxima at $\phi \sim \pi/2$ and $3\pi/2$. The η distribution of their hits is also expected to differ from the one of collision events, as most of the cosmic-ray muons enter ATLAS by crossing the two big shafts, placed above the experimental cavern, leaving most of the hits at $|\eta| < 0.6$. The impact parameter in the longitudinal plane, z_0 is different from the one of a hit originating in the PV, as such muons are not necessarily pointing to the IP.

Lastly, a hit timing pattern can be a key discriminant for cosmic-ray muons. The information associated to RPC hits can be used to build a timing discriminant for the track. As done for jets, the timing of a RPC hit is always corrected by the expected time-of-flight from the interaction point, so that muons produced in collisions will have timing $t \sim 0$. In order to build this discriminant, the timing of the hits on the three RPC layers, t_i, is used. Here $i = (1, 2, 3)$ correspond to the i-th RPC layer seen from the IP to the outside, which means that 1 and 2 correspond to the two RPC layers sandwiching the BM precision muon chambers and $i = 3$ corresponds to the RPC chambers of the BO layer. Considering the hits on the third and second layer, the correction for the time-of-flight, t_i^{tof}, is applied as:

$$\begin{aligned} t_3 &= t_3^* - t_3^{\text{tof}} \\ t_2 &= t_2^* - t_2^{\text{tof}} \, , \end{aligned}$$

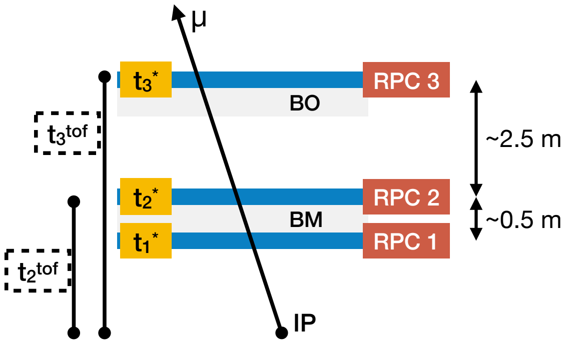

Figure 4.9. Visual representation of the variables used for the construction of the RPC timing discriminant.

where t_i^* is the uncorrected timing. Now, considering that

$$\begin{aligned} t_3* &\simeq t_1^* + (t_3^{\mathrm{tof}} - t_1^{\mathrm{tof}}) \quad \text{(for collision muons)} \\ t_1* &\simeq t_3^* + (t_3^{\mathrm{tof}} - t_1^{\mathrm{tof}}) \quad \text{(for cosmics)}\ , \end{aligned}$$

we obtain that for collision muons the timing difference between layer 3 and 1 is approximately 0, while for cosmic-ray muons entering the detector the difference is $\simeq -2(t_3^{\mathrm{tof}} - t_1^{\mathrm{tof}})$. A schematic of the variable used to compute the RPC timing difference is shown in figure 4.9. The RPC timing difference (Δt_{RPC}) is a powerful discriminant, but is useful only for hits left by cosmic-ray muons in the $\phi > 0$ region, as for $\phi < 0$ the direction of a cosmic muon is the same as particles produced in collisions and the timing difference between two RPC layers is ~ 0 in both cases. In addition, it may happen that no hit is found in the BO RPC layer, so the difference can not be computed.

Figure 4.10 show the aforementioned variables, for Stand-Alone MS tracks collected in the cosmic-ray dataset and in FRVZ signal events with dark photons of mass equal to $0.4\,\mathrm{GeV}$, produced by the decay of a SM Higgs boson. In general, the same distributions observed in signal events are also expected for any kind of μDPJ originating from the ID.

Hits left in the calorimeter can be reconstructed as cDPJ which, as in the case of BIB, are associated with a timing which is not necessarily 0. Since cosmic-ray muons are not related to the LHC beams, their expected timing is uniform within $\pm 12.5\,\mathrm{ns}$ from the bunch crossing, as visible in figure 4.11. In addition, in the case of events in which two cDPJ from cosmic-ray muons are identified, a pattern between the Δt and the $\Delta\phi$ of the two jets is expected to be found, while for a pair of collision jets the Δt is expected to be 0.

The cosmic-ray muon tagger

In order to reduce the background due to cosmic-ray muons, the four discriminating variables for Stand-Alone muons, introduced in the previous section, have been

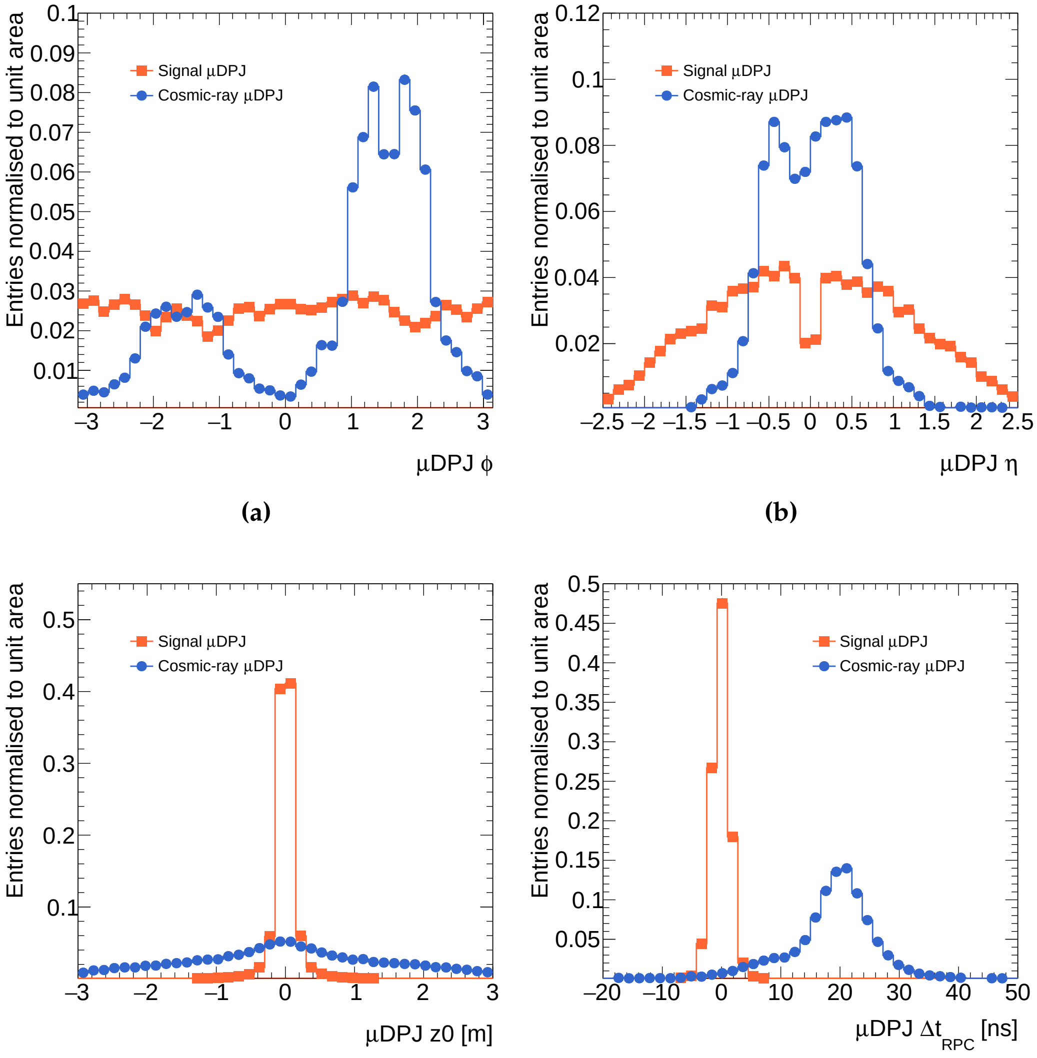

(a) **(b)**

(c) **(d)**

Figure 4.10. Variables helpful in the discrimination between Stand-Alone muon tracks from the cosmic-ray dataset and FRVZ signal events with $(m_H, m_{\gamma_d}) = (125, 0.4)\text{GeV}$. The ϕ, η coordinates of the tracks are shown in figures (a) and (b), while the impact parameter z_0 and the RPC timing difference Δt_{RPC} are shown in (c) and (d).

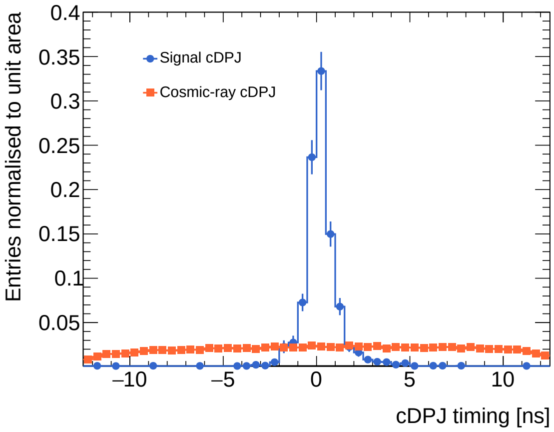

Figure 4.11. Distribution of the timing of reconstructed cDPJ in FRVZ signal events (with $m_{\gamma_d} = 0.4\,\text{GeV}$ and $m_H = 125\,\text{GeV}$) and events in the cosmic-ray dataset.

used to train a Dense Neural Network (DNN) as a binary classifier. This tagger (Cosmic-ray tagger) is trained with the purpose of assigning a score close to 1 to MS tracks which originate from the IP and 0 to the ones produced by cosmic-ray muons. As done for the other two classifier, the DNN has been implemented using Keras.

The optimal configuration for the Cosmic-ray tagger was found to be a DNN with three dense hidden layers, with 32, 64 and 32 neurons respectively. The training has been performed on a balanced sample of $\mathcal{O}(90K)$ μDPJs from the cosmic-ray dataset and μDPJs from MC samples with $m_H = 125\,\text{GeV}$ and $m_{\gamma_d} = 0.4\,\text{GeV}$, where half of the dataset have been used for validating the training procedure. As the Δt_{RPC} is not always available, a fifth *dummy* variable is passed to the DNN acting as a mask, assuming value equal to 1 when the timing information should be used, 0 otherwise. In this way, by training the network on a balanced sample of MS tracks in which this variable is 0 or 1, the network learns to use the Δt_{RPC} only when it is available, while the possibility of learning discriminating features based on the sole masking variable is avoided.

The Cosmic-ray tagger output is shown in figure 4.12 for signal and background MS tracks from the validation sample. An unoptimised cut on the DNN prediction has an efficiency, on the validation signal sample, of 0.95 and has an efficiency of rejecting tracks from cosmic-rays of 0.9. From the figure, it can be easily observed how the contribution of the Δt_{RPC} variable yield a very large separation power between the two classes.

The response of the Cosmic-ray tagger is shown, in figures 4.13a and 4.13b, for signal μDPJ generated of different signal samples, compared to the response for the cosmic-ray dataset.

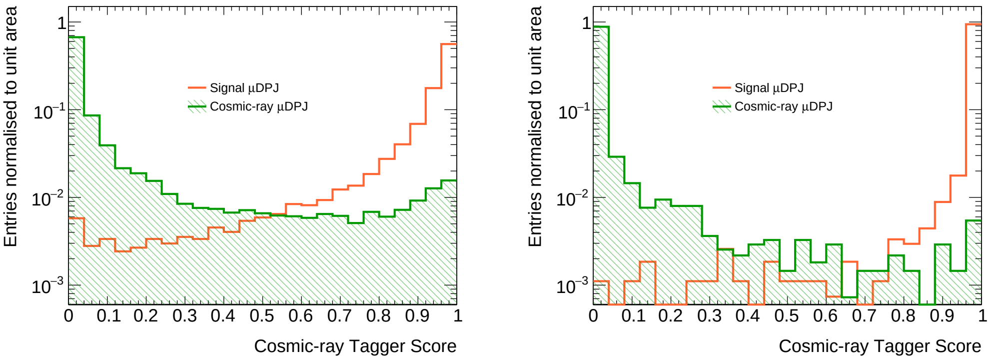

(a) **(b)**

Figure 4.12. Normalised output distributions of the Cosmic-ray tagger for muon tracks in the validation sample. (a) shows the two distributions of the DNN output regardless of the availability of the RPC timing information, while in (b) the same two distributions including only tracks for which the RPC timing information is available.

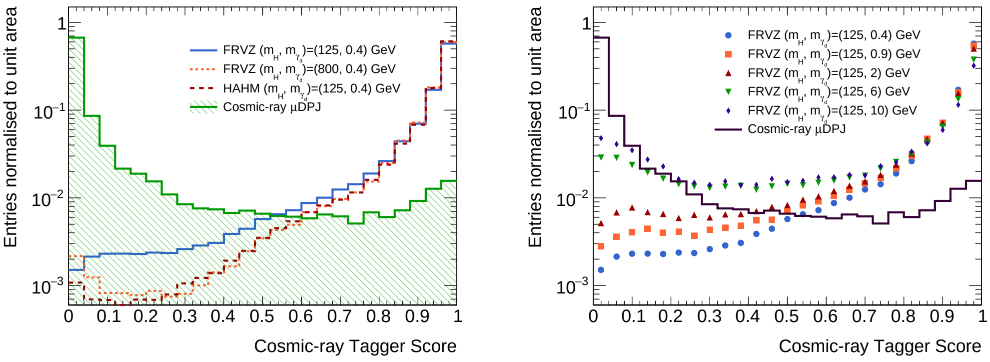

(a) **(b)**

Figure 4.13. Normalised output distributions of the Cosmic-ray tagger for muon tracks in different signal samples, compared with the cosmic-ray dataset. (a) shows the two distributions of different models with a dark photon of $0.4\,\text{GeV}$, while (b) show the response for the FRVZ model with $m_H = 125\,\text{GeV}$ and different choices of m_{γ_d}.

Chapter 5

Search for Dark-Photon Jets in the Full-Run2 dataset

This chapter will describe the analysis of $139\,\mathrm{fb}^{-1}$ of data collected by ATLAS, during the full Run-II, searching for the production of γ_d pairs that decay outside the acceptance of the ID, of which the experimental signature has been introduced in chapter 3.

Given that the probability, $\mathcal{P}$, of identifying a DPJ is small, the identification of a second one in an event can be thought, in a first approximation, as uncorrelated and thus proportional to $\mathcal{P}^2$. So, by requiring two displaced decays of γ_d, the expected background is dramatically reduced. Although this background is small, it is not non-negligible with respect to the signal and needs to be carefully estimated.

The main constituents of this background have been already discussed in chapter 4. Of all the different contributions, the one due to rare jets, from either multijet events or V+jet events, is expected to be the leading one and will be estimated with a data-driven method. Other backgrounds, when present, are either reduced to a negligible level or estimated in a control sample and taken into account during the data-driven estimation.

The event selection consists in the identification of six signal regions (SR), which will be presented in section 5.1. Each SR is optimised on signal efficiency, selecting events according to the H production mode and the type, or number of DPJs identified. The strategy adopted for the background estimation will be presented (section 5.2), followed by a discussion of the systematic uncertainties (section 5.3). Finally, an interpretation of the results, within the different models considered, will be given in section 5.4.

5.1 Event selection

For the events of the displaced DPJ analysis, two exclusive search categories are defined: gluon-gluon fusion and associated production with a W boson, based on the charged lepton multiplicity and aimed at different production mechanisms of the dark photons, where each category aims to identify the corresponding production mode of the Higgs boson.

If more than two DPJs are reconstructed according to the identification criteria described in chapter 3, the one with the highest transverse momentum, labelled as the *leading DPJ*, and the one farthest in the transverse plane from the leading one, labelled as *far DPJ*, are used to classify the event. Each search category further divides the events into three different orthogonal channels, based on the number of μDPJs and cDPJs, yielding a total of six SR that were optimised for the best discovery sensitivity.

The two search categories, with the definition of the corresponding SRs, are detailed in the following sections. For the sake of simplicity, in the following, details on the expected signal event yields will be given for a subset of the signal Monte Carlo samples presented in chapter 3 which are considered as benchmark points. The final results that will be presented in section 5.4 will consider also all the remaining MC samples.

5.1.1 Selection of events for the ggF production mode

The event selection for the ggF production mode of the Higgs boson (or the bSM Higgs-like scalar) aims to identify two DPJs by triggering on the signatures which are possibly left by a γ_d decay.

An initial set of requirements, referred to as the *pre-selection*, is applied to the events. The first requirement applied is the trigger: events must be accepted by at least one between the Tri-muon MS-only, the CalRatio and the Narrow-Scan triggers. In addition, it is required that all sub-detectors were fully operational and that the event figures in the Good Runs List. As γ_d are expected to originate from proton collisions, at least one Primary Vertex needs to be present in each event. The PV is identified, among all the vertices with at least two associated tracks with $p_{\mathrm{T}} > 0.5\,\mathrm{GeV}$, as the one with the largest sum of the p_{T}^2 of the tracks.

To ensure orthogonality with the WH category, the presence of a prompt muon or electron is vetoed. In addition, to allow a statistically-independent study of a VBF production mode in the future, events are rejected if they have $E_{\mathrm{T}}^{\mathrm{miss}} > 225\,\mathrm{GeV}$ and two jets with combined invariant mass larger than $1\,\mathrm{TeV}$. These two requirements were found to have a negligible effect on the number of signal events in each SR.

At this point the events are selected in the different ggF analysis channels, if at least two DPJs are found. Each channel is defined by a condition on the types of the leading and far DPJ found in the event, in a addition to a trigger requirement:

- For the **ggF**$_{2\mu}$ channel, both leading and far DPJ have to be of the muonic type and the event must be selected by either the Narrow-Scan or the Tri-muon MS-only trigger;

- For the **ggF**$_{2\mathrm{c}}$ channel, both leading and far DPJ need to be calorimeter DPJ and the event must be selected by the CalRatio trigger.

- For the $\mathbf{ggF}_{\mathrm{c}+\mu}$ channel, the leading and far DPJ have to be one of muonic type and other of calorimeter type. The event must be selected by the Narrow-Scan trigger;

An additional set of selections is applied to each channel, aiming to mitigate the background in each SR. The following variables have been used for the selection:

- Cosmic-ray Tagger score: the prediction of the Cosmic-ray Tagger for each μDPJ found in the event;
- t_{cDPJ}: the measured time associated to a cDPJ.
- $|\Delta t_{\mathrm{cDPJs}}|$: the absolute time difference between a pair of cDPJ. This quantity is useful to further reject contributions from cosmic rays and BIB, as they do not originate from a single interaction vertex.
- BIB Tagger score: the score assigned to each cDPJ by the BIB tagger.
- $|\Delta\phi_{\mathrm{DPJ}}|$: the azimuthal angular difference between the leading and far DPJ. Signal events are expected to contain back-to-back DPJs.
- JVT: the JVT score of a cDPJ can be used to reject candidates from multijet events, as mentioned in section 2.3.2.
- $\prod \mathrm{QCD\ tagger}$: the product of the QCD tagger scores of the two DPJs, or the score of the single cDPJ found in the event.
- $\max \sum p_{\mathrm{T}}$: the maximum value of $\sum p_{\mathrm{T}}$, among the two DPJs. $\sum p_{\mathrm{T}}$ is the scalar sum of the transverse momenta of all tracks, with $p_{\mathrm{T}} > 0.5\,\mathrm{GeV}$, enclosed within $\Delta R = 0.4$ around the direction of the DPJ momentum vector. Displaced DPJs are expected to cause very limited activity in the volume of the Inner Detector.

The selection is based on these variables and is defined by the cuts reported in table 5.1. Most of the aforementioned cuts are defined to reject as much as possible any background other than the multijet one, which estimate is finally done with a data-driven method. An explanation of this method, which relies on the $|\Delta\phi_{\mathrm{DPJ}}|$, $\max \sum p_{\mathrm{T}}$ and the $\prod \mathrm{QCD\ tagger}$ variables, will be given in section 5.2.1. The selection applied on the cDPJ timing is helpful in rejecting cosmic-ray events and reducing the BIB background to a negligible level, where the latter is additionally reduced by the use of the BIB Tagger, as it will be shown in section 5.2.3. Finally, the JVT cut was chosen to reduce the background in the $\mathrm{ggF}_{2\mathrm{c}}$ signal region which, as expected, is the one most affected by the multijet background due to the use of calorimeter-only information. The cut on the JVT is applied requiring that both cDPJs have a score less than 0.4 and was optimised maximising the signal significance.

Table 5.2 show the cut flow of the events in the three ggF analysis channels, produced processing four different signal samples. For the samples where the SM Higgs is considered, the cross section used to normalise the events is the one at

Requirement / Region	$\mathrm{SR}^{\mathrm{ggF}}_{2\mu}$	$\mathrm{SR}^{\mathrm{ggF}}_{2\mathrm{c}}$	$\mathrm{SR}^{\mathrm{ggF}}_{\mathrm{c}+\mu}$
Number of μDPJs	2	0	1
Number of cDPJs	0	2	1
Tri-muon MS-only trigger	yes	-	-
Muon narrow-scan trigger	yes	-	yes
CalRatio trigger	-	yes	-
Cosmic tagger score	< 0.5	-	< 0.5
$\lvert t_{\mathrm{cDPJ}}\rvert$ [ns]	-	< 4	< 4
$\lvert\Delta t_{\mathrm{cDPJs}}\rvert$ [ns]	-	< 2	-
BIB tagger score	-	> 0.2	> 0.2
$\lvert\Delta\phi_{\mathrm{DPJ}}\rvert$	$> \pi/5$	$> \pi/5$	$> \pi/5$
cDPJ JVT	-	< 0.4	-
$\prod$ QCD tagger	-	> 0.95	> 0.9
$\max\sum p_{\mathrm{T}}$ [GeV]	< 4.5	< 4.5	< 4.5

Table 5.1. Definition of the SRs used in the ggF selection. All SRs require at least two DPJs, but only the leading and the far DPJs are considered for the event classification. Dashes indicate the cases when the requirement is not applied.

13 TeV, already reported in table 1.1, while the branching ratio (B) of the FRVZ or HAHM processes is assumed for reference at 10%. On the other hand, for the 800 GeV Higgs-like models, the reference value of $\sigma \times \mathrm{B} = 5\,\mathrm{pb}$ is used. This value is chosen arbitrarily at this point, in order to introduce a common reference for comparing the results, which will be expressed in its terms in section 5.4.

With reference to table 5.2, the point with $m_{\gamma_d} = 0.1$ GeV shows poor sensitivity for the $\mathrm{ggF}_{2\mu}$ and the $\mathrm{ggF}_{\mathrm{c}+\mu}$ channels. This is expected, as the production of a muon pair is forbidden for this mass point and only electrons are produced. On the other hand, the analysis is more efficient in the HAHM and the 800 GeV sample, thanks to the larger boost of the γ_d.

5.1.2 Selection of events for the WH production mode

The event selection for the WH category features an initial pre-selection, starting with the requirement of a single lepton trigger among the ones presented in section 3.2.3.

As done for the ggF category, it is required that all the various ATLAS subsystems were fully operational and that the event figures in the Good Runs List, in addition to the presence of a Primary Vertex in the event.

A reconstructed prompt muon or electron is required, having the same flavour as the trigger that accepted the event. This requirement already defines the orthogonality with the ggF selection and, in addition, the orthogonality with a VBF production mode is imposed by vetoing events where two jets with combined invariant mass larger than 1 TeV are found. As for the ggF case, this additional cut is found to have negligible impact in the signal regions.

Model		FRVZ	FRVZ	FRVZ	HAHM
Process		$H \to 2\gamma_d + X$	$H \to 2\gamma_d + X$	$H \to 2\gamma_d + X$	$H \to 2\gamma_d$
m_{H} [GeV]		125	125	800	125
m_{γ_d} [GeV]		0.1	0.4	0.4	0.4
$c\tau_{\gamma_d}$ [mm]		15	50	10	25
$\sigma \times$ B [pb]		4.86	4.86	5	4.86
Selection	Cut				
Pre-selection	Initial	675500 ± 1100	675500 ± 1100	694800 ± 1700	675500 ± 1300
	Trigger	20000 ± 190	58140 ± 320	208700 ± 900	150000 ± 600
	PV, GRL, cleaning	20000 ± 190	58140 ± 320	208700 ± 900	150000 ± 600
	VH-VBF veto	19970 ± 190	57960 ± 320	204100 ± 900	149700 ± 600
	$\geq$ 2 DPJ	2550 ± 70	17220 ± 180	52400 ± 500	45750 ± 340
ggF$_{2\mu}$	2 μDPJs + (Narrow-Scan $\vee$ Tri-muon MSonly)	50 ± 9	8600 ± 120	12710 ± 230	16680 ± 200
	Cosmic-ray tagger	7.2 ± 3.5	5250 ± 100	8310 ± 190	11470 ± 170
	SR (max $\sum p_{\mathrm{T}}$ and $\lvert\Delta\phi_{\mathrm{DPJ}}\rvert$)	7.2 ± 3.5	5000 ± 90	7960 ± 180	10830 ± 160
ggF$_{\mathrm{c}+\mu}$	μDPJ + cDPJ + Narrow-Scan	453 ± 28	4400 ± 90	17890 ± 270	15650 ± 200
	Timing cuts	289 ± 23	2780 ± 70	12170 ± 220	10890 ± 170
	BIB tagger	253 ± 21	2390 ± 70	10890 ± 210	9510 ± 160
	Cosmic-ray tagger	172 ± 18	2240 ± 60	10530 ± 210	9160 ± 150
	$\lvert\Delta\phi_{\mathrm{DPJ}}\rvert$	154 ± 16	2100 ± 60	10070 ± 210	8840 ± 150
	SR (max $\sum p_{\mathrm{T}}$ and $\prod$ QCD tagger)	92 ± 13	1040 ± 40	5430 ± 150	5970 ± 120
ggF$_{2\mathrm{c}}$	2 cDPJs + CalRatio	1760 ± 60	717 ± 35	6720 ± 160	3720 ± 90
	Timing	1090 ± 40	415 ± 27	4490 ± 130	2360 ± 70
	BIB tagger	710 ± 40	284 ± 22	3480 ± 110	1670 ± 60
	$\lvert\Delta\phi_{\mathrm{DPJ}}\rvert$	671 ± 35	269 ± 22	3330 ± 110	1620 ± 60
	JVT	485 ± 30	174 ± 18	2150 ± 90	1160 ± 50
	SR (max $\sum p_{\mathrm{T}}$ and $\prod$ QCD tagger)	282 ± 23	102 ± 13	1460 ± 80	850 ± 50

Table 5.2. Detail on the pre-selection and the selection of the three different ggF channels, for different signal samples using both the FRVZ and the HAHM model. Events are normalised to the integrated luminosity of $139\,\mathrm{fb}^{-1}$. Quoted errors are statistical only.

In order to match the signature from a W boson, it is required for all events that no additional lepton with $p_{\mathrm{T}} > 10\,\mathrm{GeV}$ is found, in addition to the requirement of a $E_{\mathrm{T}}^{\mathrm{miss}}$ larger than 40GeV and the *transverse mass*[1], m_{T}, larger than 30 GeV.

W+jets background processes are reduced by requiring three or less jets with $p_{\mathrm{T}} > 30$GeV in the event. Additionally, events which include any b-tagged jets are removed, in order to suppress the $t\bar{t}$ and the single top processes. After these selections the background is dominated by W+jets events.

Events that pass the aforementioned set of cuts are divided in three orthogonal analysis channels:

- The **WH**$_c$ channel selects events where exactly 1 calorimeter DPJ is found;
- The **WH**$_{2\mathrm{c}}$ channel requires two or more reconstructed DPJs in the event, with both leading and far DPJ being of the calorimeter type.
- The **WH**$_{\mathrm{c}+\mu}$ channel, in which two or more reconstructed DPJs are present, where leading and far DPJ are one cDPJ and one μDPJ.

An initial study was also made on a purely-muonic channel, but as it was seen to have a negligible acceptance with respect to the corresponding selections of the ggF

---

[1] The transverse mass is defined as $m_{\mathrm{T}} = \sqrt{2p_{\mathrm{T}}^{\ell}E_{\mathrm{T}}^{\mathrm{miss}}(1 - \cos\Delta\phi)}$, where $\Delta\phi$ is the azimuthal angle between the vectors defining the missing transverse momentum and the lepton transverse momentum (p_{T}^{ℓ}).

analysis, it has been not developed further. Therefore, the WH analysis will focus only on the channels containing calorimeter DPJ. Thanks to the WH production mechanism and to the ability to exploit the single lepton triggers, the aim is for the WH analysis to obtain strong results in the hadronic channels and to be competitive with the ggF analysis.

The selection that has been made on the WH channels has been optimised for the signal significance and, in part, relies on the same variables, described in section 5.1.2, that are used for the ggF analysis. In addition, the following three variables have been used for the event selection:

- cDPJ width: the p_T-weighted sum of the $|\Delta R|$ between each calocluster and the jet axis. Jets from DPJs are expected to be narrower on average than ordinary jets since they are produced just before or inside the calorimeters.
- $\min(|\Delta\phi|)$: minimum azimuthal angular distance between each DPJ considered in the selection and the $E_{\mathrm{T}}^{\mathrm{miss}}$ vector.
- $\min(\mathrm{QCD\ tagger})$: the minimum QCD tagger score, computed considering up to two cDPJs.

A summary of the cuts applied in the definition of the WH signal regions is given in 5.3. As done for the ggF signal regions, the cuts on these variables are defined to reduce as much as possible the background, while keeping an acceptable signal efficiency.

Requirement / Region	$\mathrm{SR}_{\mathrm{c}}^{\mathrm{WH}}$	$\mathrm{SR}_{\mathrm{2c}}^{\mathrm{WH}}$	$\mathrm{SR}_{\mathrm{c}+\mu}^{\mathrm{WH}}$
Number of μDPJs	0	0	1
Number of cDPJs	1	2	1
Single lepton trigger (μ,e)	yes	yes	yes
$\mathrm{m_T}$ [GeV]	> 120	-	-
$\lvert t_{\mathrm{cDPJ}}\rvert$ [ns]	< 4	< 4	< 4
leading (far) cDPJ width	< 0.08	$< 0.10\ (0.15)$	< 0.1
cDPJ p_{T} [GeV]	> 30	-	-
JVT	< 0.6	< 0.6	< 0.6
$\min(\lvert\Delta\phi\rvert)$	$< 3\pi/5$	$< 3\pi/10$	$< 7\pi/20$
$\min(\mathrm{QCD\ tagger})$	> 0.99	> 0.91	> 0.9

Table 5.3. Definition of the signal regions used in the WH selection. In signal regions requiring at least two DPJs, only the leading and the far DPJs are considered for the event classification. Each DPJ SR is exclusive on the number of DPJs in the event. Dashes indicate the cases when the requirement is not applied.

In table 5.4 the cut flow of the event selection for the WH category is shown, considering four different signal samples. Events are normalised to $139\,\mathrm{fb}^{-1}$, taking into account the WH production cross section, where the W decays to a lepton-neutrino pair and a reference branching ratio of the Higgs decaying to dark sector particles of 10%.

Model		FRVZ	FRVZ	FRVZ	FRVZ
Process		$H \to 2\gamma_d + X$	$H \to 2\gamma_d + X$	$H \to 2\gamma_d + X$	$H \to 2\gamma_d + X$
m_{H} [GeV]		125	125	125	125
m_{γ_d} [GeV]		0.1	0.4	6	15
$c\tau_{\gamma_d}$ [mm]		15	50	6000	1000
$\sigma \times$ B [pb]		0.046	0.046	0.046	0.046
Selection	Cut				
Pre-selection	Initial	6410 ± 7	6410 ± 7	6410 ± 7	6410 ± 7
	Single Lepton Trigger	2387 ± 4	2378 ± 4	2378 ± 4	2344 ± 4
	Jet multiplicity	2286 ± 4	2294 ± 4	2268 ± 4	2230 ± 4
	B-jet Veto	2266 ± 4	2271 ± 4	2129 ± 4	2162 ± 4
	One Prompt lepton	1880 ± 4	1874 ± 4	1782 ± 4	1801 ± 4
	$m_{\mathrm{T}} > 30$ GeV	1753 ± 4	1753 ± 4	1639 ± 4	1668 ± 4
	$E_{\mathrm{T}}^{\mathrm{miss}} > 40$ GeV	1371.5 ± 3.3	1366.8 ± 3.3	1259.6 ± 3.2	1239.9 ± 3.2
WH$_c$	1 DPJ	311.7 ± 1.6	451.2 ± 1.9	322.1 ± 1.7	287.1 ± 2.6
	$m_{\mathrm{T}} > 120$ GeV	145.2 ± 1.1	215.8 ± 1.2	143.0 ± 1.3	127.8 ± 1.0
	1 cDPJ	132.7 ± 1.0	85.1 ± 0.8	101.4 ± 1.0	107.7 ± 1.0
	SR	16.9 ± 0.4	8.27 ± 0.28	7.83 ± 0.27	6.35 ± 0.24
WH$_{\mathrm{c}+\mu}$	1 μDPJ + 1 cDPJ	5.28 ± 0.21	43.6 ± 0.6	16.3 ± 0.4	6.77 ± 0.25
	SR	1.34 ± 0.11	7.83 ± 0.27	2.33 ± 0.15	0.62 ± 0.08
WH$_{2\mathrm{c}}$	2 reco hDPJ	34.7 ± 0.5	19.2 ± 0.4	26.0 ± 0.5	30.37 ± 0.35
	SR	2.98 ± 0.17	1.25 ± 0.11	1.03 ± 0.09	0.48 ± 0.06

Table 5.4. Detail of the pre-selection and the signal regions of four different WH FRVZ models, scaled to the integrated luminosity of 139 fb^{-1}, assuming a branching ratio of equal to 10%. Quoted errors are statistical only.

5.2 Background estimation

The estimation of the background in the signal regions of the analysis is performed with a data-driven technique named *ABCD method*, which is described in the following. This will be used to estimate the background due to multijet and W+jets events, in the ggF and WH categories, respectively. The non-collision backgrounds were found to affect only the ggF selection, and their treatment is presented in section 5.2.3.

5.2.1 The ABCD plane method

The method requires that the signal region (*region A*) is defined in terms of a selection on two variables, namely x and y, where three control regions can be obtained by inverting the selection on these two variables (namely regions *B*, *C* and *D*).

These two variables can either be continuous, e.g. the output score of a multivariate tagger, or discrete, like a veto on an additional number of jets in an event. The only requirement for the ABCD method to work is that the signal is contained in region A while the background is uniform in the plane defined by the four regions.

In the case of continuous variables, the number of background events in a given region (N_i, with $i = A, B, C, D$) is proportional to its area, hence if the four regions are defined by:

- A: $x_2 \leq x < x_3 \cap y_1 \leq y < y_2$,
- B: $x_2 \leq x < x_3 \cap y_2 \leq y < y_3$,
- C: $x_1 \leq x < x_2 \cap y_2 \leq y < y_3$,
- D: $x_1 \leq x < x_2 \cap y_1 \leq y < y_2$,

the number of expected background events in A is given by:

$$N_{\mathrm{A}} = \frac{N_{\mathrm{B}}\, N_{\mathrm{C}}}{N_{\mathrm{D}}} \,. \tag{5.1}$$

The same conclusion can be obtained also for a plane defined in terms of one or two discrete variables. A representation of an ABCD plane with the four regions defined as above is given in figure 5.1.

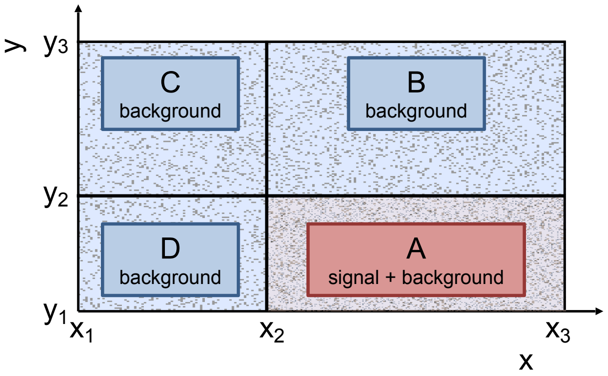

Figure 5.1. Example of the ABCD plane method, background events are distributed uniformly in the plane defined by the two variables x and y, where the signal is only contained in region A.

The presence of multiple sources of background in the plane is not an issue for the validity of the method, as long as the events from these different backgrounds yield a uniform distribution in the plane. It should be noted that the requirement of having a uniform distribution for the background is not strictly necessary for the ABCD method to work, as long as the ratios of events $N_{\mathrm{C}}/N_{\mathrm{D}}$ and $N_{\mathrm{B}}/N_{\mathrm{A}}$ are found to be equal. If this is not the case, or if a non-negligible signal leakage is observed in regions B, C and D, the method should be properly validated taking into account these effects.

In addition, event yields from a secondary background in one or more regions of the plane can be subtracted before computing the expected background for the signal region, as long as an estimate of this background is available.

This *arithmetic* approach can be extended with a likelihood-based approach, where instead of using equation 5.1 a four-bin statistical model is built, taking into account the underlying relationship between the background in the different regions. This method is more robust against control regions with small number of events and takes into account a possible small signal contamination in the control regions. The fitted likelihood describes the signal and background expectation in each region, defined by products of Poisson functions, and takes the following form:

$$\mathcal{L}(N_{\mathrm{A}}, N_{\mathrm{B}}, N_{\mathrm{C}}, N_{\mathrm{D}} | s, b, \tau_{\mathrm{B}}, \tau_{\mathrm{C}}) = \prod_{i=\mathrm{A,B,C,D}} \frac{\mathrm{e}^{-n_i} n_i^{N_i}}{N_i!} \,,$$

where N_{A}, N_{B}, N_{C}, N_{D} are the number of events observed in each region in data, τ_{B} and τ_{C} are the nuisance parameters that hold the arithmetical relation between region A and regions B, C and D. Here n_i are linear combinations of the signal and background expectation in each region, defined as follows:

$$\begin{aligned} n_{\mathrm{A}} &= s + b \\ n_{\mathrm{B}} &= s\,\varepsilon_{\mathrm{B}} + b\,\tau_{\mathrm{B}} \\ n_{\mathrm{C}} &= s\,\varepsilon_{\mathrm{C}} + b\,\tau_{\mathrm{C}} \\ n_{\mathrm{D}} &= s\,\varepsilon_{\mathrm{D}} + b\,\tau_{\mathrm{C}}\,/\,\tau_{\mathrm{B}} \end{aligned}$$

where s is the signal and b is the background yield in region A. The signal contamination in the region i is described by ε_i. All the parameter values are allowed to float in the fit to the four data regions.

In many cases a preliminary estimate of the expected number of background events can be performed using equation 5.1, but the final results of the background estimation should be extracted by the background-only fit of the aforementioned statistical model.

5.2.2 ABCD planes definition

Each SR of the analysis is defined in association with a corresponding ABCD plane, which is defined by either inverting or relaxing the cut on two variables defining the SR. Different choices of these two variables have been tested, and the following ones have been chosen, as they yield the best significance and are distributed in such a way that the ABCD method can be applied.

- $\max \sum p_{\mathrm{T}}$: Displaced DPJs are expected to be highly isolated in the ID. For the ggF analysis channels, this variable is used to define the control regions B and C, relaxing the cut up to $20\,\mathrm{GeV}$.
- $|\Delta\phi_{\mathrm{DPJ}}|$: signal DPJs are expected to be back-to-back in the transverse plane, due to the production mode in the two-body decay of a Higgs boson generated at rest. This variable is used in the definition of the $\mathrm{ggF}_{2\mu}$ ABCD plane, by inverting the cut which defines the SR.
- QCD tagger: the QCD tagger predict if the DPJ is originating from a γ_d decay and is used in the definition of all signal regions which include cDPJ. In the ggF analysis channels, the selection is made on the product of the score of all cDPJ considered and the cut defining the SR is relaxed to define regions C and D. On the other hand, in the WH analysis channels, the minimum QCD tagger score, among the cDPJ considered in the event, has been chosen as the variable defining the SR and the control regions B, C, D.

- $\min(|\Delta\phi|)$: the angular separation between DPJ and the missing transverse momentum is expected to be small for events where the WH production mode is considered. The cut on this variable, already defining the WH signal regions, is inverted in the definition of the WH ABCD planes.

More precisely, the definition of all the Control Regions (CR) B, C and D is given in table 5.5.

Requirement / Region	$\mathrm{CRB}^{\mathrm{ggF}}_{2\mu}$	$\mathrm{CRC}^{\mathrm{ggF}}_{2\mu}$	$\mathrm{CRD}^{\mathrm{ggF}}_{2\mu}$
$\lvert\Delta\phi_{\mathrm{DPJ}}\rvert$	$> \pi/5$	$(0.1, \pi/5]$	$(0.1, \pi/5]$
$\max \sum p_{\mathrm{T}}$ [GeV]	$[4.5, 20)$	$[4.5, 20)$	< 4.5
Requirement / Region	$\mathrm{CRB}^{\mathrm{ggF}}_{2\mathrm{c}}$	$\mathrm{CRC}^{\mathrm{ggF}}_{2\mathrm{c}}$	$\mathrm{CRD}^{\mathrm{ggF}}_{2\mathrm{c}}$
$\prod$ QCD tagger	> 0.95	$(0.8, 0.95]$	$(0.8, 0.95]$
$\max \sum p_{\mathrm{T}}$ [GeV]	$[4.5, 20)$	$[4.5, 20)$	< 4.5
Requirement / Region	$\mathrm{CRB}^{\mathrm{ggF}}_{\mathrm{c}+\mu}$	$\mathrm{CRC}^{\mathrm{ggF}}_{\mathrm{c}+\mu}$	$\mathrm{CRD}^{\mathrm{ggF}}_{\mathrm{c}+\mu}$
$\prod$ QCD tagger	> 0.9	$(0.75, 0.9]$	$(0.75, 0.9]$
$\max \sum p_{\mathrm{T}}$ [GeV]	$[4.5, 20)$	$[4.5, 20)$	< 4.5
Requirement / Region	$\mathrm{CRB}^{\mathrm{WH}}_{\mathrm{c}}$	$\mathrm{CRC}^{\mathrm{WH}}_{\mathrm{c}}$	$\mathrm{CRD}^{\mathrm{WH}}_{\mathrm{c}}$
$\min(\lvert\Delta\phi\rvert)$	$< 3\pi/5$	$> 3\pi/5$	$> 3\pi/5$
$\min(\text{QCD tagger})$	$[0.9, 0.99)$	$[0.9, 0.99)$	> 0.99
Requirement / Region	$\mathrm{CRB}^{\mathrm{WH}}_{2\mathrm{c}}$	$\mathrm{CRC}^{\mathrm{WH}}_{2\mathrm{c}}$	$\mathrm{CRD}^{\mathrm{WH}}_{2\mathrm{c}}$
$\min(\lvert\Delta\phi\rvert)$	$< 3\pi/10$	$> 3\pi/10$	$> 3\pi/10$
$\min(\text{QCD tagger})$	$[0.8, 0.91)$	$[0.8, 0.91)$	> 0.91
Requirement / Region	$\mathrm{CRB}^{\mathrm{WH}}_{\mathrm{c}+\mu}$	$\mathrm{CRC}^{\mathrm{WH}}_{\mathrm{c}+\mu}$	$\mathrm{CRD}^{\mathrm{WH}}_{\mathrm{c}+\mu}$
$\min(\lvert\Delta\phi\rvert)$	$< 7\pi/20$	$> 7\pi/20$	$> 7\pi/20$
$\min(\text{QCD tagger})$	$[0.8, 0.9)$	$[0.8, 0.9)$	> 0.9

Table 5.5. Definition of the control regions B, C and D used in the background estimation. All CR requirements are the same as the respective SR, with the exception of the selections reported in this table.

The distributions of signal events in the six ABCD planes are reported in figure 5.2, together with a schematic identifying the SR and CRs. Details on the signal yields in the ABCD planes are given, in tables 5.6 and 5.7 for different signal samples, respectively showing the number of signal events for the ggF and WH analysis channels. Although the majority of the events are found in the SR, a non-negligible contamination appears also in some of the CRs. This is not considered as an issue, due to the fact that in all cases the background expectation in these regions is much larger than the expected signal leakage.

For the ggF Signal Regions, the ABCD method needs to take into account potential effects due to the presence of non-collision background. In particular, the BIB background is reduced to a negligible level, while the cosmic-ray background

Model		FRVZ	FRVZ	FRVZ	HAHM
Process		$H \to 2\gamma_d + X$	$H \to 2\gamma_d + X$	$H \to 2\gamma_d + X$	$H \to 2\gamma_d$
m_{H} [GeV]		125	125	800	125
m_{γ_d} [GeV]		0.1	0.4	0.4	0.4
$c\tau_{\gamma_d}$ [mm]		15	50	10	25
$\sigma \times$ B [pb]		4.86	4.86	5	4.86
Selection	Region				
$\mathrm{ggF}_{2\mu}$	A	7.2 ± 3.5	5000 ± 90	7960 ± 180	10830 ± 160
	B	–	126 ± 15	207 ± 29	292 ± 28
	C	–	1.8 ± 1.8	–	5 ± 4
	D	–	91 ± 12	30 ± 11	203 ± 23
$\mathrm{ggF}_{\mathrm{c}+\mu}$	A	92 ± 13	1040 ± 40	5430 ± 150	5970 ± 120
	B	1.7 ± 1.7	77 ± 11	350 ± 40	395 ± 32
	C	3.6 ± 2.5	10 ± 4	42 ± 13	36 ± 9
	D	10 ± 4	95 ± 13	320 ± 40	407 ± 30
$\mathrm{ggF}_{2\mathrm{c}}$	A	282 ± 23	102 ± 13	1460 ± 80	850 ± 50
	B	–	3.8 ± 2.7	86 ± 18	31 ± 8
	C	1.7 ± 1.7	–	19 ± 9	1.8 ± 1.8
	D	113 ± 15	29 ± 8	182 ± 26	123 ± 16

Table 5.6. Signal event yields in the ABCD planes of the three different ggF channels, for different signal samples using both the FRVZ and the HAHM model. Events are normalised to the integrated luminosity of $139\,\mathrm{fb}^{-1}$ and the quoted errors are statistical only. For each channel, region A corresponds to the signal region and its number of events is reported from table 5.2. Cells denoted with a dash correspond to zero predicted events with the available MC statistics.

Model		FRVZ	FRVZ	FRVZ	FRVZ
Process		$H \to 2\gamma_d + X$	$H \to 2\gamma_d + X$	$H \to 2\gamma_d + X$	$H \to 2\gamma_d + X$
m_{H} [GeV]		125	125	125	125
m_{γ_d} [GeV]		0.1	0.4	6	15
$c\tau_{\gamma_d}$ [mm]		15	50	6000	1000
$\sigma \times$ B [pb]		0.046	0.046	0.046	0.046
Selection	Region				
WH_c	A	16.94 ± 0.39	8.27 ± 0.28	7.83 ± 0.27	6.35 ± 0.24
	B	12.03 ± 0.33	6.53 ± 0.25	8.17 ± 0.27	6.20 ± 0.25
	C	8.09 ± 0.27	3.77 ± 0.18	4.36 ± 0.20	2.04 ± 0.14
	D	7.86 ± 0.27	3.53 ± 0.18	3.33 ± 0.17	1.83 ± 0.13
$\mathrm{WH}_{\mathrm{c}+\mu}$	A	2.98 ± 0.17	1.25 ± 0.11	1.03 ± 0.09	0.48 ± 0.06
	B	0.78 ± 0.09	0.25 ± 0.05	0.34 ± 0.05	0.22 ± 0.04
	C	0.43 ± 0.06	0.30 ± 0.05	0.22 ± 0.04	0.44 ± 0.08
	D	2.44 ± 0.15	0.91 ± 0.09	1.18 ± 0.10	0.97 ± 0.10
$\mathrm{WH}_{2\mathrm{c}}$	A	1.34 ± 0.11	7.83 ± 0.27	2.33 ± 0.15	0.62 ± 0.08
	B	0.12 ± 0.03	0.54 ± 0.08	0.27 ± 0.05	0.07 ± 0.03
	C	0.01 ± 0.01	0.22 ± 0.04	0.10 ± 0.03	0.02 ± 0.01
	D	0.39 ± 0.07	3.06 ± 0.17	1.23 ± 0.11	0.49 ± 0.07

Table 5.7. Signal event yields in the ABCD planes of the three WH analysis channels, shown for different WH FRVZ models. The total number of events is normalised to the integrated luminosity of $139\,\mathrm{fb}^{-1}$ and the quoted errors are statistical only. Events in signal region A are reported from table 5.4.

is subtracted from the final ABCD plane. The next section will focus on how these additional backgrounds are treated.

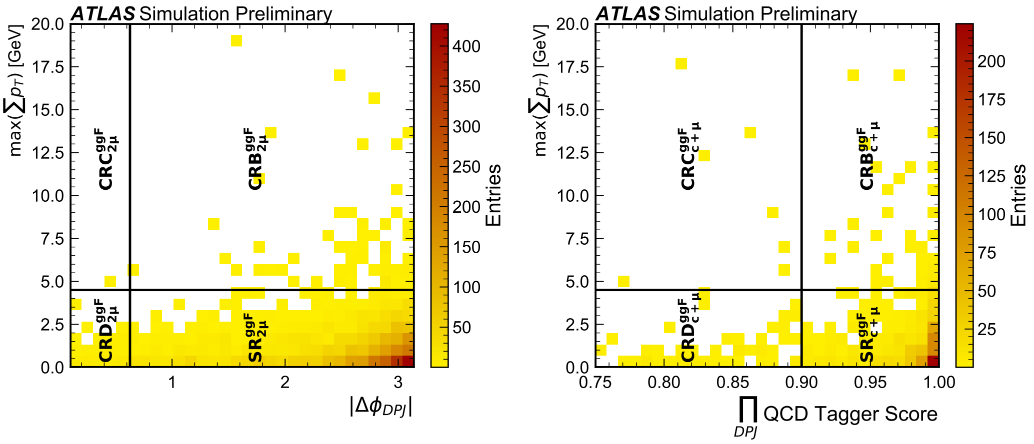

(a) ggF$_{2\mu}$ **(b)** ggF$_{c+\mu}$

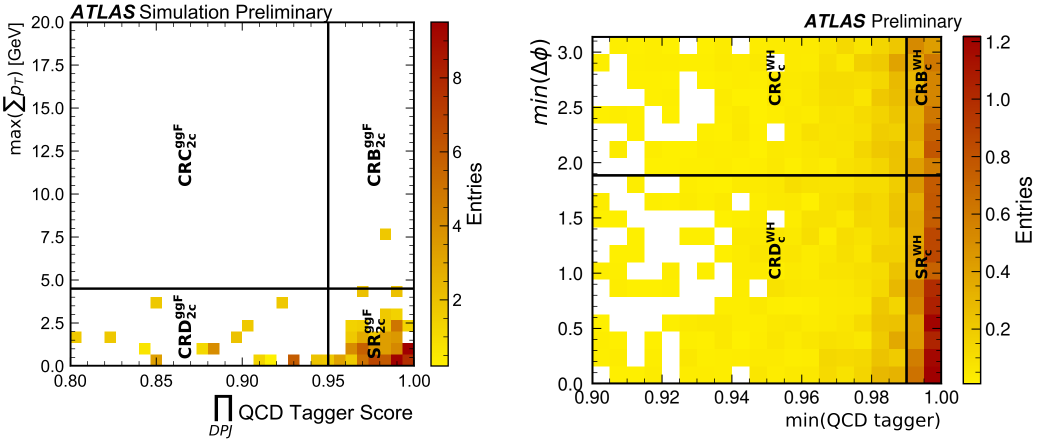

(c) ggF$_{2c}$ **(d)** WH$_c$

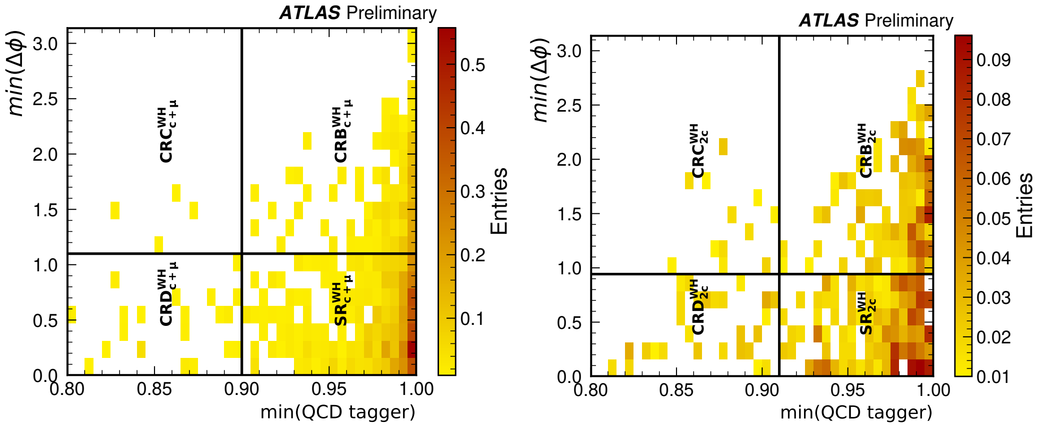

(e) WH$_{c+\mu}$ **(f)** WH$_{2c}$

Figure 5.2. The per-event distributions in the ABCD planes, defined for the six different search channels. Figures (a, b, c) show the distribution for signal samples with the ggF production of a SM Higgs boson. Figures (d, e ,f) show instead the event distribution of WH signal samples. In all cases samples with a SM Higgs boson, decaying in 2 γ_d + X are considered, while m_{γ_d} is set to 0.4 GeV for figures (a, b, c, e) and to 0.1 GeV for figures (d, f). Figures adapted from [1].

5.2.3 Non-collision background contamination in the ggF Signal Regions

Beam-Induced Background

The possibility of reconstructing BIB muons as cDPJ has been already discussed in chapter 4. The study of the BIB contamination in this analysis is performed with regard to the $\mathrm{ggF_{2c}}$ channel, which is the one where the events are collected by the CalRatio trigger and where the BIB contamination is concerning.

For this study, the following two datasets have been collected in Run-II data:

- **BIB-enhanced selection:** obtained by processing the $\mathrm{ggF_{2c}}$ analysis channel on events collected requiring the inclusive version of the CalRatio trigger and vetoing the standard one, as done in section 4.2.2. Since this sample is collected in colliding BCs and 2 cDPJ are requested, the presence of collision products (and therefore cDPJs from QCD processes) is also expected.
- **Unpaired-BC BIB selection:** obtained by processing the $\mathrm{ggF_{2c}}$ analysis channel when requiring the standard CalRatio trigger in unpaired isolated bunch crossings. Since events are selected in non-colliding bunch crossings, no requirement on PV has been made when producing this dataset.

Of all the different cuts applied in the $\mathrm{ggF_{2c}}$ channel, the ones relying on cDPJ timing, the one on $|\Delta\phi_{\mathrm{DPJ}}|$ and, of course, the one on the BIB tagger score, are helpful in rejecting BIB. In figure 5.3a the $|\Delta\phi_{\mathrm{DPJ}}|$ distribution is shown, for events from the BIB-enhanced selection and from a FRVZ benchmark sample, where it is clear that the cut on this variable helps in reducing the BIB background. On the other hand, the BIB tagger cut is optimised (see figure 5.3b) to get a signal acceptance above 0.8 while reducing the events in the BIB-enhanced dataset as much as possible. As the BIB-enhanced dataset is obtained essentially by triggering on the BIB removal flag of the CalRatio trigger, the selection is very rich in BIB and has to be thought as more contaminated by this background, with respect to the main analysis selection running on Run-II data. In addition, the effect of the selection on BIB is visible from the 2D distribution of the cDPJ η and timing, shown in figure 5.4, including both the leading and far cDPJ in the BIB-enhanced dataset, where it becomes evident that features related to BIB disappear once the cuts addressing this background are applied.

As an additional cross-check, the Unpaired-BC BIB dataset have been used as input of the $\mathrm{ggF_{2c}}$ selection. In unpaired bunch crossings, as no collisions are expected, the CalRatio trigger can easily trigger the signature left by a BIB muon; although the few events passing the trigger requirement are selected thanks to the inefficiencies of the BIB removal flag included in the HLT algorithm of the trigger, and the full selection on this dataset yields 0 events in the ABCD plane.

In conclusion, the BIB background is considered negligible once all the cuts of the analysis are applied and, as it will be shown in section 5.2.5, no anomalies in the ABCD plane are seen, indicating that if a BIB contamination is present in the plane, this will be distributed exactly as the multijet background, without affecting the background estimation.

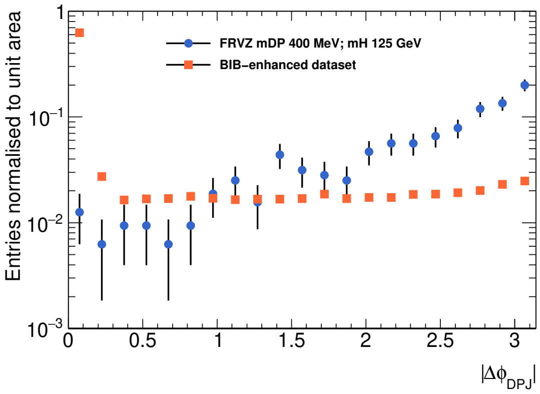

(a)

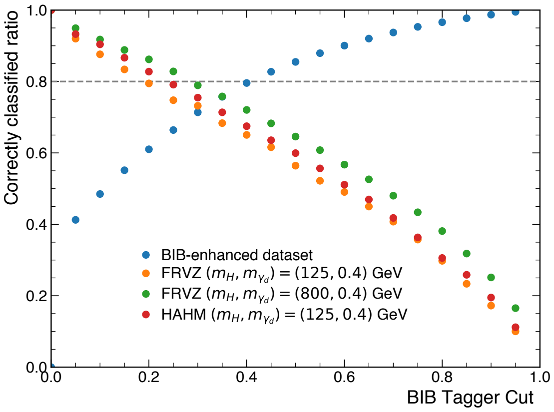

(b)

Figure 5.3. Normalised distributions of the $|\Delta\phi_{\mathrm{DPJ}}|$ (a) and of the efficiency of a cut on the BIB Tagger score (b), shown for events in the BIB-enhanced dataset and different signal samples.

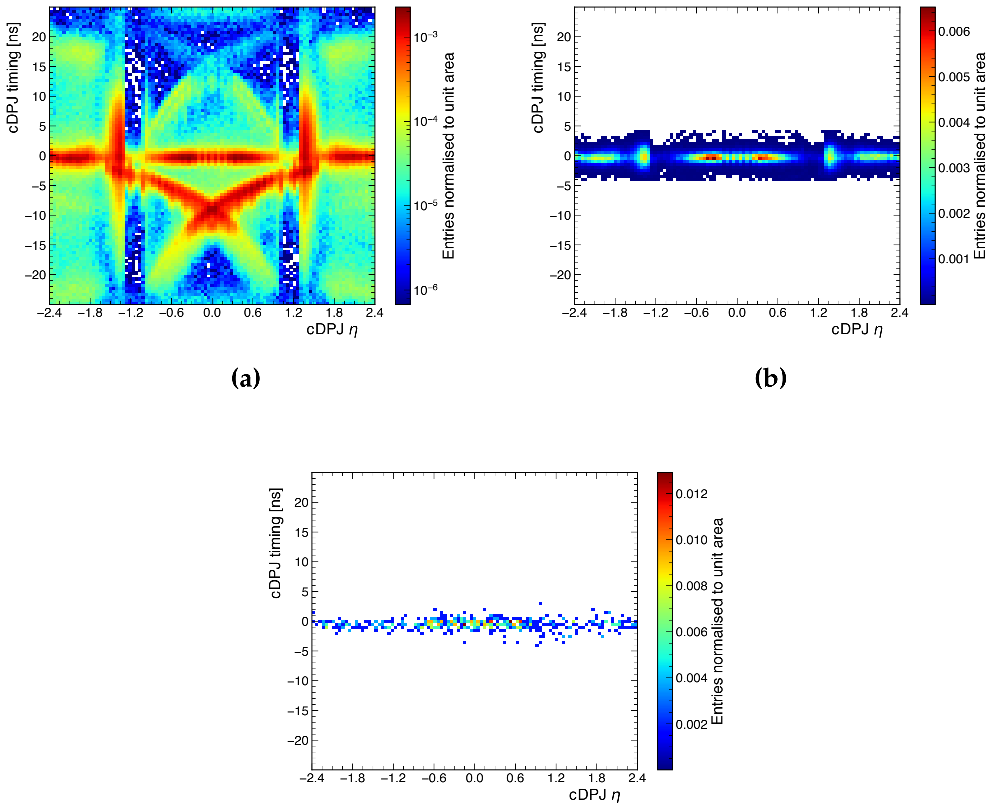

(a) **(b)**

(c)

Figure 5.4. cDPJs timing vs η distributions in the BIB-enhanced sample. (a) shows events entering the ggF$_{2c}$ channel, while Figure (b) shows the events after the timing and BIB tagger cuts. Events entering the ABCD plane are visible in (c), for which no pattern originating from BIB is observed.

Cosmic-ray background estimation

The cosmic-ray background is estimated from events entering the ggF selections when the analysis triggers are running on empty bunch crossings.

As mentioned in section 3.2, the three triggers used for the ggF selections are active without prescale on empty bunch crossings and are used to build a dataset enhanced in cosmic-rays. Apart of the different trigger condition, the same event selection is applied, except that the requirement of the PV is relaxed, given the expected lower activity in the ID for such events.

Under these conditions, a small number of events contributes to the SRs and the CRs and is subtracted from the ABCD planes computed when running on the Run-II dataset.

In order to take into account the fact that, during LHC runs, there are very few empty bunch crossings with respect to paired ones, a multiplicative weight is taken into account for such events. More precisely, the ratio of the number of filled to empty bunch crossings is used to scale the number of events to the expected one in pp collisions. These scale factors are computed separately for events selected by the Tri-muon MS-only and the CalRatio trigger, as no event was entering the signal regions when selected by the Narrow-Scan trigger in empty bunch crossings. The number of observed events, in the ggF signal regions, when running on empty bunch crossings is shown in table 5.9, where the correction factors obtained by table 5.8 are applied. A small number of events is observed and all contributions are in regions A and D of the ABCD planes, since in empty bunch crossings, a very low Inner Detector activity is expected, giving $\max \sum p_{\mathrm{T}} \sim 0$ for all these events.

	2015-2016	2017	2018
Tri-muon MS-only	2.60	3.03	3.92
CalRatio	2.20	2.20	3.06

Table 5.8. Scale factors for the triggers used in empty bunch crossings for different data-taking years.

	2015-2018 empty bunch crossing			
	A	B	C	D
ggF$_{2\mu}$	7 ± 5	-	-	-
ggF$_{c+\mu}$	-	-	-	-
ggF$_{2c}$	7 ± 4	-	-	14 ± 7

Table 5.9. Observed yields in the ggF signal regions, when running on empty bunch crossings, corrected with the correction factors of table 5.8. The dash indicates that no event was found in the corresponding region.

5.2.4 Validation of the ABCD method

Once the contamination from BIB is found to be negligible and the cosmic-ray contribution is estimated for subtraction, the full Run-II dataset is processed with the event selection. To avoid any bias in this search, which could arise from observing the number of events in the signal region, the event selection is initially processed by *blinding*[2] the SR before the approach for the background estimation is validated.

The ABCD method has to be considered valid, if the two variables chosen to define the plane are such that the relation imposed by equation 5.1 holds. To validate this approach, without *unblinding* the signal region, firstly a second A'B'C'D' plane is identified within the area of the control regions B, C and D; then, this second plane is divided in four regions where the ABCD ansatz is tested.

This approach has been applied to each ggF and WH analysis channel, identifying multiple sub-regions of their ABCD planes where equation 5.1 was found to predict the correct number of events. As an example, figures 5.5 and 5.6 show three possible subdivisions, where the closure tests of the ABCD planes of the ggF and WH analysis are performed. Taking as a reference figure 5.5a, the control regions B and C are divided in BC1, BC2, BC3 and BC4, by two boundaries at $|\Delta\phi_{\mathrm{DPJ}}| = \pi/5$ and $\max\sum p_{\mathrm{T}} = 6.8$; these boundaries are then moved to different values of $\max\sum p_{\mathrm{T}}$, where for each case the number of expected events in region BC1 is found to be in agreement, within the error, to the corresponding observed number of events, as shown in figure 5.5d.

The linear correlation factor between the variables defining the ABCD plane has been extracted from events in these sub-regions and is found to be less than 3% for the ggF channels and less than 2% for the WH ones.

---

[2] In the particle physics jargon, *blind* analysis means that the events falling in the SR are neither processed nor counted, to avoid biasing the selection.

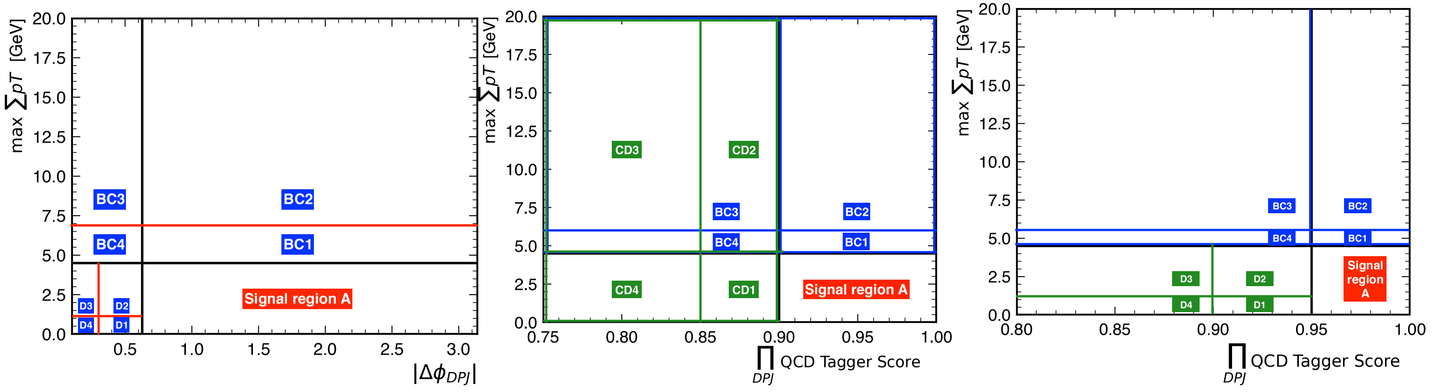

(a) $\mathrm{ggF}_{2\mu}$ **(b)** $\mathrm{ggF}_{c+\mu}$ **(c)** ggF_{2c}

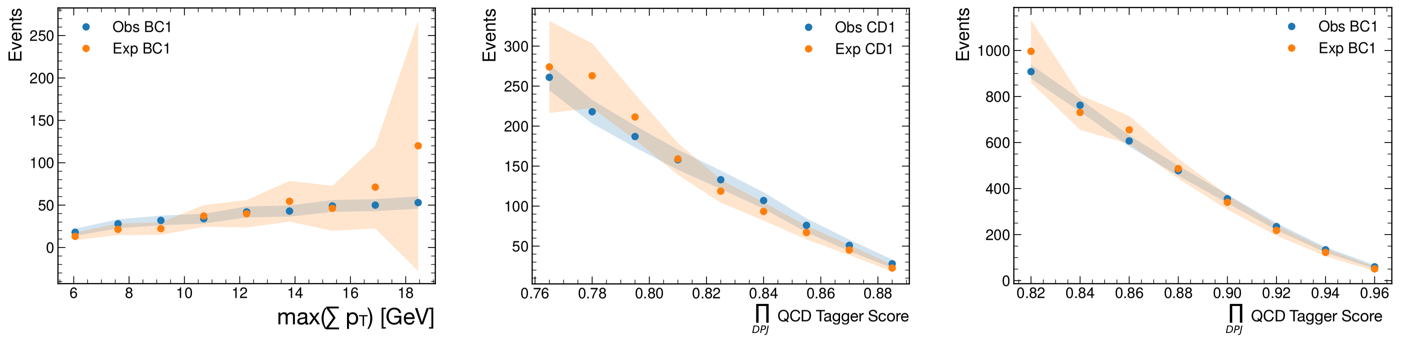

(d) $\mathrm{ggF}_{2\mu}$ **(e)** $\mathrm{ggF}_{c+\mu}$ **(f)** ggF_{2c}

Figure 5.5. In (a, b, c) a schema of possible subdivisions of control regions B, C and D is shown. In (d, e, f) a test of the ABCD ansatz is reported, for different values of the boundary that divides the sub-regions of figure (a, b, c). In figures (d, e, f) the expected number of events in each sub-region obtained from the ABCD method, together with the propagated errors according to equation 5.1, is shown by the red band, while the blue band show the corresponding number of observed events, together with its statistical error.

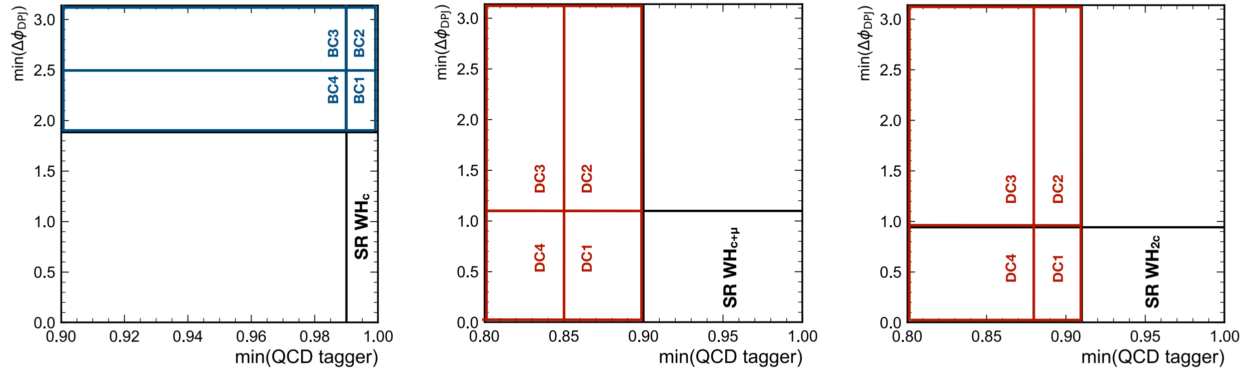

(a) WH$_c$ **(b)** WH$_{c+\mu}$ **(c)** WH$_{2c}$

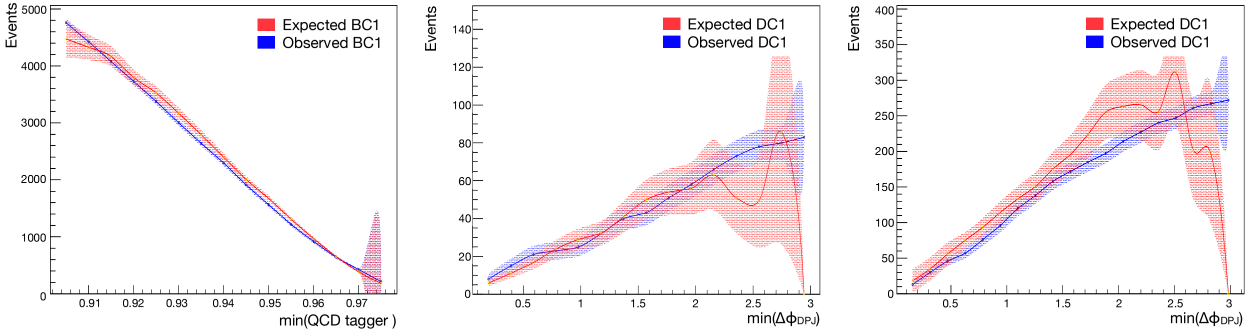

(d) WH$_c$ **(e)** WH$_{c+\mu}$ **(f)** WH$_{2c}$

Figure 5.6. In (a, b, c) a schema of possible subdivisions of control regions B, C and D is shown. In (d, e, f) a test of the ABCD ansatz is reported, for different values of the boundary that divides the sub-regions of figure (a, b, c). In figures (d, e, f) the expected number of events in each sub-region obtained from the ABCD method, together with the propagated errors according to equation 5.1, is shown by the red band, while the blue band show the corresponding number of observed events, together with its statistical error.

5.2.5 Unblinded results

Once the selection is finalised and the background estimation strategy is defined, the signal regions are finally unblinded. In the following, the number of events in each SR and CR, when running on the full Run-II dataset are shown, together with the estimate of the number of background events in each signal region. The expected number of events in the SR is shown either pre-fit and after running the ABCD fit in unblinded data assuming no signal, where the estimated contributions from cosmic-ray muons are subtracted before the fit and added back post-fit. The largest deviation between pre-fit and post-fit expected results is found to be within one standard deviation. The unblinded ABCD planes of all the ggF and WH channels are shown in figure 5.7.

Selection	Search channel	CR B	CR C	CR D	SR (A) expected pre-fit	SR (A) expected post-fit	SR (A) observed
ggF	2μ	55	61	389	357 ± 79	317 ± 47	269
	c+μ	169	471	301	108 ± 15	108 ± 13	110
	2c	97	1113	12146	1070 ± 200	1060 ± 80	1045
WH	c	1850	3011	155	95 ± 7	93 ± 12	103
	c+μ	30	49	31	19 ± 5	19 ± 8	20
	2c	79	155	27	14 ± 3	14 ± 5	15

Table 5.10. Observed and expected yields in the ABCD regions. The total uncertainty in the background expectations is given. In the ggF selection regions, the estimated contribution from cosmic-ray yields is subtracted from each of the ABCD regions before the ABCD method estimation of the multijet background.

Post-unblinding cross-check on BIB contamination

Additional cross-checks have been performed, on the unblinded ggF$_{2c}$ signal region, to support the fact that the BIB background is negligible. Considering all the events entering the ggF$_{2c}$ selection on Run-II data, the ϕ distribution shows a clear BIB contamination which disappears when looking at the events entering the SR, visible from figure 5.8. Here the two cuts defining the signal region A, namely $\prod$ QCD Tagger > 0.95 and $\max \sum p_{\mathrm{T}} < 4.5\,\mathrm{GeV}$, are always applied, clearly showing that without the analysis cuts the signal region would be otherwise rich in BIB.

As a final validation, the signal region A of the ggF$_{2c}$ selection has been divided in four sub-regions (A_i, where $i = 1, 2, 3, 4$) and the same method used in section 5.2.4, of changing the boundaries of the four sub-regions and testing the ABCD ansatz, has been adopted. The result is shown for different values of $\max \sum p_{\mathrm{T}}$ and $\prod \mathrm{QCD\ tagger}$, in figure 5.9, from which is clearly visible that the expected and observed number of events in the sub-region A_i are always compatible within the uncertainty. These two additional arguments are telling that the BIB background is efficiently suppressed by the selection applied.

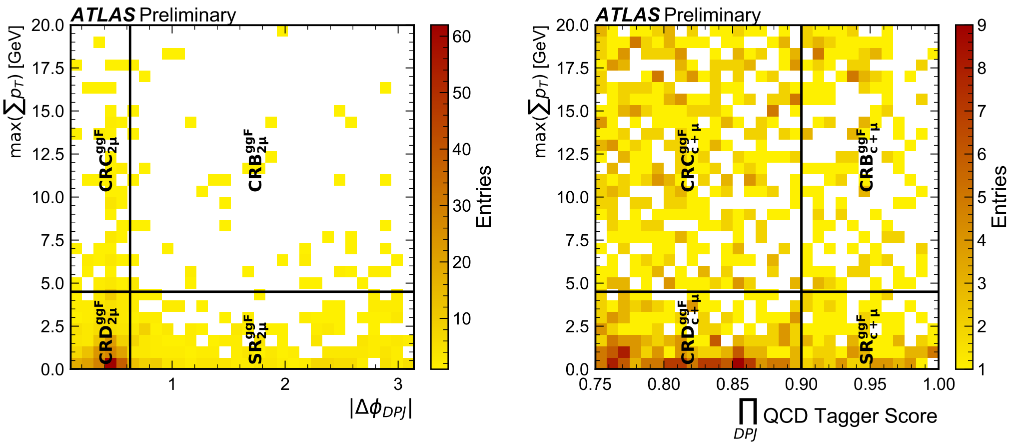

(a) ggF$_{2\mu}$

(b) ggF$_{c+\mu}$

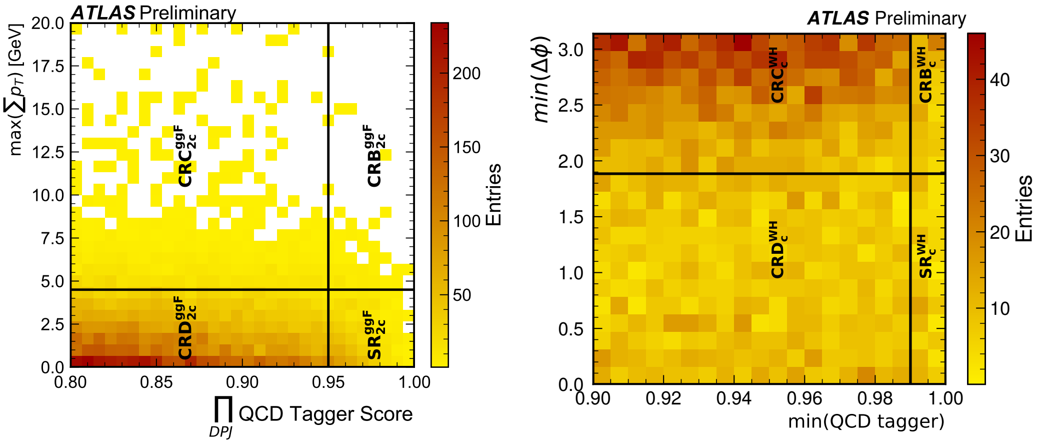

(c) ggF$_{2c}$

(d) WH$_{c}$

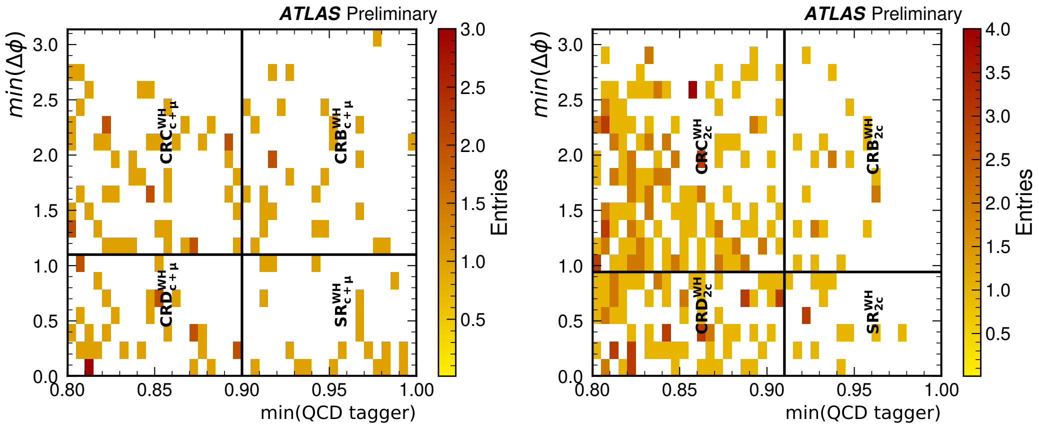

(e) WH$_{c+\mu}$

(f) WH$_{2c}$

Figure 5.7. The per-event distributions in the ABCD planes, defined for the six different search channels, shown for 139 fb^{-1} of Run-II data collected by ATLAS. Figures (a, b, c) show the distribution for the ggF analysis channels, while figures (d, e ,f) show instead the event distribution of WH channels. Figures adapted from [1].

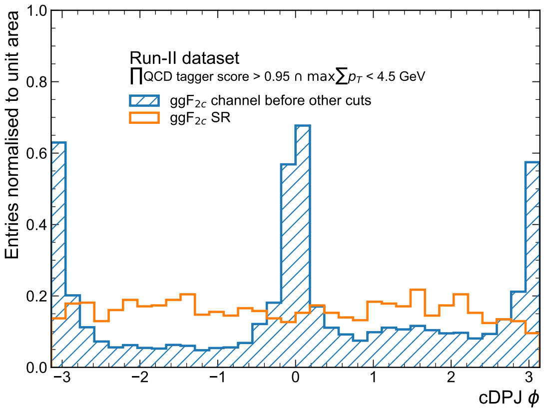

Figure 5.8. Normalised distributions of the azimuthal angle of the cDPJ identified in the main Run-II analysis dataset, for events entering the ggF$_{2c}$ channel, before any timing cut or the BIB tagger cut are applied (hatched blue) and the ones entering the corresponding SR (orange). Only events where $\prod$ QCD Tagger > 0.95 and $\max \sum p_{\mathrm{T}} < 4.5\,\mathrm{GeV}$ are selected in this plot, to show how BIB are potentially affecting the SR, but are removed by the event selection.

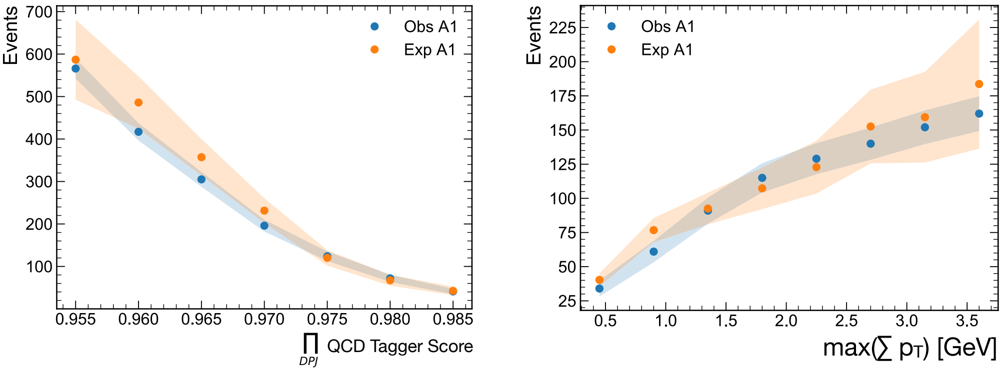

(a) **(b)**

Figure 5.9. Post-unblinding test of the ABCD method performed in the signal region of the ggF$_{2c}$ selection. The area of the signal region has been divided in four sub-regions, where the ABCD ansatz is tested for different choice of the boundaries in the two variables $\max \sum p_{\mathrm{T}}$ and $\prod \mathrm{QCD\ tagger}$. In all cases a good agreement is observed between the expected and observed number of events. This supports the fact that the BIB background is negligible after the event selection.

5.3 Systematic uncertainties

In this section, different sources of uncertainties in the final yields are considered and estimated, for both the background estimates and the Monte Carlo signal yields.

As the background estimation is entirely data-driven, the only corresponding source of uncertainty is the one obtained from the ABCD method, propagating the statistical uncertainties of the observed yields in regions B, C and D. The uncertainties reported in table 5.7 were obtained considering also, when available, eventual cosmic-ray contributions. The statistical uncertainty related to the estimate of this secondary background is potentially large, up to 80% of the expected contribution. Nevertheless, the negligible contribution of the cosmic-ray background yields a negligible effect on the overall background uncertainty.

Additional sources of uncertainties, affecting only the signal event yields, are treated in the following. These arise from differences between data and simulation, observed in the reconstruction of physical objects or in the pileup modelling. A summary of the experimental uncertainties that are associated to the signal yields is reported afterwards.

Normalisation uncertainties

A minor source of uncertainty is associated to the estimate of the integrated luminosity of the Run-II dataset, which is used for the normalisation of Monte Carlo events. The measurement of the luminosity in ATLAS is performed by multiple subsystems of the detector, as well from the LUCID-2 detector, which is described in [82]. The overall estimate of the uncertainty on the luminosity measurement is of 1.7% as documented in [83].

A second uncertainty that affects normalisation is associated to the pileup reweighting of simulated events. Indeed, the generated MC events are reweighted such that the distribution of the average number of interactions per bunch crossing matches the one measured in data. This operation is performed by weighting the generated pileup profile of MC events and by applying a scale factor to take into account possible differences in data and MC. By varying this scale factor within the corresponding uncertainty, the resulting difference in signal yields is taken as systematic uncertainty.

Close-by muon reconstruction

An experimental systematic uncertainty, on the reconstruction of close-by muons using only information from the MS, is evaluated using a tag-and-probe method applied on $J/\psi \to \mu\mu$ data and Monte Carlo events. Simulated $J/\psi \to \mu\mu$ events are generated using PYTHIA8+PHOTOS++ [84], with the A14 tune for parton showering and hadronisation and the CTEQ6L1 [85, 86] set of parton distribution functions.

This uncertainty is associated to the muonic DPJ reconstruction efficiency, motivating the use of J/ψ decay processes, as they show similar topology and kinematics as the expected signal muons originating from a γ_d decay.

The reconstruction efficiencies of two close-by muons originated by $J/\psi \to \mu\mu$ decays in MC and in the full Run-II dataset are shown, in figure 5.10, as functions of the opening angle ΔR between the two Stand-Alone muons. As expected, the reconstruction efficiency is smaller at very low ΔR values, while it becomes close to unity as soon as the two MS tracks are well separated. The discrepancy between data and MC is found to follow the same trend; being largest in the $0.02 < \Delta R < 0.08$ bin, where the largest contribution from the signal sample is expected. This discrepancy is found to be of 9.6% and is taken conservatively as a systematic uncertainty.

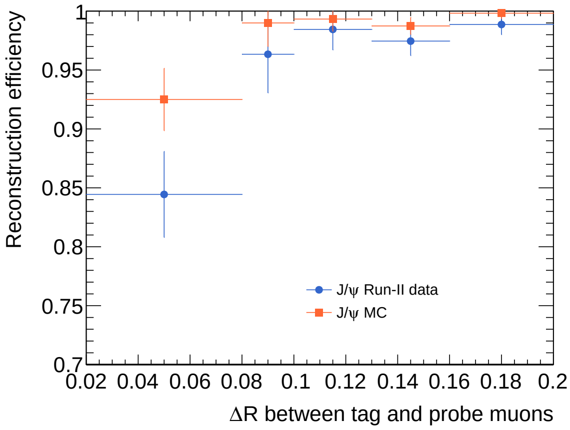

Figure 5.10. Reconstruction efficiency of close-by muons, associated to the reconstruction of single μDPJ, evaluated using the tag-and-probe method as a function of the angular aperture between the decay muons of J/ψ for data and MC samples.

Uncertainties on trigger efficiencies

The uncertainties associated to the HLT algorithms used in the identification of LLP decays at the trigger level have been studied and are presented in the following.

The uncertainties relative to the Narrow-Scan trigger and the Tri-muon MS-only trigger were computed in [2] and have been re-used, as the HLT algorithm has not changed since. The efficiencies of the aforementioned triggers have been checked for different pileup levels and are found to be compatible within the statistical uncertainty. The same approach that was used for the computation of the close-by muon reconstruction uncertainty, using $J/\psi \to \mu\mu$ events, was used also in this case to evaluate the difference in data and MC events for close-by muons. The result yielded an uncertainty of 6% for the Narrow-Scan and 5.8% for the Tri-muon MS-only.

On the other hand, in order to evaluate the uncertainty on the efficiency of the HLT algorithm of the CalRatio trigger, a different method has been adopted. As mentioned in section 3.2.2, the HLT algorithm select jets with $E_T > 30\,\text{GeV}$, $f_{\text{EM}} < 0.06$ and no ID track with $p_T > 2\,\text{GeV}$ within a $\Delta R = 0.2$ from the jet axis. The modelling of these three variables was studied in [87], where scale factors from data and MC events were obtained. Here the same set of scale factors has been applied to signal events, using an emulation of the trigger HLT algorithm.

The emulated trigger applies the same cuts implemented at the HLT and, in signal MC events, it was found to be in agreement with the HLT in more than 95% of the cases. By applying the aforementioned scale factors to the emulated trigger candidates, a different decision can be produced and the overall difference in the signal yield, with respect to the nominal trigger, has been considered as a systematic uncertainty.

This uncertainty was found to be the dominant one for the $\mathrm{ggF}_{2\mathrm{c}}$ channel, which is the only one using this trigger, where its estimated value ranges between 15% and 26%. The largest values are found in FRVZ signal models where the production from the SM Higgs is considered, corresponding to the signal points for which this trigger is less efficient.

Jet uncertainties

Experimental uncertainties are normally associated to the reconstruction and energy calibration of all jets reconstructed in ATLAS. The algorithms involved in this step have an associated set of nuisance parameters, of which the variation of one standard deviation is considered and propagated to the signal yields. The difference of the expected number of signal events, with respect to the nominal case, is evaluated for each nuisance parameter variation, taking the largest as systematic uncertainty.

Moreover, as jets identified as calorimeter DPJ are required to have a low f_{EM} and are normally selected with looser working points on the jet cleaning, an additional uncertainty on the jet energy scale is taken into account. This uncertainty is derived by comparing the jet momentum, as a function of the jet pseudorapidity and f_{EM}, in data and MC dijet event, which is then used to scale the events in signal MC samples, taking the yield difference in the signal region as a systematic uncertainty. This was evaluated to have an effect of around 3% across multiple signal samples.

Uncertainties associated to the neural network taggers

Another experimental uncertainty is associated to the neural network taggers, originated by their potential different response on real and simulated events.

The same strategy is adopted for the three taggers. Initially a binned data/MC ratio of the output score is produced by classifying object in a reference sample, then the values of this ratio are used as scale factors in signal Monte Carlo events, obtaining a set of per-event weights. The difference in the signal yields, after these weights are applied, with respect to the nominal case, is taken as a systematic uncertainty for each tagger.

The cosmic-ray tagger aims to discriminate Stand-Alone MS tracks, originating from object produced in the IP, from the ones due to cosmic-ray muons. Hence, the scale factors on this tagger output score are extracted from a reference sample of

$Z \rightarrow \mu\mu$ events, which are expected to yield signal-like MS tracks. The following selection cuts are applied to identify these events:

- Events are required to be fired by the logical OR of the single muon triggers described in Sections 3.2.3;
- Two opposite charge, combined, medium isolated muons are required. In addition, each muon must satisfy the following cuts:
  1. $p_{\mathrm{T}} > 30\,\mathrm{GeV}$
  2. $|\eta| < \ 2.4$
  3. $|\frac{\sigma_{d_0}}{d_0}| < 3.0$
  4. $|\Delta z_0 \sin(\theta)| < 0.5\,\mathrm{mm}$
- Finally, the invariant mass of the two muons, $m_{\mu\mu}$ must be within $81\,\mathrm{GeV} < m_{\mu\mu} < 101\,\mathrm{GeV}$;

By evaluating the tagger on Stand-Alone MS tracks from both muons, in data and MC events, the distribution in figure 5.11a is obtained. The ratio between data and Monte Carlo events is propagated to signal events and the final difference in the yields is taken as the systematic uncertainty. Among the different signal samples considered, this uncertainty is found to be smaller than 5%.

The same procedure is applied to the BIB tagger and QCD tagger score. To select a sample rich in cDPJ in both data and MC the best choice possible is a dataset of low-f_{EM} dijet events. To build this dataset the events have been selected with the following requirements:

- Events must be accepted by a single-jet trigger with an $E_{\mathrm{T}} > 60\,\mathrm{GeV}$ threshold, vetoing all analysis triggers.
- Two cDPJ must be reconstructed in the event, which need to satisfy the following requirements:
  1. At least one cDPJ must have a p_{T} larger than $60\,\mathrm{GeV}$;
  2. The p_{T}-imbalance between the two jets, defined as the ratio of their p_{T} difference and sum, must be smaller than 0.3.

As done for the cosmic-ray tagger, the binned ratio of the data and MC distribution of the QCD tagger and BIB tagger score, respectively shown in figures 5.11b and 5.11c, is propagated to signal events and the differences in the final yields are taken as a systematic uncertainties. This method gives, for different signal samples, an uncertainty on the response of the QCD tagger ranging from 2% to 11%, while for the BIB tagger the uncertainty is estimated to be between 3% and 13.7%.

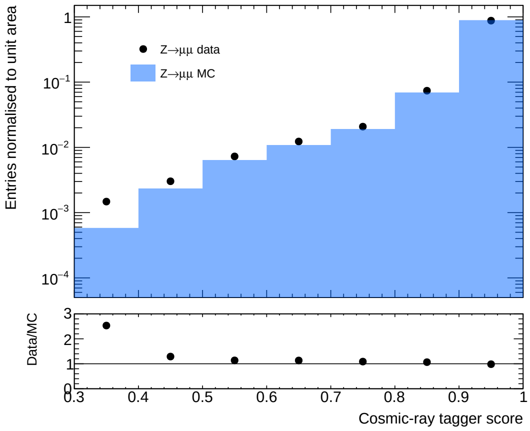

(a) Cosmic-ray tagger data/MC comparison.

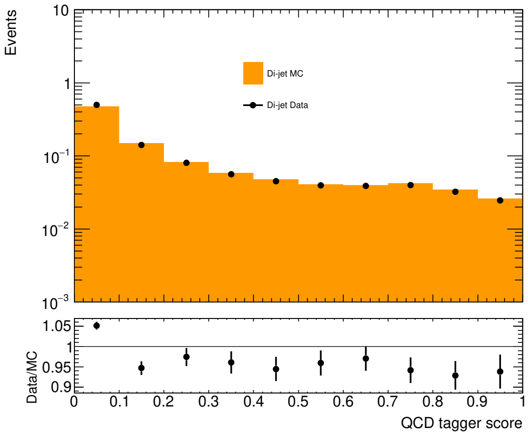

(b) QCD tagger data/MC comparison.

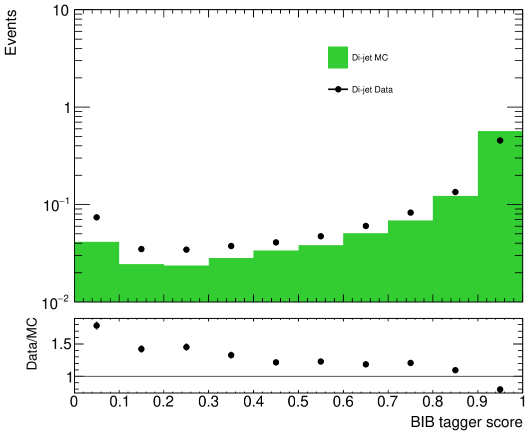

(c) BIB tagger data/MC comparison.

Figure 5.11. Distribution of the output score of the three neural-network-based taggers used in the analysis, computed for data and Monte Carlo events in different reference samples. (a) show the cosmic-ray tagger score for $Z \to \mu\mu$ events; (b) and (c) show the QCD tagger and BIB tagger score distribution for dijet events.

Summary

To give a more detailed overview on the scale of the experimental systematic uncertainties, the different contributions in each signal region are reported in the following, averaged across multiple signal samples.

For the signal samples where the FRVZ $H \to 2\gamma_d + X$ process is simulated, an overview of the systematic uncertainties affecting each ggF and WH signal region is reported in figure 5.12. Similar comparisons, related to the other signal processes are reported in the following.

With reference to the figures in this section, *Muon uncertainties* correspond to the close-by muon reconstruction uncertainty that is affecting the signal regions where μDPJ are present; *Normalisation uncertainties* report the ones associated to the luminosity and pileup; *NN taggers* gives an overview of the contributions associated to the Cosmic-ray tagger, the QCD tagger and the BIB tagger, the latter giving the largest contribution. Finally, *Triggers* show the contribution of the Narrow-Scan, CalRatio and Tri-muon triggers and *Jet uncertainties* refer to the ones associated to the jet energy scale and resolution, as well as the JES computed for low-f_{EM} jets.

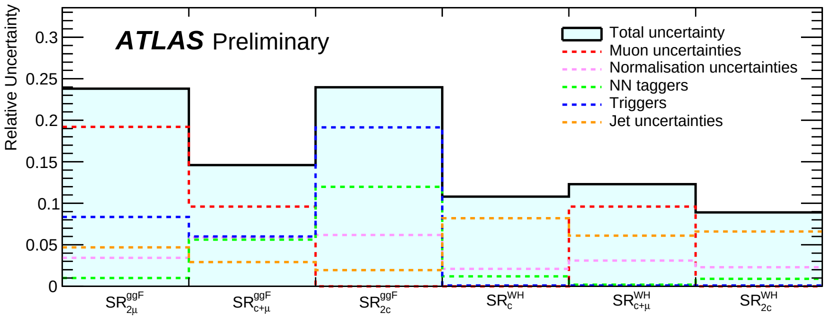

Figure 5.12. Relative signal systematic uncertainties across the six signal regions of the analysis, which are averaged across the FRVZ signal samples with two γ_d in the final state, produced by the exotic decay mode of the SM Higgs boson. Figure adapted from [1].

As previously mentioned, the leading contribution is due to the uncertainty associated to the CalRatio trigger in the ggF$_{2c}$ signal region, with larger contribution in the signal samples where this trigger is less efficient. On the other hand, other systematic uncertainties didn't show any dependence on the dark photon mass, as they are distributed with small variations around the average reported in the figure.

Similar conclusions are obtained for the additional sets of signal samples, which were generated considering the ggF production mode only, and are reported in figure 5.13.

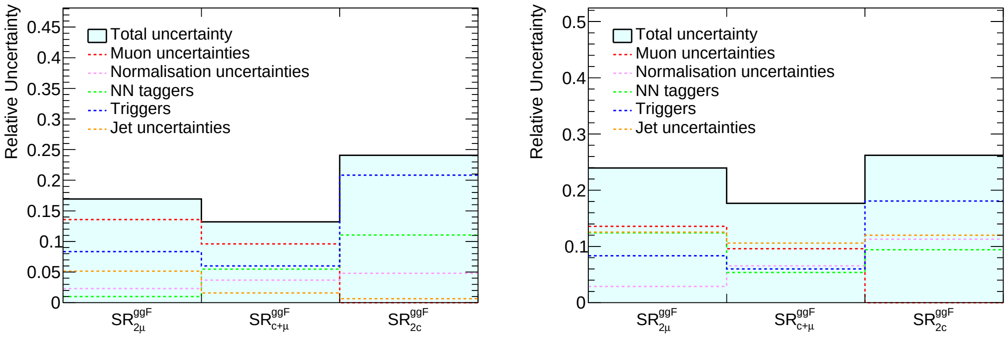

(a) HAHM $H \to 2\gamma_d$ ($m_H = 125\,\text{GeV}$) **(b)** FRVZ $H \to 4\gamma_d + X$ ($m_H = 125\,\text{GeV}$)

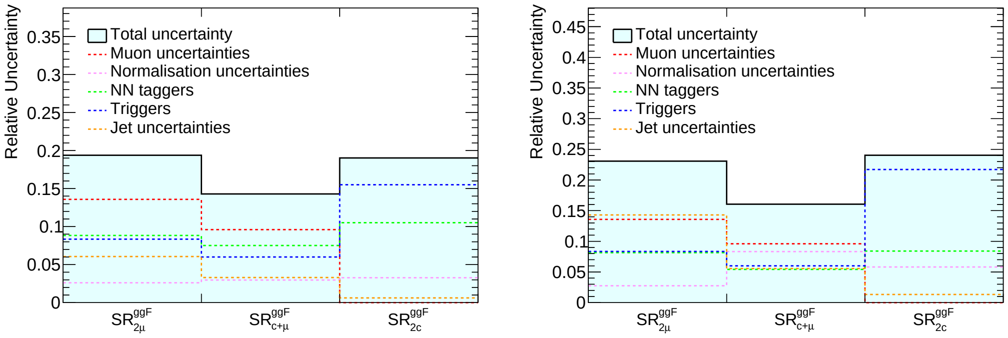

(c) FRVZ $H \to 2\gamma_d + X$ ($m_H = 800\,\text{GeV}$) **(d)** FRVZ $H \to 4\gamma_d + X$ ($m_H = 800\,\text{GeV}$)

Figure 5.13. Relative signal systematic uncertainties shown for the three ggF signal regions of the analysis, averaged across different signal samples. (a) reports the HAHM samples with $m_H = 125\,\text{GeV}$. (b) reports the case of the FRVZ model with 4 γ_d and $m_H = 125\,\text{GeV}$, while (c) and (d) report averages across the samples with a 800 GeV Higgs-like boson, with 2 or 4 γ_d in the final state, respectively.

5.4 Results and interpretation

5.4.1 Likelihood fit

The observed data in the signal region show no significant disagreement, when compared with the expected background estimated by the ABCD method, as it was shown in section 5.2.5. These results are used to derive exclusion limits, on the cross section times the Higgs boson branching fraction, of the production of γ_d via the FRVZ or the HAHM processes.

The upper limit on the signal strength is obtained with the $\mathrm{CL_s}$ method [88], performing a global simultaneous fit, with the asymptotic calculator, based on the profile likelihood test statistics [89] in order to normalise the observed data in all the regions to the signal expectation.

For each ggF and WH analysis channel a SR+CR fit is performed, testing all the available simulated signal samples. An example of the expected and observed $\mathrm{CL_s}$, obtained for different values of the signal strength, μ, of the $\mathrm{ggF}_{c+\mu}$ channel, is shown in figure 5.14. In this case, the tested signal predicts the production of a pair of γ_d, with a mass of $0.4\,\mathrm{GeV}$, originated by the decay of a SM Higgs boson produced with the ggF mechanism and decaying according to the FRVZ model. From the fit, an upper limit at 95% CL on the excluded signal strength is found to be at $\mu = 0.34$, when the signal yield is normalised to $139\,\mathrm{fb}^{-1}$ and the branching ratio, B, of $H \to 2\gamma_d + X$ is assumed to be equal to 0.01. This translates to an upper limit on B, at 95% CL, of 3.4×10^{-3}.

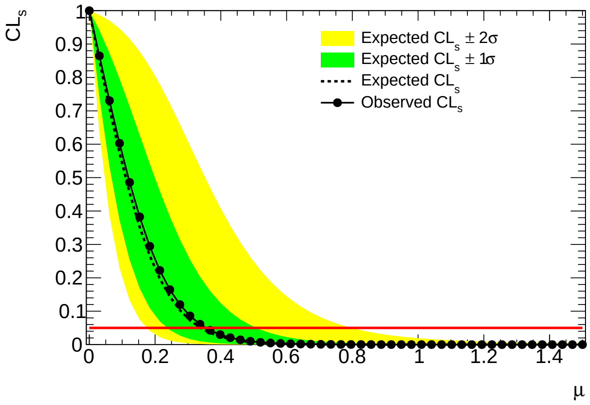

Figure 5.14. The value assumed by $\mathrm{CL_s}$ for different values of the signal strength. Here a simultaneous fit of the four ABCD regions of the $\mathrm{ggF}_{c+\mu}$ channel is performed. The signal sample considered is the ggF FRVZ sample, where 2 γ_d of $c\tau = 50\,\mathrm{mm}$ are produced by the decay of a SM Higgs boson.

All systematic uncertainties described in Section 5.3 are included in the fit as nuisance parameters with Gaussian probability density functions that multiply the fit likelihood.

In this way, starting from a given signal MC sample, with a particular choice of the $c\tau$ of the dark photon, an upper limit on the branching ratio of the Higgs boson for such signal process is set. In order to extrapolate this limit to other values of the dark photon mean proper lifetime, a weighting method, described in the next section, has been adopted.

5.4.2 Lifetime reweighting

Starting from a given signal MC sample, where long-lived particles are produced with a given mean proper lifetime, set to $c\tau_{\text{old}}$, it is possible to define a set of weights, which can be applied to the events in order to *emulate* a sample where the mean proper lifetimes of the LLPs is $c\tau_{\text{new}} \neq c\tau_{\text{old}}$.

The lifetime t of a single LLP is given by an exponential probability density function, $p(t)$, defined as

$$p(t) = \frac{1}{\tau_{\text{old}}} e^{-\frac{t}{\tau_{\text{old}}}} \, .$$

The distribution of the LLP decay lifetimes can be reweighted to a distribution with $\tau_{\text{new}} \neq \tau_{\text{old}}$ by weighting each LLP with a factor w defined as the ratio of the two probabilities:

$$w = \frac{\tau_{\text{old}}}{\tau_{\text{new}}} \exp\left[-t\left(\frac{1}{\tau_{\text{new}}} - \frac{1}{\tau_{\text{old}}}\right)\right] \, , \tag{5.2}$$

where t is, as before, the lifetime of the i-th LLP. If more than one LLP is present in each event, as their decays are independent, the product of per-LLP weights can be treated as a per-event weight.

This method can be applied to the events in each one of the analysis channels, to extrapolate the acceptance times efficiency ($A \times \epsilon$) of the analysis to different values of the γ_d mean decay lifetime. As example, in figure 5.15, the extrapolated $A \times \epsilon$ curve is shown for two FRVZ ggF samples, with two corresponding choices for the dark photon mass and $c\tau$. Additional validation samples have been generated and fully simulated, with an identical set of parameters except for a different choice of the dark photon $c\tau$; by processing these validation samples with the event selection, the obtained $A \times \epsilon$ is found in agreement with the extrapolated one, as visible from figure 5.15.

5.4.3 Limits as a function of the dark photon mean proper lifetime

All the results obtained from a given choice of a γ_d mass and $c\tau$ are extrapolated to different values of the dark photon mean proper lifetime and are translated to upper limits, at the 95% CL, on the branching ratio (B) of the SM Higgs decay or, in the case of the 800 GeV Higgs-like boson, on $\sigma \times$ B. A set of summary plots showing the observed limits for the different samples that are considered are presented in the following.

In figure 5.16 the observed upper limits are shown for a first set of FRVZ signal hypotheses, considering the SM Higgs and two γ_d in the final state. A first consideration becomes evident from the comparison of the plots involving the ggF

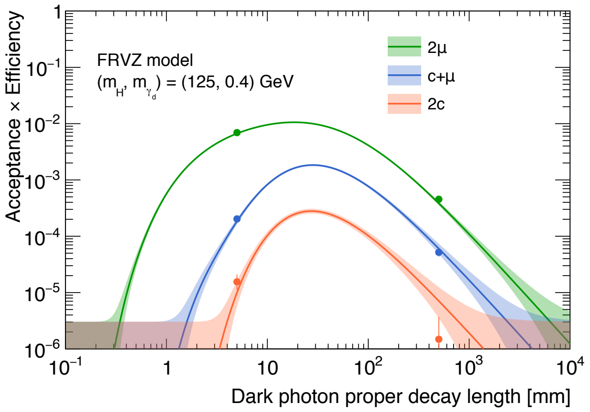

(a)

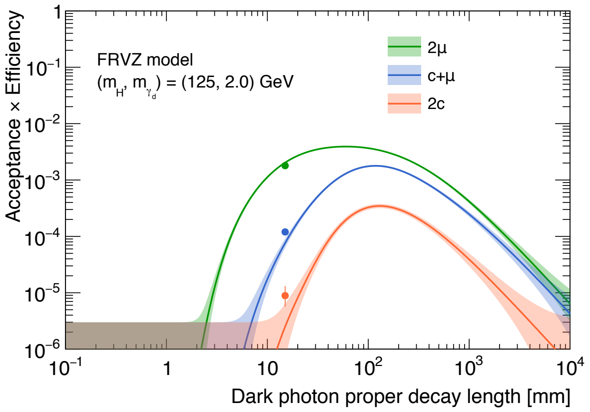

(b)

Figure 5.15. Acceptance times efficiency, extrapolated as a function of $c\tau$, for the three ggF analysis channels of two FRVZ signal MC samples, with $m_H = 125\,\text{GeV}$ and $m_{\gamma_d} = 0.4\,\text{GeV}$ and $c\tau = 50\,\text{mm}$ (a), or $m_{\gamma_d} = 2\,\text{GeV}$ and $c\tau = 175\,\text{mm}$ (b). The $A \times \epsilon$ is shown for the ggF$_{2\mu}$ (green), ggF$_{\text{c}+\mu}$ (blue) and the ggF$_{2\text{c}}$ (red) analysis channels. Markers of the same color show the relative $A \times \epsilon$, found using additional MC samples generated with different values of $c\tau$, showing agreement with the reweighting curves. For figure (a) two additional samples were generated at $c\tau$ equal to 5 and $500\,\text{mm}$, while for figure (b) the additional sample is generated at $c\tau = 15\,\text{mm}$

search category (figure 5.16 a, b and c) and the ones considering the WH production (figure 5.16 d, e and f); the exclusion limits provided by the three ggF channels are the strongest on this model, due to the larger cross section that is assumed ($48.61\,\mathrm{pb}$ for the ggF and $0.46\,\mathrm{pb}$ for the WH). The different exclusion curves show how the sensitivity of the six analysis channels varies as a function of the γ_d proper lifetime and decay mode; in particular, channels including reconstructed μDPJ are, as expected, the most sensitive ones when $\gamma_d \to \mu\mu$ decays are present with a sizable branching ratio, although they become less sensitive when the dark photon decays only to electron pairs. In this last scenario, the channels involving cDPJ are found to be the most sensitive ones. The most sensitive channels involving cDPJ have been combined in a simultaneous fit, discussed in section 5.4.5.

Exclusion limits for the HAHM model are presented in figure 5.17. In this case two γ_d are produced by the decay of a SM Higgs boson, produced with the ggF mechanism, for which the production cross section is set to $48.61\,\mathrm{pb}$. More stringent constraints are put in this case, with respect to the FRVZ model, on the branching ratio of the SM Higgs decaying in a pair of γ_d, as no other particle is involved in the process. The increased sensitivity of the $\mathrm{ggF}_{2\mathrm{c}}$ channel is clearly visible when comparing this result with the one of figure 5.16c and is mostly due to the increased efficiency of the CalRatio trigger. A general improvement of all channels is observed, as the larger p_T of the γ_d produced by the HAHM process implies an improved signal efficiency.

Limits for the additional FRVZ models are discussed in the following. Figure 5.18 show the upper limit for the ggF FRVZ samples, where 4 γ_d are produced in the final state. In these cases, two back-to-back pairs of γ_d are produced, hence the reconstruction of a single DPJ is more efficient when both γ_d are either decaying into muons or not, due to the fact that the two types of DPJ are mutually exclusive. This yields an overall smaller efficiency of the analysis and a less broad $A \times \varepsilon$ curve.

Finally, the results for the $800\,\mathrm{GeV}$ Higgs-like scalar are reported in figure 5.19 for both the case of two or four γ_d in the final state. The limits are reported in terms of the $\sigma \times$ B of the FRVZ process, as a function of the proper $c\tau$ of the dark photon. In this case, the larger p_T of the γ_d yield collimated decay products, providing good sensitivity even when heavier dark photons are involved. As expected, the reconstruction of μDPJ from $\gamma_d \to ee$ decays is less efficient, and lighter m_{γ_d} scenarios are not excluded by the $\mathrm{ggF}_{2\mu}$ and the $\mathrm{ggF}_{\mathrm{c}+\mu}$ search channels. On the other hand, as in the case of the HAHM model, the larger efficiency of the CalRatio trigger implies stronger constraints for the $\mathrm{ggF}_{2\mathrm{c}}$ channel.

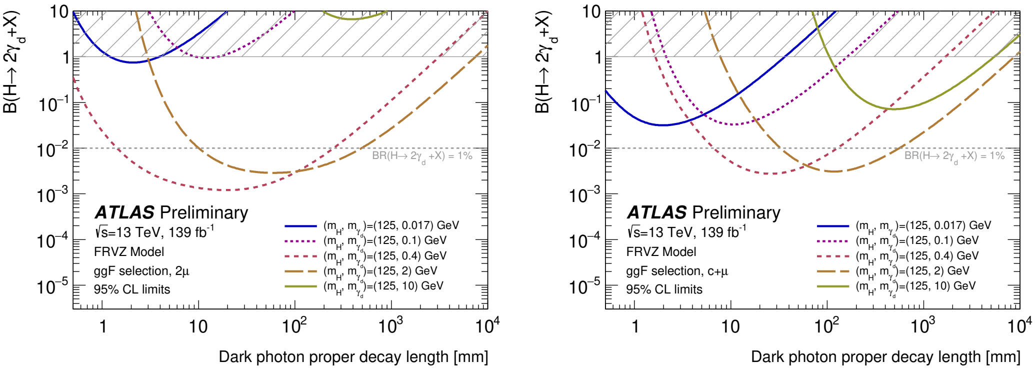

(a) ggF$_{2\mu}$ **(b)** ggF$_{\mathrm{c}+\mu}$

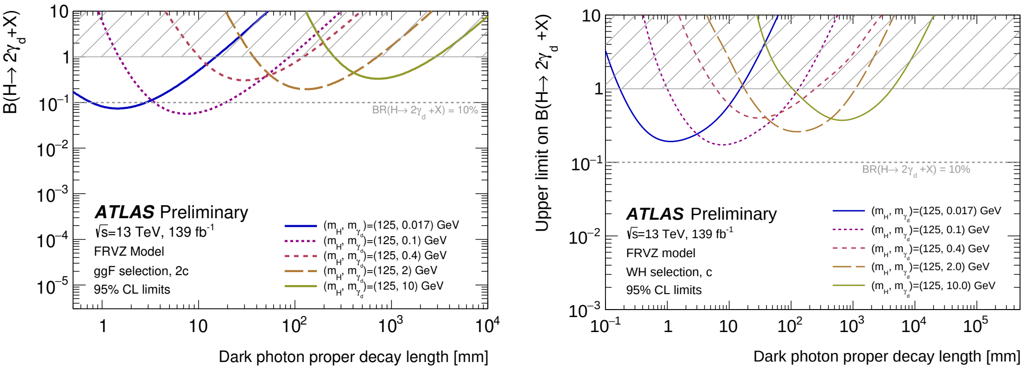

(c) ggF$_{2\mathrm{c}}$ **(d)** WH$_{c}$

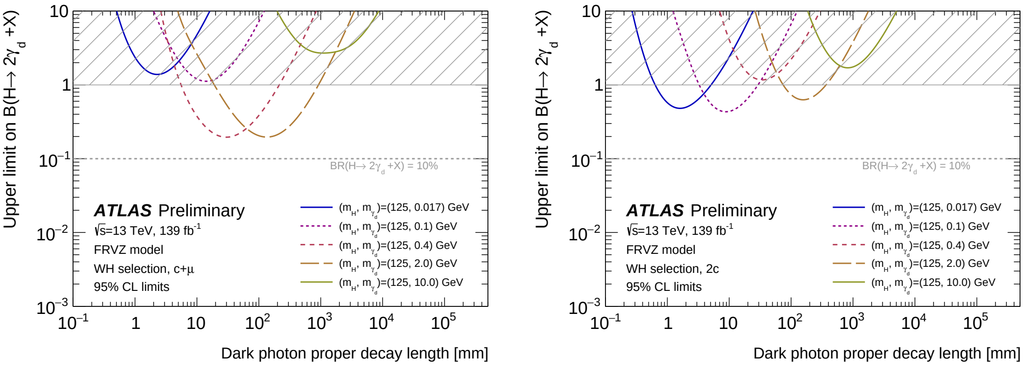

(e) WH$_{\mathrm{c}+\mu}$ **(f)** WH$_{2\mathrm{c}}$

Figure 5.16. Observed limits, at the 95% CL, on the branching ratio (B) for the process $H \to 2\gamma_d + X$, considering the FRVZ model and the SM Higgs boson. Different choice of the γ_d mass are shown and limits for the ggF search channels are reported in separated plots for the ggF$_{2\mu}$ (a), ggF$_{\mathrm{c}+\mu}$ (b), ggF$_{2\mathrm{c}}$ (c). The results from the WH search channels are reported for the WH$_{c}$ (d), WH$_{\mathrm{c}+\mu}$ (e) and the WH$_{2\mathrm{c}}$ (f). The hatched band highlight the region where the branching ratio is larger than unity. Figure adapted from [1].

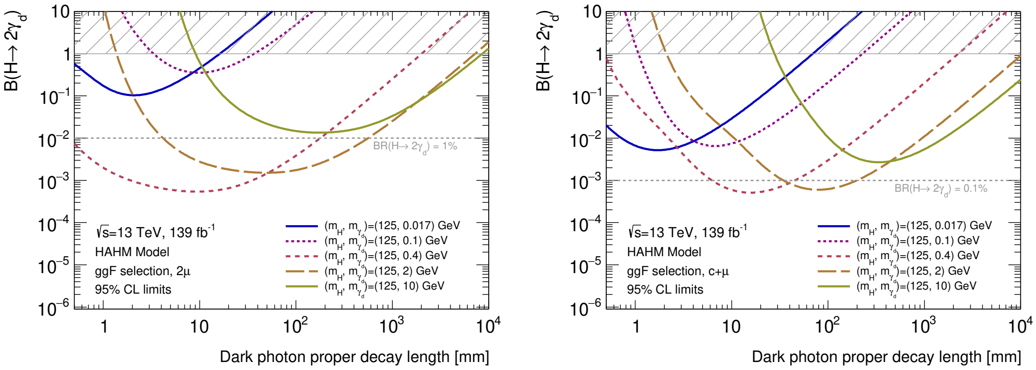

(a) ggF$_{2\mu}$

(b) ggF$_{c+\mu}$

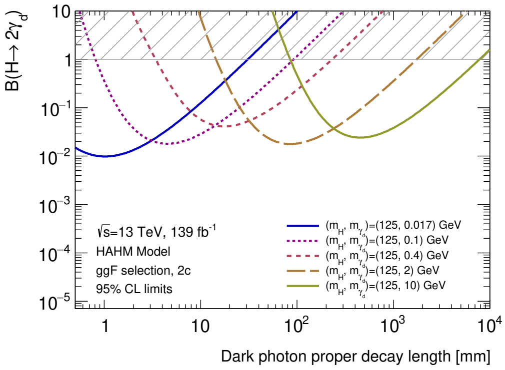

(c) ggF$_{2c}$

Figure 5.17. Observed limits, at the 95% CL, on the branching ratio (B) for the process $H \rightarrow 2\gamma_d$ of the HAHM model. Different choice of the γ_d mass are shown in corresponding figures reporting limits for the ggF$_{2\mu}$ (a), ggF$_{c+\mu}$ (b), ggF$_{2c}$ (c). The hatched band highlight the region where the branching ratio is larger than unity.

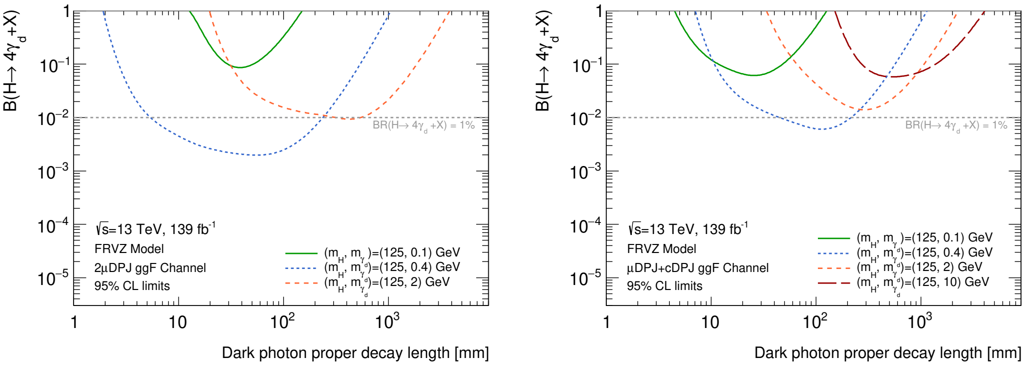

(a) $\mathrm{ggF}_{2\mu}$ **(b)** $\mathrm{ggF}_{\mathrm{c}+\mu}$

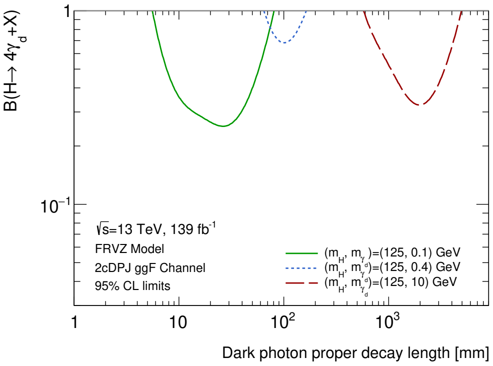

(c) $\mathrm{ggF}_{2\mathrm{c}}$

Figure 5.18. Observed limits, at the 95% CL, on the branching ratio (B) for the process $H \to 4\gamma_d + X$, considering the FRVZ model and the SM Higgs boson. Different choice of the γ_d mass are shown and limits for the sensitive channels are reported.

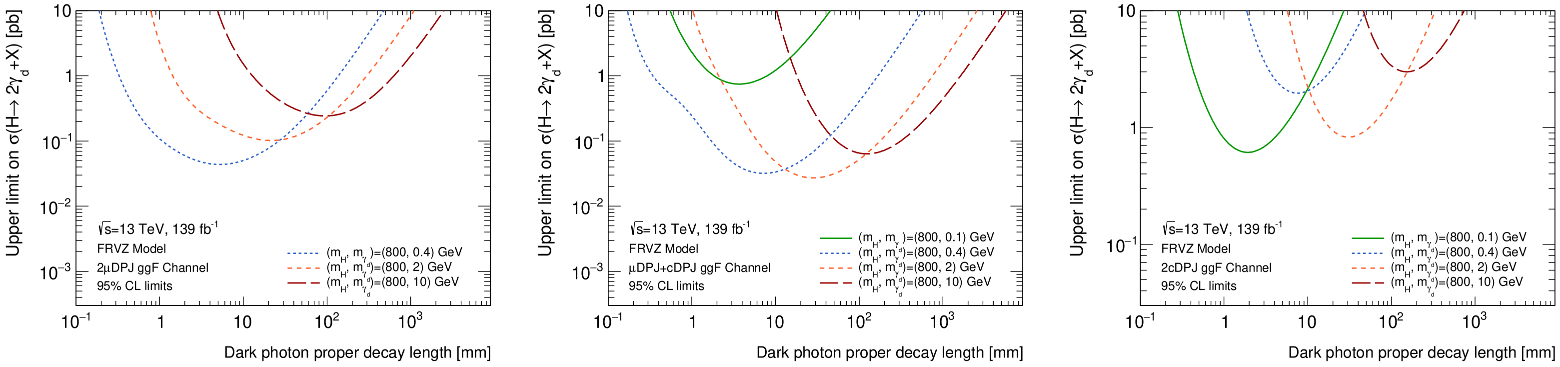

(a) ggF$_{2\mu}$ **(b)** ggF$_{c+\mu}$ **(c)** ggF$_{2c}$

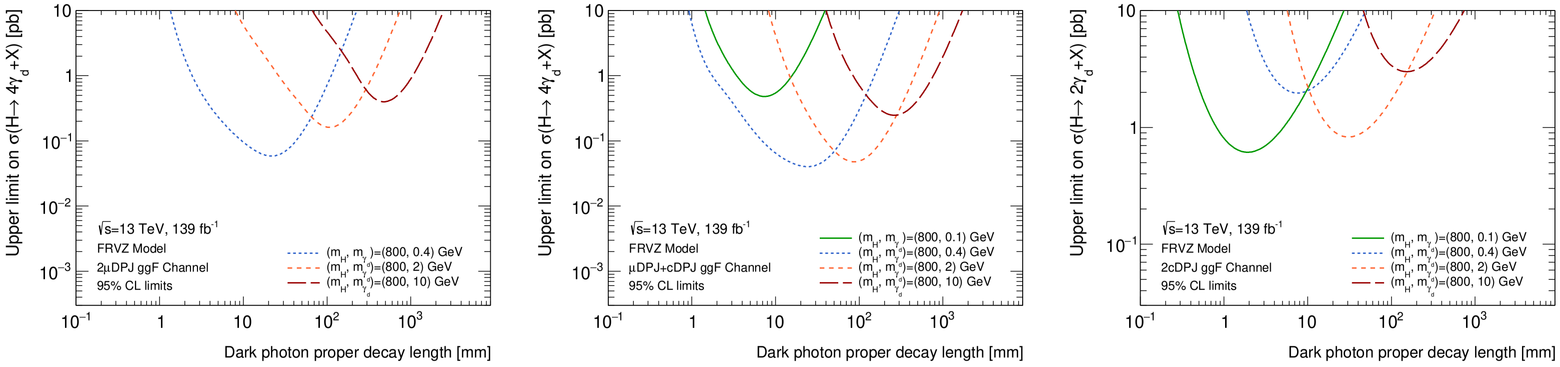

(d) ggF$_{2\mu}$ **(e)** ggF$_{c+\mu}$ **(f)** ggF$_{2c}$

Figure 5.19. Observed limits, at the 95% CL, on the $\sigma \times$ B for the FRVZ model and the 800 GeV Higgs-like boson. The three ggF search channels (ggF$_{2\mu}$, ggF$_{c+\mu}$ and ggF$_{2c}$) are shown, respectively, in (a, b, c) for the $H \rightarrow 2\gamma_d + X$ process and in (d, e, f) for the $H \rightarrow 4\gamma_d + X$. Multiple γ_d masses have been considered and the limit for the sensitive channels are reported.

The limits presented so far will be used in section 5.4.6 to produce exclusion contours in the plane of the dark photon mass and kinetic mixing coupling constant. For the sake of simplicity, the intermediate values of the mass points that were generated were not reported here, but nonetheless have been used to help in the interpolation between the different mass points, as it will described in section 5.4.6.

A more compact overview on the excluded values of the dark photon $c\tau$ is given in table 5.11, where the excluded intervals are reported for the different models considered, when assuming a branching ratio of the SM Higgs decay to the FRVZ or HAHM process of 10%, or a $\sigma \times B$ equal to 5 pb for the case of the 800 GeV Higgs-like boson.

Model	m_{γ_d} [GeV]		Excluded $c\tau$ [mm]	
		ggF$_{2\mu}$	ggF$_{c+\mu}$	ggF$_{2c}$
FRVZ $H \to 2\gamma_d + X$ $m_H = 125$ GeV	0.017	–	$0.654 < c\tau < 8.76$	$0.781 < c\tau < 2.83$
	0.1	–	$3.98 < c\tau < 39.9$	$3.50 < c\tau < 19.0$
	0.4	$0.654 < c\tau < 939$	$2.79 < c\tau < 501$	–
	2	$4.52 < c\tau < 2170$	$13.8 < c\tau < 2510$	–
	10	–	$263 < c\tau < 1030$	–
FRVZ $H \to 4\gamma_d + X$ $m_H = 125$ GeV	0.1	$29.8 < c\tau < 50.8$	$11.9 < c\tau < 47.6$	–
	0.4	$2.70 < c\tau < 534$	$10.8 < c\tau < 560$	–
	2	$31.3 < c\tau < 1850$	$65.7 < c\tau < 1070$	–
	10	–	$276 < c\tau < 1360$	–
FRVZ $H \to 2\gamma_d + X$ $m_H = 800$ GeV	0.1	–	$0.709 < c\tau < 29.3$	$0.354 < c\tau < 17.5$
	0.4	$0.219 < c\tau < 329$	$0.198 < c\tau < 393$	$2.53 < c\tau < 29.3$
	2	$0.903 < c\tau < 749$	$1.23 < c\tau < 1760$	$7.22 < c\tau < 217$
	10	$6.05 < c\tau < 1680$	$11.9 < c\tau < 3880$	$67.8 < c\tau < 406$
FRVZ $H \to 4\gamma_d + X$ $m_H = 800$ GeV	0.1	–	$1.75 < c\tau < 30.8$	$1.56 < c\tau < 36.8$
	0.4	$1.56 < c\tau < 184$	$1.06 < c\tau < 246$	$11.9 < c\tau < 32.3$
	2	$11.0 < c\tau < 598$	$9.65 < c\tau < 737$	$34.5 < c\tau < 267$
	10	$98.3 < c\tau < 1970$	$48.4 < c\tau < 1360$	$227 < c\tau < 485$
HAHM $H \to 2\gamma_d$ $m_H = 125$ GeV	0.017	–	$0.287 < c\tau < 20.3$	$0.198 < c\tau < 8.76$
	0.1	–	$1.64 < c\tau < 66.8$	$1.39 < c\tau < 25.0$
	0.4	$0.253 < c\tau < 617$	$0.860 < c\tau < 691$	$7.22 < c\tau < 55.9$
	2	$2.05 < c\tau < 2140$	$3.79 < c\tau < 3250$	$25.8 < c\tau < 469$

Table 5.11. Excluded ranges, at 95% CL, of the γ_d mean proper lifetime reported for different models and different mass samples. In the case of the SM Higgs decay, the quoted intervals correspond to a branching ratio of the exotic decay of the Higgs boson of 10% while, in the case of the 800 GeV Higgs boson, to a $\sigma \times B$ of 5 pb. Only the ggF analysis channels are reported, as no exclusion below 10% is obtained for the WH channels. Empty cells correspond to the cases in which the exclusion is not obtained, due to a small sensitivity of the analysis.

5.4.4 Comparison with state-of-the-art constraints

Figure 5.20 shows both expected and observed limits at the 95% CL, on the branching ratio of the $H \to 2\gamma_d + X$ process, considering the ggF production of a SM Higgs boson decaying in two γ_d of $m = 0.4\,\text{GeV}$ according to the FRVZ model. The results obtained by the previous ATLAS search for displaced DPJ [2], which tested the same signal hypothesis, are also shown in the figure.

Until now, the previous search provided the strongest constraints on this model, exploiting $36\,\text{fb}^{-1}$ of data collected by ATLAS during 2015 and 2016 and studied only the ggF production mechanism, with a slightly different event selection. The sensitivity gain is not only due to the larger available dataset, but multiple improvements have been obtained from the work presented in this thesis. The two most significant differences in the previous analysis are summarised in the following.

- The selection of cDPJ relied on a boosted decision tree (BDT), which was trained to reject fake-cDPJ from multijet events and select the ones originating from signal events, by using six jet-level observables as input. A significant improvement was achieved by using the QCD tagger, whose AUC[3] was found to be 18% larger than the BDT previously mentioned.
- The $\text{ggF}_{\text{c}+\mu}$ analysis channel of the previous analysis selected events with the logical OR of the Narrow-Scan and the CalRatio trigger. In the new analysis it was found that the contribution to the signal acceptance of the CalRatio trigger was negligible with respect to the one of the Narrow-Scan, hence only the latter has been used.

These two differences, together with the revised event selection, provide a large improvement in search channels based on cDPJ and are crucial to extend the sensitivity of the previous analysis, for which only the $\text{ggF}_{2\mu}$ channel was providing a limit, on the branching ratio of the $H \to 2\gamma_d + X$ process. The possibility of probing the scenario in which dark photon decays into muons are suppressed or not allowed is of particular interest, as it allows to exclude regions of the ε-m_{γ_d} plane where the dark photon decays only to electrons or hadrons, as it will be discussed in 5.4.6.

5.4.5 Combination of the ggF and WH results

A single reconstructed prompt lepton is required by the WH pre-selection, while events with a prompt lepton are vetoed by the ggF analysis channels; on the other hand, the two types of Dark-Photon Jets are exclusive, hence the six signal regions of this analysis are mutually orthogonal and can be statistically combined.

In the case of the FRVZ signal samples, the combination of different search channels helps in constraining the regions of the phase space dominated by $\gamma_d \to ee$

---

[3] The Area-Under-Curve (AUC) is a quantitative measure of the Receiver Operating Characteristic (ROC) curve, associated to a binary classifier. If two classes (signal and background) are defined, the ROC curve is defined by the signal efficiency (ratio of correctly classified signal events) expressed as a function of the background rejection power (ratio of correctly classified and total background events). The AUC of a perfect classifier is, by definition, equal to 1.

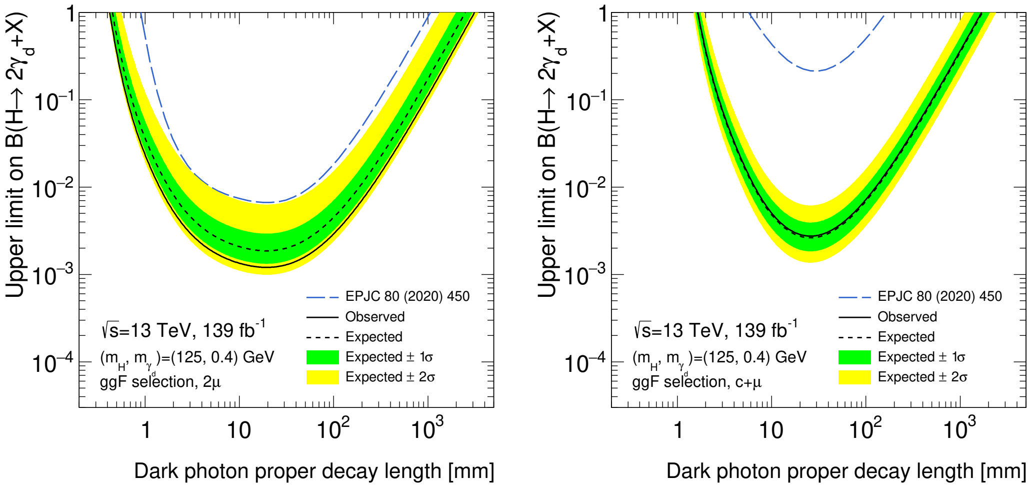

(a) $\mathrm{ggF}_{2\mu}$ **(b)** $\mathrm{ggF}_{\mathrm{c}+\mu}$

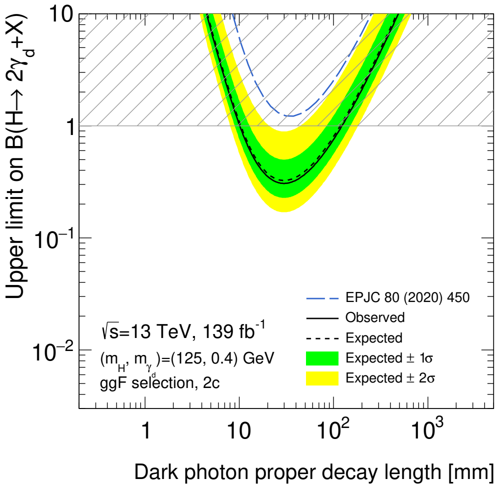

(c) $\mathrm{ggF}_{2\mathrm{c}}$

Figure 5.20. Upper limits at the 95% CL on the branching ratio of the $H \to 2\gamma_d + X$ process predicted by the FRVZ model, obtained considering a $0.4\,\mathrm{GeV}$ dark photon and the ggF production of the SM Higgs. Observed limits from the analysis presented in this thesis are compared with the ones of [2] (dashed blue lines) for the three ggF search channels. As explained in the text, the revised event selection and the introduction of the convolutional neural network taggers allowed a significant sensitivity increase in the search channels that considers cDPJ.

decays. In these cases, a combined likelihood fit of the ggF$_{2c}$, WH$_c$ and WH$_{2c}$ ABCD planes was performed, where a summed likelihood with a common signal normalisation has been implemented. The complementarity of the WH and ggF exclusions is visible in figure 5.21, reporting upper limits at the 95% CL on the branching ratio of the $H \to 2\gamma_d + X$ process, for the case of dark photons with mass equal to $0.1\,\mathrm{GeV}$. In particular, the results of the ggF channel are extended, thanks to the combination with the WH selection, for dark photon proper decay lengths shorter than $2\,\mathrm{mm}$ or larger than $50\,\mathrm{mm}$.

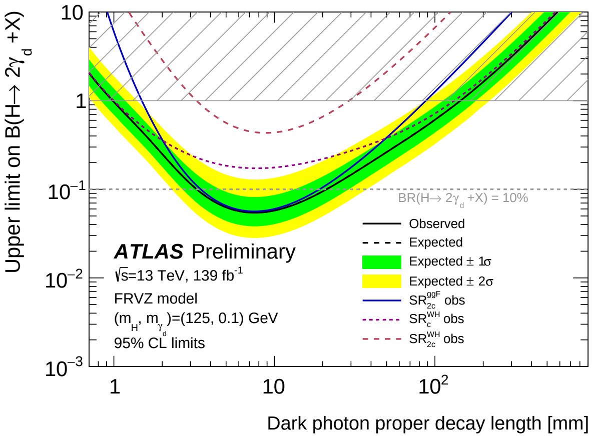

Figure 5.21. Upper limits, calculated at 95% CL, on the branching ratio (B) for the FRVZ process $H \to 2\gamma_d + X$, for a γ_d mass of 0.1 GeV and a SM Higgs boson. The solid (dashed) black lines shows the observed (expected) exclusion limits, while dashed colored lines show the individual limits of the search channels in the three search regions that are considered for the statistical combination. Figure taken from [1].

5.4.6 Exclusion limit in the ε-m_{γ_d} plane

The results obtained by this search can be compared to the other constraints on dark photon models, which were shown in figure 1.8, where the exclusion limits are shown at 90% CL, on the plane defined by the kinetic mixing parameter ε and the mass of the dark photon m_{γ_d}.

To produce such limits, the information of the results from different dark photon mass hypotheses has been used, by evaluating limits at 90% of the CL.

The branching ratio of the γ_d allows to scale the one-dimensional limits to different mass hypotheses. As two independent γ_d are present in each event, the branching ratio shown in figure 1.7 is used to build three two-γ_d weighting functions, which define the probability of having two, one, or zero dark photons decaying into muons, $P(2\gamma_d \to N_{\mu^+\mu^-})$. This probability is shown as a function of the γ_d mass in figure 5.22 and is used to scale the limits of the three ggF analysis channels to other mass hypotheses, by making the conservative assumption that μDPJ originate only from $\gamma_d \to \mu\mu$ decays, while other decay modes of the γ_d can be identified as cDPJ.

At this point the extrapolated limits are corrected by a linear interpolation

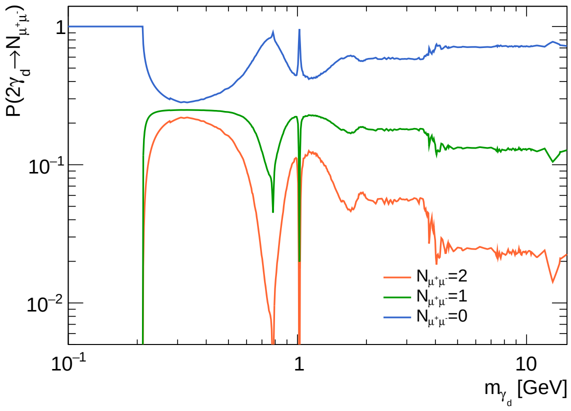

Figure 5.22. Probability of having a pair of γ_d that decay in two (orange), one (green) or zero (blue) muon pairs as a function of the dark photon mass m_{γ_d}.

between two adjacent available MC mass samples and the best exclusion limit from the three channels is considered. Below the threshold to produce two muons, i.e. for $m_{\gamma_d} < 211\,\mathrm{MeV}$, only the combination of the ggF and WH search regions that consider only cDPJ is used.

Figure 5.23 shows the contours of the upper limits on the FRVZ model, at 90% CL, for different values of the branching ratio of the $H \to 2\gamma_d + X$ process, as a function of the γ_d mass and kinetic mixing coupling constant ε. The exclusion limit from the previous displaced Dark-Photon-Jet ATLAS search [2] is also shown (dashed orange contour), as well as the limit from the Run-I prompt DPJ search [90] (red contour). A broader exclusion limit is set by this search, which thanks to the optimisation of the selections involving cDPJ, as well as to the combination with the WH channels, allowed to set limits below the threshold to produce two muons and up to the value of $m_{\gamma_d} = 11.1\,\mathrm{GeV}$, extending the exclusion contour of the previous ATLAS search.

The limit obtained in the Early Run-II search was extracted from the results of the ggF$_{2\mu}$ channel. Only a single dark photon mass point was used, with $m_{\gamma_d} = 0.4\,\mathrm{GeV}$, under the assumption that the reconstruction efficiency does not change in the 0.2-2 GeV dark photon mass interval. The upper limit was then extrapolated to other values of ε and m_{γ_d} by using the lifetime reweighting method and the ratio of the probability of having two γ_d decaying into muons, from figure 5.22.

Moreover, the same limit is derived for the HAHM model, using the results of the fit in the ggF signal regions. As before, the extrapolated limits are corrected by a linear interpolation between two adjacent γ_d mass samples and the most stringent limit from each channel is considered for each value of ε and m_{γ_d}. Given the increased sensitivity of the ggF selection on these samples, with respect to the FRVZ ones, a broader region along the ε axis is excluded.

Similar exclusion limits have been produced, using the same approach, for the remaining types of benchmark models. For the ones predicting four γ_d in the final state, the branching ratio of the γ_d has been used to obtain three four-γ_d weighting

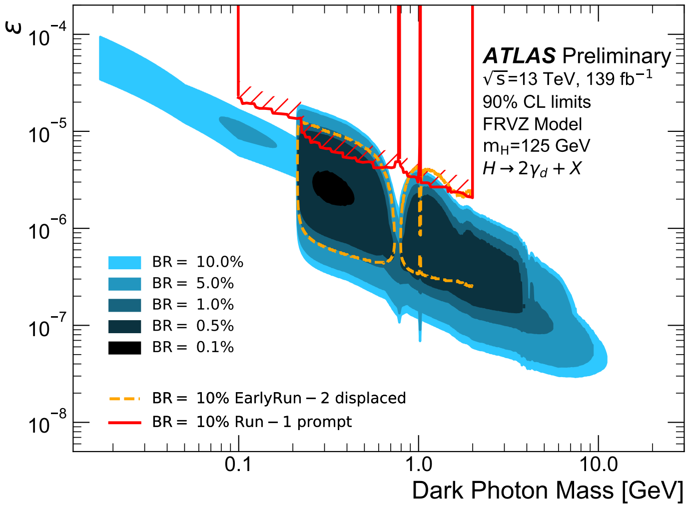

Figure 5.23. 90% CL exclusion contours regions of the SM Higgs boson as a function of the γ_d mass and of the kinetic mixing parameter ε for the FRVZ model. These limits are obtained assuming a decay branching fraction of the Higgs boson into γ_d ranging between 0.1% and 10%, where regions filled with darker shades of blue correspond to stronger choices of the branching fraction. The figure also shows excluded regions from the previous ATLAS displaced [2] (orange line) and prompt [90] (red line) Dark-Photon-Jets searches. Figure taken from [1].

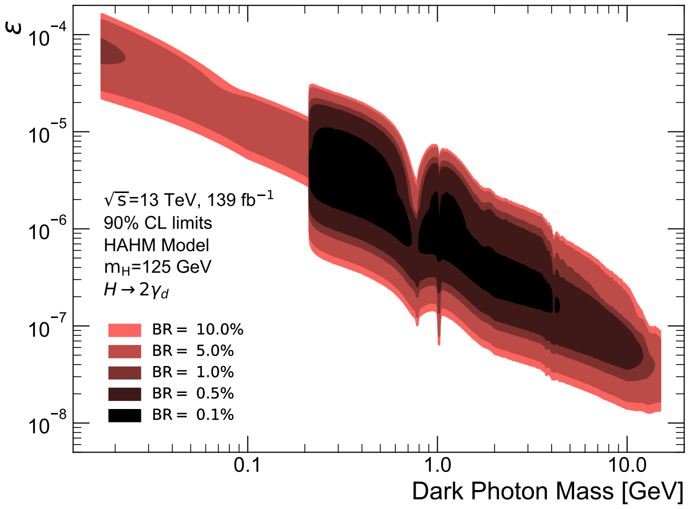

Figure 5.24. Upper limits at the 90% CL, reported as exclusion regions of the SM Higgs boson as a function of the γ_d mass and of the kinetic mixing parameter ε for the HAHM model. Regions filled with darker red tones correspond to stronger hypotheses on the $H \to 2\gamma_d$ branching fraction, ranging between 0.1% and 10%.

functions. The probability of obtaining an even number N of $\gamma_d \to \mu\mu$ decays ($P(4\gamma_d \to N_{\mu^+\mu^-})$), reported in figure 5.25, has been used to scale the events of the three ggF channels, under the conservative hypothesis that a reconstructed μDPJ can only be obtained from two collimated γ_d that decay into muons.

In figure 5.26 the 90% CL limit obtained by this analysis is reported in the $\varepsilon - m_{\gamma_d}$ plane assuming the FRVZ process $H \to 4\gamma_d + X$ and the SM Higgs boson. As in the previous cases, the limit is obtained by interpolating the results obtained for all the available simulated mass samples. Darker colours correspond to different assumptions on the SM Higgs branching ratio and the orange dashed line shows for reference the limit of the $H \to 2\gamma_d + X$ of figure 5.23. As shown by the limits as function of $c\tau$, presented in section 5.4.3, for these signal samples the excluded region is narrower along the ε axis, due to the necessity of reconstructing 2 γ_d that decay within the acceptance of the detector.

Finally, figures 5.27a and 5.27b show the excluded regions for the FRVZ processes with the production of two and four γ_d in the final state. The same approach described before has been used in producing these exclusion contours, that are reported for different assumption on the $\sigma \times B$ of the bSM $800\,\mathrm{GeV}$ Higgs-like boson. As before, the exclusion limit has been produced using all the available MC samples and, in this case, is limited by the heaviest γ_d mass point at $15\,\mathrm{GeV}$.

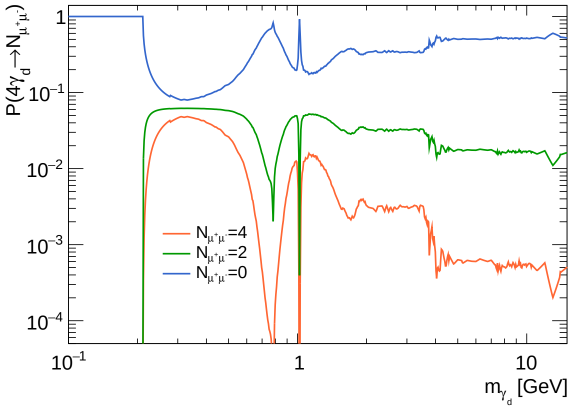

Figure 5.25. Probability of having four γ_d that decay in four (orange), two (green) or zero (blue) muons pairs, reported as a function of the dark photon mass m_{γ_d}.

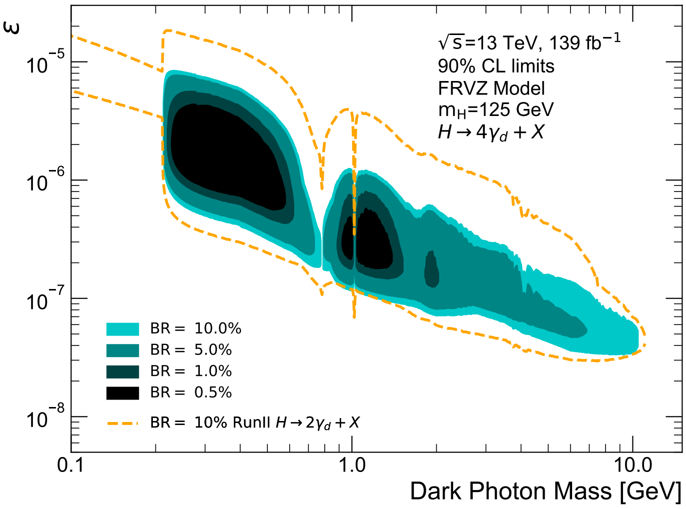

Figure 5.26. Exclusion contours of the excluded SM Higgs boson branching ratio, as a function of the γ_d mass and of the kinetic mixing parameter ε for the FRVZ process $H \to 2\gamma_d + X$.

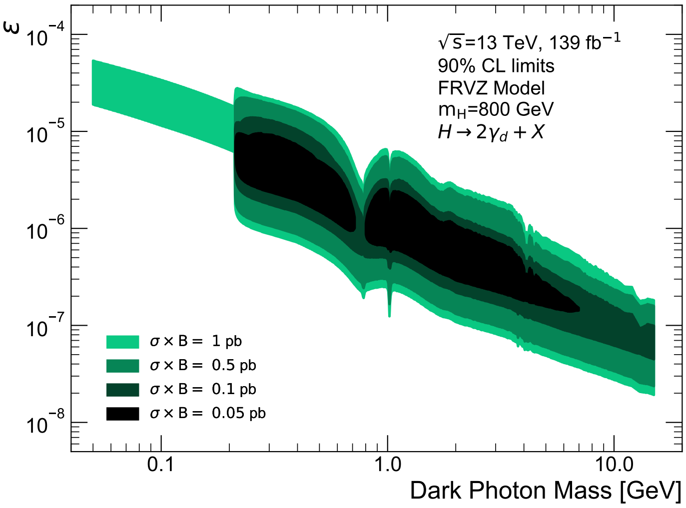

(a) $H \to 2\gamma_d + X$

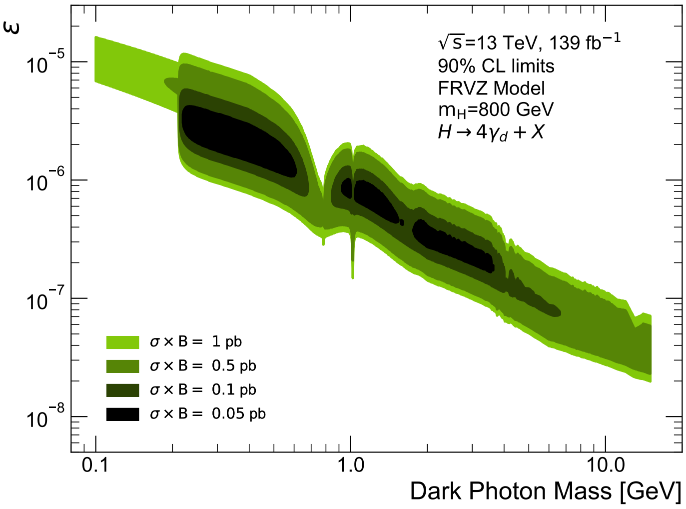

(b) $H \to 4\gamma_d + X$

Figure 5.27. Excluded values of the dark photon mass and kinetic mixing coupling constant (ε) for the $H \to 2\gamma_d + X$ (a) and $H \to 4\gamma_d + X$ (b) produced via an intermediate bSM 800 GeV Higgs-like boson. The excluded regions are reported for different choices of the $\sigma \times B$ of the Higgs-like scalar.

Chapter 6

Where to look for LLPs escaping ATLAS

In chapter 3, the signature left in ATLAS by long-lived dark photon decays is exploited to build custom reconstructed objects, which are targeted by the search described in chapter 5.

As displaced Dark-Photon Jets are already exploiting the outer regions of the ATLAS detector, a different approach is needed to study LLPs with proper decay lifetimes large enough that most of the decays happen *outside* the detector.

For this region of the phase space, in ATLAS it is possible to look at events where all the energy associated to LLPs is lost outside the detector, contributing to the $E_{\mathrm{T}}^{\mathrm{miss}}$ of the event. Final states with large missing transverse momentum recoiling against one highly energetic jet, named *monojet* events, are a striking signature for many searches of beyond-SM physics and are used, in the study presented in this chapter, to probe LLP signals in the case of very long proper lifetimes. In this scenario, the targeted signature features multiple LLPs decaying outside the detector, where the whole system is recoiling against an Initial-State-Radiation (ISR) jet.

The monojet analysis is described with great detail in [3] and its results are here interpreted in the context of two theoretical models that predict LLPs, described in section 6.1. The main aspects of the monojet search are reported in 6.2, while the result of the reinterpretation obtained with the RECAST (Request Efficiency Computation for Alternative Signal Theories) framework [91] are presented in section 6.3. The framework allows to use the background predictions of the original analysis [3] to test new physics models, and to include systematic detector-related uncertainties for the signal samples.

The results presented in this chapter have been published by the ATLAS collaboration as a public note [4] in June 2021. The results of the full Run-II displaced DPJ searches, presented in chapter 5 were not included as they have been published in January 2021 in [1]. However, some final considerations taking into account both the results from this reinterpretation study and the ones from chapter 5 will be given in the conclusions of this thesis.

m_{H} GeV	m_s [GeV]	$c\tau_s$ [mm]
125	5	223, 411
125	35	1310, 2630
125	55	1050, 5320

Table 6.1. Values of the proper lifetime and mass of the scalar s, used in the MC signal generation for the $H \to ss$ model. Table from ref. [4].

6.1 Benchmark models

The simulated signal samples that have been considered in this reinterpretation are summarised in this section.

Two of them have also been studied in the displaced DPJ analysis and are two FRVZ signal samples, where the ggF production of two dark photons is considered, for a γ_d of mass equal to $0.4\,\mathrm{GeV}$ and both the SM Higgs and the heavy bSM Higgs-like boson with mass equal to $800\,\mathrm{GeV}$. The monojet analysis is expected to be sensitive to larger values of the dark photon $c\tau$, hence multiple samples, differing only in the γ_d proper lifetime, have been considered. In particular, for the SM Higgs sample, three MC signal samples have been used, with γ_d proper lifetime set to 5, 50 and $500\,\mathrm{mm}$, while two heavy-Higgs samples are considered, with dark photon proper decay lifetime set to 10 and $100\,\mathrm{mm}$. All the other parameters are set as specified in table 3.1, while the event generation and simulation is made with the same infrastructure described in section 3.1.1.

Three signal MC samples are generated according to the $H \to ss$ model, described in 1.3.2, where two scalar particles, s, with Yukawa-like couplings are produced by an exotic decay of the Higgs boson. Masses between 5 and $55\,\mathrm{GeV}$ are chosen for the scalar s and multiple choices have been made for its mean proper lifetime, as detailed in table 6.1. MC samples for this model are generated at the leading order, using MADGRAPH5_aMC@NLO 2.6.2 [67], interfaced with PYTHIA 8.230 [68] using the A14 tune of parameters [70], with the NNPDF2.3LO[69] set of parton distribution functions.

As previously done in this thesis, for the $H \to ss$ and the FRVZ samples where a SM Higgs boson is considered, the production cross section is set to the value for the ggF production at $\sqrt{s} = 13\,\mathrm{TeV}$, quoted in table 1.1. The final results will be expressed in terms of the $H \to ss$ or the $H \to 2\gamma_d + X$ branching ratio. On the other hand, the ggF production cross section for the FRVZ samples with a $800\,\mathrm{GeV}$ Higgs boson is not quoted, as the final results will be given in terms of this quantity.

6.1.1 Higher order reweighting of signal samples

The monojet search is particularly sensitive to the shape of the $E_{\mathrm{T}}^{\mathrm{miss}}$ distribution, which is used as input for the fit in the signal and control regions, as it will be explained in section 6.2.

As the presence of a high-p_{T} ISR jet is crucial in events selected by the monojet analysis, it is expected that the events entering the SR will feature a boosted H boson. In this regime, it was found that the predictions based on the leading order (LO) and next-to-leading order (NLO) QCD calculations of the ggF process, yield a significantly different p_{T} distribution of the leading jet in the event. In particular, event yields in the samples computed at the LO, were found to be up to 50% larger at high transverse momentum.

For such reason, all the signals where the production of LLPs is initiated by the decay of the SM Higgs boson, are corrected by an appropriate set of per-event weights, which match the p_{T} predictions for the truth-level Higgs boson of the LO samples to the NLO ones. The distribution for the Higgs boson transverse momentum, calculated with NLO QCD accuracy, was available in a MC sample studied for the invisible Higgs decay process ($gg \to H \to \mathrm{inv}$), investigated in the monojet search.

After such correction, in the limit of infinite LLP lifetimes, the $E_{\mathrm{T}}^{\mathrm{miss}}$ distributions of the FRVZ and $H \to ss$ models are found to be consistent with the one of the $gg \to H \to \mathrm{inv}$ process, as expected.

The effect of this higher order reweighting was tested also in the displaced DPJ analysis described in chapter 5, where negligible differences were found in the signal regions. This is expected, as the displaced DPJ analysis is not presumed to have any dependency on the transverse momentum of the Higgs boson.

6.2 Overview of the monojet analysis

The monojet search considers the full Run-II dataset, selecting events where the main signature is a high-p_{T} jet recoiling against large missing transverse momentum.

In the following, a brief overview of the event selection is given, while the details on the simulation of the background processes and the object reconstruction criteria for the monojet analysis are not reported. For additional details the reader is referred to [3].

To constrain the estimation on the irreducible $Z \to \nu\nu$ background, high-statistic control regions are introduced, of which details are given below, together as a summary of the likelihood model adopted. The impact of the systematic uncertainties on the signal models considered is also discussed.

6.2.1 Definition of the analysis regions

Events are initially selected using calorimeter-based $E_{\mathrm{T}}^{\mathrm{miss}}$ triggers, which are measured to be fully efficient above 200 GeV. Additional single electron triggers are used in a particular event selection, leading to the CR defined below.

The $E_{\mathrm{T}}^{\mathrm{miss}}$ measured in the event is required to be larger than 200 GeV and at least one primary vertex must be found. All jets considered must have $|\eta| < 2.8$, $p_{\mathrm{T}} > 30$ GeV and they must satisfy the Loose working point defined in section 2.3.2. The requirement of this jet cleaning working point ensures a small contribution from BIB-jets, which may easily fake events where one jet is recoiling to large $E_{\mathrm{T}}^{\mathrm{miss}}$, as visible in the event shown in figure 4.4. All the jets considered must also have an associated JVT score larger than 0.59, in order to reject the ones originating from pileup.

Up to four jets are allowed in the final state, but the leading jet is required to have $p_{\mathrm{T}} > 150\,\mathrm{GeV}$ and $|\eta| < 2.4$. To ensure a genuine $E_{\mathrm{T}}^{\mathrm{miss}}$, events are requested to have an angular separation in the transverse plane, between the missing transverse momentum direction and any jet in the event of at least 0.4; this requirement is tightened at 0.6 when $E_{\mathrm{T}}^{\mathrm{miss}} < 250\,\mathrm{GeV}$, to further suppress the contribution of the multijet background. The signal region (SR) is then defined by vetoing events with reconstructed leptons or photons.

At this point the residual background is primarily dominated by the $Z \to \nu\nu$ process, which accounts for the 60% of the total background, followed by W+jets, where $E_{\mathrm{T}}^{\mathrm{miss}}$ originates from final state leptons that are not reconstructed (20% of the total background), while smaller contributions come from top quark related processes and di-bosons production.

The estimation of the different background contributions is performed using dedicated CRs, by fitting the shape of the distribution of the magnitude of the total p_{T} recoiling against hadronic activity in the event, $p_{\mathrm{T}}^{\mathrm{recoil}}$. The choice of this variable is motivated by the fact that, in the SR, it corresponds by definition to the $E_{\mathrm{T}}^{\mathrm{miss}}$ of the event.

The multijet and beam-induced backgrounds are mostly contributing to the low $E_{\mathrm{T}}^{\mathrm{miss}}$ region and both these components are estimated via pure data-driven techniques, as described in the dedicated paper.

Two orthogonal CRs, enriched in W+jet events, are defined by requiring exactly one reconstructed electron or muon. An additional requirement on the transverse mass of the lepton-$E_{\mathrm{T}}^{\mathrm{miss}}$ system is applied and events with b-tagged jets are rejected.

Although top-quark related processes are a sub-leading component (∼4%), an additional CR enriched in these events is still defined, by inverting the b-jet veto and by merging the two lepton flavours.

Two additional two-leptons CR are defined, by requiring exactly two electrons or muons with an invariant mass within $\pm 25\,\mathrm{GeV}$ around the mass of the Z.

In order to emulate the kinematic distribution of the $E_{\mathrm{T}}^{\mathrm{miss}}$ in the SR, all the selected leptons in the control regions are considered as being invisible particles. Hence, their transverse momentum is summed to the $E_{\mathrm{T}}^{\mathrm{miss}}$ measured in the event to build the total $p_{\mathrm{T}}^{\mathrm{recoil}}$ of the event against hadronic jets.

Finally, the same requirement applied in the SR on the angular distance between $E_{\mathrm{T}}^{\mathrm{miss}}$ and any jet in the event is applied in each control region, by considering the vector components of $p_{\mathrm{T}}^{\mathrm{recoil}}$ in the transverse plane. The signal leakage in the various CRs is checked to be negligible.

Figure 6.1 reports the distribution of the $p_{\mathrm{T}}^{\mathrm{recoil}}$ of total SM background, compared to three benchmark scenarios predicted by the models introduced in section 6.1.

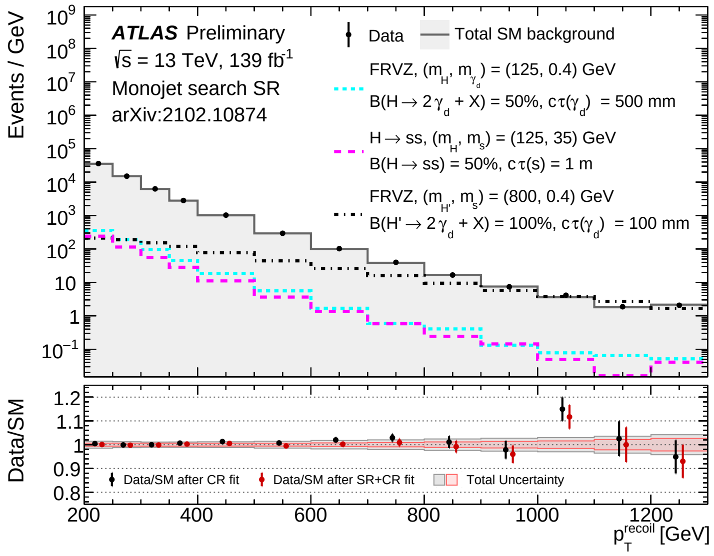

Figure 6.1. Distribution of the p_T^{recoil} in the SR of the monojet analysis, overlaid with the ones obtained from three signal models that are considered for reinterpretation. The bottom pad shows the ratio between the data and the SM prediction: black dots indicate the result after a fit to the CR only, while red dots after a CR+SR fit in the background only hypothesis. The last bin of the distribution includes all the events with $p_T^{\mathrm{recoil}} > 1.2$ TeV. Figure adapted from [4].

6.2.2 Likelihood fit

A likelihood fit of the binned p_T^{recoil} distributions is performed, across the different CR and the SR. The number of events in each bin is treated as a random variable with a Poisson distribution function, of which the expectation value is set to the prediction from all the SM processes contributing to the SR. Three free floating factors accounting for the normalisation of the SM processes are included in the fit model, respectively for the V+jets, single-top and $t\bar{t}$ event categories. Systematic uncertainties are taken into account as nuisance parameters, with Gaussian probability density functions centered around the nominal value, with a variance corresponding to the systematic uncertainty. These parameters are fully correlated among the different background processes, bins and regions.

The fit strategy foresees an initial CR-only fit, where the normalisation of the SM processes is obtained. A second fit step including the SR is performed, where an additional free-floating parameter is included, scaling the signal strength. Finally, the upper limit is obtained using the CL$_s$ method.

Figure 6.1 show no significant excess in the signal region, after the first stage of the fit including only the control regions. The same figure shows the result of SR+CR fit under the hypothesis of no signal events due to new phenomena, showing that the SM prediction are only slightly affected by the contribution of the SR in the fit.

6.2.3 Leading systematic uncertainties

The main uncertainties associated to the signal yields, for the three model considered, are summarised below.

The experimental uncertainties associated to the jet energy resolution and jet energy scale are propagated to the event yields for the various models considered. FRVZ signal samples, where the production of γ_d is initiated by an exotic decay of the SM Higgs boson, feature yield variations between 3.5% at low $p_{\mathrm{T}}^{\mathrm{recoil}}$ and 3% at high $p_{\mathrm{T}}^{\mathrm{recoil}}$, while yield variations between 1.2% and 6.3% are obtained when considering FRVZ samples with a $800\,\mathrm{GeV}$ Higgs-like boson. For the $H \to ss$ samples considered, the yields are found to vary between 3% and 7%, increasing with $p_{\mathrm{T}}^{\mathrm{recoil}}$.

The uncertainties associated to the $E_{\mathrm{T}}^{\mathrm{miss}}$ reconstruction, resolution and its scale are found to have an impact on the signal yields. For the FRVZ model with a SM Higgs boson, variations from 2.5% to 1.4%, with increasing $p_{\mathrm{T}}^{\mathrm{recoil}}$ are found, while for the $800\,\mathrm{GeV}$ Higgs boson the yield is found to vary between 0.5% and 0.3%. The yield variation for the $H \to ss$ model, associated to the $E_{\mathrm{T}}^{\mathrm{miss}}$ uncertainties, is found to be between 3.5% and 0.2%.

The impact of the most relevant systematic uncertainties is summarised in table 6.2.

Source of uncertainty and impact on the prefit signal yields (%)	
FRVZ model, m$_H$ = 125 GeV, m$_{\gamma_d}$ = 400 MeV, cτ_d = 500 mm	
Jet energy scale	1.8 – 2.4
Jet energy resolution	1.0 – 2.1
Jet quark/gluon composition and response	0.9 – 2.8
$E_{\mathrm{T}}^{\mathrm{miss}}$ scale and resolution	1.2 – 2.6
Hss model, m$_H$ = 125 GeV, m$_s$ = 5 GeV, cτ_s = 411 mm	
Jet energy scale	1.7 – 2.3
Jet energy resolution	1.0 – 3.3
Jet quark/gluon composition and response	0.7 – 3.1
$E_{\mathrm{T}}^{\mathrm{miss}}$ scale and resolution	0.1 – 2.9

Table 6.2. Effect on the pre-fit signal yields of different components of the systematic uncertainties for two benchmark signal points. Table from ref. [4].

The already discussed uncertainty on the measurement of the integrated luminosity is also taken into account, assuming a possible variation of 1.7% of the signal yields of each model.

6.3 Reinterpretation results

A lifetime reweighting procedure is used provide exclusion limits as function of the LLP $c\tau$.

The reweighting procedure that has been adopted in this case extends the one described in section 5.4.2, by exploiting multiple signal samples, generated with different values of the LLPs mean proper lifetime. In this way the extrapolation is less sensitive to the limited statistics of a single sample, and is more reliable at mean proper lifetimes which are significantly different than the one used in the simulation.

As an example, let us consider two signal samples, A and B, generated with the same parameters except the mean proper lifetime of the LLPs, which are set to $\tau_A < \tau_B$. To obtain a set of per-event weights, that would give the corresponding event yields of a third sample, generated with different LLP mean proper lifetime, the following procedure is adopted. At first a *critical* value of the LLP mean proper lifetime is computed, $\hat{\tau}$, corresponding to the value for which the two exponential probability density functions with τ_A and τ_B are equal. This corresponds to

$$\hat{\tau} = 2 \ln \left(\frac{\tau_B}{\tau_A} \right) / \left(\frac{1}{\tau_A} - \frac{1}{\tau_B} \right) ,$$

where the factor 2 is included to account for two LLPs per event. At this point, events from the sample A(B) are used for the lifetime reweighting, only if the sum of the proper lifetimes of the two LLPs is smaller(larger) than $\hat{\tau}$; the multiplicative weight is computed for each LLP from equation 5.2, where τ_{old} is equal to $\tau_A(\tau_B)$.

As the monojet fit strongly depends on the shape of the $p_{\mathrm{T}}^{\text{recoil}}$ distribution of the signal events, the lifetime reweighting is applied to the events that enter the SR, producing different distributions of the $p_{\mathrm{T}}^{\text{recoil}}$ shape for a set of $c\tau$ choices. A limit on the signal strength is then extracted for each choice of the $c\tau$. In support of the method, a perfect agreement was found between the $E_{\mathrm{T}}^{\text{miss}}$ distribution of the $H \rightarrow$ inv process and the one obtained by the lifetime reweighting of a sample with LLPs in the limit of very large $c\tau$.

6.3.1 Limits for the FRVZ model

In order to have a direct comparison with the results from the displaced DPJ analysis, the events of the FRVZ models have been studied also for separate decay modes of the γ_d. In particular, the following three analysis channels have been considered, based on truth-level requirements:

- **Muonic channel:** both γ_d in the event decay into a pair of muons;
- **Hadronic channel:** both γ_d decay into a pair of electrons or light hadrons;
- **Mixed channel:** a γ_d decays into a pair of muons and the other decays into either a pair of electrons or in a quark-antiquark pair.

Upper limits at the 95% of CL, on the branching fraction of the Higgs boson into a pair of γ_d, are reported in figure 6.2 as a function of the dark photon mean proper lifetime. The limits set in [2] show a large hierarchy in the three different channels, while the results of the monojet reinterpretation are similar among the three channels, in the limit of large dark photon lifetimes, as expected.

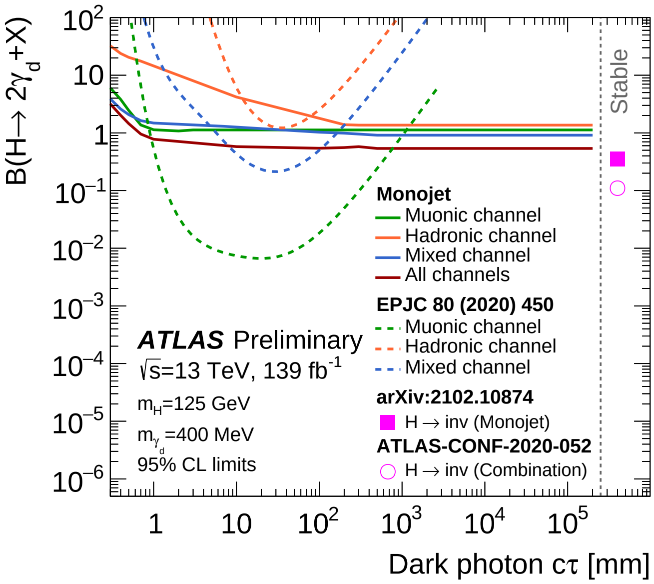

Figure 6.2. Exclusion limits at the 95% CL on the branching ratio of the process $H \to 2\gamma_d{+}X$, with the SM Higgs boson and $m_{\gamma_d} = 400\,\mathrm{MeV}$, in the Muonic (green), Hadronic (orange) and Mixed (blue) channels. The red line shows the inclusive exclusion limit, obtained when events of all the three channels are considered. The results are compared to the exclusion limits of the dedicated ATLAS search (dashed lines with same colour scheme)[2]. The $B(H \to \mathrm{inv})$ limit from the monojet [3] analysis and the combination of ATLAS Run-1 and Run-2 results [18] are also shown in the asymptotic regime of infinite lifetime. Figure from [4].

For lower values of $c\tau$ the efficiency of the monojet analysis varies for different γ_d decay modes: a dark photon decaying in two muons may go completely undetected if the muon reconstruction requirements, as defined in [3], are not satisfied. Indeed, the monojet analysis applies a veto on combined muons satisfying $|z_0 \sin\theta| < 0.5\,\mathrm{mm}$, requirements that are easily not met as soon as the $\gamma_d \to \mu\mu$ vertex is found outside the first layers of the ID. Moreover, the sensitivity loss in the case of γ_d decaying in electrons or quark pairs, is due to the fact that displaced $\gamma_d \to ee$ decays are easily reconstructed as photons, as the track identification requirements are not fulfilled, while displaced decays in electrons or quarks yield energy deposits which do not met the requirements imposed by the Loose jet cleaning criteria. However, the sensitivity decreases rapidly for more prompt-like regimes, as the decay products of the γ_d are better identified.

In the limit of very large lifetimes, $c\tau_d \gtrsim 10^2$ mm, the observed limits tend to be flat. This is expected since most of the LLPs decay outside the detector acceptance. For this reason, starting from the value of $c\tau$ for which the $E_{\mathrm{T}}^{\mathrm{miss}}$ distribution of the

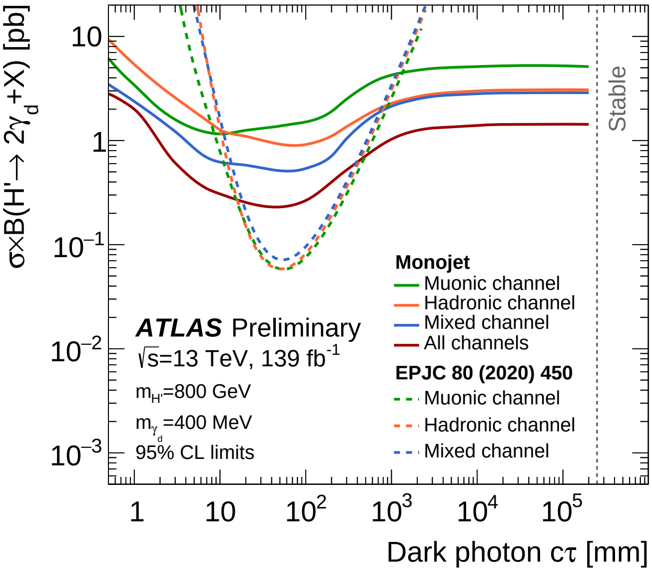

Figure 6.3. Upper limits at the 95% CL, obtained for a γ_d with $m_{\gamma_d} = 400\,\text{MeV}$ in the Muonic (green), Hadronic (orange) and Mixed (blue) channels, produced by the decay of the Higgs with $m_H = 800\,\text{GeV}$. The red line shows the exclusion limit obtained in this reinterpretation when combining the three aforementioned channels. The results are compared to the exclusion limits of the dedicated ATLAS search (dashed lines with same colour scheme) [92]. Figure taken from [4].

signal and of the $gg \to H \to$ inv process match, the observed limits are extrapolated up to very large lifetimes. The limit of the $H \to$ inv process is also reported in figure 6.2, yielding a stronger exclusion on the Higgs branching ratio than the one obtained for the $H \to 2\gamma_d + X$; this is expected, as for the latter, only the ggF production mechanism is considered, which account for the 73% of the total cross-section of the former process.

In the case where the FRVZ process is produced by the decay of a $800\,\text{GeV}$ Higgs, the results obtained are complementary to the one ones reported in [92], as visible from figure 6.3, which reports the 95% CL upper limits on the cross-section times branching fraction of the heavy scalar particle. In this case, the larger boost of the γ_d yield a stronger limit at $c\tau < 1\,\text{mm}$, while in the regime of infinite lifetimes the combined limit reaches asymptotically $\sigma \times B(H \to 2\gamma_d + X) = 1.5\,\text{pb}$, extending the existing results. The shape of the exclusion contours, as for the previous case, are related to the reconstruction efficiency of the decay products of the dark photons for the different lifetimes.

6.3.2 Limits for the $H \to ss$ model

A comparison of the limits obtained in this reinterpretation study and by other ATLAS searches [93, 87, 94] is presented in figure 6.4. As in the previous cases, the limit is presented at the 95% CL on the branching ratio of the exotic decay of the

SM Higgs boson, as function of the mean proper lifetime of the scalar particle s.

Different mass hypotheses for the scalar s yield corresponding different ranges of excluded $c\tau$. This is expected, as in the case of chapter 5, since the lifetime of s was optimised to maximise the fraction of their decays according to the acceptance of the dedicated searches.

The prompt [93] and inner detector searches based on displaced vertices [94], assume negligible signal efficiency for decays other than $s \to b\bar{b}$ and are focused on the limit of very small mean proper lifetimes. Larger values are probed by the combination of the calorimeter-based and MS-based displaced vertex searches and the corresponding limits are reported from [87]. The $B(H \to \text{inv})$ limit from the monojet analysis [3], as well as the combination of ATLAS Run-1 and Run-2 results [18], are shown in the asymptotic regime of infinite lifetime for comparison.

In this context, the monojet reinterpretation can extend the current upper limits to higher s lifetimes. The monojet result approaches asymptotically, as the mean proper lifetime approaches infinity, the value of $B(H \to ss) = 50\%$, which is, as in the case of the FRVZ interpretation, the value obtained by probing the $H \to \text{inv}$ signature produced in the gluon-gluon fusion process. This asymptotic limit is extrapolated to smaller mean proper lifetimes, as long as the $p_{\mathrm{T}}^{\mathrm{recoil}}$ distribution of this process matches with the one found by applying the lifetime reweighting method to the $H \to ss$ samples. Results at lower lifetimes are produced by running, as in the FRVZ interpretation, the monojet fit for multiple values of the lifetime-reweighted $p_{\mathrm{T}}^{\mathrm{recoil}}$ distribution.

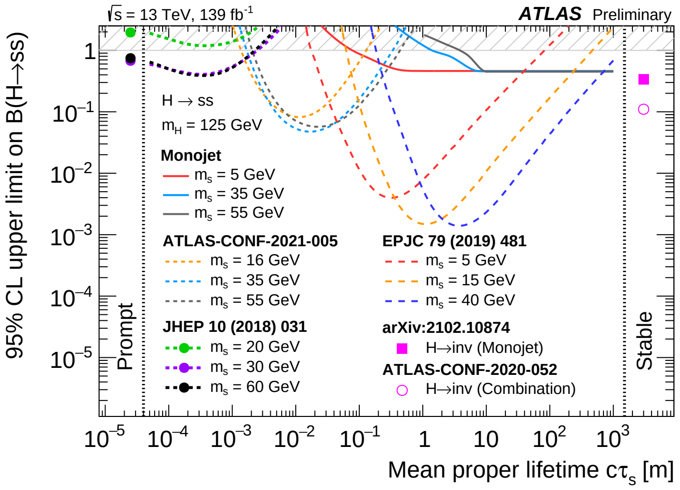

Figure 6.4. Exclusion limits, at the 95% CL, on the $B(H \to ss)$ obtained in the interpretation of the monojet analysis, shown as a function of the s proper decay length. Limits from dedicated ATLAS searches [93, 87, 94], detailed in the text, are also reported. Asymptotic limits at infinite lifetimes, for the $H \to \text{inv}$ process, are reported from the monojet analysis [3] and the combination of ATLAS Run-1 and Run-2 results [18]. The dashed area indicates the region with $B(H \to ss) > 1$. Figure taken from [4].

Chapter 7

The Phase-II upgrade of the ATLAS Barrel Muon Trigger

Within the next 10 years, a series of upgrades to the LHC subsystems will aim to an increase of its instantaneous luminosity of a factor five. The High-Luminosity LHC (HL-LHC) will rely on cutting-edge technologies such as superconducting magnets with novel design, able to generate fields from 11 to 12 T, as well as compact RF cavities and new technologies for beam collimation and control.

An extensive upgrade plan of the experiments is foreseen, to cope with the extreme conditions that will be reached at the HL-LHC, such as an average of 200 simultaneous interactions per bunch crossing. The total integrated luminosity that will be delivered by HL-LHC will be up to $3000\,\mathrm{fb}^{-1}$, approximately 20 times the one of the Run-II. A more detailed introduction, as well as a technical overview of the HL-LHC goes beyond the scope of this thesis, but the reader is referred to [95] for further information.

The Rome group of the Italian institute of Nuclear Physics (INFN) is involved in the development and the maintenance of the ATLAS MS Barrel Trigger. I have been involved in the development of the firmware of the Phase-II RPC on-detector boards and the radiation-resistance test of their electronic components. A description of these studies will be given later in this chapter, after a large-scope overview of the Phase-II upgrade of the ATLAS experiment.

7.1 ATLAS Phase-II

Different ATLAS subsystems demand advanced upgrades in order to cope with the higher pileup level, the increased data rate and the more radioactive environment. The most important upgrades are briefly summarised in the following.

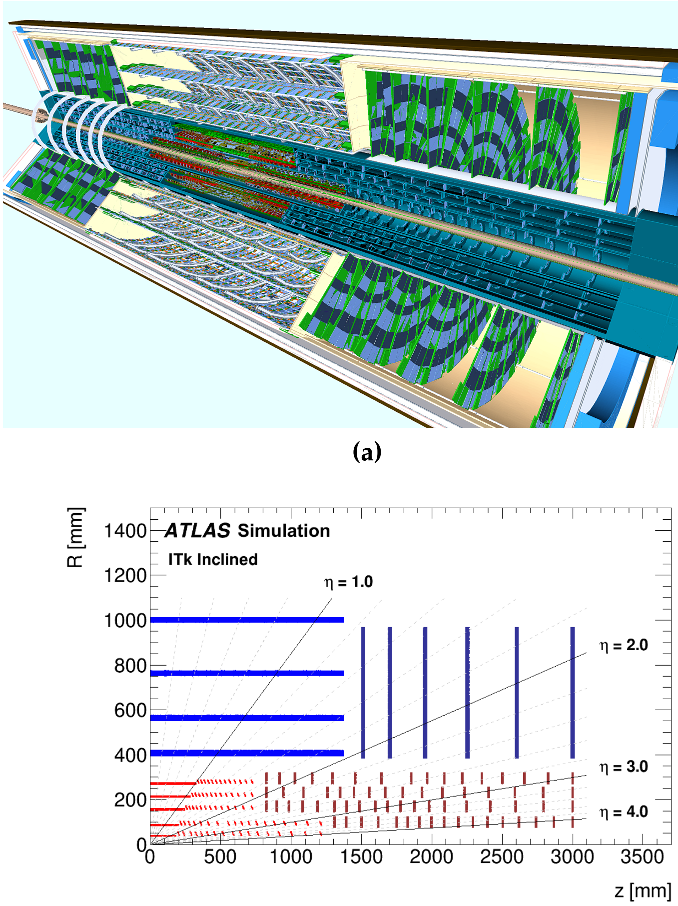

(a)

(b)

Figure 7.1. Top: rendering of the ITK detector [97]. Bottom: view in the r-z plane of a quadrant of the ITK sensitive detector area. Regions colored in blue correspond to the Strip detector, while the regions colored in red correspond to the Pixel detector [96].

ITK

A significant upgrade consists in the replacement of the entire Inner Detector with the Inner TracKer (ITK), entirely based on semiconductor technology.

The upgraded tracker will feature an innermost region (at radii smaller than $350\,\mathrm{mm}$) based on a 5-layered Pixel detector and, in the outermost part, a four-layered silicon Strip detector, of which a graphical representation is given in figure 7.1a. A detailed description of the currently foreseen design for these two sub-detectors is given in [96] and [97], respectively.

The ITK coverage will reach $|\eta| = 4$ which, compared to the actual limit at $|\eta| = 2.5$, will allow the track reconstruction in the forward region and give complementary information to the forward calorimeters.

To better achieve the desired performance at large pseudorapidity, and to limit the material traversed by particles produced at large $|\eta|$, one of the layouts proposed for the innermost Pixel detector is designed with an *inclined* layout, where the pixels of the most forward regions of the barrel are tilted, as visible in figure 7.1b.

The Strip detector covers the volume that is now occupied partially by SCT and by the TRT. It consists in four cylindrical layers in the barrel region, plus six wheels in each endcap, with a pseudorapidity coverage up to $|\eta| = 2.7$.

HGTD

In the forward region of the ITK, the track reconstruction and track-vertex association will become a major challenge. The limited longitudinal impact parameter resolution will be complemented by a precise timing information associated to the tracks, which will be provided by the High-Granularity Timing Detector (HGTD) [98].

The HGTD is a disk-shaped detector that will be installed in the volume between the forward calorimeter and the ITK, where the limited available space puts a hard constraint on its size. Two identical detectors will be placed at $|z| = \pm 3.5\mathrm{m}$, and will be based on silicon technology. An intensive challenge is to provide a precise timing resolution on the hits, of the order of $30\,\mathrm{ps}$, which will allow a reliable rejection of out-of-time pileup tracks in a harsh radiation environment.

Calorimeter system

The LAr calorimeter has been monitored intensively during the Run-I and Run-II ATLAS operations, where no significant deterioration was observed in correspondence of the increased luminosity and radiation levels. The sensitive part of the detector is expected to remain reliable during the operation of the HL-LHC, as documented in [99].

On the other hand, the trigger and data acquisition requirements imposed by the increased luminosity, on the TDAQ rate and latency, imply a revision of all the readout electronics. Part of the TDAQ electronics of the LAr is being upgraded before the start of the Run-III, as documented in [100], but a full replacement of the Run-I and Run-II electronics is foreseen in time for HL-LHC.

This will allow, at the lowest trigger level, to exploit the full calorimeter granularity and the three-dimensional information on the shower development, which are expected to increase the performance and the capabilities with respect to the current L1Calo trigger algorithms.

Muon System

For the ATLAS Muon System, a series of upgrades is foreseen before the beginning of the HL-LHC operations [101]. A substantial upgrade has been recently installed, during the Long Shutdown II, in which the two endcap Small Wheels have been replaced with upgraded detectors based on small Thin Gap Chambers (sTGC) and MicroMegas chambers. These two New Small Wheels are expected to provide

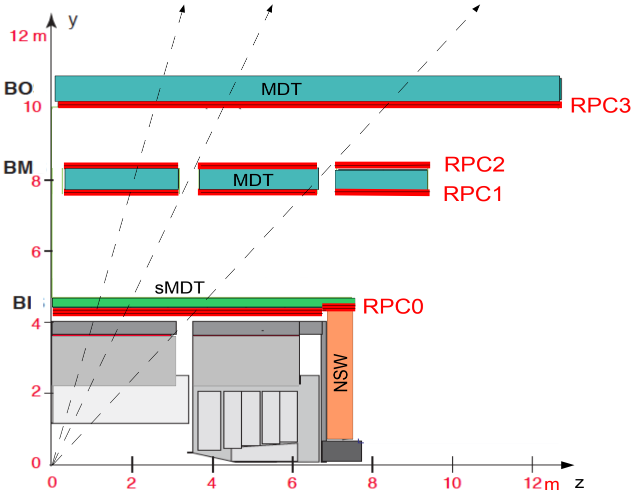

Figure 7.2. Schematics of the detectors for the Phase-II Muon Barrel trigger. The inner layer of RPC is visible, as well of the smaller MDT (sMDT) chambers. The dashed lines correspond to muons that cross four, two and three RPC chambers. Figure adapted from [103].

information valid for both trigger and precision measurements, allowing to reduce the large trigger rate observed in the MS endcap during Run-I and Run-II and to cope with the higher hit rate at a better efficiency, as documented in [102].

The remaining upgrades are focused on the Muon Trigger detectors. In the barrel, new triplets of RPC detectors will be installed on the BI muon stations, replacing the MDT chambers that are currently installed with more compact ones. While few of these newer BI chambers have already been installed during the Long Shutdown II, a replacement of the remaining ones is foreseen before HL-LHC starts. A sketch of the Phase-II Muon Barrel trigger detectors is visible in figure 7.2.

In addition, the on-detector electronics, currently providing the L1 trigger logic for RPC and TGC detectors, will be entirely replaced with data collector boards, able to transmit the information of each trigger chamber to the off-detector electronics, on which the trigger logic will be implemented. MDT electronics will be replaced as well, as the new trigger system is planned to use also their information for the lowest trigger level.

TDAQ system

As mentioned already, a significant upgrade involving all ATLAS subsystems consists in a revised trigger and data acquisition system, which is crucial to cope with the increase in instantaneous luminosity [103]. The design of the Phase-II trigger is based on a single Level-0 (L0) hardware trigger, providing a rate of 1 MHz and a 10 μs latency, with the option of a dual level (L0+L1) trigger, in case the conditions due to the higher pileup are more challenging than the expected.

The on-detector electronics of the Phase-II sub-detectors is expected to stream digitised data to off-detector systems at a $40\,\mathrm{MHz}$ rate, where the trigger logic and readout is performed.

The hardware-based L0 trigger is composed of a calorimeter-based trigger (L0Calo), a muon trigger (L0Muon), and the Global Trigger. This last one is able to exploit granular information from the entire calorimeter and run sophisticated offline-like algorithms, that can implement clustering of the calorimeter cells, improved identification of e, τ and γ, lepton isolation and better identification of exotics objects, as well as replacing the functionality of the L1Topo. The final L0 trigger decision is made by the Central Trigger Processor, which is also responsible of applying prescale factors to the trigger and dead time, if needed.

In the next section, additional details will be given on the electronics of the L0 barrel muon trigger.

7.2 Level-0 Barrel Muon Trigger Electronics

The electronics of the L0 Barrel Muon Trigger will rely on two types of devices, a on-detector board named *Data Collector Transmitter* (DCT) and a off-detector *barrel Sector Logic* (SL) board. As adopted among all the Phase-II trigger subsystems, the information is sent from the DCTs, via optical links, to the SL boards placed in the service cavern USA15, of which the position is visible from figure 2.5.

A total of 32 barrel Sector Logic boards are installed in the USA15 room, one for each sector of the barrel MS[1]. Each board implements the triggering algorithm, using the information of the RPC hits of the different layers, then transmits the RoI to the trigger processor of the MDTs, where thanks to the better spatial resolution a more precise estimate of the muon p_{T} can be obtained. The final trigger decision is sent from the SL board to the other ATLAS TDAQ systems.

In the following, the main characteristics of the DCT boards are given. For additional details on the SL and the DCT the reader is referred to [101] and [103].

7.2.1 The Data Collector Transmitter boards

The DCTs are directly interfaced to the front-end electronics of the RPC detectors, which will be kept from the current ATLAS layout. The current design of the front-end boards produces a digitised signal which, in the Phase-II upgrade, will be directly read by the DCTs, which will implement a Time-To-Digital Conversion (TDC) of the signal and transmit the measurement of the time of the leading edge to the SL.

The intrinsic resolution of the RPC detectors has been measured from $Z \to \mu\mu$ events to be smaller than $1.7\,\mathrm{ns}$ [104], therefore a digital timing resolution of the same order of magnitude is preferred for the DCTs.

The boards are based on a Field Programmable Gate Array (FPGA) which

---

[1] The barrel MS is divided in two sides (A and C), each containing 8 small and 8 large sectors.

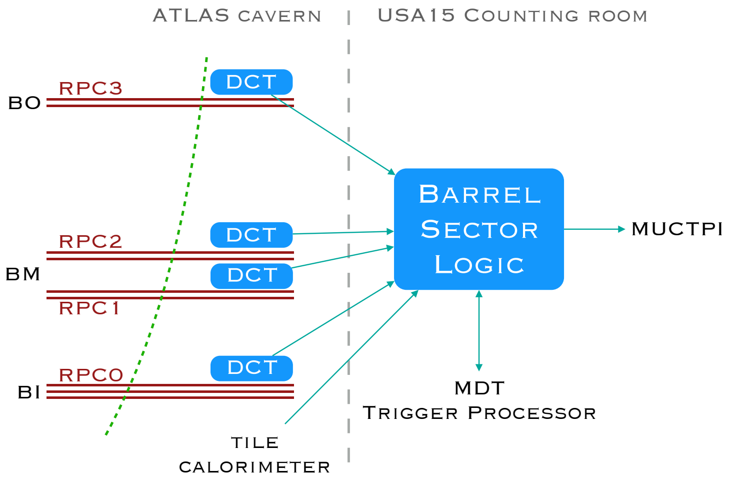

Figure 7.3. L0 Barrel Muon Trigger scheme. The DCTs present on the different RPC detectors transmit their data to 32 off-detector SL boards, which run the trigger algorithm and are interfaced with the other sub-systems of the Phase-II trigger.

hosts the programmable logic that implements the DCT functionalities. The FPGA considered is a commercial device of the Xilinx Artix-7 family and has 500 available pins for input-output functionalities.

The number of RPC strips read by a single DCT varies according to the type of RPC chamber, with a maximum of 288 strip read by a single board. This implies that the FPGA of the DCT must be able to read and process up to this number of parallel input channels. A different setup is foreseen for the DCT of the BI chambers, as their front-end electronics (currently being designed) foresee a TDC that provides digitised measurements of the leading and trailing edge of the RPC signal. In this case, the DCT will act as a more simple data collector, reading these signals and transmitting them to the SL without the need of the TDC functionality.

A total of about 1570 DCT boards is required to cover the whole detector. A single DCT will read the RPC doublet on the BO chambers, two of them are needed for the two BM doublets and the BI RPC triplet will be read by a single DCT, as visible from the scheme in figure 7.3.

Overview of the board

As mentioned above, the DCT board is based on a FPGA and it must be able to receive up to 288 digitised signals from the RPC front-end boards. A set of flat connectors allow the retro-fitting of the cabling currently in use in ATLAS, which provides differential (LVDS) signals, that are adapted to unipolar signals processed by the FPGA. A simplified scheme of the DCT board is given in figure 7.4.

The figure also shows the other key components of the DCT. The FPGA has access to a flash memory in which the firmware can be stored, allowing a faster set-up time of all the DCTs. With the only exception of the signals from the RPC front-end, all the input/output transmissions with the DCT are realised via a optical

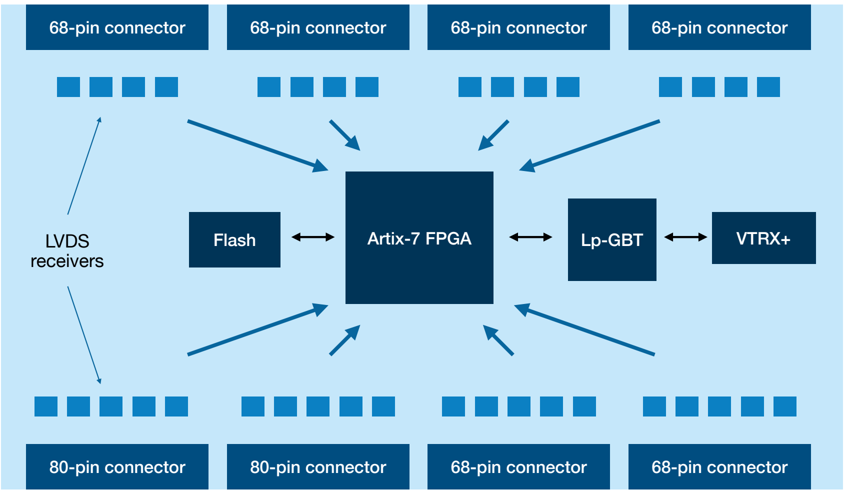

Figure 7.4. Scheme showing the different components on the DCT boards.

transceiver (VTRX+ in figure 7.4), which is interfaced to the Low-power GigaBit Transceiver (Lp-GBT), which is developed by CERN as a reliable data transmission device for HL-LHC detectors [105].

The interface between the Lp-GBT and the Artix-7 FPGA, on which the data collection and processing is performed, is realised via a total of 39 connections, which need to handle all kinds of data communication with the SL board. These include 27 channels entirely dedicated to the transmission of the hit time data, plus additional monitoring data and dedicated channels for clock distribution and firmware programming.

The board is designed to be compatible with the power distribution system of the current on-detector devices installed in ATLAS. To correctly power the different devices present on the board, five Low-DropOut (LDO) voltage regulators are installed on the DCT (not visible in figure 7.4), providing five corresponding voltages between 1.0 and 3.3 V.

The radiation-resistance of the various sub-components of the DCT need to be ensured, in order to avoid permanent damage or unexpected malfunctioning of the different devices. In the context of this thesis, multiple irradiation campaigns have been performed, to ensure that commercial LDO voltage regulators can be used on the DCT boards without problems. Details on this study are given in section 7.3.

DCT firmware and timing resolution

The FPGA of the DCT is required to process all the signals of up to 288 RPC strips, collecting their data and sending them to the SL board, with an identifier of the corresponding bunch crossing. A preliminary version of the FPGA firmware, implementing the data collection and timing measurement, has been developed within the context of this thesis and its main characteristics are summarised in the following.

The bunch crossing is uniquely identified from a $40\,\mathrm{MHz}$ clock, synchronous to the LHC collisions. Hence, the FPGA must implement a 12-bit counter, which gets incremented on each rising-edge transitions of this clock. A *bunch crossing reset* signal is also provided by the LHC, and is used by the DCT FPGA to reset this internal counter.

Other clocks are provided by the Lp-GBT and are used, with a clock multiplier implemented in the FPGA, to produce three clocks with a frequency of 200, 320 and $600\,\mathrm{MHz}$.

In order to provide the desired resolution of the TDC, a period of $25\,\mathrm{ns}$ must be sampled with at least the same number of bits. The uncertainty of $1.7\,\mathrm{ns}$ includes the contribution of the hit digitisation frequency of the current trigger boards, which operating at $320\,\mathrm{MHz}$ lead to a 18% increase of the intrinsic uncertainty of the RPCs. With the current FPGA model, it has been found that the $25\,\mathrm{ns}$ period can be sampled with up to 30 bits, corresponding to a sampling frequency of $1.2\,\mathrm{GHz}$. This yield a resolution of the digitisation step of $0.24\,\mathrm{ns}$, which is a negligible contribution to the $1.4\,\mathrm{ns}$ intrinsic resolution of the RPC.

In order to achieve such digitisation frequency on the FPGA, high-frequency deserialisers are used, sampling the RPC hit signals on both positive and negative edge of the $600\,\mathrm{MHz}$ clock. Then the measurement of the hit time is made, producing 5-bit sequences that are temporarily buffered in the FPGA, after which the zero-suppressed measurements are transmitted to the SL via the Lp-GBT.

A first prototype of the DCT board has been realised and the test of its functionalities, as well of its firmware, are foreseen in the next months.

7.3 Radiation tolerance studies for the on-detector components

The radiation levels in the ATLAS Muon Spectrometer are sufficiently low to permit the use of commercial electronics, as long as their tolerance to the expected levels has been verified.

A series of irradiation tests has been performed to select appropriate LDO voltage regulators, which are foreseen in different ATLAS on-detector boards. The required voltages on the different data collector boards, including the DCTs, as well as analogous boards of the MDT and TGC [101], range between 1.0 to $3.3\,\mathrm{V}$, with currents up to $3\,\mathrm{A}$. In addition, LDOs are foreseen also in the front-end electronics of the MDTs, where two voltages ($V_{\mathrm{out}} = 1.2\,\mathrm{V}$ and $3.3\,\mathrm{V}$) are required with a maximal current of approximately $0.3\,\mathrm{A}$. For these different devices, the voltages provided by the power supply are in the range between 3.5 and $4.5\,\mathrm{V}$.

Seven types of adjustable LDOs, listed in table 7.1, have been selected as candidates for on-board power distribution. Only two of them (TPS7A85 and ISL80103) are suitable for use in data collector boards, as they can provide sufficient output current and sufficiently low V_{out}; the others can only be used in MDT front-end.

The irradiation tests performed to select the appropriate LDOs are described in

LDO model name	Readout channel
TPS7A8500RGRT	A
TLV75101PDSQR	B, B1.2 (dual)
TLV75901PDRVT	C
ISL80102IRAJZ-TK	D
ISL80103IRAJZ-TK	E
LP3964EMP-ADJ/NOPB	F
LP3856ESX-ADJ/NOPB	G

Table 7.1. Model names of the LDO voltage regulators tested and corresponding readout channel names used during the tests.

this section.

7.3.1 Radiation damage in ATLAS

Proton-proton collisions at current conditions of the LHC originates $\sim 7 \times 10^8$ inelastic events per second. Particles originated in such events will deposit their energy in the detector components, either by ionisation or ion displacement, leading to unavoidable effects on the electronic devices. A thorough discussion of the different types of damage that can affect semiconductor devices in high energy physics experiments can be found in [106, 107]. However, a few details are briefly mentioned in the following.

Total Ionising Dose

Ionising particles crossing a semiconductor can create hole-electron pairs. If such semiconductors are biased, the electrons will escape the lattice, leaving trapped charges which accumulates over time. The progressively accumulated charge can create different kinds of damage, according to the semiconductor type and technology. This energy deposition is named *dose*, or Total Ionising Dose (TID), which is measured in Gy.

Single Event Effects

Single Event Effects (SEE) are a class of radiation effects on electronic devices, which originate from a large energy deposit left by the ionisation of an energetic particle. These effects can be either destructive or non-destructive, a list of few examples is:

- **Non-destructive effects**
    - **Single Event Upset (SEU)**, where the ionisation leads to a change of status in a bi-stable circuit;
    - **Single Event Transient (SET)**, in which the charge left by an ionising particle gets collected as a signal;

- **Destructive effects**
  - **Single Event Latchup (SEL)**, where a highly ionising particle temporarily alters the structure of some electronic devices, leading to a self-sustained current which may damage the device;
  - **Single Event Burnout (SEB)**, where the large current created by the ionisation left by heavy ions and energetic protons/nucleons, can potentially melt or cause permanent physical damage to the semiconductor.

Displacement damage

Elastic scattering of a particle with nuclei of a semiconductor can displace an atom from its site, originating an atom-vacancy pair which builds up extended defects of the lattice. This kind of damage is expected to depend on the particle energy, mass and the possible presence of other reactions (e.g. neutronic capture). In order to define a quantity that is not dependent on the properties of the scattering particles, the concept of *Non-Ionising Energy Loss* (NIEL) must be introduced. This concept can be applied to all the different types of interactions in which the energy imparted by the incoming particle result in atomic displacements or is dissipated in lattice.

The NIEL concept is based on the assumption that the probability of having defects due to these types of interaction scales linearly with the integrated flux of particles over time: the particle fluence (Φ). In addition, it is also assumed that the damage due to different sources can be scaled, using an appropriate *damage function*, to the one induced by a $1\,\mathrm{MeV}$ neutron source on silicon.

The resistance of electronic components is qualified in terms of the $1\,\mathrm{MeV}$-neutron-equivalent fluence on Si, Φ_{eq}, which is also referred to as the NIEL dose, and is expressed in $\mathrm{n\,cm^{-2}}$ $(1\mathrm{MeV\ eq.\ on\ Si})$.

The equivalent fluence of $1\,\mathrm{MeV}$ neutrons on silicon can be calculated by scaling the fluence Φ of a given particle spectrum by the *hardness factor* κ, defined in:

$$\Phi_{\mathrm{eq}} = \Phi \cdot \kappa = \Phi \cdot \frac{\displaystyle\int D(E)\phi(E)dE}{D(E_n = 1\,\mathrm{MeV}) \cdot \displaystyle\int \phi(E)dE} .$$

Here $D(E)$ is the damage function, shown for protons, neutrons and pions in Fig. 7.5; $D(E_n = 1\,\mathrm{MeV})$ is the damage function for $1\,\mathrm{MeV}$ neutrons on Silicon (which corresponds to an energy deposit of $95\,\mathrm{MeV mb}$) and $\phi(E)$ is the energetic spectrum of a particle.

ATLAS prescription

In order to use commercial electronic components in ATLAS on-detector devices, the current prescription is that at least ten devices are tested up to a dose corresponding to a pre-defined Radiation Tolerance Criterion (RTC) and no significant performance deterioration occurs after the test.

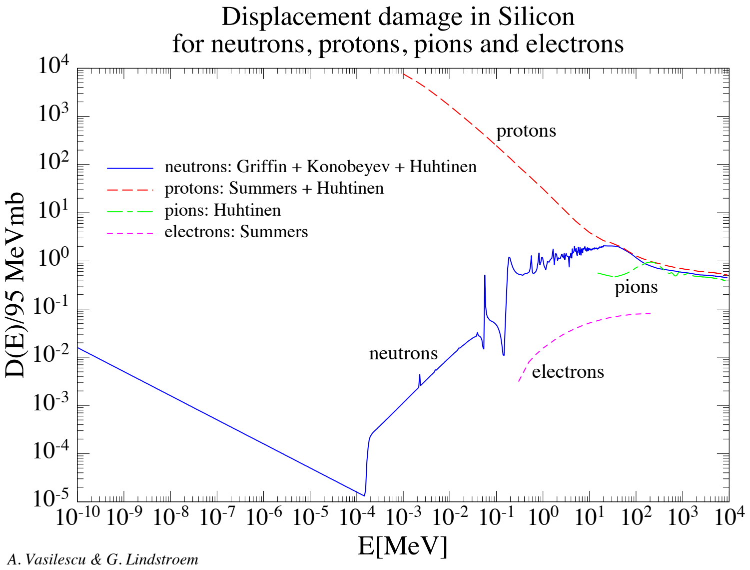

Figure 7.5. Damage function for neutrons, protons, electrons and pions, normalised to $95\,\mathrm{MeV mb}$ (i.e. normalised to the energy released by $1\,\mathrm{MeV}$ neutrons on silicon) [108].

	TID	NIEL	SEE
Safety factor	4.5	5.85	9
RTC	Gy	$\mathrm{n\,cm^{-2}}$ ($1\,\mathrm{MeV}$ eq on Si)	$\mathrm{h\,cm^{-2}}$ ($E > 20\,\mathrm{MeV}$)
MDT Front-end	300	8.5	2.5×10^{12}
Data collecor boards	100	7	2×10^{12}

Table 7.2. Safety factors and Radiation Tolerance Criterion (including the safety factors) for the MDT front end and the data collector boards (including the DCTs) [101].

The RTC is obtained as the product of the simulated radiation level for ten years of HL-LHC operation [109] multiplied by safety factors that depends on the type of radiation and the type of test, which are reported in 7.2. These are computed for TID, NIEL and for single event effects due to a flux of hadrons with $E > 20\,\mathrm{MeV}$.

The applied safety factors are 4.5, 5.85 and 9 for TID, NIEL and SEE, respectively. The SEEs should be divided in destructive SEEs (e.g. single-event burnouts) which must not be observed, and recoverable effects (e.g. single-event transients, SET) which can be tolerated, provided the rate is low enough to permit reliable and efficient operation.

7.3.2 Experimental setup

The LDOs listed in table 7.1 have been irradiated with neutrons provided by a reactor, to test their resistance to NIEL, and with $200\,\mathrm{MeV}$ protons, to test their tolerance to TID and SEE.

A set of *LDO test boards*, like the one visible in figure 7.6a, has been produced, each one is equipped with the seven different LDO models. Two stacks of ten identical test boards each (figure 7.6), have been used for irradiation with neutrons and protons.

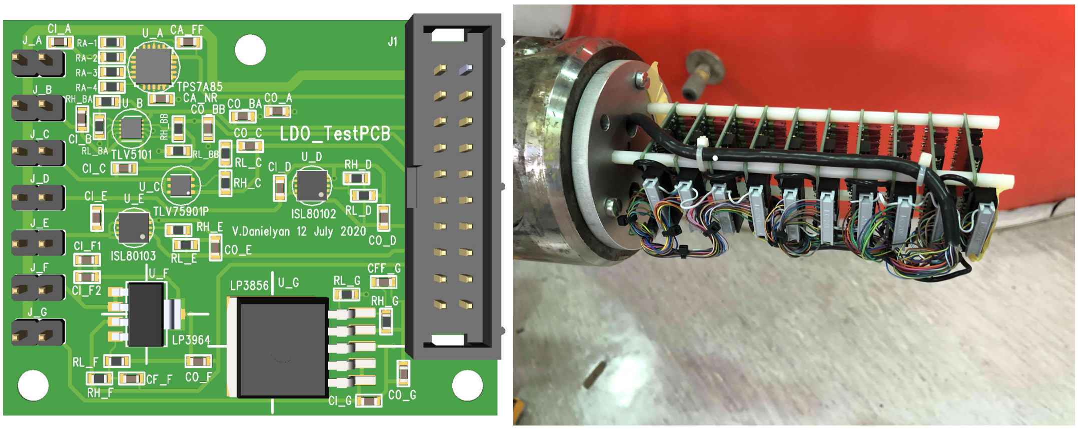

(a) **(b)**

Figure 7.6. (a) Rendering of one LDO Test Board. (b) Side view of the LDO stack before the neutron irradiation.

The input voltage of the LDOs was $4.2\,\mathrm{V}$, compatible with the value of the low-voltage power distribution foreseen in ATLAS Phase-II. The output voltage was adjusted with resistors to select between 3 and $3.3\,\mathrm{V}$, a value typical of the expected application in ATLAS electronics; two exceptions are the TPS7A85, which was set to $3.8\,\mathrm{V}$ and the TLV75101 which has a secondary output set to $1.2\,\mathrm{V}$. Each LDO channel had a load resistor of $100\,\Omega$, thus providing a typical current of $33\,\mathrm{mA}$.

The LDO test boards were connected to a relay-based *multiplexer board*, which allowed to connect the eight LDOs output voltages, of one board at a time, to eight readout channels. The readout was performed with another board, equipped with a microcontroller and a 24-bit ADC data logger, allowing the remote control of the relays of the multiplexer board and the logging of the LDO output voltages. In order to monitor SEEs, during the first proton irradiation, an oscilloscope was connected to four LDOs (corresponding to channels A, E, F, G of table 7.1).

A different setup was used in the second proton irradiation, as some results from the first one required additional studies, as it will be explained in section 7.3.4. A new stack of ten LDO test boards (mounting only ISL80103) was used, together with an additional board, specially designed for SET monitoring of TPS7A85. The LDOs on the special TPS7A85 test board were adjusted to produce different V_{out}, from $1.0\,\mathrm{V}$ to $3.3\,\mathrm{V}$, with different load resistors to draw up to $1\,\mathrm{A}$ per channel, providing an operation mode very close to the foreseen application in ATLAS. The V_{out} was monitored for four devices with ADCs, while waveforms were acquired and counted with a DRS4 evaluation board [110] and with an oscilloscope.

7.3.3 Neutron irradiation

The neutron irradiation has been performed at the RSV TAPIRO [111], a fast nuclear reactor available at the *Centro Ricerche ENEA Casaccia* (ENEA research center) near Rome.

The stack of 10 LDO test boards have been placed in a cylindrical irradiation volume of the *Radial Channel 1* of the reactor, with a diameter of $121\,\mathrm{mm}$ and length of $200\,\mathrm{mm}$, with a minimum distance from the reactor core of $480\,\mathrm{mm}$.

A simulation of the neutron spectrum in the irradiation volume was obtained with the MCNP software [112], convoluted with the damage function of figure 7.5, to compute the expected NIEL on each LDO. The neutron spectrum of the reactor ranges from thermal neutrons to approximately $10\,\mathrm{MeV}$. According to the simulation, the $1\,\mathrm{MeV}$ equivalent neutron fluence in the irradiation volume, when the reactor operates at $1\,\mathrm{kW}$ for one hour, is estimated to be $\Phi_{\text{eq}} = 2.07 \times 10^{12}\,\mathrm{n\,cm^{-2}}$.

The estimated NIEL is validated by the measurement of the gamma line from the neutron activation of gold foils, placed in the volume before the irradiation, through the $^{197}\mathrm{Au}(n,\gamma)^{198}\mathrm{Au}$ reaction. A second estimate is given by six BPW34F p-i-n diodes, which were also put in the irradiation volume.

These diodes have been studied and characterised at CERN as devices sensitive to displacement radiation damage and are currently used in radiation monitoring devices (RadMon) [113, 114]. A detailed characterisation of this specific diode is reported in [115]. After the neutron irradiation, the diodes have been extracted and, from a measurement of the increase of the forward voltages, it was possible to infer the equivalent fluence with the calibration formula reported in [114]. Good agreement is observed between the simulated fluence and the one estimated with Au foils, as well as the one obtained from the BPW34F, within the expected calibration uncertainty of 20%.

Three irradiation runs have been performed, after which a total average neutron fluence $\Phi_{\text{eq}} = 5.11 \times 10^{13}\,\mathrm{n\,cm^{-2}}$ in the irradiation volume was reached. The LDO output voltages have been recorded and monitored during each irradiation, during which the devices have been power-cycled multiple times.

Only at very large NIEL, above $\Phi_{\text{eq}} = 5.33 \times 10^{13}\,\mathrm{n\,cm^{-2}}$, some LDO started to fail, producing $V_{\text{out}} = 0$ in most of the cases, or showing decreased or increased output voltages. In more than 90% of the cases, failures of the LDO happened right after a power cycle.

The corresponding NIEL dose at the time of the first failure (or at the end of the irradiation runs) is reported in table 7.3 for each device. In figure 7.7, two examples of the LDO failures detailed in table 7.3 are shown. As no regulator failed for $\Phi_{\text{eq}} < 10^{13}\,\mathrm{n\,cm^{-2}}$, all the LDO types satisfied the requirement on NIEL.

7.3.4 Proton irradiation

To test the LDO resistance to TID and different types of single-event effects, the second stack of LDO test boards has been irradiated with $200\,\mathrm{MeV}$ protons at the

	Φ_{eq} at failure or after irradiation [$\times 10^{13}\,\mathrm{n\,cm^{-2}}$]							
Board	A	B	B1.2	C	D	E	F	G
1	5.7	5.7	5.7	5.8	5.7	5.9	5.8	5.8
2	6.1	6.1	6.1	6.1	$6.1^\bullet$	$5.9^\bullet$	6.0	6.0
3	6.5	6.4	6.4	6.5	6.4	$5.8^\bullet$	6.4	6.4
4	7.2	7.2	7.2	7.3	$6.9^\bullet$	$5.9^\bullet$	7.1	7.1
5	7.8	7.5^*	7.0^*	7.5^*	$6.5^\bullet$	$6.2^\bullet$	7.8	7.8
6	8.8	6.7^*	6.7^*	6.7^*	$6.3^\bullet$	5.4^*	8.8	8.8
7	9.7	6.1^*	$6.1^\dagger$	$6.1^\dagger$	$6.1^\bullet$	6.0^*	9.8	9.8
8	10.8	6.4^*	6.3^*	6.1^*	$6.8^\bullet$	6.7^*	12.2	12.2
9	12.7	6.7^*	5.8^*	5.8^*	6.0^*	8.2^*	14.4	14.4
10	14.5	5.3^*	5.7^*	5.5^*	$5.9^\dagger$	$5.8^\bullet$	16.7	16.7

Table 7.3. $1\,\mathrm{MeV}$ equivalent neutron fluence on each LDO after full irradiation or, in case of failure, at failure time (marked cells). The corresponding LDO model of each readout channel is given in table 7.1, while the board index increases as the LDO test boards are placed closer to the neutron source. Different failure types have been observed and the corresponding cells of this table are marked as follows: LDOs which suddenly gave $V_{\mathrm{out}} = 0$ (*), LDOs whose V_{out} decreased by at least 10% after a power cycle (•) (see figure 7.7) , LDOs which gave $V_{\mathrm{out}} = 0$, similarly to the first type, then recovered for a while and finally failed again (†).

Proton Irradiation Facility (PIF) of the Paul Scherrer Institut (Villigen) [116]. The stack of 10 boards was installed on a movable support, allowing the proton beam to be correctly aligned with the boards, as visible from figure 7.8.

The proton rate was constant during the irradiation, while the beam profile was approximately flat within a circular region of $50\,\mathrm{mm}$ of diameter, which covers the area of a test board. This is sufficient to assume that all the LDOs on the test boards received the same dose.

To check if any significant beam degradation effect was present, due to the interaction of the protons with the material of the test boards, a GEANT4 [44] simulation of the proton beam and the LDO stack has been made. The intensity of a simulated $200\,\mathrm{MeV}$ proton beam, covering the transverse profile of the stack, was found to decrease by less than 15%. After the first irradiation test a total fluence of $2.1 \times 10^{12}\,\mathrm{p\,cm^{-2}}$ was delivered to the LDOs, corresponding to a total dose of $1.2\,\mathrm{kGy}$ according to calibration from PSI beam team. As done during the neutron irradiation, the LDOs have been power-cycled at different times and their output voltages were recorded remotely.

Multiple failures have been observed and, as during the neutron irradiation, most of them happened right after a power cycle.

The readout channels A, E, F and G were also monitored with a AC-coupled oscilloscope and the last three of them didn't show any effect related to the beam. For the LDO of channel A (TPS7A85), several drops in its V_{out} were observed during the irradiation with protons, lasting approximately $1\,\mathrm{\mu s}$ and followed by voltage oscillations that could be attributed to SET. On the other hand, several failures of

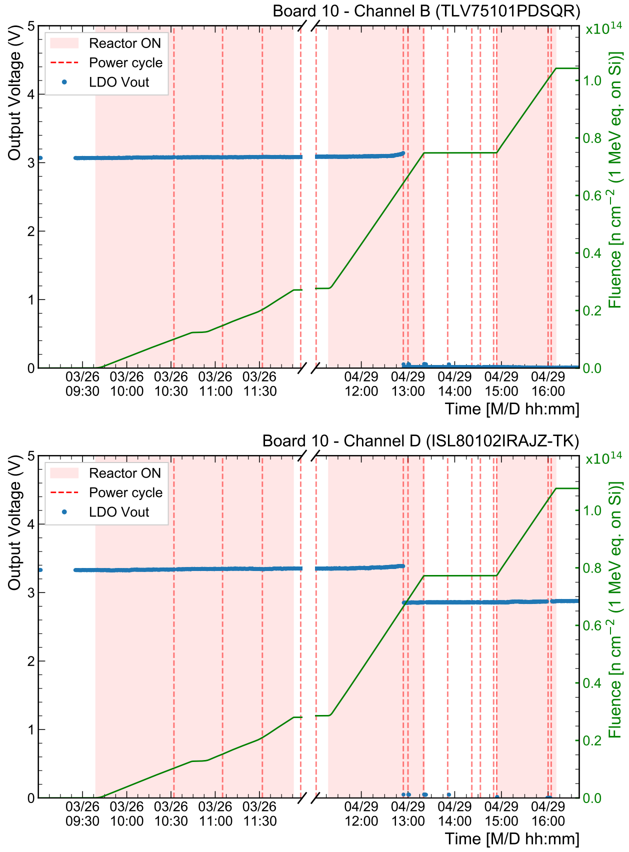

Figure 7.7. Behaviour of the V_{out} of two LDOs during two runs of the neutron irradiation. Figure (a) shows a LDO (TLV75101PDSQR) which fails and gives $0\,\mathrm{V}$ as output. Figure (b) shows a LDO (ISL80102IRAJZ-TK) which suddenly decreases its output voltage. The pink area denotes the period in which the reactor was turned on, while red dashed lines denote the times at which a power cycle of all the boards have been performed. The green line and axis report the fluence on the corresponding LDO as a function of the irradiation time.

the LDOs of channel E (ISL80103) were observed during the first power cycle of the device, after a total ionising dose of $307\,\mathrm{Gy}$. Since this value is very close to the RTC for these devices, the hypothesis that a previous power cycle would have revealed a failure at lower dose can not be excluded. These two behaviours were not understood after the first test and motivated a second proton irradiation.

During the second proton irradiation a proton fluence of $1.05 \times 10^{12}\,\mathrm{p\,cm^{-2}}$, corresponding to $607\,\mathrm{Gy}$ was provided. In order to study the effect of the ten ISL80103 devices, power cycles were done every 2 to 4 minutes (corresponding to 20 - $40\,\mathrm{Gy}$), while the four TPS7A85 were constantly monitored.

All the ten devices of channel E failed between 280 and $500\,\mathrm{Gy}$ and neither voltage drops nor any other type of failure were observed for the four TPS7A85. The total ionising dose after the full irradiation, or after the first failure observed corresponding to each LDO, is reported in table 7.4.

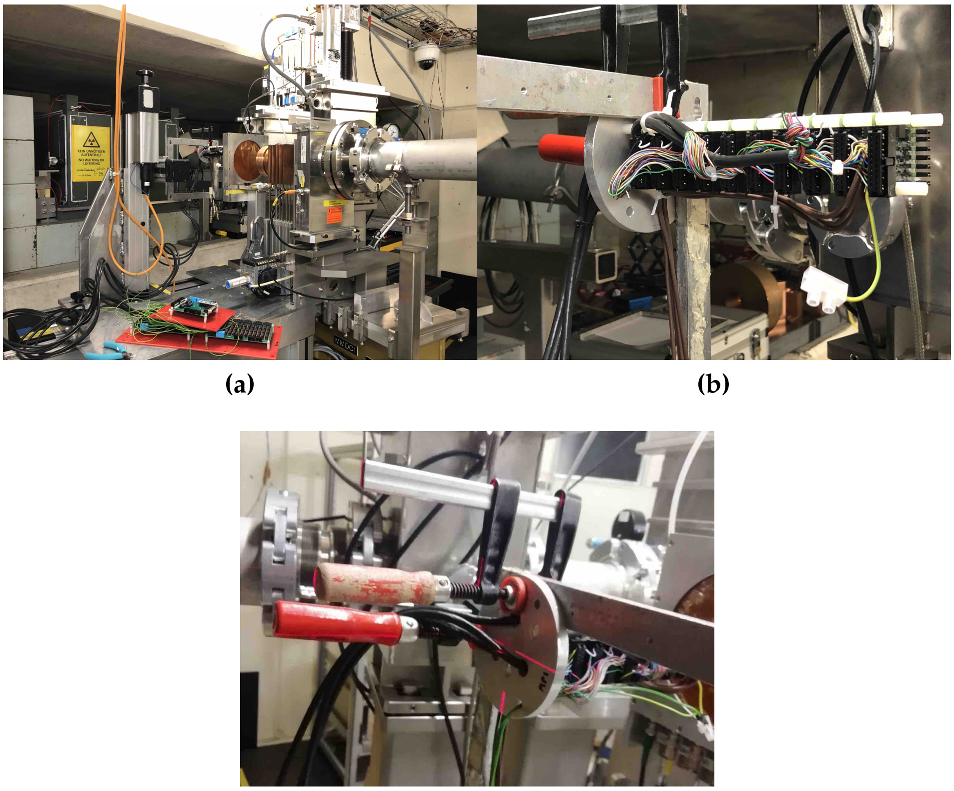

(a) (b)

(c)

Figure 7.8. (a) View of the stack of LDO test boards, mounted on the supporting structure aligned with the beam. (b) Zoomed view. (c) Rear view of the LDO stack, showing the beam alignment laser.

7.3.5 Final considerations

The resistance of the electronic components to different kinds of radiation damage is an important requirement for the experiments of the LHC. The tests described in this section aimed to identifying devices that will be used during the operation of HL-LHC on different components of the ATLAS MS.

The low-dropout voltage regulators of table 7.1 have been tested up to a NIEL of minimum $5.3 \times 10^{13}\,\mathrm{n\,cm^{-2}}$ $(1\mathrm{MeV\ eq.\ on\ Si})$, which is over six times the required test dose for displacement damage. Identical devices have been irradiated with protons, where a stable V_{out} was observed up to approximately $300\,\mathrm{Gy}$, corresponding to an hadron fluence of 0.54×10^{12} h cm^{-2} for each LDO. This implies that the TID test must be considered successful, except for the ISL80103, for which failures at $280\,\mathrm{Gy}$ were observed.

In general, all of the failures of each device type happened after a similar integrated dose, indicating an effect related to the accumulated NIEL damage or TID, rather than caused by irrecoverable SEE.

Single Event Transients have been monitored for the LDOs of channels A, E,

	TID at failure or after irradiation [Gy]									
	First test								Second test	
Board	A	B	B1.2	C	D	E	F	G	A	E
1	1200	497$^\bullet$	497$^\bullet$	497$^\bullet$	413†	307*	1200	1200	600	400$^\bullet$
2	786	497$^\bullet$	497$^\bullet$	497$^\bullet$	413$^\bullet$	307†		786$^\diamond$	600	500$^\bullet$
3	1200	497$^\bullet$	497$^\bullet$	497$^\bullet$	413$^\bullet$	359$^\bullet$	1200	1155$^\diamond$	600	440$^\bullet$
4	1200	497$^\bullet$	497$^\bullet$	497$^\bullet$	413†	307†	1200	842$^\diamond$	600	400$^\bullet$
5	1200	515$^\bullet$	497$^\bullet$	497$^\bullet$	413†	307$^\bullet$	1200	812$^\diamond$		280$^\bullet$
6	1200	441$^\bullet$	413$^\bullet$	497$^\bullet$	413$^\bullet$	413*	1200	642$^\diamond$		400$^\bullet$
7	1200	600$^\bullet$	497$^\bullet$	600$^\bullet$	497†	497†	685$^\diamond$	576$^\diamond$		400$^\bullet$
8	1200	497$^\bullet$	497$^\bullet$	497$^\bullet$	307*	413$^\bullet$	1160$^\diamond$	573$^\diamond$		400$^\bullet$
9	1200	497$^\bullet$	600$^\bullet$	497$^\bullet$	413$^\bullet$	307$^\bullet$	1020$^\diamond$	579$^\diamond$		350$^\bullet$
10	1200	497$^\bullet$	497$^\bullet$	497*	413$^\bullet$	413†	1200	558$^\diamond$		400$^\bullet$

Table 7.4. TID for each LDO after full irradiation with protons or, in case of failure, at failure time (marked cells). Results are shown for the first irradiation (left), and for the second irradiation (right) in which only 10 LDOs of type E and 4 of type A have been tested. The proton fluence can be obtained from TID as $\Phi_\mathrm{p} = \mathrm{TID} \cdot 1.75 \times 10^{12}\,[\mathrm{p\,cm^{-2}\,kGy^{-1}}]$. Failure types are: LDOs which failed giving $V_\mathrm{out} = 0$ (*); LDOs with V_out changed by at lest 10% after a power cycle ($\bullet$); LDOs giving $V_\mathrm{out} = 0$, similarly to the first type, then recovering for a while and finally failing again (†); LDOs with a steady increase of V_out, exceeding 10%, without any correlation to the power cycles ($\diamond$).

F and G. While no effect was observed for the last three LDO types, some rapid decrease in its V_out was observed for channel A, which disappeared after improving the setup. The LDO planned for being used in the RPC DCT, the TPS7A85, was found to satisfy all the required test. Future studies on the irradiated devices are planned, as soon as they will be available again after the irradiation.

Conclusions

In this thesis a search for New Physics has been performed exploring the paradigm of long-lived particles.

According to different theoretical models, neutral long-lived particles may be produced in pp collisions, by exotic decay modes of the SM Higgs boson or by the decay of bSM scalar particles.

In the scenario in which a low-mass, long-lived neutral dark photon decays outside the acceptance of the ATLAS Inner Detector, collimated muon bundles or narrow jets can be produced. The displaced Dark-Photon-Jet analysis, of which the key aspects were described along the chapters 3, 4 and 5, has been developed to explore this region of the phase space. Comparing to the previous iteration of the analysis [2], the search presented in this thesis was based on $139\,\mathrm{fb}^{-1}$ of data collected by ATLAS and, thanks to many improvements, increased the discovery potential of the previous one. These includes additional search channels, like the one of the WH category, a renovated event selection for the channels of the ggF category and the introduction of the new neural-network-based taggers for background reduction. Given that no significant disagreement with the SM was observed, the results were used to constrain the parameters of the FRVZ and HAHM models.

Searching for long-lived particles in the outermost regions of a detector that, by design, is optimised for the identification of prompt objects, always represents a challenge. When the predicted particles have a decay lifetime so long that a significant fraction of the decays happens outside ATLAS, no custom object reconstruction can help. Instead, the results of a search for invisible objects like the monojet one [3] can be interpreted in terms of long-lived particles. Using the full Run-II dataset, the results of the monojet search are used to put constraints on the FRVZ and $H \to ss$ models in the regime of very large mean proper lifetimes.

The results presented in this thesis show how the ATLAS detector is sensitive to models that admit an interaction between the SM photon and the dark photon via a vector portal, when the production of the latter is admitted via the Higgs portal. This is clearly visible, for the case of the FRVZ model, in figure 7.9. The figure reports the most recent ATLAS results for the displaced search and monojet interpretation, presented in this thesis, as well as the results from the prompt search from ATLAS [90] and CMS [117], compared to the 90% CL exclusion limits on the vector portal already shown in figure 1.8.

None of these searches would have been possible without the effort of the

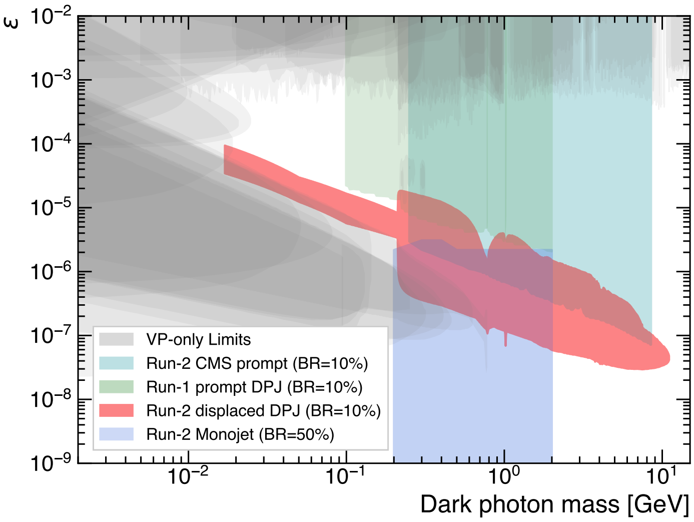

Figure 7.9. Exclusion regions at the 90% CL for the FRVZ model, as a function of the dark photon mass and vector portal coupling ε. Limits from this thesis are reported including the full Run-II displaced DPJ search and the monojet interpretation. The results from prompt searches from ATLAS [90] and CMS [117] are also shown, overlaid to the excluded regions obtained assuming the vector portal for both production and decay of the γ_d.

people of the collaborations and their past and present work related to the detector construction and operation. The upgrade of the LHC will increase dramatically the instantaneous luminosity and continuous efforts are made by the people to adapt the detector to the harsh conditions of the HL-LHC. My personal contributions related to the on-detector boards foreseen for the Phase-II Muon Barrel Trigger have been documented in this thesis. The studies related to the firmware of the DCT boards will help in constructing a definitive version of the data collector algorithm that will be needed for a fully operational muon trigger, while the radiation-tolerance tests that have been performed were crucial in the decision of which voltage regulator device is more suitable for the operation during the HL-LHC era.

Appendix A

Comparison with recent results and future prospects

In this appendix a comparison of the results obtained in this thesis with two recent results from the CMS Collaboration is presented. Moreover, a brief summary of the prospects of the search for displaced Dark-Photon Jets at HL-LHC is also discussed.

A.1 Comparison with results from the CMS Collaboration

The Hidden Abelian Higgs Model, presented in section 1.3.2 and investigated in chapter 5, was also studied by the CMS collaboration exploiting the muonic decay channel of the dark photon. Two recent results are discussed in the following.

The most recent study presents a search for secondary vertices produced by dark photons decaying in muon pairs [118]. The search exploits $97.6\,\text{fb}^{-1}$ corresponding to the data-taking periods of 2016 and 2018. Events are initially selected using a di-muon trigger, based on the sole information of the muon spectrometer. Stand-alone muons (STA) are then reconstructed without a constraint on the interaction point in order to reach the best efficiency for γ_d decays occurring outside the inner tracker. Then, a matching between STA muons and muons reconstructed using both the tracker and the muon system information (TMS) is performed at this stage. Muons that are STA and are successfully associated to TMS ones are discarded, keeping the latter for analysis purposes.

By using this approach, the efficiency of identifying a muon pair from displaced decays can be extended to the full acceptance of the detector, as visible from figure A.1.

Muon pairs which satisfy a set of requirements on their distance of closest approach are fitted in order to find a secondary vertex, keeping at maximum two displaced vertices in each event. The combined use of TMS and STA muons, as well as a selection optimised on the properties of muons and secondary vertices, allow this search to be sensitive in a broad range of possible γ_d proper decay lifetimes.

As no deviation from the expected background is found, the results are used to constrain the branching ratio of the Higgs decaying in a dark photon pair, as predicted by the HAHM model. Figure A.2 show the 95% CL limit on the product of the branching ratio of $H \rightarrow 2\gamma_d$ and the branching ratio of $\gamma_d \rightarrow \mu\mu$, where it becomes clear how crucial the combined use of TMS and STA muons allow to constrain such models for a range of $c\tau$ that goes between fractions of millimeter to several kilometers.

Another, though less recent CMS result [119], exploits a dedicated data-processing stream to set limits on the HAHM model. This approach, known as *data scouting*, allows to use triggers with reduced momentum thresholds, recording only a limited amount of information available at the HLT. During normal data-taking runs, triggers with an excessive output rate are prescaled in order to limit the total HLT event rate to $\sim 1\,\text{kHz}$, before data storage. For the case of data scouting triggers, the full event reconstruction is not run and the reduced amount of recorded information allows to increase the output rate to about $3\,\text{kHz}$.

In this study, the analysis is performed on data collected during 2017 and 2018, corresponding to $101\,\text{fb}^{-1}$. Events are selected by a scouting trigger that requires two opposite-sign muons with $p_{\text{T}} > 3\,\text{GeV}$. At this stage, the recorded events are processed searching for at least one muon pair with a corresponding secondary vertex. Finally, a fit of the di-muon mass distribution is performed in different regions of the L_{xy} of the secondary vertex, searching for an excess of events that could be attributable to a narrow resonance.

As no excess is found in the fitted invariant mass distribution of two muons, limits are set on the production of a pair of γ_d according to the HAHM model. Figure A.3 show the 95% CL limit on the product of the branching ratio of $\gamma_d \rightarrow \mu\mu$ times the branching ratio of the $H \rightarrow 2\gamma_d$ process, as function of the dark photon mass.

The results of these two studies is shown in the $\varepsilon - m_{\gamma_d}$ plane in figure A.4, where the HAHM limit from chapter 5 is also reported for comparison. The figure clearly show how the three studies are complementary in m_{γ_d}. ATLAS is able to exclude where $\gamma_d \rightarrow \mu\mu$ decays are forbidden or suppressed due to the presence of hadronic resonances, thanks to the powerful background rejection methods introduced in this thesis. On the other hand, the two CMS searches target higher masses of the γ_d, being able to probe this model for a wide spectrum of dark photon lifetimes thanks to the scouting trigger and to an efficient identification of secondary vertices.

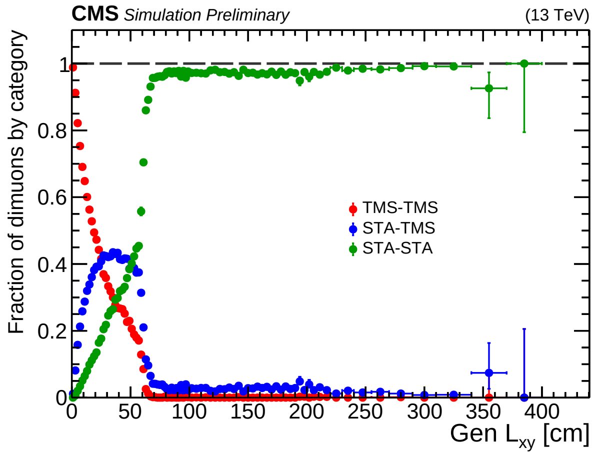

Figure A.1. Fraction of signal events with zero (STA-STA), one (STA-TMS) and two (TMS-TMS) muons that were successfully matched from STA to TMS. The efficiency is shown as function of the true L_{xy} of a long-lived particle decaying in a pair of muons and it is normalised to the number of events where at least two STA muons are found. Figure taken from [118].

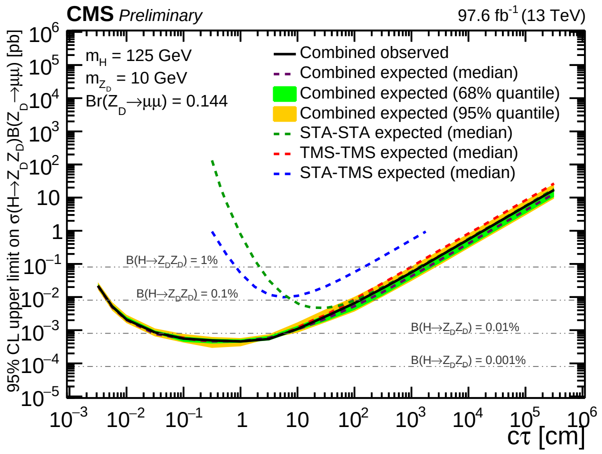

Figure A.2. 95% CL upper limit on the product of the dark photon branching ratio to a muon pair times the branching ratio of the $H \to 2\gamma_d$ process (γ_d is reported as Z_D in the figure). Limits are shown for a dark photon mass of $10\,\mathrm{GeV}$ produced by the decay of the SM Higgs boson, as predicted by the HAHM model. Figure from [118].

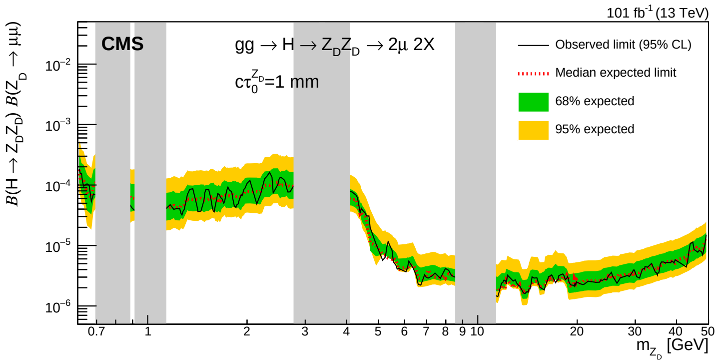

Figure A.3. Exclusion limits at 95% CL on the product of the branching ratios of $H \to 2\gamma_d$ and $\gamma_d \to \mu\mu$, shown as function of the dark photon mass and for $c\tau_{\gamma_d} = 1\,\mathrm{mm}$ (γ_d is reported as Z_D in the figure). The vertical gray bands correspond to mass regions that are masked for this search, as they contain known SM resonances. Figure taken from [119].

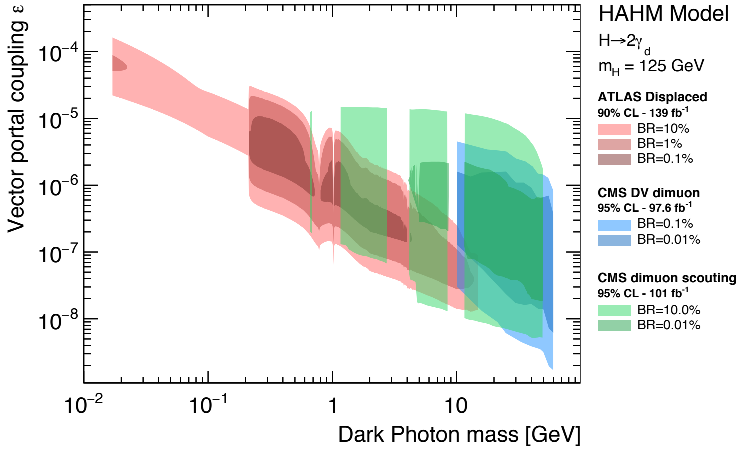

Figure A.4. Exclusion limits on the HAHM model, reported for different assumption of the branching ratio of $H \to 2\gamma_d$ on the $\varepsilon - m_{\gamma_d}$ plane. Contours depicted in red correspond to the 90%CL ATLAS results obtained in this thesis, while the regions colored in blue and green correspond to the 95% limits obtained by CMS, by the displaced di-muon search performed with standard triggers [118], and the scouting trigger [119], respectively.

A.2 Dark-Photon Jets at HL-LHC

This section will briefly summarise the prospects of the displaced Dark-Photon Jet searches at HL-LHC, which were published in [120].

This study was conducted by the ATLAS Collaboration in 2019, starting from the expected performance of the Early Run-II displaced DPJ search. Only dark photons predicted by the FRVZ model and decaying in muon pairs were considered. During the operation of HL-LHC it is expected that the center-of-mass energy of the collisions will reach the nominal value of $14\,\text{TeV}$ and that $3000\,\text{fb}^{-1}$ will be delivered to the experiments. At these energies the value of the cross section of ggF production of the Higgs boson will increase by 12%, as shown in table 1.1.

A summary of the upgrades that are foreseen for ATLAS has been presented in chapter 7. The L1 muon trigger, which is nowadays a limiting factor for this analysis will be improved thanks to the additional RPC layer and a re-design of the TDAQ system. A dedicated study was presented in [120] showing two ideas for improving the L0 barrel muon trigger, which can be summarised as follows.

Muons from dark photon decays can be highly collimated, as shown in figure 3.3b, and are likely to fall within the same RoI of the muon trigger, corresponding to a $\Delta\eta \times \Delta\phi$ region of 0.2×0.2. A *multi-muon scan* trigger can be implemented to overcome this issue and select multiple muons falling in the same RoI. In this way a L0 trigger can be defined as the logical OR of a muon trigger with $p_\text{T} > 20\,\text{GeV}$ and a multi-muon scan with $p_\text{T} > 10\,\text{GeV}$.

Non-pointing muons from slow γ_d are not identified by the current trigger algorithm, which is based on a constraint on the interaction point. Nevertheless, such non-pointing muons with $p_\text{T} > 20\,\text{GeV}$ can simulate a lower momentum track and fire a low-p_T threshold of $5\,\text{GeV}$ which is usually prescaled during normal runs. In order to be able to trigger on these muons, the sagitta of their track can be extracted from the geometrical information of the RPC hits. Hence, a new L0 trigger (*L0 muon sagitta trigger*) can be defined by applying a requirement on the measured sagitta, in addition to a $5\,\text{GeV}$ threshold.

The results of the Early Run-II search for displaced DPJs are extrapolated to HL-LHC, after taking into account the improved trigger acceptance, as well as the increase in luminosity and the extrapolated systematic uncertainties, which are recomputed to take into account the higher pile-up levels of HL-LHC.

Figure A.5 show the expected limits at 95% CL, on the product of the cross section and the branching ratio of $H \to 2\gamma_d + X$, as function of the γ_d decay lifetime, obtained considering a dark photon with $m = 0.4\,\text{GeV}$ produced according to the FRVZ process. For a choice of the Higgs branching fraction of 10%, the corresponding excluded $c\tau$ values are the ones between $0.97\,\text{mm}$ and $597\,\text{mm}$. For comparison, the interval reported in table 5.11, which is made with the same hypothesis on the Higgs boson branching ratio, correspond to $0.654\,\text{mm} < c\tau < 939\,\text{mm}$. The improvements obtained with the full Run-II iteration of the analysis are already visible at this stage, highlighting how the extrapolation to the Phase-II conditions of the displaced DPJ result should be considered outdated.

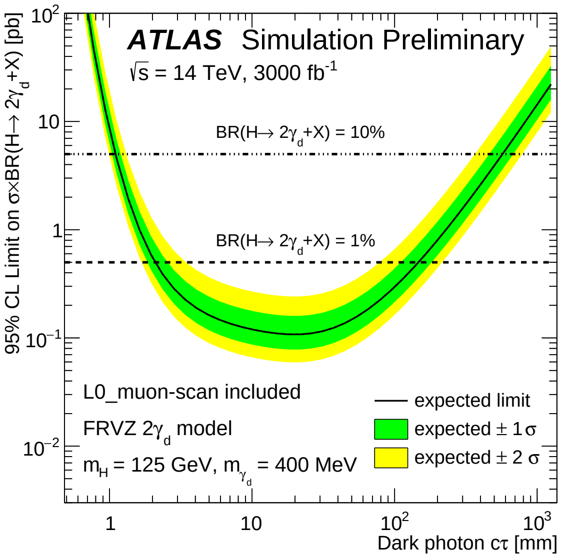

Figure A.5. 95% CL limit on the cross section times branching fraction of the FRVZ process, shown as a function of the γ_d lifetime. This limit is obtained by considering the Early Run-II result and extrapolating it to $3000\,\mathrm{fb}^{-1}$ and taking into account the foreseen improvements of the muon trigger for HL-LHC. Figure from [120].

Bibliography

[1] ATLAS Collaboration. "Search for light long-lived neutral particles that decay to collimated pairs of leptons or light hadrons with the ATLAS detector in $139\,\mathrm{fb}^{-1}$ of data collected in proton-proton collisions at $\sqrt{s} = 13$ TeV". ATLAS-CONF-2022-001. 2022. URL: http://cds.cern.ch/record/2799602.

[2] ATLAS Collaboration. "Search for light long-lived neutral particles produced in pp collisions at $\sqrt{s} = 13$ TeV and decaying into collimated leptons or light hadrons with the ATLAS detector". *The European Physical Journal C* 80.5 (May 2020), p. 450. DOI: 10.1140/epjc/s10052-020-7997-4. URL: https://doi.org/10.1140/epjc/s10052-020-7997-4.

[3] ATLAS Collaboration. "Search for new phenomena in events with an energetic jet and missing transverse momentum in pp collisions at $\sqrt{s} = 13$ TeV with the ATLAS detector". *Physical Review D* 103.11 (June 2021). DOI: 10.1103/physrevd.103.112006. URL: http://dx.doi.org/10.1103/PhysRevD.103.112006.

[4] ATLAS Collaboration. "Constraining the dark sector with the monojet signature in the ATLAS experiment". ATL-PHYS-PUB-2021-020. 2021. URL: https://cds.cern.ch/record/2772627.

[5] S. Weinberg. "A Model of Leptons". *Phys. Rev. Lett.* 19 (1967), pp. 1264–1266. DOI: 10.1103/PhysRevLett.19.1264.

[6] A. Salam et al. "Weak and electromagnetic interactions". *Nuovo Cim.* 11 (1959), pp. 568–577. DOI: 10.1007/BF02726525.

[7] "Standard Model Summary Plots June 2021". Tech. rep. Geneva: CERN, July 2021. URL: http://cds.cern.ch/record/2777014.

[8] ATLAS Collaboration. "Observation of a new particle in the search for the Standard Model Higgs boson with the ATLAS detector at the LHC". *Physics Letters B* 716.1 (Sept. 2012), pp. 1–29. DOI: 10.1016/j.physletb.2012.08.020. URL: http://dx.doi.org/10.1016/j.physletb.2012.08.020.

[9] CMS Collaboration. "Observation of a new boson at a mass of 125 GeV with the CMS experiment at the LHC". *Physics Letters B* 716.1 (Sept. 2012), pp. 30–61. DOI: 10.1016/j.physletb.2012.08.021. URL: http://dx.doi.org/10.1016/j.physletb.2012.08.021.

[10] P.A. Zyla et al. "Review of Particle Physics". *PTEP* 2020.8 (2020), p. 083C01. DOI: 10.1093/ptep/ptaa104.

[11] ATLAS Collaboration. "A combination of measurements of Higgs boson production and decay using up to 139 fb^{-1} of proton–proton collision data at $\sqrt{s} = 13$ TeV collected with the ATLAS experiment". ATLAS-CONF-2020-027. 2020. URL: https://cds.cern.ch/record/2725733.

[12] CMS Collaboration. "Combined Higgs boson production and decay measurements with up to 137 fb^{-1} of proton-proton collision data at $\sqrt{s} = 13$ TeV". Tech. rep. Geneva: CERN, 2020. URL: https://cds.cern.ch/record/2706103.

[13] Brian Shuve. "Theory overview of long-lived particles at the LHC". 2017.

[14] Brian Batell et al. "Probing a secluded U(1) at B-factories". *Physical Review D* 79.11 (June 2009). DOI: 10.1103/physrevd.79.115008. URL: http://dx.doi.org/10.1103/PhysRevD.79.115008.

[15] David Curtin et al. "Illuminating dark photons with high-energy colliders". *Journal of High Energy Physics* 2015.2 (Feb. 2015). DOI: 10.1007/jhep02(2015)157. URL: http://dx.doi.org/10.1007/JHEP02(2015)157.

[16] Philip Ilten et al. "Serendipity in dark photon searches". *Journal of High Energy Physics* 2018.6 (June 2018). DOI: 10.1007/jhep06(2018)004. URL: http://dx.doi.org/10.1007/JHEP06(2018)004.

[17] "Darkcast GitLab repository". URL: https://gitlab.com/philten/darkcast.

[18] ATLAS Collaboration. "Combination of searches for invisible Higgs boson decays with the ATLAS experiment". ATLAS-CONF-2020-052. 2020. URL: https://cds.cern.ch/record/2743055.

[19] Adam Falkowski et al. "Hidden Higgs decaying to lepton jets". *Journal of High Energy Physics* 2010.5 (May 2010). DOI: 10.1007/jhep05(2010)077. URL: http://dx.doi.org/10.1007/JHEP05(2010)077.

[20] Adam Falkowski et al. "Discovering Higgs Boson Decays to Lepton Jets at Hadron Colliders". *Physical Review Letters* 105.24 (Dec. 2010). DOI: 10.1103/physrevlett.105.241801. URL: http://dx.doi.org/10.1103/PhysRevLett.105.241801.

[21] David Curtin et al. "Exotic decays of the 125 GeV Higgs boson". *Phys. Rev. D* 90 (7 Oct. 2014), p. 075004. DOI: 10.1103/PhysRevD.90.075004. URL: https://link.aps.org/doi/10.1103/PhysRevD.90.075004.

[22] Lyndon Evans et al. "LHC Machine". *JINST* 3.08 (2008), S08001. URL: http://stacks.iop.org/1748-0221/3/i=08/a=S08001.

[23] Esma Mobs. "The CERN accelerator complex". Aug. 2018. URL: https://cds.cern.ch/record/2636343.

[24] ATLAS Collaboration. "The ATLAS Experiment at the CERN Large Hadron Collider". *JINST* 3.08 (2008), S08003. URL: http://stacks.iop.org/1748-0221/3/i=08/a=S08003.

[25] CMS Collaboration. "The CMS detector at the LHC". *JINST* 3.08 (2008), S08004. URL: http://stacks.iop.org/1748-0221/3/i=08/a=S08004.

[26] The LHCb Collaboration. "The LHCb Detector at the LHC". *JINST* 3.08 (2008), S08005. URL: http://stacks.iop.org/1748-0221/3/i=08/a=S08005.

[27] The ALICE Collaboration. “The ALICE experiment at the CERN LHC”. *JINST* 3.08 (2008), S08002. URL: http://stacks.iop.org/1748-0221/3/i=08/a=S08002.

[28] ATLAS Collaboration. “Luminosity Public Results Run-2”. URL: https://twiki.cern.ch/twiki/bin/view/AtlasPublic/LuminosityPublicResultsRun2.

[29] R Bailey et al. “Standard Filling Schemes for Various LHC Operation Modes”. Tech. rep. Geneva: CERN, Sept. 2003. URL: https://cds.cern.ch/record/691782.

[30] ATLAS Collaboration. “Characterisation and mitigation of beam-induced backgrounds observed in the ATLAS detector during the 2011 proton-proton run”. *Journal of Instrumentation* 8.07 (July 2013), P07004–P07004. DOI: 10.1088/1748-0221/8/07/p07004. URL: https://doi.org/10.1088/1748-0221/8/07/p07004.

[31] Joao Pequenao. “Computer generated image of the whole ATLAS detector”. Mar. 2008. URL: https://cds.cern.ch/record/1095924.

[32] ATLAS Collaboration. “ATLAS Technical Co-ordination: Technical Design Report”. ATLAS-TDR-13; CERN-LHCC-99-001. 1999. URL: https://cds.cern.ch/record/385482.

[33] ATLAS Collaboration. “ATLAS Magnet System: Magnet Project Technical Design Report, Volume 1”. ATLAS-TDR-6; CERN-LHCC-97-018. 1997. URL: https://cds.cern.ch/record/338080.

[34] ATLAS Collaboration. “Study of the material of the ATLAS inner detector for Run 2 of the LHC”. *Journal of Instrumentation* 12.12 (Dec. 2017), P12009–P12009. DOI: 10.1088/1748-0221/12/12/p12009. URL: https://doi.org/10.1088/1748-0221/12/12/p12009.

[35] ATLAS Collaboration. “ATLAS Insertable B-Layer: Technical Design Report”. ATLAS-TDR-19; CERN-LHCC-2010-013. 2010. URL: https://cds.cern.ch/record/1291633. Addendum: ATLAS-TDR-19-ADD-1; CERN-LHCC-2012-009. 2012. URL: https://cds.cern.ch/record/1451888.

[36] ATLAS Collaboration. “ATLAS Liquid Argon Calorimeter: Technical Design Report”. ATLAS-TDR-2; CERN-LHCC-96-041. 1996. URL: https://cds.cern.ch/record/331061.

[37] B. Aubert et al. “Construction, assembly and tests of the ATLAS electromagnetic barrel calorimeter”. *Nucl. Instrum. Methods Phys. Res., Sect. A* 558.2 (2006), pp. 388–418. DOI: https://doi.org/10.1016/j.nima.2005.11.212. URL: https://www.sciencedirect.com/science/article/pii/S016890020502382X.

[38] ATLAS Collaboration. “ATLAS Muon Spectrometer: Technical Design Report”. ATLAS-TDR-10; CERN-LHCC-97-022. CERN, 1997. URL: https://cds.cern.ch/record/331068.

[39] ATLAS Collaboration. “ATLAS Level-1 Trigger: Technical Design Report”. ATLAS-TDR-12; CERN-LHCC-98-014. 1998. URL: https://cds.cern.ch/record/381429.

[40] ATLAS Collaboration. “Performance of the ATLAS muon triggers in Run 2”. *JINST* 15.09 (2020), P09015. DOI: 10.1088/1748-0221/15/09/p09015. arXiv: 2004.13447 `[physics.ins-det]`.

[41] Rosa Simoniello. “The ATLAS Level-1 Topological Processor: from design to routine usage in Run-2”. *2018 IEEE Nuclear Science Symposium and Medical Imaging Conference Proceedings (NSS/MIC)*. IEEE. 2018, pp. 1–4.

[42] The ATLAS collaboration. “Operation of the ATLAS trigger system in Run 2”. 15.10 (Oct. 2020), P10004–P10004. DOI: 10.1088/1748-0221/15/10/p10004. URL: https://doi.org/10.1088/1748-0221/15/10/p10004.

[43] ATLAS Collaboration. “The ATLAS Simulation Infrastructure”. *The European Physical Journal C* 70.3 (Dec. 2010), pp. 823–874. DOI: 10.1140/epjc/s10052-010-1429-9. URL: https://doi.org/10.1140/epjc/s10052-010-1429-9.

[44] V.N Ivanchenko. “Geant4 toolkit for simulation of HEP experiments”. *Nucl. Instrum. Methods Phys. Res., Sect. A* 502.2 (2003), pp. 666–668. DOI: https://doi.org/10.1016/S0168-9002(03)00538-2.

[45] ATLAS Collaboration. “Athena”. May 2021. DOI: 10.5281/zenodo.2641996. URL: https://doi.org/10.5281/zenodo.2641996.

[46] G. Barrand et al. “GAUDI — A software architecture and framework for building HEP data processing applications”. *Computer Physics Communications* 140.1 (2001), pp. 45–55. DOI: https://doi.org/10.1016/S0010-4655(01)00254-5. URL: https://www.sciencedirect.com/science/article/pii/S0010465501002545.

[47] ATLAS Collaboration. “Event Displays from Run-2 physics analyses not included in publications”. URL: https://twiki.cern.ch/twiki/bin/view/AtlasPublic/EventDisplayRun2Physics.

[48] R. Frühwirth. “Application of Kalman filtering to track and vertex fitting”. *Nucl. Instrum. Methods Phys. Res., Sect. A* 262.2 (1987), pp. 444–450. DOI: https://doi.org/10.1016/0168-9002(87)90887-4. URL: https://www.sciencedirect.com/science/article/pii/0168900287908874.

[49] ATLAS Collaboration. “Track Reconstruction Performance of the ATLAS Inner Detector at $\sqrt{s} = 13$ TeV”. ATL-PHYS-PUB-2015-018. 2015. URL: https://cds.cern.ch/record/2037683.

[50] ATLAS Collaboration. “Performance of the ATLAS track reconstruction algorithms in dense environments in LHC Run 2”. *The European Physical Journal C* 77.10 (Oct. 2017), p. 673. DOI: 10.1140/epjc/s10052-017-5225-7. URL: https://doi.org/10.1140/epjc/s10052-017-5225-7.

[51] ATLAS Collaboration. “Reconstruction of primary vertices at the ATLAS experiment in Run 1 proton–proton collisions at the LHC”. *The European Physical Journal C* 77.5 (May 2017), p. 332. DOI: 10.1140/epjc/s10052-017-4887-5. URL: https://doi.org/10.1140/epjc/s10052-017-4887-5.

[52] ATLAS Collaboration. “Topological cell clustering in the ATLAS calorimeters and its performance in LHC Run 1”. *The European Physical Journal C* 77.7 (July 2017), p. 490. DOI: 10.1140/epjc/s10052-017-5004-5. URL: https://doi.org/10.1140/epjc/s10052-017-5004-5.

[53] Matteo Cacciari et al. “The anti-ktjet clustering algorithm”. *Journal of High Energy Physics* 2008.04 (Apr. 2008), pp. 063–063. DOI: 10.1088/1126-6708/2008/04/063. URL: http://dx.doi.org/10.1088/1126-6708/2008/04/063.

[54] ATLAS Collaboration. “Jet reconstruction and performance using particle flow with the ATLAS Detector”. *The European Physical Journal C* 77.7 (July 2017), p. 466. DOI: 10.1140/epjc/s10052-017-5031-2. URL: https://doi.org/10.1140/epjc/s10052-017-5031-2.

[55] ATLAS Collaboration. “Jet energy scale and resolution measured in proton–proton collisions at $\sqrt{s} = 13$ TeV with the ATLAS detector”. *The European Physical Journal C* 81.8 (Aug. 2021), p. 689. DOI: 10.1140/epjc/s10052-021-09402-3. URL: https://doi.org/10.1140/epjc/s10052-021-09402-3.

[56] ATLAS Collaboration. “Tagging and suppression of pileup jets with the ATLAS detector”. ATLAS-CONF-2014-018. 2014. URL: https://cds.cern.ch/record/1700870.

[57] ATLAS Collaboration. “Selection of jets produced in 13 TeV proton–proton collisions with the ATLAS detector”. ATLAS-CONF-2015-029. 2015. URL: https://cds.cern.ch/record/2037702.

[58] ATLAS Collaboration. “Optimisation and performance studies of the ATLAS b-tagging algorithms for the 2017-18 LHC run”. ATL-PHYS-PUB-2017-013. 2017. URL: https://cds.cern.ch/record/2273281.

[59] ATLAS Collaboration. “ATLAS b-jet identification performance and efficiency measurement with $t\bar{t}$ events in pp collisions at $\sqrt{s} = 13$ TeV”. *The European Physical Journal C* 79.11 (Nov. 2019). DOI: 10.1140/epjc/s10052-019-7450-8. URL: http://dx.doi.org/10.1140/epjc/s10052-019-7450-8.

[60] ATLAS Collaboration. “Secondary vertex finding for jet flavour identification with the ATLAS detector”. ATL-PHYS-PUB-2017-011. 2017. URL: https://cds.cern.ch/record/2270366.

[61] ATLAS Collaboration. “Topological b-hadron decay reconstruction and identification of b-jets with the JetFitter package in the ATLAS experiment at the LHC”. ATL-PHYS-PUB-2018-025. 2018. URL: https://cds.cern.ch/record/2645405.

[62] ATLAS Collaboration. “Electron and photon performance measurements with the ATLAS detector using the 2015–2017 LHC proton-proton collision data”. 14.12 (Dec. 2019), P12006–P12006. DOI: 10.1088/1748-0221/14/12/p12006. URL: https://doi.org/10.1088/1748-0221/14/12/p12006.

[63] ATLAS Collaboration. “Improved electron reconstruction in ATLAS using the Gaussian Sum Filter-based model for bremsstrahlung”. ATLAS-CONF-2012-047. 2012. URL: https://cds.cern.ch/record/1449796.

[64] J. Illingworth et al. "A survey of the hough transform". *Computer Vision, Graphics, and Image Processing* 44.1 (1988), pp. 87–116. DOI: https://doi.org/10.1016/S0734-189X(88)80033-1. URL: https://www.sciencedirect.com/science/article/pii/S0734189X88800331.

[65] ATLAS Collaboration. "Muon reconstruction and identification efficiency in ATLAS using the full Run 2 pp collision data set at $\sqrt{s} = 13$ TeV". *The European Physical Journal C* 81.7 (July 2021), p. 578. DOI: 10.1140/epjc/s10052-021-09233-2. URL: https://doi.org/10.1140/epjc/s10052-021-09233-2.

[66] ATLAS Collaboration. "$E_{\mathrm{T}}^{\mathrm{miss}}$ performance in the ATLAS detector using 2015–2016 LHC pp collisions". ATLAS-CONF-2018-023. 2018. URL: https://cds.cern.ch/record/2625233.

[67] J. Alwall et al. "The automated computation of tree-level and next-to-leading order differential cross sections, and their matching to parton shower simulations". *Journal of High Energy Physics* 2014.7 (July 2014). DOI: 10.1007/jhep07(2014)079. URL: http://dx.doi.org/10.1007/JHEP07(2014)079.

[68] Torbjörn Sjöstrand et al. "An introduction to PYTHIA 8.2". *Comput. Phys. Commun.* 191 (2015), p. 159. DOI: 10.1016/j.cpc.2015.01.024. arXiv: 1410.3012 `[hep-ph]`.

[69] Richard D. Ball et al. "Parton distributions with LHC data". *Nuclear Physics B* 867.2 (Feb. 2013), pp. 244–289. DOI: 10.1016/j.nuclphysb.2012.10.003. URL: http://dx.doi.org/10.1016/j.nuclphysb.2012.10.003.

[70] ATLAS Collaboration. "ATLAS Pythia 8 tunes to 7 TeV data". ATL-PHYS-PUB-2014-021. 2014. URL: https://cds.cern.ch/record/1966419.

[71] ATLAS Collaboration. "Performance of the ATLAS Trigger System in 2010". *Eur. Phys. J. C* 72 (2012), p. 1849. DOI: 10.1140/epjc/s10052-011-1849-1. arXiv: 1110.1530 `[hep-ex]`.

[72] ATLAS Collaboration. "Triggers for displaced decays of long-lived neutral particles in the ATLAS detector". *Journal of Instrumentation* 8.07 (July 2013), P07015–P07015. DOI: 10.1088/1748-0221/8/07/p07015. URL: https://doi.org/10.1088/1748-0221/8/07/p07015.

[73] ATLAS Collaboration. "Performance of electron and photon triggers in ATLAS during LHC Run 2". *Eur. Phys. J. C* 80.1 (2020), p. 47. DOI: 10.1140/epjc/s10052-019-7500-2. arXiv: 1909.00761 `[hep-ex]`.

[74] Yu.L Dokshitzer et al. "Better jet clustering algorithms". *JHEP* 08 (1997), pp. 001–001. DOI: 10.1088/1126-6708/1997/08/001. arXiv: hep-ph/9707323 `[hep-ph]`.

[75] Josh Cogan et al. "Jet-images: computer vision inspired techniques for jet tagging". *Journal of High Energy Physics* 2015.2 (Feb. 2015). DOI: 10.1007/jhep02(2015)118. URL: http://dx.doi.org/10.1007/JHEP02(2015)118.

[76] Luke de Oliveira et al. "Jet-images — deep learning edition". *Journal of High Energy Physics* 2016.7 (July 2016). DOI: 10.1007/jhep07(2016)069. URL: http://dx.doi.org/10.1007/JHEP07(2016)069.

[77] ATLAS Collaboration. "Quark versus Gluon Jet Tagging Using Jet Images with the ATLAS Detector". ATL-PHYS-PUB-2017-017. 2017. URL: https://cds.cern.ch/record/2275641.

[78] "Keras: the Python deep learning API". URL: https://keras.io.

[79] M. Abadi et al. "TensorFlow: Large-Scale Machine Learning on Heterogeneous Systems". 2015. URL: https://www.tensorflow.org/.

[80] "Keras API reference". URL: https://keras.io/api.

[81] Richard D. Ball et al. "Parton distributions with LHC data". *Nucl. Phys. B* 867 (2013), p. 244. DOI: 10.1016/j.nuclphysb.2012.10.003. arXiv: 1207.1303 `[hep-ph]`.

[82] G. Avoni et al. "The new LUCID-2 detector for luminosity measurement and monitoring in ATLAS". *Journal of Instrumentation* 13.07 (July 2018), P07017–P07017. DOI: 10.1088/1748-0221/13/07/p07017. URL: https://doi.org/10.1088/1748-0221/13/07/p07017.

[83] ATLAS Collaboration. "Luminosity determination in pp collisions at $\sqrt{s} =$ 13 TeV using the ATLAS detector at the LHC". ATLAS-CONF-2019-021. 2019. URL: https://cds.cern.ch/record/2677054.

[84] Piotr Golonka et al. "PHOTOS Monte Carlo: a precision tool for QED corrections in Z and W decays". *Eur. Phys. J. C* 45 (2006), pp. 97–107. DOI: 10.1140/epjc/s2005-02396-4. arXiv: hep-ph/0506026.

[85] J. Gao et al. "CT10 next-to-next-to-leading order global analysis of QCD". *Phys. Rev. D* 89 (2014), p. 033009. DOI: 10.1103/PhysRevD.89.033009. arXiv: 1302.6246 `[hep-ph]`.

[86] J. Pumplin et al. "New Generation of Parton Distributions with Uncertainties from Global QCD Analysis". *JHEP* 07 (2002), p. 012. DOI: 10.1088/1126-6708/2002/07/012. arXiv: hep-ph/0201195.

[87] ATLAS Collaboration. "Search for lived neutral particles in pp collisions at $\sqrt{s} = 13$ TeV that decay into displaced hadronic jets in the ATLAS calorimeter". *The European Physical Journal C* 79.6 (June 2019). DOI: 10.1140/epjc/s10052-019-6962-6. URL: http://dx.doi.org/10.1140/epjc/s10052-019-6962-6.

[88] A. L. Read. "Presentation of search results: the CL_s technique". *J. Phys. G* 28 (2002), pp. 2693–2704. DOI: 10.1088/0954-3899/28/10/313.

[89] Glen Cowan et al. "Asymptotic formulae for likelihood-based tests of new physics". *Eur. Phys. J. C* 71 (2011), p. 1554. DOI: 10.1140/epjc/s10052-011-1554-0. arXiv: 1007.1727 `[physics.data-an]`. Erratum: *Eur. Phys. J. C* 73 (2013), p. 2501. DOI: 10.1140/epjc/s10052-013-2501-z.

[90] ATLAS Collaboration. "A search for prompt lepton-jets in pp collisions at $\sqrt{s} = 8$ TeV with the ATLAS detector". *JHEP* 02 (2016), p. 062. DOI: 10.1007/JHEP02(2016)062. arXiv: 1511.05542 `[hep-ex]`.

[91] Kyle Cranmer et al. "RECAST: Extending the Impact of Existing Analyses". *JHEP* 04 (2011), p. 038. DOI: 10.1007/JHEP04(2011)038. arXiv: 1010.2506 `[hep-ex]`.

[92] ATLAS Collaboration. “Search for light long-lived neutral particles produced in pp collisions at $\sqrt{s} = 13$ TeV and decaying into collimated leptons or light hadrons with the ATLAS detector”. *Eur. Phys. J. C* 80 (2020), p. 450. DOI: 10.1140/epjc/s10052-020-7997-4. arXiv: 1909.01246 `[hep-ex]`.

[93] M. Aaboud et al. “Search for the Higgs boson produced in association with a vector boson and decaying into two spin-zero particles in the $H \to aa \to 4b$ channel in pp collisions at $\sqrt{s} = 13$ TeV with the ATLAS detector”. *JHEP* 10 (2018), p. 031. DOI: 10.1007/JHEP10(2018)031. arXiv: 1806.07355 `[hep-ex]`.

[94] ATLAS Collaboration. “Search for exotic decays of the Higgs boson to long-lived particles in pp collisions at $\sqrt{s} = 13$ TeV using displaced vertices in the ATLAS inner detector”. ATLAS-CONF-2021-005. 2021. URL: https://cds.cern.ch/record/2759209.

[95] I. Zurbano Fernandez et al. “High-Luminosity Large Hadron Collider (HL-LHC): Technical design report”. 10/2020 (Dec. 2020). Ed. by I. Béjar Alonso et al. DOI: 10.23731/CYRM-2020-0010.

[96] ATLAS Collaboration. “ATLAS Inner Tracker Pixel Detector: Technical Design Report”. ATLAS-TDR-030; CERN-LHCC-2017-021. 2017. URL: https://cds.cern.ch/record/2285585.

[97] ATLAS Collaboration. “ATLAS Inner Tracker Strip Detector: Technical Design Report”. ATLAS-TDR-025; CERN-LHCC-2017-005. 2017. URL: https://cds.cern.ch/record/2257755.

[98] ATLAS Collaboration. “A High-Granularity Timing Detector for the ATLAS Phase-II Upgrade: Technical Design Report”. ATLAS-TDR-031; CERN-LHCC-2020-007. 2020. URL: https://cds.cern.ch/record/2719855.

[99] ATLAS Collaboration. “ATLAS LAr Calorimeter Phase-II Upgrade: Technical Design Report”. ATLAS-TDR-027; CERN-LHCC-2017-018. 2017. URL: https://cds.cern.ch/record/2285582.

[100] ATLAS Collaboration. “ATLAS Liquid Argon Calorimeter Phase-I Upgrade: Technical Design Report”. ATLAS-TDR-022; CERN-LHCC-2013-017. 2013. URL: https://cds.cern.ch/record/1602230.

[101] ATLAS Collaboration. “ATLAS Muon Spectrometer Phase-II Upgrade: Technical Design Report”. ATLAS-TDR-026; CERN-LHCC-2017-017. 2017. URL: https://cds.cern.ch/record/2285580.

[102] ATLAS Collaboration. “ATLAS New Small Wheel: Technical Design Report”. ATLAS-TDR-020; CERN-LHCC-2013-006. 2013. URL: https://cds.cern.ch/record/1552862.

[103] ATLAS Collaboration. “ATLAS TDAQ Phase-II Upgrade: Technical Design Report”. ATLAS-TDR-029; CERN-LHCC-2017-020. 2017. URL: https://cds.cern.ch/record/2285584.

[104] ATLAS Collaboration. “Performance of the ATLAS RPC detector and Level-1 muon barrel trigger at $\sqrt{s} = 13$ TeV”. *JINST* 16 (2021), P07029. DOI: 10.1088/1748-0221/16/07/P07029. arXiv: 2103.01029 `[hep-ex]`.

[105] "LpGBT-FPGA Documentation". URL: http://lpgbt-fpga.web.cern.ch/doc/html/.

[106] James R. Schwank et al. "Radiation Effects in MOS Oxides". *IEEE Transactions on Nuclear Science* 55.4 (2008), pp. 1833–1853. DOI: 10.1109/TNS.2008.2001040.

[107] Michael Moll. "Radiation damage in silicon particle detectors: Microscopic defects and macroscopic properties". Dr. Universität Hamburg, 1999, p. 251. URL: https://bib-pubdb1.desy.de/record/300958.

[108] A. Vasilescu and G. Lindstroem. "Displacement damage in silicon". 2000. URL: https://rd50.web.cern.ch/niel/.

[109] ATLAS Collaboration. "Interactive web pages for radiation environment exploration of ATLAS". ATL-SOFT-PUB-2020-003. 2020. URL: https://cds.cern.ch/record/2742378.

[110] Stefan Ritt. "DRS4 Evaluation Board User's Manual". 2015. URL: https://1508c6b5-f844-4547-af43-8c66fbe7f04a.filesusr.com/ugd/7c1aba_83d38c6ff3e44dada8b116b490018e62.pdf.

[111] Michele Prata et al. "Italian Neutron Sources". *The European Physical Journal - Plus* (Jan. 2014).

[112] MCNP Development Team. "MCNP 6.2.0 Release Testing". Sept. 2017. URL: https://mcnp.lanl.gov/pdf_files/la-ur-17-29011.pdf.

[113] G. Spiezia et al. "A New RadMon Version for the LHC and its Injection Lines". *IEEE Transactions on Nuclear Science* 61.6 (2014), pp. 3424–3431. DOI: 10.1109/TNS.2014.2365046.

[114] M. Moll F. Ravotti M. Glaser. "SENSOR CATALOGUE Data compilation of solid-state sensors for radiation monitoring". URL: https://edms.cern.ch/document/590497/1.

[115] Federico Ravotti. "Development and Characterisation of Radiation Monitoring Sensors for the High Energy Physics Experiments of the CERN LHC Accelerator". 2006. URL: https://cds.cern.ch/record/1014776.

[116] "Proton Irradiation Facility - PSI". http://pif.web.psi.ch/.

[117] CMS Collaboration. "A search for pair production of new light bosons decaying into muons in proton-proton collisions at 13 TeV". *Phys. Lett. B* 796 (2019), pp. 131–154. DOI: 10.1016/j.physletb.2019.07.013. arXiv: 1812.00380 `[hep-ex]`.

[118] CMS Collaboration. "Search for long-lived particles decaying to a pair of muons in proton-proton collisions at $\sqrt{s} = 13$ TeV". CMS-PAS-EXO-21-006. Geneva, 2022. URL: https://cds.cern.ch/record/2799212.

[119] "CMS Collaboration". "Search for long-lived particles decaying into muon pairs in proton-proton collisions at $\sqrt{s} = 13$ TeV collected with a dedicated high-rate data stream". *Journal of High Energy Physics* 2022.4 (Apr. 2022), p. 62. DOI: 10.1007/JHEP04(2022)062. URL: https://doi.org/10.1007/JHEP04(2022)062.

[120] ATLAS Collaboration. “Search prospects for dark-photons decaying to displaced collimated jets of muons at HL-LHC”. ATL-PHYS-PUB-2019-002. 2019. URL: https://cds.cern.ch/record/2654518.

Acknowledgments

I can not start this section without expressing my gratitude to Stefano Giagu, for being not only a supervisior, but a guidance during this three-year journey. I would like to thank him for providing the right input at the right moment, pushing me to do better and allowing me to follow my own interests in physics.

This work would not have been possible without the help of Cristiano Sebastiani, who constantly supported me and the team of my analysis during my PhD. I would like to thank him for being a good friend, for having a lot of patience with me and for teaching me to find when it's the right time to stop overthinking and making things more complicated (I must admit that I still learning this last thing). I want to thank also the other people involved in the analysis, in particular Alessandro Biondini that contributed to the studies of the WH analysis channels.

I would like to thank Massimo Corradi and Riccardo Vari, for their fundamental support during the work related to the ATLAS upgrade. I am very happy to have been involved in these activities that I believe are fundamental in the background of a particle physicist.

A special thanks goes to Valerio Ippolito, for his willingness to share his experience when I needed. I am very thankful to him and also to Matteo Bauce and Giuliano Gustavino, for the time they dedicated to me, answering my questions and proposing many solutions to overcome the problems that I found.

I have to admit that this journey would have not been the same without my friends and collegues Guglielmo Frattari, Luigi Sabetta, Simone Francescato and Damiano Vannicola (and, again, Cristiano Sebastiani). I am very happy for the time we spent together inside and outside our ~~office~~ *saletta*, discussing about various non-physics and physics-related topics, sharing fancy trips and living a large collection of funny moments. The path that I followed as a PhD student would have been a hundred times more difficult without your presence. Thanks also to the other people that joined the *saletta* its related adventures: Maria Carnesale, Lorenzo Santi, Elena Pompa Pacchi, Giovanni Padovano and Federico Morodei.

A huge thanks goes to the people that crossed my path before and after moving to Geneva: Raffaella Tramontano, Leonardo Vannoli, Dario Baffari, Andrea Ciarma, Silvia Auricchio, Luca Martinelli, Federica Riti, Valerio D'Amico, Chiara Arcangeletti and Lorenzo Massa (and many others). I really enjoyed the time we spent staying together.

Many thanks to my University friends Michele Meo, Noemi Domizi, Gian Luca Lancia, Emanuele Marconato and Mattia Eluchans for the time we spent together between lectures and outside. A huge thanks goes to Fabiana Natali, for being always by my side. A special thanks to all my other friends that supported me before and during my PhD, even if I disappeared quite a lot of times during these years I've always appreciated the time we spent together. In particular, I would like to thank Riccardo Valeri and Marco Pontecorvo for being always there for me, no matter what.

Grazie di cuore alla mia famiglia, ma in particolare grazie a mio padre Vittorio, mia *madre Daniela e mia sorella Clelia. Se non fosse stato per il vostro continuo incoraggiamento e supporto non sarei mai arrivato dove sono, ricordatevi sempre che questo lavoro è anche frutto del vostro aiuto.*

Un grazie speciale a zia Claudia, se oggi sono qui a scrivere questi ringraziamenti è anche merito tuo per aver alimentato la mia curiosità sin da piccolo.

Infine, un immenso grazie a Eleonora, per cui le parole non saranno mai abbastanza. Grazie per aver avuto quella santa pazienza di amarmi e sopportarmi e, sin dall'inizio di questo viaggio, per aver sempre creduto in me.